

Nanocrystalline Silicon-Germanium Alloy Thin Films: Synthesis, Characterization and Optimization for Silicon Solar Cells

Thesis Submitted For The Degree Of

Doctor of Philosophy (Science)

In

Physics (Experimental)

To The

JADAVPUR UNIVERSITY

2022

by

AMARESH DEY

(Index No. 1/18/Phys./25)

Energy Research Unit,
School of Materials Sciences,
Indian Association for the Cultivation of Science,
Jadavpur, Kolkata - 700032, INDIA



इंडियन एसोसियेशन फर दि कल्चिवेशन आफ साइंस
इंडियन एसोसियेशन फर दि कल्चिवेशन आफ साइंस
INDIAN ASSOCIATION FOR THE CULTIVATION OF SCIENCE

Certificate from the Supervisor

This is to certify that the thesis entitled "**Nanocrystalline Silicon-Germanium Alloy Thin Films: Synthesis, Characterization and Optimization for Silicon Solar Cells**" submitted by **Sri Amaresh Dey** who got his name registered on **04.01.2018** [Index No. 1/18/Phys./25] for the award of Ph.D. (Science) degree of the Jadavpur University, is absolutely based upon his own work under the supervision of **Prof. Debajyoti Das** and that neither this thesis or any part of it has been submitted for any degree / diploma or any other academic award anywhere before.

Date: 25/4/2022

Debajyoti Das

(Prof. Debajyoti Das)

(Email: erdd@iacs.res.in)



Dr. Debajyoti Das

Sr. Professor

Energy Research Unit

Indian Association for the Cultivation of Science
Jadavpur, Kolkata - 700 032

(Signature of the Supervisor with official seal)

र. एंड पी. एच. एच. वि. मल्लिक रोड, जदवपुर, कोलकाता 700 032 2A & B, RAJA S C MULLICK ROAD, JADAVPUR, KOLKATA - 700 032

दूरभाष / Phone : 473-4971, 3372, 3073 / FAX (91) (33) 473 2805 / GRAM : इंडासन / INDASSON, जदवपुर / JADAVPUR

Declaration

I hereby declare that the work entitled "**Nanocrystalline Silicon-Germanium Alloy Thin Films: Synthesis, Characterization and Optimization for Silicon Solar Cells**" submitted to the Jadavpur University, Kolkata is a record of original work by me under the guidance of Prof. Debajyoti Das, Senior Professor, Energy Research Unit, School of Materials Sciences, I.A.C.S., Kolkata. This work has not performed the basis for the award of any other degree.

Amaresh Dey. 25/04/22

(Amaresh Dey)

Mobile: 8017070072 / 9874381420

Email: amareshdey23phys@gmail.com

Index No.: 1/18/Phys./25

Date of Registration: 04.01.2018

Dedicated to my Family...

*For their endless love, support, encouragement and
prayers*

Acknowledgement

I would like to express my thanks to several people who helped me with various aspects of conducting research and the writing of this thesis.

*It is my privilege to express my sincere thanks, deep sense of gratitude and indebtedness to my teacher and Ph.D. supervisor **Prof. Debajyoti Das**, Energy Research Unit, School of Materials Sciences, Indian Association for the Cultivation of Science, Kolkata, for his active guidance, stimulating initiation, advice, whole-hearted encouragement and unflinching support in accomplishing the present investigation. Besides his contagious excitement, he was critical in providing unlimited ideas. He taught me that scientific research requires perseverance, endurance and dedicated quest. I am very much grateful to him for extending all the research opportunities in his laboratory to me and providing encouragement for successful pursuance of my Ph.D. program. His dynamism, incredible stamina and vigilant supervision on every second detail are constant sources of inspiration to me.*

*I want to acknowledge to the **Council of Scientific & Industrial Research (CSIR)** for the financial assistance in the form of Research Scholarship, to continue the research work.*

*I record my acknowledgement to my institute, **Indian Association for the Cultivation of Science (IACS)** for providing me all opportunities to pursue the research work and the administrative support during the tenure.*

I sincerely thank all the faculties, scholars and staff of Indian Association for the Cultivation of Science (IACS). I want to express my sincere thanks to Mr. Sutapesh Datta, Mr. Indranath Bhowmik, Mr. Dinabandhu Prasad, Mr. Dipankar Majumdar, Dr. Manas Ghosh, Dr. Shasanka Maji, Mr. Suman Guchait for their constant technical support throughout my research work.

I am especially thankful to my seniors Dr. Amit Banerjee, Dr. Debjit Kar and Dr. Praloy Mondal for sharing their understandings and giving correctional inputs regarding my task in the early stage of my research career. I want to heartily thank all my lab-mates Dr. Subhashis Samanta, Dr. Ajay Roy, Dr. Laxmikanta Karmakar, Dr. Pronay Makal, Prami Nandi, Kalyan Sarkar, Chandralina Patra, Sucharita Saha, Payel Sahu, Sukalyan Shyam and Brijmohan Paramanik enormous support whenever needed and for sharing some great times in the lab. I would like to extend my gratitude to Dr. Arindam Kole for his help to learn to operate the PECVD reactor.

I would like to dedicate this thesis to the most important persons in my life to my parents (Ajoy Kumar Dey and Lalita Dey), my elder brother (Animesh Dey), and

my sister-in-law (Sarmistha Dey) for their unconditional love and support throughout my life. Because of their hard work and sacrifices of my parents, I never had to worry about anything. They all kept me going, and this journey would not have been possible without them.

I would like to express my love and gratitude to Tanisha, who is always there with her love, understanding, whole-hearted support and never-ending encouragement.

Finally, I want to thank all of my teachers and all other elders who have contributed for what I am today.

**IACS, Kolkata.
April, 2022**

Amaresh Dey.
(Amaresh Dey) 25/04/22

Table of Contents

Abstract	v
List of Figures	vi-x
Glossary of Acronyms	xi-xiii
List of publications	xiv
Conference and Symposium	xv
Brief introduction to the author and energy research unit	xvi
Chapter 1: General introduction and motivation	1-13
2.1 Introduction	2
2.2 Motivation	7
1.3 Framework of the thesis.....	10
1.4 References.....	12
Chapter 2: Silicon and germanium solar cell materials and solar cells	14-31
2.1 Introduction	15
2.2 Silicon.....	15
2.3 An overview of different forms of Si used in photovoltaics	16
2.3.1 Crystalline silicon (c-Si)	16
2.3.2 Amorphous silicon (a-Si:H).....	17
2.3.3 Micro-/Nanocrystalline silicon ($\mu\text{c}/\text{nc-Si}$).....	19
2.3.4 Doped nanocrystalline silicon (p-type or n-type nc-Si).....	21
2.4 Germanium	23
2.5 Alloying Si with Ge	23
2.5.1 Amorphous silicon-germanium alloy (a-SiGe:H).....	23
2.5.2 Nanocrystalline silicon -germanium alloy (nc-SiGe:H)	24
2.6 Different types of silicon-based solar cells.....	24
2.6.1 Bulk crystalline silicon (c-Si) solar cell.....	24
2.6.2 Amorphous silicon (a-Si) solar cell.....	26
2.6.3 Micro/Nano-crystalline silicon ($\mu\text{c}/\text{nc:H}$) solar cell	27
2.6.4 nc-Si multi-junction or tandem-structure solar cell.....	28
2.7 References.....	29
Chapter 3: Thin film deposition techniques	32-53
3.1 Introduction.....	33
3.2 Processing techniques of thin film deposition	33

3.3	Physics vapour deposition (PVD).....	33
3.3.1	Vacuum thermal evaporation	34
3.3.2	Pulsed laser deposition (PLD).....	35
3.3.3	Sputtering	36
3.3.4	Ion beam deposition (IBD)	39
3.4.	Chemical vapor deposition.....	39
3.4.1	Plasma Enhanced Chemical Vapour Deposition (PECVD)	39
3.4.1.1	Capacitively coupled PECVD	41
3.4.1.2	Inductively coupled PECVD	44
3.4.1.3	Microwave PECVD.....	45
3.5.	Growth mechanism of thin film deposition.....	46
3.6.	Plasma physics and chemistry in the PECVD system	47
3.7.	Role of ions in PECVD	48
3.8.	References.....	50

Chapter 4: Thin film characterization techniques 54-81

4.1	Introduction.....	55
4.2	Optical characterization and determination of thickness	55
4.2.1	Optical properties by UV-Vis-NIR spectroscopy	55
4.2.2	Spectroscopic ellipsometry	57
4.2.3	Experimental determination of thickness and refractive index	58
4.2.3.1	Thickness measurement by Quartz crystal thickness monitor.....	58
4.2.3.2	Thickness measurement by profilometer.....	60
4.2.3.3	Thickness measurement by Swanepoel method.....	61
4.3	Structural characterization	64
4.3.1	Raman spectroscopy	64
4.3.2	X-ray diffraction (XRD)	66
4.3.3	Fourier transform infrared spectroscopy (FTIR)	68
4.3.4	Transmission electron microscopy (TEM)	69
4.3.5	Atomic force microscopy (AFM)	70
4.3.6	Field emission scanning electron microscopy (FESEM)	72
4.4	Compositional characterization.....	74
4.4.1	X-ray photoelectron spectroscopy (XPS)	74
4.5	Electrical characterization.....	76
4.5.1	Temperature dependent dark conductivity	76
4.5.2	Hall measurement.....	77
4.6	Measurement of I-V characteristics of solar cell.....	79
4.7	References	80

Chapter 5: Effect of RF power in opto-electronic and structural properties of hydrogenated nanocrystalline SiGe thin film in RF-PECVD 82-113

5.1	Introduction.....	83
5.2	Experimental details.....	84
5.3	Results.....	85
5.4	Discussion.....	103
5.5	Conclusion.....	109
5.6	References.....	109

Chapter 6: Optimal H₂-dilution playing key role in accomplishing significant nanocrystallinity with both Si and Ge moieties in SiGe nanocomposite thin film network..... 114-133

6.1	Introduction.....	115
6.2	Experimental details.....	116
6.3	Results.....	117
6.3.1	Raman analysis.....	117
6.3.2	XRD analysis.....	119
6.3.3	TEM analysis.....	120
6.3.4	Electrical properties.....	122
6.3.5	Optical band gap.....	123
6.3.6	Deposition rate.....	124
6.3.7	FTIR spectroscopy analysis.....	124
5.4	Discussion.....	127
5.5	Conclusion.....	129
5.6	References.....	130

Chapter 7: Ge-rich narrow band gap nc-Si_xGe_{1-x} absorber layer for tandem structure nc-Si solar cells..... 134-154

7.1	Introduction.....	135
7.2	Experimental details.....	136
7.3	Results.....	137
7.4	Discussion.....	149
7.5	Conclusion.....	151
7.6	References.....	151

Chapter 8: Low temperature synthesis of nc-SiGe:H thin films prepared in sputtering technique for nc-Si tandem solar cell..... 155-172

8.1	Introduction.....	156
8.2	Experimental details.....	157
8.3	Results and discussion.....	158

8.4	Conclusion.....	169
8.5	References.....	170
Chapter 9: Summary, conclusion and future outlook		173-177
8.1	Summary.....	174
8.2	Conclusion.....	176
8.3	Future outlook.....	177

Abstract

Title: Nanocrystalline Silicon-Germanium Alloy Thin Films: Synthesis, Characterization and Optimization for Silicon Solar Cells

Author: Amaresh Dey (Index No. 1/18/Phys./25)

The aim of this thesis is the one-step synthesis and optimization intrinsic nanocrystalline silicon-germanium(nc-SiGe:H) thin films through low-temperature (within 300°C) 13.56 MHz Plasma-CVD processing and 13.56 MHz sputtering deposition technique, compatible for potential device fabrication and their application to thin-film silicon tandem-structured solar cells. In first part of the thesis, the development of nanocrystalline silicon-germanium thin films by making optimal incorporation of Ge atoms in nc-Si network at ~220 °C using (SiH₄ + GeH₄ + H₂) plasma and their systematic analysis and optimization using various spectroscopic and microscopic tools and electrical characterization for photovoltaic application has been undertaken. The second part involves the systematic development of intrinsic nc-SiGe:H films with accomplishing nanocrystallinity in both Si and Ge in the film network, through increasing the hydrogen dilution optimally in the (SiH₄ + GeH₄)-plasma at ~220 °C in the device-friendly Plasma-CVD reactor, and the optimization of the optoelectronic and structural properties of the films through comprehensive analysis. In third part, Ge-rich nc-SiGe thin film has been prepared in RF-PECVD through the efficient incorporation of the Si atoms in the nanocrystalline Ge network via increasing the SiH₄ gas flow ratio in the (SiH₄ + GeH₄) plasma; as the growth conditions consistent for nc-Ge growth are completely different from the deposition conditions compatible for nc-Si growth. It has been confirmed that the decomposition of SiH₄ under nc-Ge compatible growth conditions occurs in a controlled manner that is beneficial for sustaining the nanocrystallinity in the binary SiGe alloy containing a Ge-dominated atomic composition that can provide the required infrared response and electrical transport for strategic applications in photovoltaics. In the last part of the thesis, nanocrystalline silicon germanium thin films have been achieved at a low temperature of 250 °C, from a one-step process by co-sputtering of Ge target (99.999% purity) and nc-Si wafers, using (Ar + H₂) plasma in the RF magnetron sputtering deposition system. Changes in the structural morphology and optical band gap due to the change in composition are studied.

List of Figures

Fig. 1.1	Global module demand forecast for 2020 and 2021	2
Fig. 1.2	NREL reported methodological improvements in best research-cell efficiencies.....	3
Fig. 1.3	Chronological evolution of the technology market share	4
Fig. 2.1	(a) The face-centred diamond lattice structure of the crystalline silicon (<i>c</i> -Si). (b) 2-D schematic diagram of the <i>c</i> -Si.....	15
Fig. 2.2	Realistic band structure of the crystalline silicon.....	16
Fig. 2.3	Lattice of a-Si:H, with Si-Si and Si-H bonds, as well as dangling bonds.....	18
Fig. 2.4	Schematic diagram of the density of states $N(E)$ for intrinsic amorphous silicon...	18
Fig. 2.5	Schematic diagram of the microstructural features of μc /nc-Si:H film growth	20
Fig. 2.6	Absorption coefficient α vs. energy for <i>c</i> -Si, μc -Si:H and a-Si:H	20
Fig. 2.7	Schematic diagram of (a) <i>n</i> -type Si and (b) <i>p</i> -type Si	22
Fig. 2.8	Schematic of a silicon solar cell.....	25
Fig. 2.9	Schematic of the basic structure of a p-i-n a-Si solar cell	26
Fig. 2.10	Schematic diagram of the <i>p-i-n</i> nc-Si silicon solar cell	27
Fig. 2.11	Schematic of an all-Si based tandem solar cell.....	28
Fig. 3.1	Schematic diagram of the vacuum thermal evaporation unit	34
Fig. 3.2	Schematic diagram of the pulsed laser deposition unit	35
Fig. 3.3	Schematic representation of a typical sputtering system with working mechanism.....	37
Fig. 3.4	The photograph of the sputtering system in our lab, used for synthesis of the nc-SiGe thin films	38
Fig. 3.5	Schematic diagram of the ion beam sputtering unit.....	39
Fig. 3.6	The schematic diagram of the capacitively coupled PECVD	41
Fig. 3.7	Real photograph of the 13.56 MHz PECVD system	43
Fig. 3.8	The schematic diagram of a planer inductively coupled PECVD.....	44
Fig. 3.9	The photograph of the planer inductively coupled PECVD in our lab	45
Fig. 3.10	The schematic view of the active plasma zone in a microwave PECVD.....	46
Fig. 3.11	Schematic representation of the thin film growth process steps	47
Fig. 4.1	Tauc plot of a 500 nm thick nc-Si:H/a-Si:H thin film on the glass substrates	56
Fig. 4.2	The measurement principle of the ellipsometry.....	58
Fig. 4.3	Schematic diagram of a spectroscopic ellipsometer	58

Fig. 4.4	(a) Block diagram of thin film thickness monitor connected within a vacuum chamber. (b) Photograph of a typical thickness monitor head. (c) The front and back contact of a thickness monitor head. (d) The schematic diagram of the fundamental shear mode used	59
Fig. 4.5	Expanded view of the specimen, fixture, and profilometer	60
Fig. 4.6	Schematic illustration of transmission of light through a film/substrate system. Intensity of the ordinary incident beam has the intensity as I_0 . I_T is the intensity of the transmitted beams, which is the superposition of the straight transmitted light (solid line) and the beam transmitted after suffering the multiple reflections at the air/film and film/substrate interfaces (dashed line)	61
Fig. 4.7	Transmission spectrum of a 500 nm thick nc-SiGe film grown on a glass substrate	63
Fig. 4.8	Schematic diagram of the Raman microscope	65
Fig. 4.9	Illustration of formation of Stokes and anti-Stokes lines through Rayleigh and Raman scattering.....	66
Fig. 4.10	A schematic illustration of the X-ray diffraction within a material	67
Fig. 4.11	Schematic diagram of FTIR spectrophotometer with the main components	68
Fig. 4.12	(a) Schematic of TEM showing the main components (b) TEM set-up	69
Fig. 4.13	The working principle of a typical AFM	71
Fig. 4.14	Schematic diagram of tip action of different modes of operation of AFM operates in various regions of the force-distance curve.....	72
Fig. 4.15	(a) Schematic representation of SEM instrument with an electron path diagram. (b) A schematic diagram of different processes taking place during electron-solid interaction	73
Fig. 4.16	Schematic diagram of (a) production of photoelectron and (b) working mechanism of XPS	74
Fig. 4.17	Schematic diagram of the electrical conductivity measurement set-up.....	76
Fig. 4.18	The schematic diagram of Hall measurement configuration.....	78
Fig. 4.19	Solar cell I-V characteristic curve	80
Fig. 5.1	(a) Raman spectra for $Si_{1-x}Ge_x:H$ films prepared at different RF powers, $P = 50$ to 150 W; (b) Deconvolution of Raman Spectra of the film grown at $P = 150$ W; (c) Blue shift of Si-Si TO peak with increasing RF power.....	86
Fig. 5.2	Deposition rate of the SiGe films at different applied RF power.....	88
Fig. 5.3	(a) X-ray diffraction spectra of SiGe films grown at different RF power. (b) Changes in the average grain size and micro-strain in the film network, as a function of applied RF power	89
Fig. 5.4	(a) TEM micrograph of nc- $Si_{1-x}Ge_x$ film representing the growth of silicon nanocrystals embedded in amorphous matrix, (b) HRTEM image of arbitrarily chosen Si-nano-crystal of $\langle 220 \rangle$ crystallographic orientation, corresponding (c) FFT image, (d) inter-planar spacing, (e) SAED pattern showing different crystal orientations and (f) size distribution of Si-ncs	91
Fig. 5.5	Absorption Co-efficient spectra of the SiGe thin films in the Tauc's plot, (b) presents the variations of optical band gap (E_g) and Tauc's constant (B) on increasing RF power.....	92

Fig. 5.6	(a) AFM 3D surface morphologies of Si _{1-x} Ge _x :H thin films deposited at P= 50 W, 100 W and 150 W. (b) RMS roughness of the films grown at various RF power 93
Fig. 5.7	(a) The wide scan XPS spectrum for the nc-Si _{1-x} Ge _x :H film prepared at P=100 W. Deconvoluted spectrum into possible satellite components for (b) Ge 3d and (c) Si 2p; Pie chart at the Inset demonstrates the relative intensity of different sub-levels of the orbital 94
Fig. 5.8	The FTIR absorption spectra with corresponding deconvoluted components for the nc-Si _{1-x} Ge _x :H sample grown at P =100 W..... 95
Fig. 5.9	Deconvoluted GeH and SiH wagging modes and SiH _n rocking mode components of IR absorption 96
Fig. 5.10	Bonded H-content, C _H , and the relative strength of SiH _n (n≥2) rocking mode, ΔI ₆₇₀ , as a function of RF power 96
Fig. 5.11	IR absorption spectra around wave number range of 750– 925 cm ⁻¹ , accommodating di-hydride bending and poly-hydride wagging modes 97
Fig. 5.12	Changes in the relative strength of poly-hydride wagging mode components for both Ge and Si, (GeH ₂) _n and (SiH ₂) _n , at elevated RF powers 98
Fig. 5.13	IR absorption spectrum deconvoluted into Ge and Si monohydride and dihydride along with the bond-centred hydrogen, Si–H–Si, components with increase of RF power 99
Fig. 5.14	Effect of varying RF powers changing the structure factors, R _{Si} and R _{Ge} , of the nc-Si _{1-x} Ge _x :H films..... 100
Fig. 5.15	Effect of applied RF powers changing the surface passivation index, S, in nc-Si _{1-x} Ge _x :H network 100
Fig. 5.16	Arrhenius plots of the dark conductivity (σ _D) of nc-Si _{1-x} Ge _x films deposited at different RF powers..... 101
Fig. 5.17	Variation of the room temperature dark conductivity (σ _D) and changes in its activation energies at high temperature (ΔE _H) and low temperature (ΔE _L) regions, with applied RF power..... 102
Fig. 5.18	Pre-exponential factor (σ _{0H}) of dark conductivity as function of high temperature activation energy ΔE _H 103
Fig. 5.19	Variations of the dark conductivity (σ _D) as function of the changing optical band gap of the SiGe:H network..... 108
Fig. 6.1	a) Raman spectra of the SiGe thin films prepared at different hydrogen dilution, R(H ₂); (b) Deconvoluted Raman spectrum of the sample grown at R(H ₂) = 50, into satellite components; (c) Magnified view of (494-506) cm ⁻¹ Raman peaks (d) Deconvolution of the (195-325) cm ⁻¹ Raman peaks, showing the crystalline and amorphous Ge-Ge components; (e) Variations in the integrated area ratios of the c-(Ge-Ge) to a-(Ge-Ge) components 117
Fig. 6.2	(a) XRD pattern of the SiGe films prepared at different hydrogen dilution, R(H ₂). (b) Changes in the grain size of the Si-ncs in <111> and <220> orientations and (c) I<220> / I<111> ratio, with the change in R(H ₂) 119
Fig. 6.3	(a) The TEM image of the nc-SiGe thin film deposited at (a-i) R(H ₂) = 25 and (b-i) R(H ₂) = 50 with the corresponding transmission electron diffraction (TED) pattern at the inset. (a-ii) and (b-ii) are the corresponding HR-TEM image showing well-defined c-Si nanocrystals in different orientations. (a-iii) and (b-iii) are the corresponding EDAX spectra, identifying the presence of Si and Ge with individual intensities 121

Fig. 6.4	Variation of dark conductivity (σ_D) and activation energy (E_a) of the SiGe films prepared with different H ₂ -dilution ratios, R(H ₂), along with the plot of $\ln(\sigma_D)$ as a function of 1000/T in the inset.....	122
Fig. 6.5	(a) Tauc's plot of the SiGe thin film prepared at different hydrogen dilutions, R(H ₂). (b) Variation in the optical band gap (E_g) and Tauc constant (B) with R(H ₂)	123
Fig. 6.6	Variation in the deposition rate of SiGe thin films with hydrogen dilution ratio, R(H ₂)	124
Fig. 6.7	(a) The deconvolution of the vibrational spectra into Si and Ge wagging modes. (b) Changes in hydrogen content (C_H) with hydrogen dilution ratio, R(H ₂).....	125
Fig. 6.8	(a) Changes in the deconvoluted vibrational spectra in stretching mode with the increase in hydrogen dilution ratio, R(H ₂). (b) Effect of variation in R(H ₂) on the structure factors of Ge (R_{Ge}) and of Si (R_{Si}) in nc-Si _{1-x} Ge _x :H films	126
Fig. 7.1	(a) XRD patterns obtained for the samples deposited at various SiH ₄ concentrations (SC). The variation in (b) $I_{<220>}/I_{<111>}$ and (c) grain size upon increasing the SC	137
Fig. 7.2	(a) Raman spectra obtained for the samples prepared at different SiH ₄ concentrations (SC = 0 to 0.3) and (b) deconvoluted Raman spectrum of the film grown with SC = 0.3.....	139
Fig. 7.3	Tauc plot [$(\alpha E)^{1/2}$ vs E] estimating the band gap for the films prepared with SC = 0 and 0.1; the inset demonstrates the changes in the optical band gap upon changing the SC	141
Fig. 7.4	(a) The deconvolution of the FTIR absorption co-efficient spectra in the range of 500–700 cm ⁻¹ , (b) changes in the hydrogen content (C_H) upon increasing the SiH ₄ concentration (SC), (c) the deconvoluted FTIR absorption spectra in the range of 1800–2200 cm ⁻¹ , and (d) the effect of varying the SC on the structure factor (R_{Si} , R_{Ge}) and the surface passivation index (S)	143
Fig. 7.5	Surface morphologies of the films prepared using two different SiH ₄ concentrations: (a) SC = 0 & (b) SC = 0.1. (c) The RMS surface roughness upon increasing the SC estimated from AFM data	145
Fig. 7.6	(a) Plane-view bright field HRTEM-image of the film prepared at SC = 0.1, (b) corresponding SAED pattern, (c) magnified TEM images with distinguished planes, (d) selected area dark-field TEM images with elemental mapping of (e) Ge and (f) Si atoms in the film and (g) identification of the elemental components Ge and Si using EDAX	146
Fig. 7.7	The variation in the temperature-dependent dark conductivity of nc-Si _x Ge _{1-x} films	147
Fig. 7.8	Room-temperature dark conductivity and activation energy (E_a) of the films as a function of the SiH ₄ concentration (SC)	148
Fig. 7.9	A comparison of the room temperature dark conductivity (σ_D) vs optical band gap (E_g) data for the various nc-Si _x Ge _{1-x} thin films available from past works	150
Fig. 8.1	XRD diffraction spectra of the SiGe films grown at different Ψ , with average grain size given in the table in the inset.....	158
Fig. 8.2	Raman spectra of the SiGe films grown at different area opening of Ge target covered by Si wafer strips and the shift of the Si–Si peak shown in the inset.....	159
Fig. 8.3	Deconvoluted Raman spectra obtained for the SiGe films prepared with (a) $\Psi = 40\%$, (b) $\Psi = 24\%$	160
Fig. 8.4	Variation in the Tauc's plot with the change in the Ge content via an increase in the specific surface area of Ge target (Ψ) and the corresponding modification in the band gap is presented in the inset.....	161

Fig. 8.5	(a) Deconvoluted FTIR spectra in the range 500–700 cm ⁻¹ . (b) Variation of the total bonded hydrogen content in the film matrix with Ψ . (c) Bar diagram showing the individual contribution of hydrogen bonded with the Ge and Si in the C _H	163
Fig. 8.6	(a) Deconvoluted FTIR spectra in the range 1800–2200 cm ⁻¹ . (b) Variation of the Ge structure-factor (R_{Ge}) and Si structure-factor (R_{Si}) with Ψ	164
Fig. 8.7	(a) Plane-view HRTEM image of the sample prepared with $\Psi = 24\%$, with the corresponding diffraction pattern presented in the inset. (b) Magnified TEM micrograph with prominent crystallographic planes with FFT image presented in (b-i). (c) EDX spectra recognizing the elements, with mentioning the elemental atomic percentage of Si and Ge.....	165
Fig. 8.8	Typical 5 $\mu\text{m} \times 5 \mu\text{m}$ three-dimensional AFM images of nc-SiGe films prepared with (a) $\Psi = 0\%$, (b) $\Psi = 24\%$, (c) $\Psi = 40\%$ and (d) $\Psi = 49\%$	166
Fig. 8.9	Variation of the RMS roughness of the nc-SiGe films with change in Ψ	167
Fig. 8.10	Variation of the dark conductivity and activation energy of the nc-SiGe films with change in Ψ	168
Fig. 8.11	Changes in the dark conductivity as a function of the changing optical band gap of the nc-SiGe network.....	169

Glossary of Acronyms

PV	Photovoltaics
DC	Direct current
GW	Gigawatt
TF	Thin film
Si	Silicon
Ge	Germanium
c-Si	Crystalline silicon
CdS	Cadmium sulfide
CdTe	Cadmium telluride
CIGS	Copper indium gallium selenide
a-Si	Amorphous silicon
$\mu\text{c-Si:H}$	Microcrystalline silicon
nc-Si:H	Nanocrystalline silicon
<i>n</i> -Si	<i>n</i> -type Silicon
<i>p</i> -Si	<i>p</i> -type silicon
<i>n-nc-Si</i>	<i>n</i> -type nanocrystalline silicon
<i>p-nc-Si</i>	<i>p</i> -type nanocrystalline silicon
SiO	Silicon oxide
SiN	Silicon nitride
SiC	Silicon carbide
TCO	Transparent conducting oxide
LED	Light emitting diode
SWE	Staebler -Wronski effect
PCE	Power conversion efficiency
DB	Dangling bond
GB	Grain boundary
DOS	Density of states
RF	Radio frequency
VHF	Very high frequency
H	Hydrogen
O	Oxygen
C	Carbon
Cu	Copper
Ar	Argon
SiH ₄	Silane
GeH ₄	Germane
PH ₃	Phosphine
B ₂ H ₆	Diborane

n_e	Concentration of electron
n_h	Concentration of hole
μ_e	Electron mobility
μ_h	Hole mobility
nm	Nanometer
μm	Micrometer
PVD	Physical vapor deposition
CVD	Chemical vapor deposition
PLD	Pulsed laser deposition
IBD	Ion beam deposition
PECVD	Plasma enhanced chemical vapor deposition
ICP	Inductively coupled plasma
UHV	Ultra-high vacuum
HWCVD	Hot wire chemical vapor deposition
MWCVD	Microwave plasma chemical vapor deposition
LTE	Local thermodynamic equilibrium
ECR	Electron cyclotron resonance
SCCM	Standard cubic centimeter per minute
RTA	Rapid thermal annealing
MIC	Metal induced crystallization
SPC	Solid-phase crystallization
XRD	X-Ray diffraction
FTIR	Fourier transform infrared spectroscopy
AFM	Atomic force microscopy
RMS	Root mean square
Avg	Average
Eqn	Equation
XPS	X-ray photoelectron spectroscopy
Fig	Figure
SE	Spectroscopic ellipsometry
TA	Transverse acoustic
LA	Longitudinal acoustic
LO	Longitudinal optical
TO	Transverse optical
FWHM	Full width at half maximum
TEM	Transmission electron microscopy
HRTEM	High resolution TEM
TED	Transmission electron diffraction
SAED	Selected area electron diffraction
MNR	Meyer Neldel rule
MN plot	Meyer Neldel plot
E_g	Band gap
C_H	Hydrogen content

E_a	Activation energy
E_c	Conduction band edge
E_v	Valence band edge
E_F	Fermi energy
e-h	Electron-hole
σ	Conductivity
σ_{dc}	Dark conductivity
K_B	Boltzmann constant
σ_0	Pre-factor of dark conductivity
T_s	Substrate temperature
e.g	Example
I-V	Current-Voltage
J-V	Current density-voltage
V_{oc}	Open circuit voltage
I_{sc}	Short circuit current
FF	Fill factor
V_{mp}	Maximum voltage point
η	Efficiency

List of publications

1. **Amaresh Dey** and Debajyoti Das, Optimization of growth of nanocrystalline silicon germanium thin films synthesized by RF-PECVD, *AIP Conference Proceedings* 1942 (2018) 080069.
2. Debajyoti Das and **Amaresh Dey**, Optimization in the nanostructural evolution of hydrogenated silicon germanium thin film in RF-PECVD, *Physica E: Low-dimensional Systems and Nanostructures* 111 (2019) 20–28.
3. **Amaresh Dey** and Debajyoti Das, Narrow band gap high conducting nc-Si_{1-x}Ge_x:H absorber layers for tandem structure nc-Si solar cells, *Journal of Alloys and Compounds* 806 (2019) 1529–1535.
4. **Amaresh Dey** and Debajyoti Das, Effect of Si incorporation to produce Ge-rich nc-Si_xGe_{1-x} absorber layer for nc-Si solar cells, *AIP Conference Proceedings* 2220 (2020) 090010.
5. **Amaresh Dey** and Debajyoti Das, Optoelectronic and structural properties of Ge-rich narrow band gap nc-Si_xGe_{1-x} absorber layer for tandem structure nc-Si solar cells, *Journal of Physics and Chemistry of Solids* 154 (2021) 110055.
6. **Amaresh Dey** and Debajyoti Das, Correlation of microstructure factor with the electronic properties of nanocrystalline silicon–germanium thin films [DOI: 10.1016/j.matpr.2022.02.432] *Materials Today: Proceedings* (2022).
7. **Amaresh Dey** and Debajyoti Das, Optimal H₂-dilution playing key role in accomplishing significant nanocrystallinity with both Si and Ge moieties in SiGe nanocomposite thin film network (*Under review in Applied Surface Science*).
8. Debajyoti Das and **Amaresh Dey**, Low temperature synthesis of nc-SiGe:H thin films prepared in sputtering technique for nc-Si tandem solar cell (*Communicated*).

Conference and Symposium

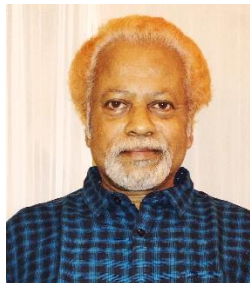
1. DAE Solid State Physics Symposium 2017 (**DAE SSPS 2017**) [26-30 December, 2017] (**Poster presentation**)
2. International Conference on Condensed Matter and Applied Physics (**ICC 2019**) [14-15 October, 2019] (**Poster presentation**)
3. International Conference on Physics of Materials and Nanotechnology (**ICPN 2021**) [28-30 October, 2021] (**Poster presentation**)
4. International Conference on Emerging Trends in Materials Science and Technology (**ICETMT-2022**) [10-11 February, 2022] (**Recieved best poster presentation award**)

Brief introduction to the author and energy research unit



Amaresh Dey

Amaresh Dey, is a Master of Science in Physics from the Department of Physics, IIT Madras and right now a senior research fellow in the Energy Research Unit, School of Materials Sciences, Indian Association for the Cultivation of Science (IACS), Kolkata. Amaresh has co-authored three scientific journal publications and three conference proceedings publications presented in four national and international conferences during his tenure of Ph.D. His current research interest includes development of nanocrystalline silicon-germanium alloy thin film and other intrinsic and doped silicon nanocrystallites embedded in various dielectric matrices for e.g. silicon oxide (SiO), silicon nitride (SiN), silicon carbide (SiC), etc. for energy applications e.g. silicon tandem solar cell and light emitting devices. Alongside the pursuit of high academic goals, Amaresh is keenly interested in photography, cricket and writing.



Prof. Debajyoti Das

Energy Research Unit under the leadership of **Prof. Debajyoti Das**, Senior Professor at the School of Materials Sciences, Indian Association for the Cultivation of Science, is the premier research group with the thrust of development of materials and fabrication technology for Thin Film Silicon Solar Cells. Prof. Das has co-authored numerous highly cited scientific papers, owns several awards and patents and membership of learned bodies. His current research interests: Development of Nanomaterials for Energy Applications (Photovoltaic and Photocatalytic): (Silicon and Germanium Quantum-Dots, Nano-rods, Nanotips & Superlattice structures; Carbon Nano-tubes, Nano-Diamond, DLC & Graphene; TCO films e.g., ITO, SnO₂ & doped ZnO₂ nanostructures, and also various composite nanostructures of TiO₂ and ZnO). The nano-materials developed by the Energy Research Unit are potential candidate for industrialization and the group proudly stands as the front runner in the path of R & D and industry collaborations for the Indian Prime Ministers ambitious call for 'make in India' initiative.



Chapter 1

**General introduction and
motivation**

1.1 Introduction

Global energy demand continuously increases with the growing population of the world and continuous industrial revolution taking place in the last few decades. People have been using fossil fuels like coal, petroleum, and natural gas for a long time to fulfil their energy requirements. The transformation of fossil fuels from their origin involves a geological process that takes millions of years. Higher consumption of non-renewable energy resources leads to faster depletion of fossil fuels. Its use has several negative consequences on the community and environment. The excessive use of fossil fuels results in enormous emissions of greenhouse gases such as carbon-di-oxide, methane, etc., in the atmosphere, causing global warming and ocean acidification. Additionally, people suffer from different air pollution diseases due to the harmful gases and particulates emitted from the combustion of fossil fuels. The recognition of the pollution, accelerating climate crisis and the negative environmental impacts on nature also urge mitigating efforts for a quick solution. Therefore, the world is trying to switch from conventional fossil fuels sources for electrical energy generation to eco-friendly sources like solar energy, wind energy, biomass, tidal energy, hydroelectricity, nuclear power, geothermal power etc., which are termed "green energy" sources due to their less carbon dioxide emission into the atmosphere. Among the various "green energy" sources, the large radiation coming from the sun is the most promising source of renewable energy.

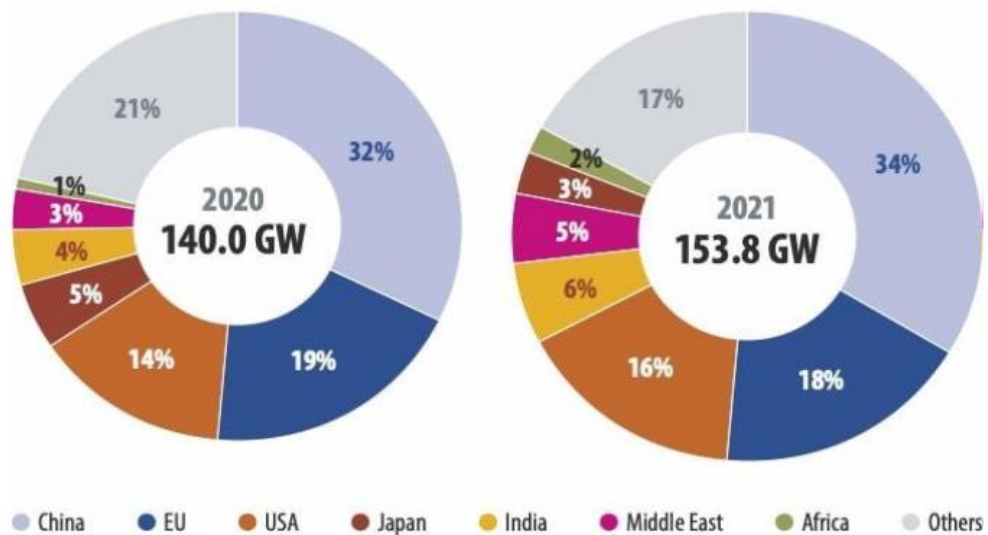


Fig. 1.1. Global module demand forecast for 2020 and 2021 (Source: PV magazine)

Accordingly, many developing countries have tried to restructure their energy sectors by promoting solar energy as an alternating energy source in everyday life. It is reported that the global photovoltaic (PV) demand is growing faster each year, and the PV installation surpassed 150 GW in 2021 [1], as shown in **Fig. 1.1**.

The method of producing direct current (DC) electricity from sunlight via technology based on the photovoltaic effect is solar photovoltaics (PV). As the photoelectric cell (which is the building block of a solar panel) is irradiated by the solar radiation, an electric potential difference is produced between the two faces of the cell's electrodes, resulting in electrons flowing from one to the other, generating DC-electric current. In 1954, the scientists Daryl Chapin, Calvin Fuller, and Gerald Pearson created the first practical solar cell using silicon in the Bell Laboratories. In the beginning, solar panels were used to power various parts of earth-orbiting satellites. Later, progress in PV technology toward its performance and quality reduced its cost. It opened up opportunities to power remote terrestrial applications with low-power needs, including battery charging for navigational aids, signals, and telecommunications equipment. The energy crisis during this period also encouraged momentous attention globally to develop PV power systems for residential and commercial uses. Solar cells became popular as a power source for ordinary electronic devices such as calculators, watches, radios, lanterns, and other small battery-charging applications.

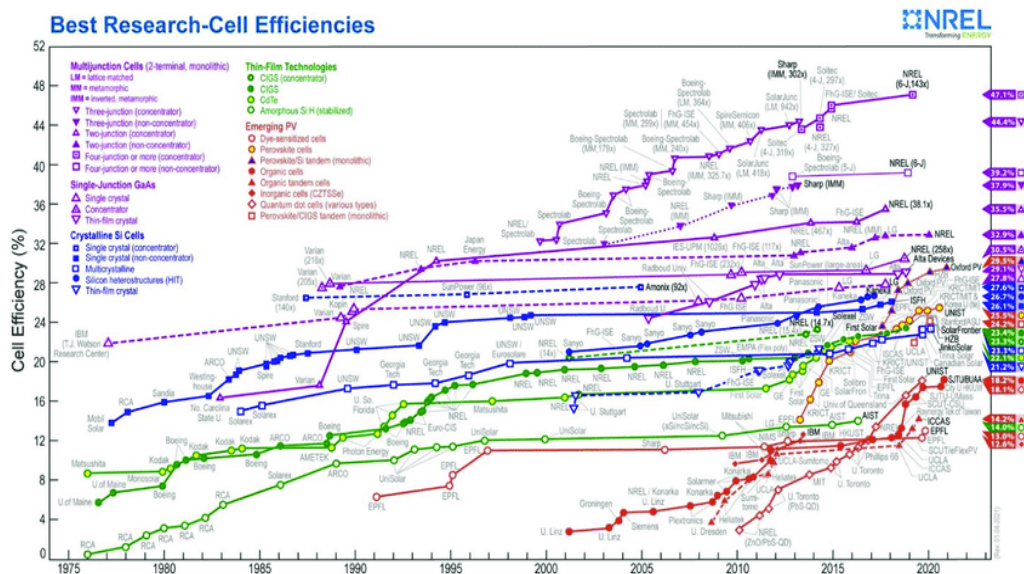


Fig. 1.2. NREL reported methodological improvements in best research-cell efficiencies (Source: www.en.wikipedia.org/wiki/Solar_cell).

Apart from the numerous advantages of photovoltaics, the recent global move towards its growth is mainly motivated by the criteria of eco-friendliness, sustainability, and self-reliability of the energy source. It is noticeable in the history of photovoltaics that efficiency and cost-effectiveness have progressed tremendously. The improvement of the efficiency of the PV technologies is portrayed in **Fig. 1.2**.

The International Energy Agency's photovoltaic (PV) roadmap estimates that by 2050 [2], PV will provide around 11% of global electricity production. Silicon has large abundance in the Earth's crust and the silicon solar cell has a combination of advantages such as low cost, high efficiency and a long lifetime. Modules made of silicon are intended to survive for 25 years or more, still provide more than 80% of their original power at this time. These all together make silicon technology to take the leading role in solar PV. The crystalline silicon (c-Si) and polycrystalline silicon (pc-Si) based solar cells still dominate even with the emergence of other solar cell technologies (like cadmium telluride (CdTe), copper indium gallium selenide (CIGS) etc.) (**Fig 1.3**) [3]. Concentrator photovoltaics (CPV) using high-efficiency III-V-based solar cells are already in the market and contribute to total production.

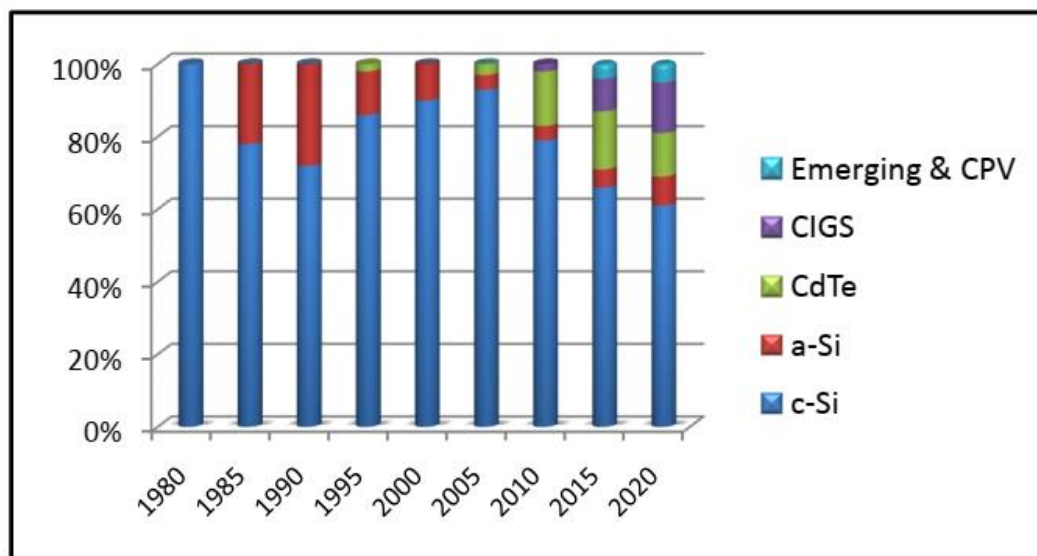


Fig 1.3. Chronological evolution of the technology market share.

Solar cells can be divided into different categories depending on the particular semiconducting materials they are composed of. Furthermore, the types of solar cells also vary, as some are equipped to be used in space, whereas some are made to be used near the Earth's surface. The progress of the solar cell technologies is divided into three

generations by photovoltaic researchers globally as 1st, 2nd and 3rd generation solar cells [4]. Solar cells consisting of basic c-Si belong to first-generation photovoltaics. The thin film based solar cells like amorphous silicon (a-Si), CdTe, CIGS etc., come under the second generation, and third-generation photovoltaics include new and emerging technologies like multijunction solar cells, organic semiconductor-based solar cells, etc. [5,6]. Research is going on to find more contemporary materials to produce solar cells cheaper. For example, some promising organic-based emerging technologies like dye-sensitized solar cells (DSSC) and perovskite solar cells have evolved recently.

Silicon is the most prevalent semiconductor material used in solar cells, accounting for over 95% of recent solar modules. It is also the second most abundant element (after oxygen) and the most reliable semiconductor material applied in electronics devices. Since the beginning of the microelectronics industry, silicon has received a high priority due to several properties, as described below:

- Si can be extracted and purified from the source material using a variety of industrial procedures in a cost-effective way, which makes it more affordable.
- At the same time, Si is the most stable and non-toxic semiconductor material.
- Silicon can be found in its intrinsic state.
- Si can be easily doped with suitable impurities by using advanced doping techniques.
- The crystalline Si with a band gap of 1.1 eV, efficiently responds well to AM 1.5 solar radiation that falls on the earth's surface.

Besides traditional c-Si and poly-Si, silicon-based solar cell technology includes amorphous silicon (a-Si), microcrystalline silicon (μ c-Si) and the heterojunction intrinsic thin layer "HIT" solar cell. In these solar cells, new concepts are utilized to enhance solar cell efficiency at a reduced cost. Other high-efficiency photovoltaics aims to use advanced conversion concepts like intermediate band solar cell, plasmonic solar cell etc., which use novel, innovative materials and are mostly at the initial stage of the research. Several new ideas involve quantum confined materials, predicting a huge enhancement of the conversion efficiency by better utilization of the solar spectrum.

Many research groups have attempted development, optimization, and commercialization through evolving new technologies and materials to achieve high-performance solar cells at a low cost of production (i.e., solar cells of the third generation) [7–10]. Current investigations into the well-established Si-based technology aim to

convert the maximum part of the energy received from the sun into electrical power. In this aspect, the idea of a tandem structure (multi-junction) solar cell has been employed, in which the output of the solar cell is gradually improved by stacking more cells on top of each other [11–13]. The Si-based solar cell technology's multi-junction concept targets increasing efficiencies and maintaining cost-effectiveness, demanding the development of suitable Si-alloy (amorphous or nanocrystalline) materials with the desired optoelectronic properties. The tandem solar cells require both high and low band gap materials to efficiently absorb the photons of long and short wavelengths, which can be converted to electric power, leading to enhanced efficiency of the cell. To achieve absorber layers with different band gaps, other elements are added to the nc-Si network with less compromising on the charge-carrier transport in the layers. Silicon is generally alloyed with germanium (Ge), tin (Sn), etc., to reduce the optical band gap, and with carbon (C), nitrogen (N), oxygen (O), etc., to widen the optical band gap. The band gaps of each absorbing layer decrease from the top to the bottom cells monotonically.

For a three-cell tandem-structured nc-Si solar cell, the optimal optical band gap for the absorber layer in the top, middle, and bottom sub-cell is nearly 2.0 eV, 1.7–1.8 eV and less than 1.5 eV, respectively. The top and middle sub-cell are designated to absorb the visible range of the sunlight. In the last few decades, extensive research has been carried out to successfully prepare wide band gap silicon oxide, silicon carbide, and silicon nitride materials for the top or window layer of the nc-Si tandem-structured solar cell [14–19]. The commonly used and widely accepted material for the absorber layer in the middle cell is hydrogenated nanocrystalline silicon, with an optical band gap in the range of 1.6–1.8 eV. The bottom sub-cell requires a narrow band gap material to efficiently absorb the near-infrared part of the sunlight. Primarily, nanocrystalline silicon (nc-Si) with a suitably low band gap was used here, but it holds a poor optical absorption coefficient in the infrared part of the solar radiation [20,21]. Therefore, it requires a thicker absorber layer and a higher production cost [22]. Nevertheless, significant recombination loss occurs in an absorber layer with a thickness larger than the carrier's diffusion length, reducing carrier collection and a poor built-in potential that worsens solar cell performance [23]. The nc-Ge layer has the inherent capability of absorbing long-wavelength; however, the tandem solar cell consisting of Ge bottom sub-cells is expected to suffer from the low open-circuit voltage (V_{OC}) due to its low band gap of 0.7 eV. In a multi-junction solar cell, the lowest sub-cell current determines the total cell

current, and the sum of the sub-cell voltages gives the total cell voltage. So, the lower sub-cell contributes to the cell voltage by lowering the cell current. As the efficiency is proportional to the open-circuit voltage of the total cell, the V_{OC} of the bottom sub-cell should be raised sufficiently to enhance the cell efficiency effectively [24]. In this context, the use of silicon-germanium alloy in the bottom sub-cell becomes appealing. Intrinsic amorphous silicon germanium (a-SiGe) has been used in the bottom sub-cell of the Si tandem solar cell [25–27]. However, a-SiGe has poor stability against exposure to light [28]. In this context, nanocrystalline silicon germanium (nc-SiGe) thin film appeared as an alternative material for the absorber layer at the bottom sub-cell. It meets the optimal requirement of improved infrared absorption than nc-Si and better stability against light-induced degradation than amorphous silicon germanium.

1.2 Motivation

Silicon is the backbone of the semiconductor industry, with versatile and environment-friendly applications in most electronics and photovoltaic devices. Silicon is a non-toxic element with a very high abundance in the earth's crust. Although many new materials like cadmium telluride, copper indium gallium selenide, etc., have been developed, Si-based solar cells have gained extreme importance because of silicon solar cells' following properties: relatively low-cost, higher efficiency, longer lifetime, etc. The solar cell produced with crystalline silicon is the most popular for its stability, however, its production cost is very high. Furthermore, its absorption coefficient in the visible range is significantly low. Therefore, the photovoltaic industry has recognized amorphous silicon (a-Si) as prime low-cost material for solar cells as it possesses high absorption co-efficient. However, amorphous silicon layers are generally defect-rich, resulting in inefficient doping and reduced stability against light exposure, which impede the widespread use of a-Si in solar cells. With the advent of nanotechnology, the development of nanocrystalline Si (nc-Si:H) attracted attention of the photovoltaic researchers. nc-Si is a two-phase material consisting of nanometer-sized crystallites embedded in an amorphous matrix. It demonstrates higher electrical conductivity, a tunable optical band gap, and better stability against light-induced degradation, making it promising for possible use in photovoltaic cells. Currently, nc-Si:H thin film has become a material of choice in Si-based solar cells, with superior carrier mobility and higher doping efficiency [21,29].

To achieve high-efficiency solar cells at a low production cost, utilization of the wider range of the solar radiation is one of the objectives of researchers in the photovoltaic industry. Using the tandem structure of solar cells can gradually improve efficiency by stacking more cells on top of one another by combining multiple absorber layers with numerous optical band gaps. The optical band gap of each absorber layer needs to be suitably tuned without compromising the charge-carrier transport in the layers. Researchers have made several attempts to successfully develop nanocrystalline silicon oxide, carbide and nitride materials with wide optical band gaps, that efficiently absorb the visible wavelength part of the sunlight. However, less attention has been paid so far in optimizing the low band gap absorber material for utilizing the infrared part of the sunlight in the solar cell. For that consideration, the nc-SiGe alloy thin film is a good candidate for it. Incorporating germanium atoms in the $\mu\text{c}/\text{nc-Si}$ network enhances the optical absorption, specifically in the infrared wavelength part. However, the inclusion of Ge atoms increases the number of dangling bonds enormously in the nc-Si network, hindering the nanocrystallization in the film matrix and destroying its electrical properties. So, it is vital to develop a narrow band gap and highly conducting nc-SiGe film for further improvement of the nc-Si tandem solar cells. Accordingly, our prime interest is in growing intrinsic nanocrystalline silicon-germanium alloy thin film.

The most frequently used precursor gases are GeH_4 and SiH_4 in preparing nc-SiGe materials in PECVD. The rapid dissociation of GeH_4 in the plasma because of its lower dissociation energy than SiH_4 causes the rapid accumulation of Ge-hydrides at the film growth sites [30]. It results in the extensive residence of Ge atoms in the film, thereby degrading the nanocrystallinity of the alloy network and weakening its electrical properties. Grossly different chemical reaction behaviors of the precursor gases make it difficult to attain crystallinity in the material. In contrast, substantial inclusion of the Ge atoms in the film network is necessary for narrowing the optical band gap in view of the superior absorption of the infrared part of solar radiation. The research plan includes tuning the optoelectronic and structural properties of the nc-SiGe films through optimal incorporation of Ge atoms in the nanocrystalline Si-network. Further, avoiding any annealing process and pursuing low-temperature growth of the nc-SiGe network is one of the important agenda of current research.

Accommodating more Ge atoms in the nc-Si network increases defect density due to dangling bonds. Ge has less tendency to bond with hydrogen atoms than Si,

resulting in the non-uniform distribution of hydrogen bonding in the SiGe network. These altogether weaken the overall electronic properties of the binary alloy material. Furthermore, the growth of two-phase heterostructure and uneven crystallization in Si and Ge in the alloy network restricts in the improvement of the film quality and the adjustability of its band gap. In the literature, it has been noted that the H₂ dilution method is adopted as one of the finest techniques to improve the film quality and reduce the defect density in the plasma synthesis of numerous Si-alloy materials. Present work involves the detailed investigation of the nanostructural evolution of SiGe thin films and accomplishing the nanocrystallinity in the Si-Si and Ge-Ge networks by virtue of providing excess hydrogen in the plasma via higher hydrogen dilution.

Adding more Ge atoms to the Si-rich SiGe film network increases tunability by decreasing the optical band gap; however, it destroys the film's nanocrystallinity and progressively leads to complete amorphization of the overall network; thereby deteriorating the electrical properties drastically. Therefore, this issue hinders producing low band gap nc-SiGe alloy thin films. The parametric deposition conditions compatible with nc-Ge growth are grossly different from the growth conditions consistent with nc-Si growth. In this concern, it might be beneficial to employ a tactical approach in preparing good quality low band gap nc-SiGe alloy thin films by incorporating Si atoms through controlled dissociation of SiH₄ in nc-Ge compatible growth conditions, which have not been explored before. The research plan includes the synthesis of Ge-rich nc-SiGe alloy films via insertion of Si atoms under parametric conditions, compatible for nc-Ge growth.

Beyond the PECVD method, an environmentally friendly approach for preparing the nc-SiGe alloy is the sputtering deposition technique, as no harmful gases such as SiH₄ and GeH₄ are involved. In the conventional method, two separate Si and Ge sputtering targets are used to grow the SiGe thin film. In this process, the nanocrystallization of the SiGe alloy occurs via solid-phase crystallization that demands a high thermal budget as the Ge and Si both possess considerably high melting points of 937 °C and 1414 °C, respectively [24,31]. It follows higher production costs and limits its usefulness in stacked-layer device applications and low-cost substrates with lower melting points. In most studies on SiGe alloy thin films deposited in the sputtering process, post-deposition high-temperature annealing or laser-induced annealing is used [32–36]. So, synthesis of the nc-SiGe film at a low temperature in a single-step process is a challenging job. In that

consideration, the strategic use of an nc-Si wafer partially covering a Ge target is attempted to grow nc-SiGe alloy thin film. It can be beneficial for the crystallization of the alloy network as Si moieties can be included in the film matrix in the form of Si-nanocrystallites from the nc-Si wafer in nc-Ge growth compatible conditions. It imposes a less persistent hindrance in attaining nanocrystallinity in the alloy film network. Accordingly, the current research project deals with the low-temperature synthesis of nc-SiGe by using a combined nc-Si wafer and Ge target. Many structural defects and disorders originate in the growth of SiGe in the sputtering process, which sets back the nanocrystallization process across the material. H₂ gas is employed with sputtering gas Ar, to minimize the defect density and facilitate the nanocrystalline growth of the alloy material.

Considering all of these, the objective of this thesis work is to prepare device quality nanocrystalline silicon-germanium thin film at a low temperature (<300 °C) using 13.56 MHz capacitively coupled plasma CVD and 13.56 MHz RF magnetron sputtering deposition system for their potential application in nc-Si tandem-structure multi-junction solar cell wherein the accommodation of Ge atoms in the alloy material, preferentially in its crystalline form via optimizing the plasma parameters is attempted. Detailed investigations of the nanostructured materials on their structural, optical and electrical properties have been done in view of their optimization and utilization in the devices.

1.3 Framework of the thesis

This thesis aims to the one-step synthesis and optimization of intrinsic nanocrystalline silicon-germanium alloy (nc-SiGe:H) thin films through low temperature (within 300°C) 13.56 MHz RF-Plasma CVD processing and sputtering deposition technique, compatible for potential application in thin film nc-Si solar cells.

After the brief introduction, in *chapter 2*, silicon and germanium solar cell materials and solar cells are discussed.

Chapter 3 designates the several methods used in the thin film deposition including a special discussion of 13.56 MHz capacitively coupled plasma-enhanced chemical vapour deposition (CC-PECVD) system and RF magnetron sputtering system (13.56 MHz), which is used for growing silicon-germanium alloy thin films.

Chapter 4 describes the different measurement tools for the characterization techniques of the optical, electrical, and structural properties and surface morphologies of the silicon germanium thin film.

Chapter 5 demonstrates the development of narrow band gap nanocrystalline silicon-germanium alloy (nc-SiGe:H) thin films in a conventional 13.56 MHz capacitive-coupled PECVD system at low substrate temperature ~ 220 °C, incorporating a substantial amount of Ge into the nanocrystalline Si-network at an optimum RF power. Systematic analysis and optimization using various spectroscopic and microscopic tools and electrical characterization for photovoltaic applications have been undertaken. Furthermore, how the film network's nanocrystallization plays a critical role in lowering the optical band gap, overcoming the consequence of Ge's restricted presence via the changed dissociation behaviour of the two source gases GeH_4 and SiH_4 in different RF power, discussed in detail in this chapter.

Chapter 6 deals with the synthesis with the characterization of intrinsic nc-SiGe thin films in PECVD with the increase in hydrogen dilution. This work emphasized accomplishing the nanocrystallization of both Si-Si and Ge-Ge networks in the nanocomposite SiGe thin film via the optimal increase in hydrogen dilution in the $(\text{SiH}_4 + \text{GeH}_4 + \text{H}_2)$ plasma.

Chapter 7 demonstrates the successful synthesis of Ge-rich nc-SiGe thin films with very narrow band gap and good electrical properties. In this work, it is envisaged that the disintegration of SiH_4 in $(\text{GeH}_4 + \text{SiH}_4)$ plasma happens in a controlled manner under nc-Ge compatible growth conditions, which is advantageous for maintaining nanocrystallinity in the binary SiGe alloy containing a Ge-dominated atomic composition that can provide the required infrared response and electrical transport for strategic applications in photovoltaics.

Chapter 8 discusses the synthesis of narrow band gap nc-SiGe alloy thin films in a one-step process, without using post-deposition annealing, at a low temperature of ~ 250 °C by reactive magnetron sputtering system through co-sputtering of the c-Si wafer and pure Ge target, in the $(\text{Ar} + \text{H}_2)$ plasma.

Chapter 9 contains the summary and conclusion of the thesis and discusses the future aspects of this thesis work.

1.4 References

- [1] Global PV installations to surpass 150 GW in 2021, Issue 02-2021 February 11, 2021 PV Magazine, <https://www.pv-magazine.com/magazine-archive/global-pvinstallations-to-surpass-150-gw-in-2021/>
- [2] The European Photovoltaic Industry Association G. “Solar generation 6 - solar photovoltaic electricity empowering the world”, (2011).
- [3] International Energy Agency, “Technology Roadmap - Solar Photovoltaic Energy”, (2010).
- [4] M.A. Green, Progress in photovoltaics 9 (2001) 123.
- [5] M.A. Green, Third generation photovoltaics: ultra-high efficiency at low cost, Springer Verlag, Berlin (2003).
- [6] G. Conibeer, Third-Generation Photovoltaics, Materials Today 10 (2007) 42.
- [7] B.S. Richards, Sol. Energy Mater. Sol. Cells 90 (2006) 2329–2337.
- [8] M.A. Green, Prog. in Photovolt.: Res. and Appl. 9 (2001) 123–135.
- [9] I. Perez-Wurfl, X. Hao, A. Gentle, D.H. Kim, G. Conibeer, M.A. Green, Appl. Phys. Lett., 95 (2009) 153506.
- [10] A.J. Nozik, M.C. Beard, J.M. Luther, M. Law, R.J. Ellingson, J.C. Johnson, Chem. Rev. 110 (2010) 6873–6890.
- [11] J. Müller, B. Rech, J. Springer, M. Vanecek, Sol. Energy 77 (2004) 917–930.
- [12] A. V. Shah, H. Schade, M. Vanecek, J. Meier, E. Vallat-Sauvain, N. Wyrsh, U. Kroll, C. Droz, J. Bailat, Prog. in Photovolt.: Res. and Appl. 12 (2004) 113–142.
- [13] J. Yang, A. Banerjee, S. Guha, Appl. Phys. Lett. 70 (1997) 2975–2977.
- [14] D. Das, B. Sain, J. Appl. Phys. 114 (2013) 073708.
- [15] A. Samanta, D. Das, Sol. Energy Mater. Sol. Cells 93 (2009), 588–596.
- [16] B. Sain, D. Das, Phys. Chem. Chem. Phys. 15 (2013) 3881–3888.
- [17] D. Kar, D. Das, J. Mater. Chem. A 1 (2013), 14744–14753.
- [18] D. Das, S. Samanta, Appl. Surf. Sci. 428 (2018) 757–766.
- [19] A. Samanta, D. Das, J. Mater. Chem. 21 (2011) 7452–7458.
- [20] J. Yang, A. Banerjee, S. Guha, Appl. Phys. Lett. 70 (1997) 2975–2977.
- [21] H. Keppner, J. Meier, P. Torres, D. Fischer, A. Shah, Appl. Phys. A 69 (1999) 169–177.

- [22] M. Berginski, B. Rech, J. Hupkes, G. Schope, M.N. van den Donker, W. Reetz, T. Kilper, M. Wuttig, 21st European Photovoltaic Solar Energy Conference, 2006, p. 1539.
- [23] S. Pizzini, *Advanced Silicon Materials for Photovoltaic Applications*, Wiley, 2012.
- [24] C.Y. Tsao, Z. Liu, X. Hao, M.A. Green, *Appl. Surf. Sci.* 257 (2011) 4354–4359.
- [25] B. Yan, G. Yue, X. Xu, J. Yang, S. Guha, *Phys. Status Solidi* 207 (2010) 671.
- [26] D. Das, *J. Phys. D: Appl. Phys.* 36 (2003) 2335–2346.
- [27] D. Das, P. Mondal, *Appl. Surf. Sci.* 416 (2017) 980–987.
- [28] S. Schicho, D. Hrunski, R. van Aabel, A. Gordijn, *Prog. Photovoltaics Res. Appl.* 18 (2010) 83–89.
- [29] M. Kondo, M. Fukawa, L. Guo, A. Matsuda, *J. Non-Cryst. Solids* 266–269 (2000) 84–89.
- [30] S. Kim, C. Park, J. Lee, J. Cho, Y. Kim, *Curr. Appl. Phys.* 13 (2013) 457–460.
- [31] I. Nakamura, T. Ajiki, H. Abe, D. Hoshi, M. Isomura, *Vacuum* 80 (2006) 712–715.
- [32] F. Qiu, W. Shin, M. Matsumiya, N. Izu, N. Murayama, *Jpn. J. Appl. Phys.* 2 (42) (2003) 1563–1567.
- [33] K. Tajima, F. Qiu, W. Shin, N. Sawaguchi, N. Izu, I. Matsubara, N. Murayama, *Jpn. J. Appl. Phys.* 43 (2004) 5978–5983.
- [34] W.K. Choi, L.K. Teh, L.K. Bera, W.K. Chim, A.T.S. Wee, Y.X. Jie, *J. Appl. Phys.* 91 (2002) 444–450.
- [35] E.V. Jelenkovic, K.Y. Tong, Z. Sun, C.L. Mak, W.Y. Cheung, *J. Vac. Sci. Technol. A* 15 (1997) 2836–2841.
- [36] D.D. Cannon, J. Liu, D.T. Danielson, S. Jongthammanurak, U.U. Enuha, K. Wada, J. Michel, L.C. Kimerling, *Appl. Phys. Lett.* 91 (2007) 252111–252113.



Chapter 2

Silicon and germanium solar cell materials and solar cells

2.1 Introduction

Silicon and germanium are the most commonly used materials in the photovoltaic industry and strong candidates for photonics applications. Both share the same column in the periodic table with four valence electrons in the outer orbits. Germanium and other semiconductors may have good properties such as better conductivity, bandgap, higher mobility, and so on, silicon based devices have dominated the semiconductor micro-electronics industry for several decades because Si is a mature, low cost, and highly manufacturable technology.

2.2 Silicon

Silicon is a group IV element that is a non-toxic semiconductor and the second most abundant element (28.2%). The name '*silicon*' originates from the Latin word "silex" or "silicis," whose meaning is "flint" or "hard stone" [1]. Silicon has atomic number 14 and an atomic radius of 0.132 nm, with the electronic configuration $[\text{Ne}](3s)^2(3p)^2$. Silicon belongs to the face-centred diamond lattice structural group with a lattice spacing of 0.54307 nm, which means that each atom has four closest neighbours at the tetrahedron's vertices at the nearest neighbour distance of 0.235 nm (Fig. 2.1(a)) [2,3]. The crystal structure of crystalline silicon (c-Si) is organized, with each atom ideally resting in a predetermined location (Fig. 2.1 (b)).

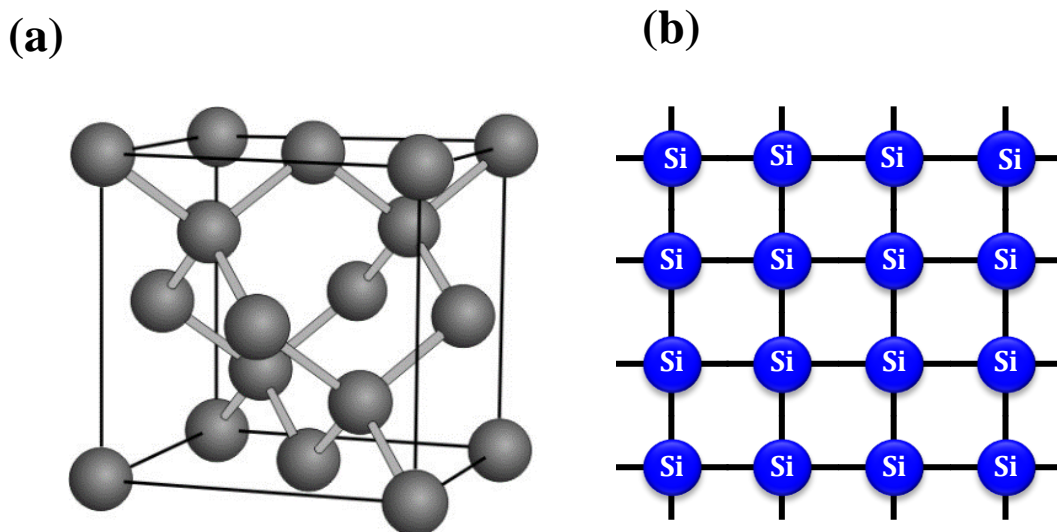


Fig. 2.1. (a) The face-centred diamond lattice structure of the crystalline silicon (c-Si).
(b) 2-D schematic diagram of the c-Si.

2.3 An overview of different forms of Si used in photovoltaics

Three different kinds of silicon are crystalline, amorphous, and nanocrystalline silicon, which are generally used to prepare Si photovoltaic cells.

2.3.1 Crystalline silicon (c-Si)

Crystalline silicon is the dominant semiconducting material utilised in photovoltaic technology to manufacture solar cells. These cells are integrated into solar panels as components of a photovoltaic system to generate solar electricity from sunlight. The conduction band's minima and the valence band's maxima are not in the same k (wave vector) value; crystalline silicon is categorised as an indirect band gap material, as illustrated in its specific band structure in **Fig. 2.2**. c-Si has an optical band gap of 1.1 eV. However, the band gap can be tailored by changing the network structure through varying different process parameters like pressure, temperature, excitation power, doping density etc. The optical band gap varies with temperature due to two separate processes. The first is caused by changes in bond length temperature and may be ascribed to the energy gap's pressure coefficient via compressibility and thermal expansion coefficient [4]. The electron-phonon interaction provides the second contribution, which predominates at high temperatures ($T > 100$ K), causing a decrease in band-gap energy as temperature rises. Theoretically, the contribution of electron-phonon interaction can be computed at different levels of sophistication. Theoretically, it is predicted that the

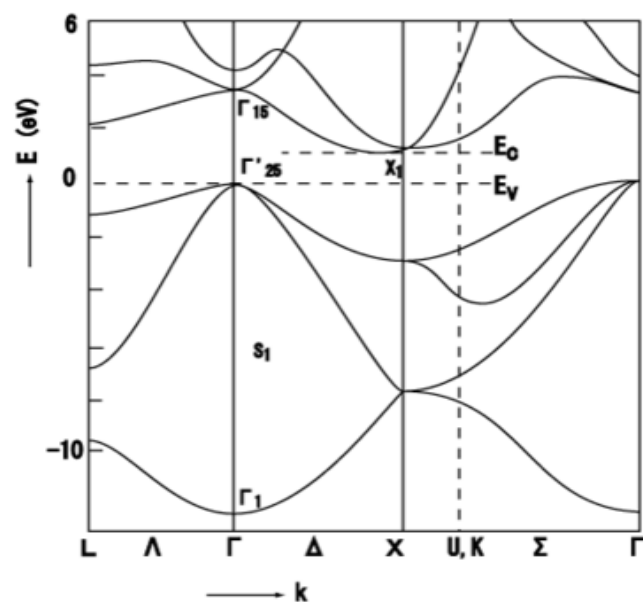


Fig. 2.2. Realistic band structure of the crystalline silicon.

energy band gap varies slowly and shows a non-linear behaviour at low temperatures before attaining linearity at a higher temperature. This behaviour is also identified by fitting the experimental data using multiple semi-empirical analytical equations.

The following four analytical equations are found in the literature that agrees to fit the experimental data with three or four parameters [5–8].

$$E_g(T) = E_g(0) - \frac{\alpha T^2}{(T+\beta)} \quad (2.1)$$

$$E_g(T) = E_B - a_B \left[1 + \frac{2}{\left(\exp\left(\frac{\theta}{T}\right) - 1\right)} \right] \quad (2.2)$$

$$E_g(T) = E_g(0) + BT + CT^2 \quad (2.3)$$

$$E_g(T) = E_B - \frac{\alpha\theta}{2} \left[p \sqrt{1 + \left(\frac{2\theta}{T}\right)^p} - 1 \right] \quad (2.4)$$

The effects of electron-phonon interaction and thermal expansion are not explicitly included or taken separately in all the above empirical relations. Therefore, the physical importance of the above parameters is not perceptible—however, Eqn. (2.1) is the most commonly cited empirical relation used to represent the temperature dependence of the band gap (E_g). The main difference between the two Eqns. (2.1) and (2.2) outcomes in the low-temperature region (<50 K): an exponential dependence in Eqn. (2.2) replaces the quadratic dependence given in Eqn. (2.1) and the band gap is represented by Bose-Einstein relations [9]. On the other hand, higher pressure and high doping narrow the band gap [10].

2.3.2 Amorphous silicon (a-Si)

Amorphous silicon (a-Si:H) is an array of silicon atoms organised spatially on a lattice with short-range ordering but without any long-range ordering, as shown schematically in **Fig. 2.3**. The average bond angles between neighbouring atoms in amorphous silicon (a-Si) are random compared to crystalline silicon (c-Si), resulting in charge carrier scattering, uncertainty in the electron's wave vector, and broadening the electronic density of states. As a result, the optoelectronic properties of the material change dramatically. The dangling bonds (DB) or unsaturated bonds produce energy levels within the band gap, causing a-Si material to have poor semiconducting characteristics. Saturation of the DBs with hydrogen atoms substantially reduces these

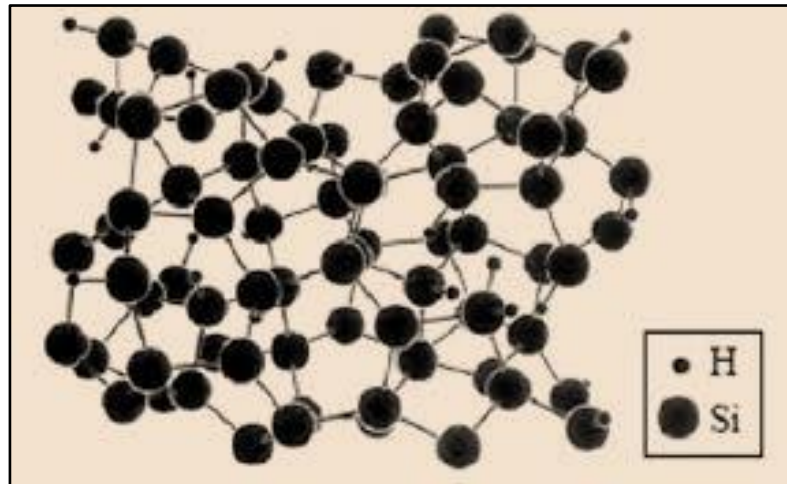


Fig. 2.3. Lattice of the a-Si:H, with Si-Si and Si-H bonds, as well as dangling bonds.

defect concentrations, making the amorphous silicon (a-Si:H) more suitable for constructing semiconductor devices, such as transistors, solar cells, LEDs, etc.

A schematic of the density of states (DOS) in a-Si:H is illustrated in **Fig. 2.4**. The formation of localized ‘band-tail’ states occurs due to structural defects and disorders. However, in hydrogenated amorphous silicon, the rough categorization in the valence band (E_V) and conduction band (E_C) still holds. The bond distortion causes band tails near the valence and conduction bands. The electrons (or holes) do not directly participate in electronic transport, as the wave functions of electrons (or holes) are spatially localized in these band tails. The dangling connections form profound, highly

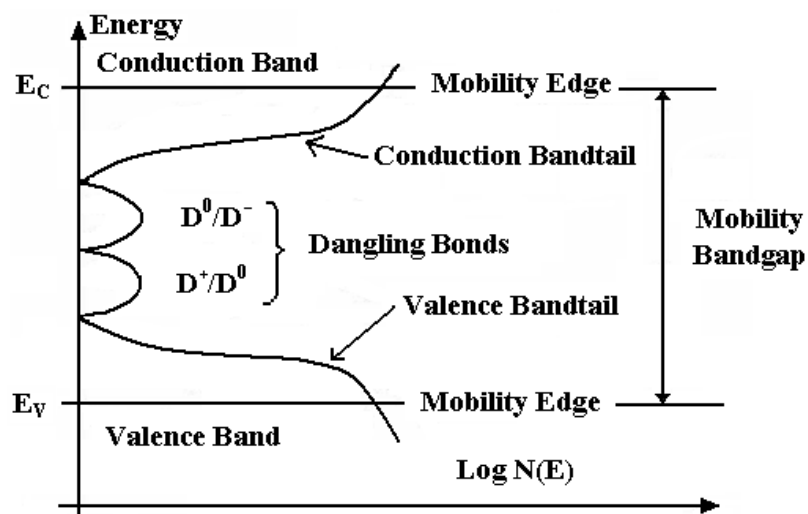


Fig. 2.4. Schematic diagram of the density of states $N(E)$ for intrinsic amorphous silicon.

localised electrical states near the centre of the band gap. The unsaturated dangling bonds generate deep and highly localized electronic states in the mid-gap positions. These defects arising from unsaturated dangling bonds act as the primary recombination centres for free electrons, and holes in a-Si:H can either be positive (D^+), neutral (D^0), or negative (D^-). The recombination paths are: one over D^0/D^- and one over D^+/D^0 . Estimating the optical band gap in a-Si:H becomes very tough due to the presence of localized states between the valence and the conduction band. So, the concept of a mobility gap is also used as an alternative approach. Charge carrier mobility drops sharply by several orders of magnitude because of the localized nature of the tail states. Thus, the optical band gap a-Si:H is substantially higher ($E_g \sim 1.7$ eV) than the band gap of c-Si ($E_g \sim 1.1$ eV).

2.3.3 Micro-/Nanocrystalline silicon ($\mu\text{c}/\text{nc-Si}$)

Nanocrystalline silicon (nc-Si) and microcrystalline silicon ($\mu\text{c-Si}$) are two-phase materials consisting of crystalline grains embedded in the amorphous tissue of silicon, where the average grain size varies from a few nanometers to a few micrometers. Specifically, when the hydrogen atoms saturate the Si dangling bonds in the grain boundaries and amorphous tissues, the resulting material is hydrogenated nanocrystalline silicon (nc-Si:H). However, this two-phase material was first referred to as microcrystalline silicon ($\mu\text{c-Si:H}$). Over time, depending on the size of the nanocrystals and the growing phase of the Si material, nomenclatures like 'polycrystalline', 'polymorphous', and 'nanocrystalline' silicon are used. The classical theory of crystal growth and nucleation is used to understand the variation of the crystal size during the growth process, representing a linear relation between crystal size and crystallinity [11].

A model of the nanostructural evolution of the $\mu\text{c}/\text{nc-Si:H}$ material [12], is schematically presented in **Fig. 2.5**. The transition from primarily crystalline to mostly amorphous growth from the left side to the right side of the diagram can be easily noticed. The nucleation sites near the substrates are the source of crystalline growth in the highly crystalline growth zone. The average grain size increases as the substrate's distance increases, giving rise to a columnar-like structure. Depending on process factors such as the nature of substrates, deposition temperature and deposition rate, the area between these crystallites is filled with a-Si tissues, voids, or cracks [13,14]. This growth zone is called the incubation zone. Over a certain period, the crystalline columns with stable grain boundaries grow fast. In this steady-state growth phase, the thickness of the film

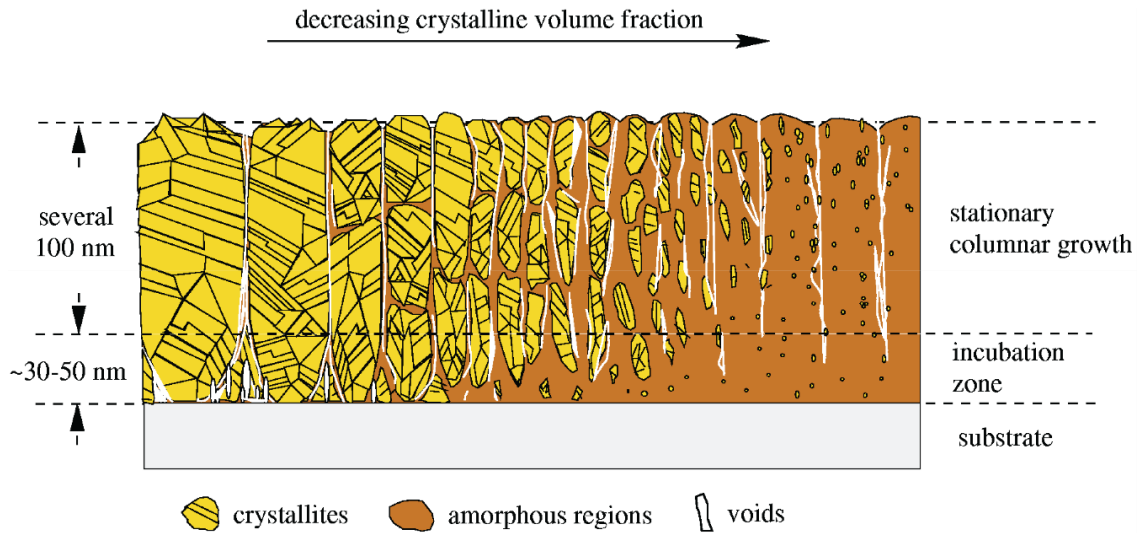


Fig. 2.5. Schematic diagram of the microstructural features of $\mu\text{c}/\text{nc-Si:H}$ film growth.

does not affect grain sizes or phase compositions. The disordered network exists at grain boundaries between the crystalline columns. However, the silicon structure within these columns is not crystalline, and it shows many twin defects, disorders and stacking faults [11,15]. The presence of voids is particularly noticeable under highly crystalline development conditions, resulting in the porous structure of the nc-Si material obtained in this growth regime [13,15]. In general, such voids are generally observed within the nucleation zone, close to the substrate and also at the boundary areas of larger-sized crystallites. The sizes of the nanocrystals are varied by changing the parametric

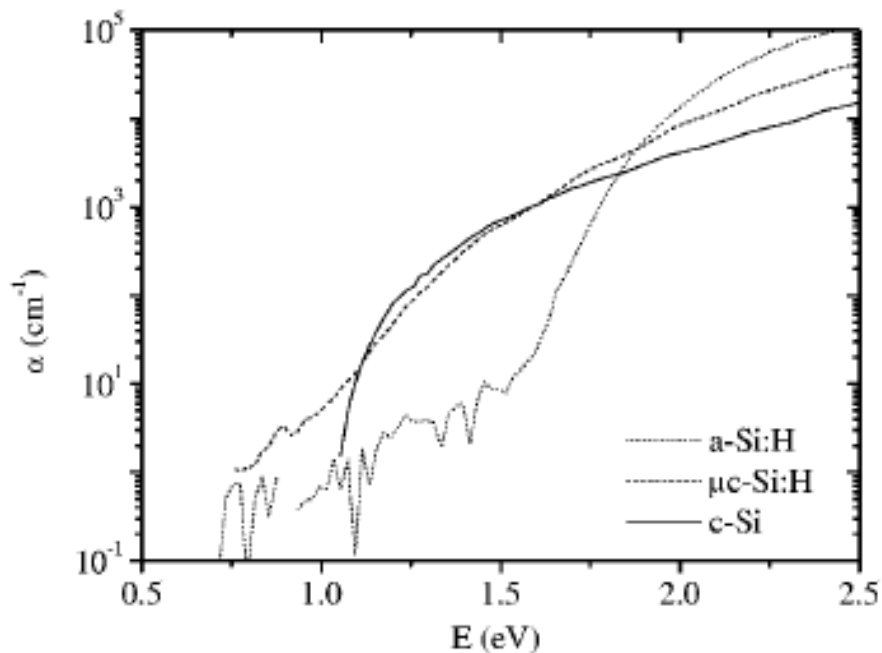


Fig. 2.6. Absorption coefficient α vs. energy for the c-Si, $\mu\text{c-Si:H}$ and a-Si:H.

conditions (plasma pressure, RF plasma power, substrate temperature, etc.). At the onset of the growth of nanocrystalline to amorphous materials, the most noticeable consequence is the reduction in column diameter. In contrast, the inclusion of a prolonged disordered phase occurs only within the nucleation layer. The size of the nanocrystal embedded in amorphous tissue reduces due to interruptions in the growth direction of the columns.

The material characteristics transform dramatically at the phase transition between microcrystalline and amorphous-like growth. In many aspects, microcrystalline silicon is similar to crystalline silicon (c-Si). However, only the absorption coefficient (α) of $\mu\text{c-Si:H}$ is considerably higher than that of c-Si at high photon energies because of the high absorption coefficient (α) of the amorphous silicon component present in the microcrystalline Si thin film ($\mu\text{c-Si:H}$) (Fig. 2.6) [16].

2.3.4 Doped nanocrystalline silicon (*p*-type/*n*-type nc-Si)

Doping is the intentional introduction of a foreign impurity into a host semiconductor material to modify its electrical, optical, and structural properties for device applications [17]. In a pure intrinsic semiconductor, the concentration of electrons (n_e) is equivalent to the concentration of holes (n_h), which can be written as follows:

$$n_i = n_e = n_h \quad (2.5)$$

At absolute zero temperature, the behaviour of intrinsic semiconductors is similar to that of insulators, as no free charge carriers are available to conduct electricity. However, at room temperature, the thermal energy is enough to generate very few free charge carriers, which are attributed to conductivity (σ), defined as,

$$\sigma = e(n_e\mu_n + n_h\mu_h) \quad (2.6)$$

where e represents the charge of electron/hole, μ_n and μ_h denote electron and hole mobility, respectively. As the electron concentration is equal to the hole concentration in a pure semiconductor, the conductivity of the intrinsic semiconductor becomes,

$$\sigma = en_i(\mu_n + \mu_h) \quad (2.7)$$

However, the electrical conductivity of an intrinsic semiconductor is too small for any practical use. The conductivity of intrinsic Si thin films can be significantly increased by adding a small quantity of pentavalent/ trivalent impurities. Doping is the process of controlled inclusion of impurity atoms into the intrinsic semiconductor. The added

impurity atoms are called the dopants. Extrinsic semiconductors are of two types: n-type and p-type.

(i) **n-type Si:** When semiconductor material from group IV like silicon (Valence electron: 4) is doped with atoms from group V (Arsenic /Phosphorus: Valence electron: 5), it replaces a Si atom in the crystal lattice. Four of the five valence electrons of the impurity atom form covalent bonds with one valence electron, each of the four Si atoms surrounding it. The fifth valence electron becomes free to move in the crystal at room temperature and acts as an additional charge carrier in the structure. The dopant atom is called an electron donor and becomes positively charged ionized in this n-type semiconductor [Fig. 2.7(a)]. In an n-type Si, electrons remain the majority carriers, and holes are the minority carriers.

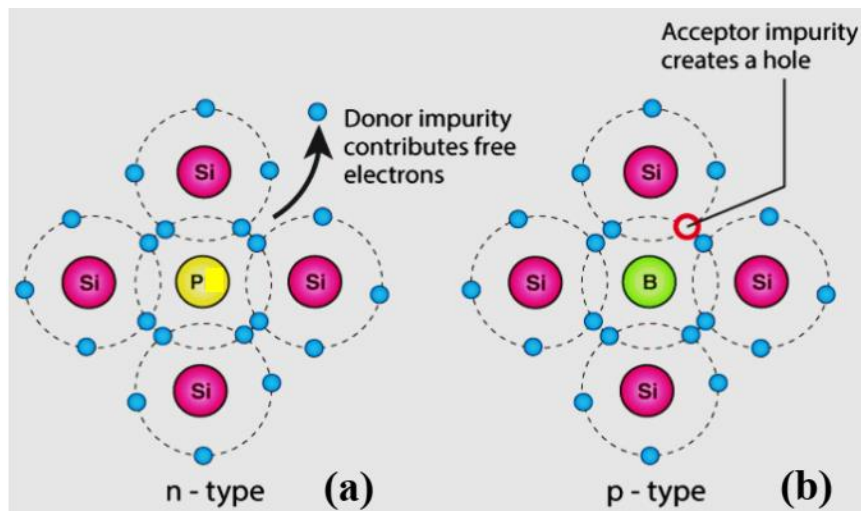


Fig. 2.7. Schematic diagram of (a) n-type Si and (b) p-type Si.

(ii) **p-type Si:** When a group IV semiconductor is doped with an atom of trivalent group III material (such as Boron/Aluminium/Gallium: Valence electron: 3), the dopant serves as an electron acceptor because it has one less valence electron than the semiconductor and subsequently creates an empty state, called 'hole', which acts as an excess charge carrier through the structure, which makes the p-type semiconductor [Fig. 2.7(b)]. A shortage of electrons, i.e., the positive holes, is the majority charge carrier in p-type semiconductors.

The concentration of one type of carrier is always larger than the other type of carrier; the charge carrier of the higher concentration is termed as "majority carrier", while the charge carrier of a lesser concentration is known as the "minority carrier."

However, p-type Si and n-type silicon behave similarly during the current flow. The number of free charge carriers increases as the number of dopants increases.

2.4 Germanium

Germanium is also a group IV element that is a non-toxic semiconductor and is scarce, having about 1.5 parts per million in the crust of the Earth. Germanium has atomic number 32 and an atomic radius of 0.211 nm, with the electronic configuration $[\text{Ar}](3d)^{10}(4s)^2(4p)^2$. Germanium also belongs to the face-centred diamond lattice structural group, similar to silicon, with a lattice spacing of 0.5658 nm.

2.5 Alloying Si with Ge

Ge is a more expensive material than Si. Researchers have drawn their attentions in SiGe alloy with the desire to keep using cost-effective fabrication facilities that are well established for Si-based technology. As bulk Si and Ge both have the diamond lattice structure and Ge is fully miscible with Si, any random alloy in the form of $\text{Si}_{1-x}\text{Ge}_x$ ($0 < x < 1$) can be prepared. Furthermore, the band gap of Ge made it suitable in view of efficient utilization of longer wavelength part of the solar spectrum by the device and integrates it in existing Si technology.

In PECVD synthesis, silicon and germanium can be easily alloyed by adding the respective source gases GeH_4 or GeF_4 with SiH_4 . The optical band gap of the silicon germanium alloy material can be tailored over a wide span by altering the amount of Ge in the Si matrix. For instance, with significant Ge inclusion in the Si-matrix, the nominal band gap of the a-Si:H may be decreased to 1.0 eV. In general, distinct sub-cells in multi-junction tandem solar cells are made up of specific materials with a tunable band gap for optimal solar radiation utilization.

2.5.1 Amorphous silicon-germanium alloy (a-SiGe:H)

The hydrogenated amorphous silicon-germanium (a- $\text{Si}_{1-x}\text{Ge}_x\text{:H}$) alloy is a capable candidate for the absorber layer of the bottom sub-cell in the multi-junction solar cell and the infrared detector. Synthesis of a-SiGe:H alloy materials in the glow discharge process was first reported by Chittick et al., using a gas mixture of silane and germane [18]. Several deposition processes, such as r.f. or d.c. glow discharge [19,20],

photochemical vapor deposition (CVD) [21], microwave-CVD [22], r.f. sputtering [23,24], as well as various sources [25] and diluent gases [26], were used for the preparation of device quality alloy materials. The optical band gap in the amorphous silicon germanium may be changed over a wide range between ~ 1.1 – 1.7 eV, by changing the Si/Ge composition in the alloy network [27]. Many linear empirical formulas between the band gap (E_g) and the Ge fraction (X_{Ge}), and hydrogen fraction (X_H) have been reported in the literature [28–30]. According to the literature, SiGe alloy films with high Ge content, in the range $0.4 \leq X_{Ge} \leq 0.6$, having optical band gaps ~ 1.4 eV would have more efficient absorption in the near-infrared part of the solar radiation and appear useful as the bottom cell material in multi-junction devices to improve solar absorption [31,32]. With higher Ge content, more chemical disorder increases structural defects such as dangling bonds (DB), vacancies, and micro-voids, lowering optoelectronic parameters like photocurrent responsiveness, carrier mobilities, and lifetime [33–36].

2.5.2 Nanocrystalline silicon-germanium alloy (nc-SiGe:H)

According to the literature, nanocrystalline silicon germanium (nc-SiGe:H) alloy has a similar structure to nanocrystalline silicon (nc-Si:H) wherein nanocrystalline silicon grains are embedded in the a-SiGe:H matrix instead of the a-Si:H matrix. In the last decades, nanocrystalline silicon-germanium alloy has received attention in photovoltaic technology as an alternative to nc-Si and a-SiGe material in the multi-layer nc-Si solar cell [37–39]. The reason behind it lies in the reduced light-induced degradation in nc-SiGe, compared to a-SiGe, and better electrical properties. The substantial amount of Ge incorporation maintaining suitable nanocrystallinity in the Si-network increases the optical absorption in the near-infrared part of the solar radiation.

2.6 Different types of silicon-based solar cells

2.6.1 Bulk crystalline silicon (c-Si) solar cell

Si-based solar cells comprised of crystalline silicon wafers (c-Si) make up approximately 90% of the photovoltaic modules in the world. For photovoltaic applications, c-Si is very suitable because its optical band gap (1.1 eV) is comparable for generating the maximum electron-hole pair in the solar radiation. Two types of c-Si are

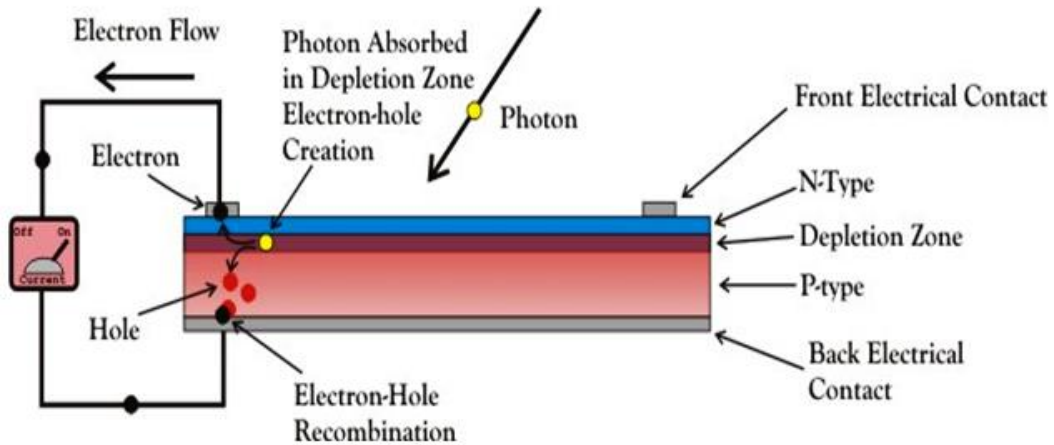


Fig. 2.8. Schematic of a silicon solar cell
 (source: <http://2.wollo.aufraeumfee.de/solar-cell-diagram.html>).

used to manufacture PV modules: one is single-c-Si, also known as mono-c-Si, and the other is multi-c-Si silicon, also known as poly-c-Si. The mono-c-Si PV modules have a power conversion efficiency (PCE) 10–12% is higher than that of poly-c-Si PV modules. The mechanism of these cells is based on the concept of the *p-n* junction [Fig. 2.8].

In a c-Si solar cell, a relatively thin layer of highly doped *n*-type semiconductor is grown on a thick *p*-type crystalline wafer. A few more thin electrodes are placed on the *n*-type semiconductors. These electrodes ensure not to obstruct the sunlight much from reaching the top of the *n*-type semiconductor, and a current collecting electrode is provided at the bottom of the *p*-type layer. The entire system is enclosed in thin glass to protect the solar cell from mechanical shock.

When light reaches the *p-n* junction through the very thin *n*-type layer, the energy of the incident light in the form of photons creates many electron-hole pairs (e^-h^+ pairs). The free electrons and holes in the depletion region quickly come to the *n*-type side and *p*-type side of the junction, respectively, due to the pre-existing electric field at the junction's depletion region. Once the newly created free electrons and holes reach the opposite ends, these are unable to cross the junction due to the high barrier potential. So, the electron's concentration and the hole's concentration increase on the *n*-type and *p*-type sides, respectively. The *p-n* junction functions similar to a small battery cell, and a small current (in the range of mA) flows across the junction when a small load is put across it [40]. Single-junction crystalline Si solar cells are more stable over time but have limited efficiency. However, its production cost is very high because its production

procedure consists of heat treatment in a high-temperature vacuum furnace, requiring additional electrical energy that is not commercially favoured.

2.6.2 Amorphous silicon (a-Si) solar cell

Amorphous Si or a-Si solar cells belong to silicon thin film solar cells. Thin film solar cell technology has been employed to eliminate the high production cost of the c-Si solar cell. Here, it is talked about 'thin film' since a layer thickness of $1\ \mu\text{m}$ or less is enough to absorb all the light. On the other hand, pure a-Si is a poor conductor and not so worthy since it contains a huge amount of "dangling bonds (DB)" that introduce various electronic states in the band gap at high density. a-Si performs as a direct band gap semiconductor with an optical band gap of roughly $1.7\ \text{eV}$ when these dangling

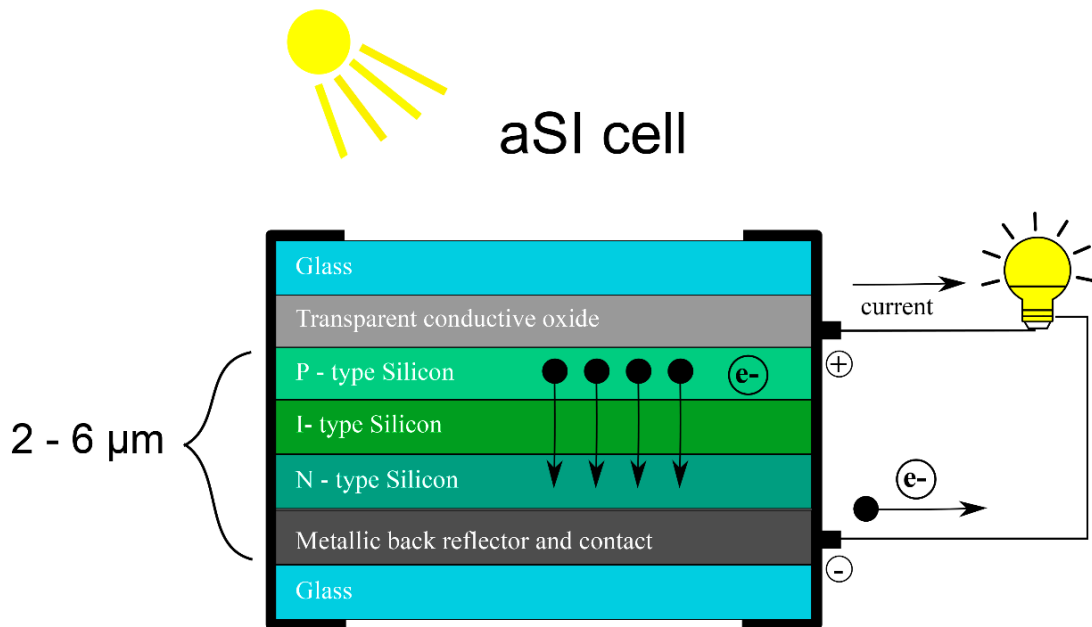


Fig. 2.9. Schematic diagram of the basic structure of a *p-i-n* a-Si solar cell.

bonds are passivated with hydrogen atoms (H). Even though the density of dangling bonds is considerable but still less than 1% of total bonds in a-Si, it is needed to put 5% to 30% of H-atoms into the a-Si to achieve reasonable semiconducting characteristics for application. Amorphous silicon is generally referred to as amorphous silicon hydride, and it is abbreviated as a-Si:H [41–43].

The a-Si thin film solar cell mainly has the *p-i-n* or *n-i-p* of duality in the structure, where the *n*-layer and *p*-layer are usually used to lead an internal electric field in *i*-layer, made of amorphous hydrogenated silicon (a-Si:H) [Fig. 2.9]. The intrinsic

layer (*i*-layer) usually has a 2000-5000 nm thickness as amorphous silicon possesses a high absorption coefficient. The amorphous silicon's optical band gap is between 1.1 and 1.7 eV, which grossly differs from that of crystalline silicon, which has an optical band gap of ~1.1 eV.

Being a direct band-gap material, a-Si requires only about 1% of the silicon used to make c-Si solar cells, reducing the production cost. Furthermore, the material can be deposited at low temperatures, below 300 °C, on inexpensive substrates such as glass, stainless steel, plastic, etc. Therefore, a-Si based PV technology is a good candidate for using lightweight, flexible substrates and roll-to-roll fabrication techniques. However, when a-Si:H solar cells are exposed to light for an extended period, the Staebler-Wronski effect occurs. Their efficiency η drops by up to 30%, and the power conversion efficiency (PCE) is also low for a-Si:H solar cells.

2.6.3 Micro/Nano-crystalline silicon ($\mu\text{c}/\text{nc-Si:H}$) solar cell

Veprek and Marecek developed nanocrystalline silicon (nc-Si:H) via a plasma-assisted low-temperature deposition technique [44]. Later, Usui and Kikuchi discovered that doping nc-Si:H layers is significantly easier than doping a-Si:H layers. Additional

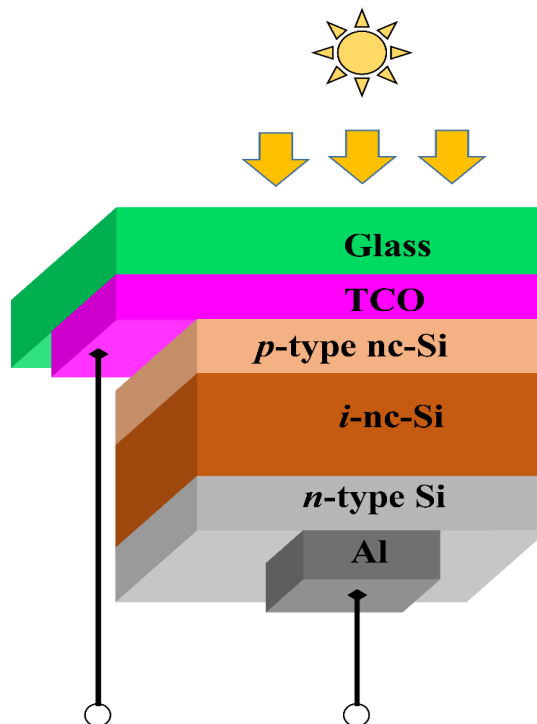


Fig. 2.10. Schematic diagram of the *p-i-n* nc-Si silicon solar cell.

defects induced by the dopant atoms incorporation are not present in $\mu\text{c-Si:H}$ layers [45]. Considering the low quality of the first $\mu\text{c-Si:H}$ layers (due to their comparatively high defect density) and the n -type behaviour of the layers produced without the use of doping gases, it was originally believed that it would not be possible to make reasonable solar cells with an $\mu\text{c-Si:H}$ intrinsic layer acting as the main photo conversion layer [46]. However, in 1996, J. Meier *et al.* achieved an efficiency of 7.7% in an entirely $p-i-n$ -type microcrystalline thin film silicon solar cells [47]. In particular, the Staebler–Wronski effect is less pronounced in such $\mu\text{c-Si:H}$ solar cells than in $a\text{-Si:H}$ solar cells. The $p-i-n$ or $n-i-p$ configuration is still used for the manufacturing of $\mu\text{c-Si:H}$ solar cells since the diffusion lengths in $\mu\text{c-Si:H}$ material are far too short, just like in $a\text{-Si:H}$, requiring drift-assisted collection. A schematic of a $p-i-n$ -type $\mu\text{c-Si:H}$ solar cell is shown in Fig. 2.10.

2.6.4 $\mu\text{c-Si}$ multi-junction or tandem-structure solar cell

A tandem cell is a device with more than one $p-n$ junction containing photon-absorbing materials. Compared to single-junction solar cells, constructing $p-n$, $p-i-n$, or any other diode structure with various band gap semiconductors and combining them

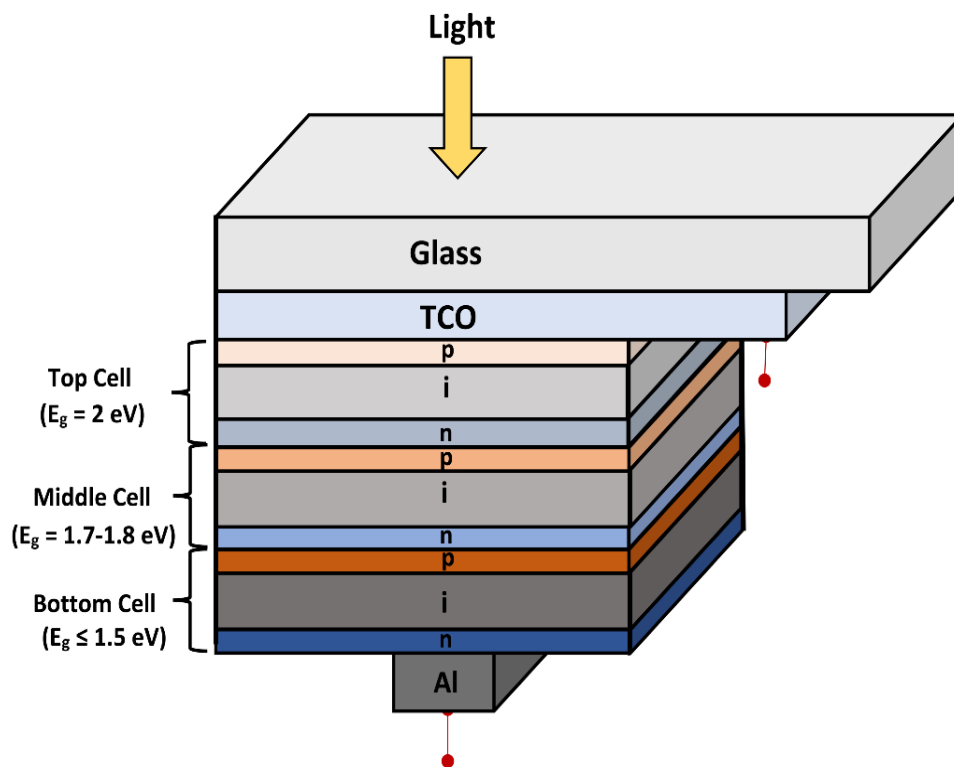


Fig. 2.11. Schematic diagram of an all-Si based tandem solar cell.

improves the photovoltaic power conversion efficiency. A multi-junction solar cell may absorb sunlight across multiple wavelength ranges due to the usage of various layers with different band gaps. The top cell is designed to absorb higher energy, and the succeeding cells (i.e. middle cell, bottom cell, etc.) would absorb the lower energies that the top cell or preceding cells don't absorb, which is the primary concept of this multi-junction tandem solar cell. The tandem solar cells have higher efficiency as these could absorb a wider spectrum of solar radiation for energy conversion. Although increasing the number of cells in a tandem cell can theoretically raise a solar cell's maximum efficiency, there is still a limit to the efficiency. The theoretical maximum efficiency of a single cell is 31%, the highest efficiency of a two-cell tandem solar cell is 42.5%, the maximum efficiency for a three-cell solar cell is 48.6%, and so on. The theoretical maximum efficiencies may keep rising, but the highest efficiency of an infinite stack of practical solar cells is only 68.2%. **Fig. 2.11** demonstrates the schematic diagram of a silicon-based or "all-silicon" tandem solar cell.

2.7 References

- [1] M.A. Sommers, *Silicon* 181 (2008) S6559.
- [2] G.F. Cerofolini, L. Meda, *Appl. Surf. Sci.* 89 (1995) 351–360.
- [3] M.E. Straumnts, E.Z. Aka, *J. Appl. Phys.* 23 (1952) 330–334.
- [4] P. Lautenschlager, P.B. Allen, M. Cardona, *Phys. Rev. B* 31 (1985) 2163.
- [5] Y.P. Varshni, *Physica* 34 (1967) 149.
- [6] K.P. O'Donnell, X. Chen, *Appl. Phys. Lett.* 58 (1991) 2924.
- [7] W. Bludau, A. Onton, W. Heinke, *J. Appl. Phys.* 45 (1974) 1846.
- [8] R. Pässler, *Sol. Stat. Electron.* 39 (1996) 1311.
- [9] L. Vina, S. Logothetidis, M. Cardona, *Phys. Rev. B* 30 (1967) 149.
- [10] R. Hull, *Properties of Crystalline Silicon*, INSPEC Publication, London (1999).
- [11] O. Vetterl, F. Finger, R. Carius, P. Hapke, L. Houben, O. Kluth, A. Lambertz, A. Muck, B. Rech, H. Wagner, *Sol. Energy Mater. Sol. Cells* 62 (2000) 97.
- [12] L. Houben, *Plasmaabscheidung von mikrokristallinem Silizium: Merkmale der Mikrostruktur und deren Deutung im Sinne von Wachstumsvorgängen*, Ph.D. thesis, Heinrich-Heine-Universität Düsseldorf (1998), p. 25.
- [13] M. Tzolov, F. Finger, R. Carius, P. Hapke, *J. Appl. Phys.* 81 (1997) 7376.

- [14] M. Luysberg, P. Hapke, R. Carius, F. Finger, *Philosophical Magazine A* 75 (1997) 31.
- [15] L. Houben, M. Luysberg, P. Hapke, R. Carius, F. Finger, H. Wagner, *Philosophical Magazine A* 77 (1998) 1447.
- [16] T. Roschek, Microcrystalline silicon solar cells prepared by 13.56 MHz PECVD prerequisites for high quality material at high growth rates, Thesis, (2003).
- [17] I. Marri, E. Degoli, S. Ossicini, *Progress in Surface Science* 92 (2017) 375–408.
- [18] R.C. Chittick, *J. Non-Cryst. Solids* 3 (1970) 255.
- [19] J. Bullo, M. Gafin, M. Gauthier and B. Bourdon, *J. Phys (paris)*, 44 (1983) 713.
- [20] B.V. Roedern, D.K. Paul, J. Blake, R.W. Collins, G. Moddel, W. Paul, *Phys. Rev. B* 25 (1982) 7678.
- [21] P.K. Banerjee, R. Dutta, S.S. Mitra and D.K. Paul, *J. Non-Cryst. Solids* 50 (1982) 1.
- [22] S.Z. Weisz, M. Gomez, J.A. Mujer, O. Resto, R. Perez, Y. Goldstien, B. Ables, *Appl. Phys. Lett.* 44 (1984) 634.
- [23] S.S. Hegedus, R.M. Tullman, H.S. Lin, J.M. Gebulka, W.A. Buchanan, R. Dozier, R.E. Rocheleau, *Proceed. 19 th IEEE Photovoltaic Specialist Conf. New Orleans, May 4-8, 1987*, p867.
- [24] T. Watanabe, M. Tanaka, K. Azuma, M. Nakatani, T. Sonabe, T. Shimida, *Jpn. J. Appl. Phys.* 26 (1987) L288.
- [25] S. Guha, J.S. Payson, S.C. Agarwal, S.R. Ovshinsky, *J. Non-Cryst. Solids* 97–98 (1987) 1455.
- [26] M. Stutzmann, R.A. Street, C.C. Tsai, J.B. Boyce, S.E. Ready, *J. Appl. Phys.* 66 (1989) 569.
- [27] J. Chevalier, H. Wieder, A. Onton, C.R. Crounrier, *Solid State Commun.* 26 (1977) 887.
- [28] S. Wagner, V. Chu, J. P. Conde, J. Z. Liu, *J. Non-Cryst. Solids* 114 (1989) 453.
- [29] K.D. Mackenzie, J.H. Burnett, J.R. Eggert, Y.M. Li, W. Paul, *Phys. Rev. B* 38 (1988) 6120.
- [30] M.E. Gueunier, J.P. Kleider, R. Bruggemann, S. Lebib, P. Roca i Cabarrocas, R. Meaudre, B. Canut, *J. Appl. Phys.*, 92 (2002) 4959.
- [31] J. Yang, A. Banerjee, S. Guha., *Appl. Phys. Lett.* 70 (1997) 2975.

- [32] S. Guha, X. Xu, J. Yang, A. Banerjee, *Appl. Phys. Lett.* 66 (1995) 595.
- [33] K.C. Palinginis, J.D. Cohen, J.C. Wang, S. Guha, *J. Non-Cryst. Solids* 266-269 (2000) 665.
- [34] S. Guha, J. Yang, *Appl. Phys. Lett.* 61 (1992) 1444.
- [35] K.D. Mackenzie, J.R. Eggert, D.L. Leopold, Y.M. Li, S. Lin, W. Paul, *Phys. Rev. B* 31 (1985) 2198.
- [36] S.J. Jones, Y. Chen, D.L. Williamson R. Zedlitz, G. Bauer, *Appl. Phys. Lett* 62 (1993) 3267.
- [37] G. Ganguly, T. Ikeda, T. Nishimiya, K. Saitoh, M. Kondo, A. Matsuda, *Appl. Phys. Lett.* 69 (1996) 4224–4226.
- [38] T. Matsui, H. Jia, M. Kondo, *Prog. Photovolt. Res. Appl.* 18 (2010) 48–53.
- [39] Y. Cao, Y. Liu, J. Zhou, Y. Wang, J. Ni, J. Zhang, *Sol. Energy Mater. Sol. Cells* 151 (2016) 1–6.
- [40] K. Jäger, O. Isabella, A.H.M. Smets, R.A.C.M.M. van Swaaij, M. Zeman, *Solar energy fundamentals, technology, and systems*, Delft University of Technology (2014).
- [41] A. Nowshad, *High efficiency amorphous silicon thin film solar cells* paperback, Lambert Academic publishing, 11 Jun 2014.
- [42] R.A. Street, *Hydrogenated Amorphous Silicon*, Cambridge University Press, ISBN 9780521019347 (2005).
- [43] B. Wilson, J. McGill, D. Weaire, *Recent progress in Thin-film Solar Cells*, *Advances in Physics* 27 (1978) 365–385.
- [44] S. Vepek, V. Mareek, *Solid-State Electronics* 11 (1968) 683.
- [45] S. Usui, M. Kikuchi, *J. Non-Cryst. Solids* 34 (1979) 1.
- [46] W.E. Spear, G. Willeke, P.G. Le Comber, A.G. Fitzgerald, *Le Journal De Physique Colloques* 42 (1981) 257.
- [47] J. Meier, P. Torres, R. Platz, S. Dubail, U. Kroll, J.A.A. Selvan, N.P. Vaucher, C. Hof, D. Fischer, H. Keppner, A. Shah, K.D. Ufert, P. Giannoules, and J. Koehler, *Proceed. Mater. Res. Soc. Symposium* 420 (1996) 3.



Chapter 3

Thin film deposition techniques

3.1 Introduction

A thin film is a three-dimensional layer of material that extends infinitely along with any two directions but can have a restricted thickness ranging from a few nanometers to several micrometers only, formed by arranging one after the other molecular/ionic/atomic species of the matter.

3.2 Processing techniques of thin film deposition

The synthesis techniques used for the thin film's growth are categorized in numerous processes and each technique has its advantages and disadvantages, none is ideal in all the desired aspects (cost of apparatus, nature of the substrate and deposition parameters, etc.). The physical vapour deposition (PVD) and chemical vapour deposition (CVD) processes are of massive interest among all other processes for their fruitful application in the low-cost manufacturing of photovoltaic and optoelectronic devices. In these two processes, the controlled synthesis of a material is achieved on the substrates in a vacuum system, in a thin layer, referred to as deposition. The ability to deposition of uniform and the device quality thin film is the most important advent of the vacuum technology used in the physical and chemical vapour deposition technique. The low temperature (≤ 300 °C) synthesis of the nanostructured thin films is mainly categorized into two classes: chemical vapour deposition (CVD) and physical vapour deposition (PVD). Here the processes which are generally used to synthesize the basic nc-SiGe thin films and the Al electrodes, are presented in this thesis, are discussed in brief.

3.3 Physical vapor deposition

In this method, the material is progressively transported from the solid phase to the vapour phase and back to the solid phase, which gradually forms a film on the substrate's surface [1]. Physical vapor deposition approaches provide several advantages, including the simple and low-cost, excellent quality, cleanliness, thin-film dry processing, and compatibility with semiconductor integrated circuit (IC) manufacturing. Certain drawbacks are also present, such as it is difficult to control the stoichiometry because of the requirement of the high process temperature and the low deposition rate. It is also challenging to make dielectric materials evaporate. In some cases, post-annealing treatment is used for crystallization leading to high capital cost [2].

3.3.1 Vacuum thermal evaporation

Vacuum thermal evaporation is one of the oldest, most popular low-cost thin film deposition techniques due to its simplicity. This method is widely used in the research laboratories and industry for depositing metal, semiconductor and their alloys on various substrates such as glass, wafer, PET, etc. In this process, a solid substance is heated to its evaporation point in a high-vacuum chamber (10^{-5} to 10^{-7} Torr) [3]. This low chamber pressure aids in the material's evaporation and reaches the substrate. The schematic diagram of a vacuum thermal evaporation system is illustrated in **Fig. 3.1**. The system consists of a 'boat' made of Molybdenum or Tungsten, into which the solid material in the form of wires, sheets or powders is inserted to be evaporated. The evaporated material travels from the heated 'boat' to the substrate, where it nucleates to produce a thin film layer of decent quality.

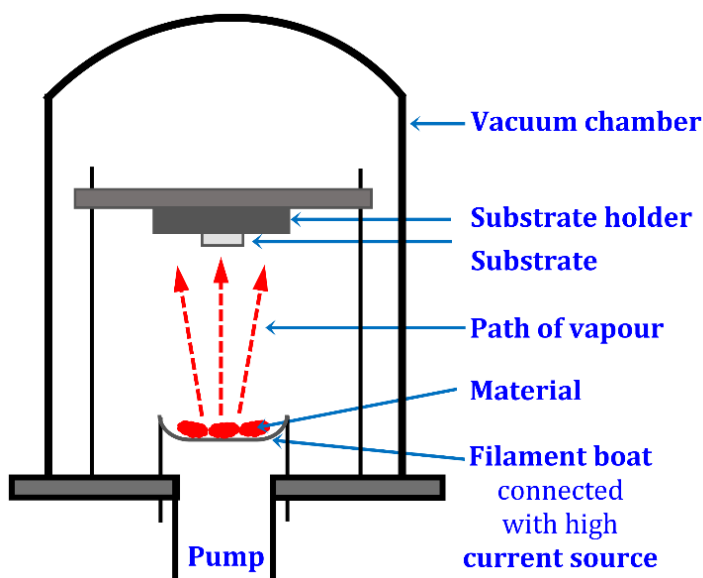


Fig. 3.1. Schematic diagram of the vacuum thermal evaporation unit.

As a standard electrically resistive heating element or filament is used, this approach is called resistive evaporation. E-beam evaporation is another standard method of thermal evaporation. An e-beam or electron beam is targeted towards the source material, resulting in local heating followed by the evaporation of the source material. A few of the advantages of thermal evaporation are – (a) the high-purity source material can be used to deposit high-purity films, (b) it is the cheapest PVD method when compared to other PVD processes such as sputtering techniques, (c) area of deposition can be controlled using a mask on the deposited substrate, (d) film thickness can be

regulated using a shutter in between the source and the substrate etc. The thermal evaporation technique has the following disadvantages: (a) it is limited to low melting point solids as the depositing material, (b) it is pretty tough to make many alloy and compound compositions, (c) filament size limits the amount of material that can be deposited, (d) the presence of high radiant heat in the deposition system, and (e) poor density and reduced adhesion etc.

This vacuum thermal evaporation technique is utilized in the present work to deposit Al electrodes on the silicon germanium thin films to measure the electrical properties.

3.3.2 Pulsed laser deposition (PLD)

In a pulsed laser deposition (PLD) process, thin films are prepared by the ablation of one or more targets illuminated by a focused high-powered ultraviolet pulsed laser beam. The materials are then vaporized from the target and deposited on a substrate as a thin film. In general, substrates are mounted in parallel to the target surface at a distance of typically 2-10 cm. The schematic diagram of the laser deposition setup is shown in **Fig. 3.2**. By adjusting the count of laser pulses, the desired film thickness can be achieved. The deposition method is executed in an ultrahigh vacuum (UHV) chamber or reactive gas atmosphere, which allows preparing of all kinds of oxides, carbide, nitride-based materials. In addition, it is possible to prepare complex thin films with nearly similar stoichiometry as the target, called stoichiometry transfer [4]. Silicon nanoparticles can be prepared using a contamination free pulsed laser deposition process [5]. The possibility of modifying laser characteristics such as wavelength, pulse length,

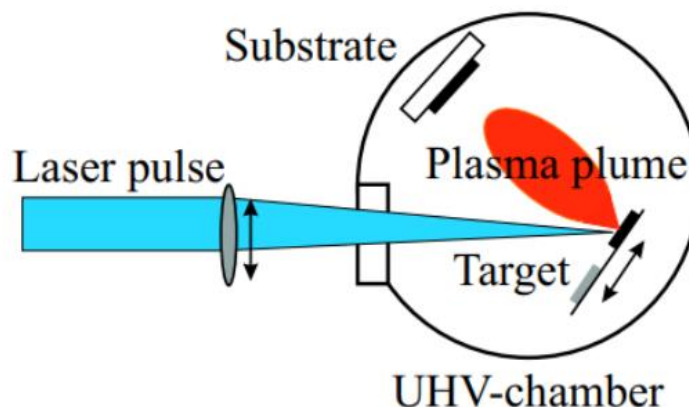


Fig. 3.2. Schematic diagram of the pulsed laser deposition unit.

and the deposition parameters like substrate temperature, target to substrate distance demonstrates the enormous versatility of PLD technique.

3.3.3 Sputtering

Sputtering is the most versatile physical vapor deposition technique for the deposition of thin films with optimized properties. The atoms from a target material are released and rest on the substrate. This technique helps to prepare thin films with the desired composition in films with good adherence, with better control of its thickness. In this process, a plasma is produced using an inert gas (Ar gas, in general) by applying DC/RF voltage between the target as cathode and the substrate as anode electrodes [6–8]. Momentum is transferred from energetic bombarding ions to surface atoms and finally ejects the atoms from the target material. The schematic representation of a basic sputtering system is shown in **Fig. 3.3**. Generally, three different types of sputtering systems are used in film deposition as follows:

(i) DC sputtering: A negative DC source is applied to the target material in this sputtering system. Due to the opposite polarity of the electric charge and transfer of linear momentum, ionized Ar^+ ions get attracted toward the target material and finally sputters the atoms from the target. Then, the ejected target materials are deposited on the substrate. The drawback of the DC sputtering is the decrease in the ejection rate of target materials due to the accumulation of Ar^+ on the insulating target which finally decreases the deposition rate.

(ii) RF sputtering: The drawback of DC sputtering can be solved by using an RF source at the target. The polarity of the electric target is periodically changed, so the Ar^+ does not accumulate on the insulated target. Also, another benefit of applying the RF source is that it can produce plasma at lower pressure with lower power. The drawback in RF sputtering is that the deposited films can be etched out due to Ar^+ ions in the plasma.

(iii) Magnetron sputtering: In the magnetron sputtering, a magnetic field is employed near the top of the target further to enhance the deposition rate in the sputtering system. This field forces electrons to move along the magnetic field lines near the target in a spiral route rather than being drawn to the substrate. This has the benefit of confining the plasma to a small area near the target, preventing the damage of the thin film being

formed as Ar^+ does not disturb deposited material because the ions are trapped in the path generated by the perpendicular electric and magnetic field, and this eliminates the problems that occur in DC and RF sputtering [9]. So, the deposition rate in the RF magnetron sputtering system is increased altogether. Therefore, the RF magnetron sputtering technique is a cost-effective process suitable for applications. Various magnetrons (planar, cylindrical, etc.) are available for using in different specific applications.

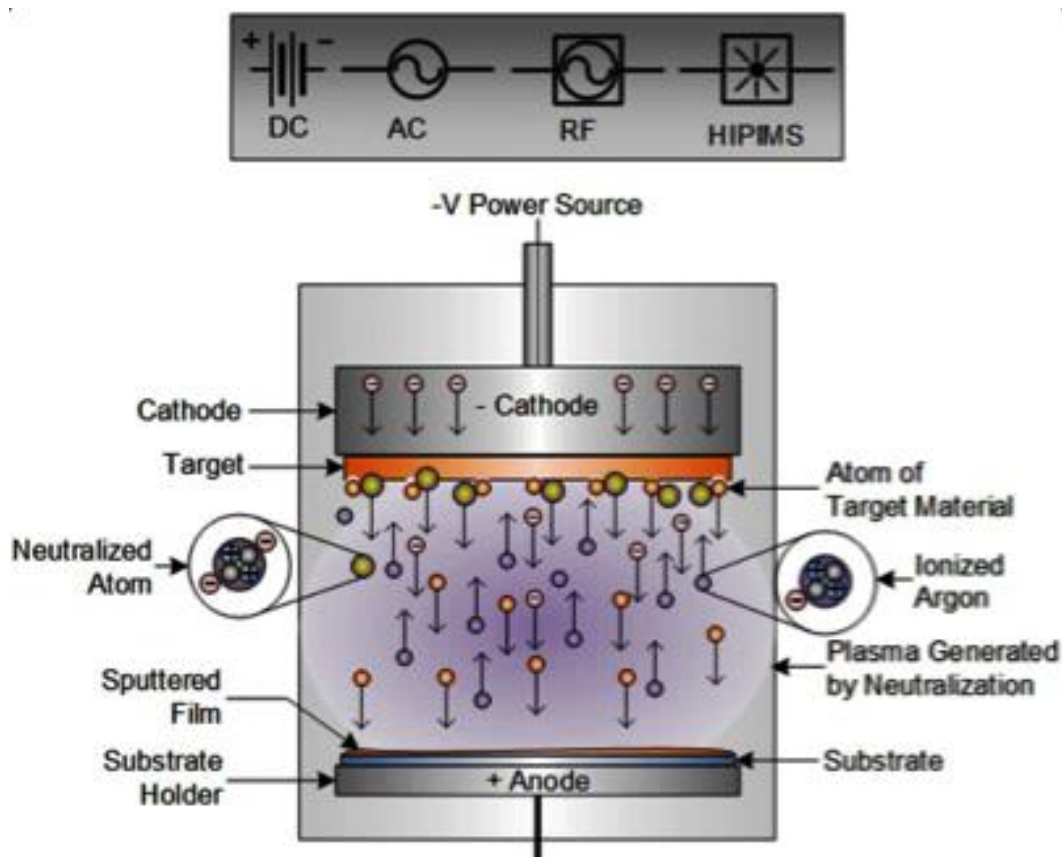


Fig. 3.3. Schematic representation of a typical sputtering system with the working mechanism.

The sputtering process without a hydrogen-ambient leads to defects and voids in the material. Initially, the applicability of the photovoltaic thin films produced through the sputtering process is quite questionable because of the high density of dangling bond defects. Later, the passivation of the dangling bonds was confirmed by using Ar as a sputtering gas in reactive ambient hydrogen gas [10,11]. In literature, Lewis *et al.* [12] first emphasized the idea of preparing amorphous germanium (a-Ge:H) films from the Ge target in a gas mixture of Ar and H_2 . Later, Catalano *et al.* [13], Paul *et al.* [14], and Moustakas [15] prepared device grade amorphous silicon (a-Si:H) by RF-sputtering with

Si target and using Ar/H₂ mixture. Baghdad *et al.* [16] and Hasim *et al.* [17] described the fabrication of nanocrystalline silicon (nc-Si:H) films at room temperature using an undoped c-Si target. All the growth parameters in sputtering strongly influence the grown film properties like crystallinity, surface roughness, etc. Recently, nanostructural evolution of Si:H films by introducing H₂ with Ar in 13.56 MHz RF Magnetron sputtering at 200 °C [18]. The hydrogen absorption into the Si-network declines with the increasing concentration of hydrogen gases which facilitates better nucleation and superior growth of nanocrystallites. Several investigations on the growth of various alloys' thin silicon films (SiO, SiN, SiC, etc.) have also been carried out using the sputtering technique [19–23]. The main advantage in preparing any silicon thin films or their different alloys in the sputtering process is that no toxic gases such as silane, methane, phosphine and diborane are used here. The sputtering method is expected to realize lower-cost safety larger area deposition processes. Furthermore, it is possible to delicately modify the optoelectronic properties of nc-Si:H and nc-Ge:H thin films within a wide range by close control of the sputtering technique [24].



Fig. 3.4. The photograph of the sputtering system in our lab, used for synthesis of the nc-SiGe thin films.

RF magnetron sputtering system is shown in **Fig. 3.4** used for part of the thesis work in our laboratory. The additional features in this system are (i) quartz crystal thickness monitor used for measuring the thickness of deposited materials and for preparation of thin films with suitable thickness, (ii) the substrate holder can rotate, which helps to prepare the uniform film, (iii) heating arrangement with substrate holder, (iv)

chilled water flows under the target to protect the target from the breaking due to heating in plasma.

3.3.4 Ion beam deposition (IBD)

Ion beam deposition (IBD) or ion beam sputtering (IBS) is a method that employs an ion source to sputter a target material (metal or dielectric) and consequently, the sputtered materials are deposited onto a nearby substrate to form a thin film. Usually, an ion beam deposition system comprises an ion source, ion optics, and a target. Optionally it is possible to incorporate a mass analyzer in the system. In comparison to the conventional PVD (physical vapor deposition) method, the ion beam sputtering deals with the monoenergetic and highly collimated ions, allowing to control the thickness and deposit a dense and high-quality film. However, the IBD technique achieves lower deposition rates of the order of $1\text{\AA}/\text{s}$ because of the limited efficiency of the source.

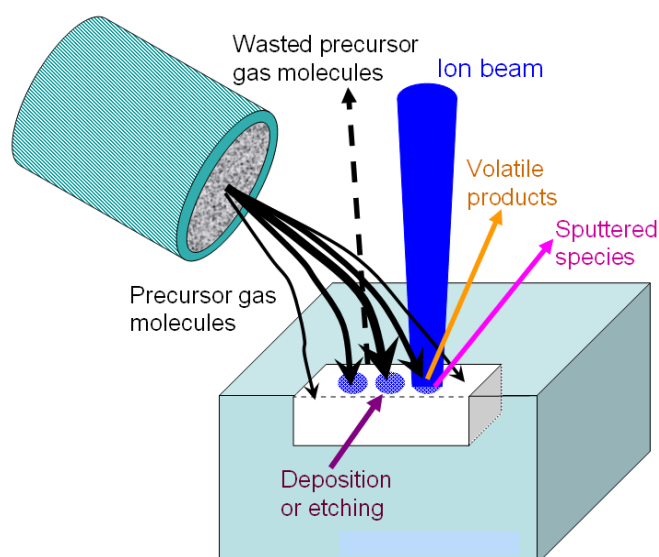


Fig. 3.5. Schematic diagram of the ion beam sputtering unit.

3.4 Chemical vapor deposition

Chemical vapour deposition is a process in which volatile/non-volatile compounds of the material decompose on the substrate after chemically reacting with each other [25]. In a CVD system, the gases are decomposed in the plasma state by chemical processes and deposited on the substrate surface [26–29]. The pumping mechanism removes the created by-products from the reactor chamber in a less harmful form to the environment. This technology is frequently utilised in the semiconductor

industry to deposit a-Si, nc-Si, c-Si, SiO₂, SiN_x, SiC, diamond, and other thin films. The CVD technique has the advantages such as – (a) it is a flexible technology with excellent purity (99.99%) and density (100%) of deposited films, (b) films can be deposited at a lower temperature than the melting point of the material, (c) any form of film shape (including net-like) may be deposited using CVD methods and (d) CVD is a low-cost method that allows several pieces to be coated at the same time. However, the intricate chemical processes and thermodynamics are complicated to understand correctly. In most cases, the by-products are frequently very poisonous, caustic, or explosive, and the volatile by-products are sometimes incorporated as an impurity in the films. There might also be a restriction on substrate selection.

3.4.1 Plasma Enhanced Chemical Vapour Deposition (PECVD)

Thin films may be produced from a gas-phase chemical reaction in the plasma state at a low temperature via plasma-enhanced chemical vapour deposition (PECVD). Plasma comprises ions, electrons, and neutral species, but it has no charge. Plasma can be created in a gas chamber with low pressure by adding high frequency (Radio-frequency, RF, microwave frequency, or ultra-high frequency) voltage [30]. The species formed in the plasma are deposited on the substrate to produce the thin film. It is a commonly accepted commercial technique, particularly for the thin film deposition of the materials like micro/nanocrystalline silicon [31], silicon germanium [32,33], silicon oxide [34,35], silicon nitride [36], silicon carbide [37] etc. The main reason for its wide acceptance is its relatively low-temperature growth process than the thermally driven CVD. For instance, a temperature of 700-900°C is essential to produce thin films of silicon nitride, silicon carbide or silicon oxide by thermal CVD, whereas only 250-350°C is adequate to grow similar films in PECVD [38]. In the PECVD system, adding electrical energy with thermal energy makes it possible to reduce the required temperature for the synthesis. Investigations over the deposition of amorphous, micro/nanocrystalline silicon thin films in large substrate areas in PECVD have been encountered because of strong adhesion, low defect-density, less stress, well control of film composition and thickness and the simple growth process [39,40].

The basic principle of all CVD processes is the decomposition of used gaseous sources. In the simplest case, in thermal CVD, the decomposition process takes place with the thermal energy of the substrate. This thermal CVD produces good quality Si

thin films with reasonable high deposition rates in the semiconductor industry. Radio-frequency capacitively coupled PECVD, inductively coupled PECVD, micro-wave PECVD, direct current (DC) PECVD, very high-frequency (VHF) PECVD and electron cyclotron resonance CVD (ECR-CVD) are some of the PECVD methods used to deposit Si-based thin films. The 13.56 MHz (RF-PECVD) is widely used in industrial applications. This technology decomposes gaseous molecules using high-energy electrons produced in glow discharges, resulting in chemically active radicals and ions. This chemical reaction facilitates for production of a wider range of materials on temperature-sensitive substrates like polymer substrate or metal substrate with a low melting point, without using large thermal energy.

PECVD has two specific advantages over conventional thermal CVD. Firstly, electron impact collisions create reactive chemical species, thus eliminating kinetic limitations that may occur in the CVD method. In addition, the discharge produces positive ions, neutral, metastable species, photons and electrons which bombard surfaces dipped in the plasma, thus altering surface chemistry. In general, the ion bombardment at the growth surface plays a significant role in nucleation, growth, and structural composition. According to the structural format, the PECVD system is classified into the following classes: (i) capacitively coupled PECVD (ii) inductively coupled PECVD, (iii) microwave RECVD.

3.4.1.1 Capacitively coupled PECVD

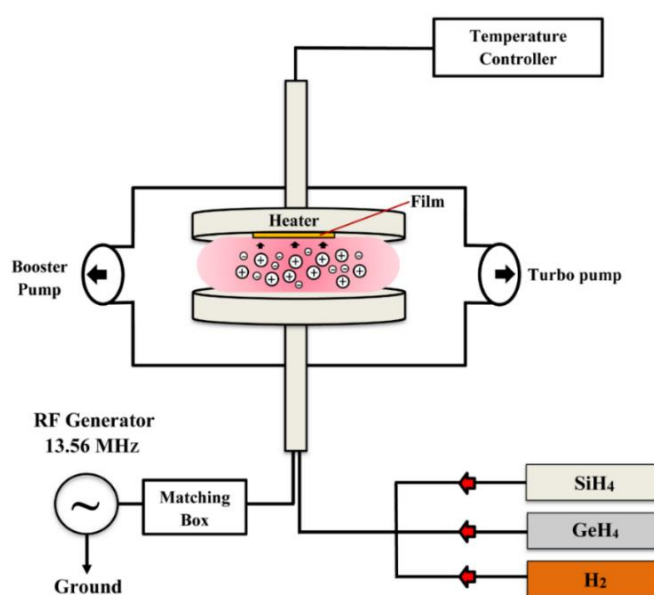


Fig. 3.6. The schematic diagram of the capacitively coupled PECVD.

The industrially used PECVD system is then a capacitively coupled plasma (CCP) system. This system consists of two parallel metal plates that act as the two electrodes of a capacitor; one connects with power and another with ground [41]. A typical CCP system is operated by 13.56 MHz RF power. When RF power is applied to the capacitor, the gases are ionized, plasma is formed within the capacitor, and the plasma species are deposited on the substrate. A schematic diagram of a typical capacitively coupled plasma system is presented in **Fig. 3.6**.

❖ 13.56 MHz capacitively coupled PECVD (CC-PECVD)

Synthesis of the silicon-germanium thin films described in the first part of the present work was carried out in a single-chamber capacitively coupled 13.56 MHz PECVD reactor. The main parts of the CC-PECVD system consist of a deposition chamber, pumping system, gas-control system, pressure control system and gas exhaust system. Furthermore, an exhaust system to pump the exhaust gases with a scrubber unit is also present to neutralize the gases after coming out from the deposition chamber. All the gas flow control system components, such as mass-flow controllers (MFC) and pneumatic valves, are coupled to a control panel. Including a 13.56 MHz RF generator and an impedance matching box, vacuum gauge controllers, pneumatic valves, throttle valves, and vacuum pumps. In the following text, each of these elements is discussed in detail. **Fig. 3.7** displays the actual photograph of the PECVD reactor. The present PECVD deposition system consists of the following essential parts:

- **Deposition chamber:** The capacitively coupled RF-PECVD is confined to a rectangular deposition plasma chamber made of stainless steel, with sides of 20 cm and 20 cm, where the 13.56 MHz RF power is being applied to the bottom disc of parallel plate square-shaped electrodes of side 10 cm mounted at an inter-electrode separation of 20 mm, whereas the top electrode held the substrates with the film. The electrodes have been mounted horizontally inside the chamber. The top electrode is connected to the heater associated with a temperature controller and is heated from behind. Additionally, the reactor chamber is fitted with a plasma display window made of quartz glass.

- **Pumping system:** Two separate systems are used to pump with the deposition chamber. The first, consisting of a rotary and a turbo-molecular pump, produces a high vacuum ($\sim 10^{-7}$ Torr) prior to the deposition process. The second unit pumps out the residue and excess of the reactive gases. It comprises a roots booster pump and a rotary

pump. Various pressure gauges like the Perini gauge, penning gauge, and absolute gauge are used to measure the vacuum level of pressure and pressure through the deposition process.

- **Gas control system:** The gas control system of the PECVD includes gas cylinders, pressure regulators, mass flow controllers, various gas valves, connecting pipes, etc. Silane (SiH_4) gas is used mainly as a raw material to form silicon or its compound. It must be treated with extreme care as it is toxic spontaneously flammable. To produce silicon alloy thin films, generally, methane (CH_4) for silicon carbide, carbon dioxide (CO_2) for silicon oxide and ammonia (NH_3) for silicon nitride is added as additional process gases. To prepare silicon-germanium alloy, another precursor gas germane (GeH_4) is used along with silane (SiH_4). To produce a thin film with *p*-type doping, a gas containing boron (diborane; B_2H_6) or, for *n*-type doping, a gas containing phosphorus (phosphine; PH_3) are used. This system also has facilities of using different types of necessary diluents gases like Hydrogen and Argon. The source gases (SiH_4 and GeH_4) and the dilution gases (H_2 and Ar, etc.) used were an ultra-pure grade (99.999% pure) to incorporate minimum impurity. Mass-Flow-Controller (MKS, AALBORG and ALICE) controls flow rates of different gases with very decent accuracy. The connecting pipe joints and fittings are high-quality stainless steel to confirm stiffness and avoid accidents.



Fig 3.7. Real photograph of the 13.56 MHz CC-PECVD system.

- **Pressure control system:** This system involves a Baratron® capacitance manometer gauge, ionization gauges, and a throttle valve for monitoring the deposition-chamber pressure. Gases are introduced via mass flow controllers, and the chamber pressure is maintained using the butterfly valve, with feedback from the capacitance manometer.

- **Gas exhaust system:** The gases used in this deposition process must be diluted before mixing with the atmosphere as those are poisonous and flammable. The current system includes a water scrubber to dilute the gases before they are released into the atmosphere.

3.4.1.2 Inductively coupled PECVD

Another PECVD type is the inductively coupled plasma (ICP) system, which is expensive. However, it can deposit high-quality thin films with a higher deposition rate because it operates at a low plasma pressure at lower temperatures [42]. Here, the electric

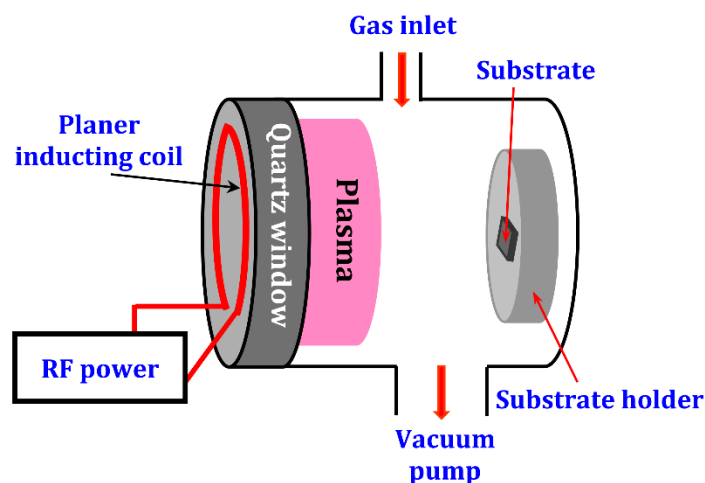


Fig. 3.8. The schematic diagram of a planer inductively coupled PECVD.

current flows through the inductor and produces an electromagnetic wave that supplies energy to the gas chamber. The ICP system may be (i) planar and (ii) cylindrical. A schematic diagram of a planar inductively coupled PECVD system is presented in **Fig. 3.8**. The significant advantages of ICP-CVD are as follows [43]: (a) plasma density in ICP is higher than that in CCP, (b) deposition rate is high due to low plasma pressure, (c) the operating temperature is nearly room temperature, (d) less chance of cracking of the deposited layer from the substrate (e) step coverage for deposition and etching is very good compared to other PECVD systems. However, the limitations of the ICP-CVD are

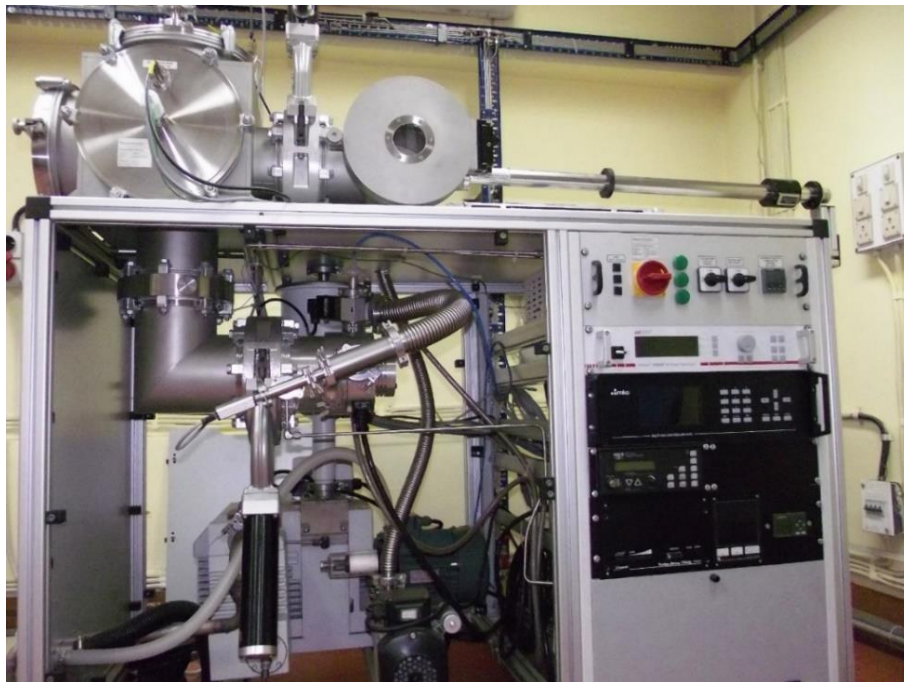


Fig. 3.9. The photograph of the planer inductively coupled PECVD in our lab.

that the ICP instrument is expensive compared to other PECVD systems and the produced by-products in ICP-CVD are toxic and need additional instruments to convert more minor health-hazard components in some cases. The ICP-CVD instrument in our laboratory, which is efficient for synthesis of Si-NSs as well as Si and Si-alloy thin films, is shown in **Fig. 3.9**.

3.4.1.3 Microwave PECVD

Microwave plasma-enhanced CVD is another high-density plasma CVD that has been utilised widely for the development of thin films. Microwave plasmas vary from other types of plasmas in that the microwave frequency causes the electrons to oscillate. The collision of an oscillating electron with gaseous atoms produces ionized atoms. This thin film growth process offers several benefits over existing plasma thin film development methods. Because microwave plasma CVD deposition is an electrode-free method, contamination of the films caused by electrode degradation can be avoided. Furthermore, a higher frequency (2.45 GHz) than RF frequency is used to produce microwave discharge, facilitating the growth of a superior quality thin film by generating a higher density of atomic hydrogen and other precursors. A schematic diagram of the active plasma zone in microwave PECVD is presented in **Fig. 3.10**.

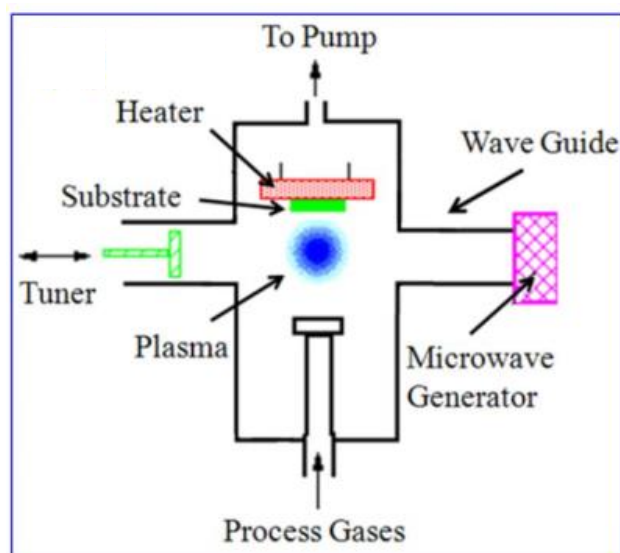


Fig. 3.10. The schematic view of the active plasma zone in a microwave PECVD.

3.5 Growth mechanism of thin film deposition

The thin film deposition on the substrate is performed by an arrangement of atoms called clusters or nuclei. If the substrate and films are the same, then the nucleation is known as homogeneous nucleation, and when they are not the same, it is called heterogeneous nucleation. The thin films are formed by three basic steps [44]:

- (i) Different atoms, molecules, clusters are formed in the plasma phase.
- (ii) The produced particles are transported to the substrate.
- (iii) The particles get absorbed by the substrate and produce the film.

The several steps for growing thin films on the substrate are schematically represented in **Fig. 3.11**. The steps are as follows [45],

- (i) The radicals lose the component of velocity normal to the substrate when they interact with the substrate and are then absorbed by the substrate.
- (ii) Initially, the species are not in thermal equilibrium with the substrate surface, so they migrate across it and interact to create a larger cluster.
- (iii) The thermodynamically unstable clusters may desorb in time. The clusters collide with each other and grow the bigger cluster. After a certain cluster size, they overcome the barrier of nucleation by thermodynamically stable configuration. This step is called the nucleation stage.
- (iv) Before the saturation of nucleation, the nuclei grow in number and size. The nucleus can grow both laterally and perpendicularly to the substrate.

However, lateral growth is energetically dominant than perpendicular growth. This nucleus is termed as island.

- (v) Now the small islands coalesce each other and form bigger islands. At that time new nuclei may also be formed. This step is known as a coalescing stage.
- (vi) The larger islands cover the holes and uncovered substrate surface and the islands change to porous network and finally make a thin layer of film.

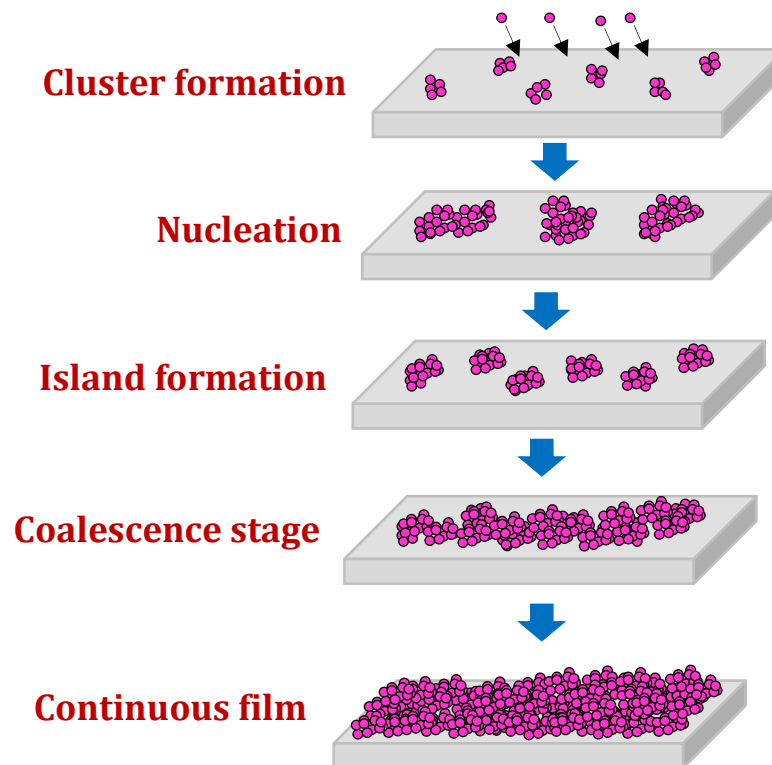


Fig. 3.11. Schematic representation of the thin film growth process steps.

3.6 Plasma physics and chemistry in the PECVD system

Plasma is produced when gases are subjected to high temperatures or extremely strong electric or magnetic fields. Local thermodynamic equilibrium (LTE) is maintained by the electrons, ions, and neutral species within the thermal plasma. The electrons and ions in non-equilibrium or 'cold' plasma are generally become more energised than the neutral species. Almost majority of the glow discharge plasmas used for plasma deposition for thin film are non-equilibrium glow discharge plasmas, which are created by exposing the gas to an RF electric field. The electric field interacts with the free

electrons in the gas at first. On the other hand, the ions are initially unaffected by the applied electric field due to their considerably larger mass interacting with it. In elastic collisions with gas species with significant mass difference, accelerated electrons do not lose much energy. However, in inelastic collisions such as excitation and ionisation, these electrons don't lose any energy until they reach the requisite threshold energies (e.g., in the case of argon, the excitation energy is 11.56 eV and the ionisation energy is 15.8 eV) [46]. When high-energy electrons collide with gas species, highly reactive species such as excited neutrals and free radicals, ions, and more electrons are formed. The energy of electrons produces reactive and charged species without considerably raising the temperature of the gas in this process.

Due to the small amount of positive ions, the potential in the core region and the bulk plasma becomes slightly positive in terms of electrodes. The plasma potential refers the greatest speed at which ions may migrate from the sheath edge to the ground electrode substrate. As a result, Ion-surface interactions such as accelerated adatom diffusion, surface atom displacement, incoming ion trapping, sputtering, and implantation can occur as a result. Electrons are ejected from the sheaths, stimulating all the ionisation and dissociation processes in the bulk plasma. Bulk plasma has light as a result of exciting emissions, however, plasma sheaths are dark. Physical and chemical interactions between the newly generated reactive plasma species have lower energy barriers than their parent species, allowing them to react at lower temperatures. Positive ions and radicals to the substrate through the process of drift and diffusion, where they are subjected to surface and subsurface reactions throughout the deposition process. In PECVD, thin films are prepared using these reactive species at lower temperature than thermal CVD. Charged species in the glow may also have an impact on the film's characteristics [47].

3.7 Role of ions in PECVD

In PECVD, ion bombardment is either beneficial or detrimental depending on the plasma conditions of the deposition. According to Hamers *et al.* [48], the deposition of micro/nanocrystalline silicon is driven by ion which can contribute up to 70% of the deposited film in PECVD. The suppression of ion energy effectively improves the crystallinity of the film, mainly at higher growth rates.. The energy of the ions is plasma depends on the gas pressure, excitation frequency, inter-electrode spacing, and electrode

shape. The density of plasma ions is determined by the density of electrons, and the kinetic energy of the ions is described by the temperature of the electrons [49]. High excitation frequencies result in a larger electron density and lower electron temperature [50]. With increasing frequency, the electron's average energy reduces [51]. In a diode-form reactor, the frequency of the plasma excitation source is correlated directly to ion energy. Radicals have been acknowledged as the main precursors for the growth of both amorphous and micro/nanocrystalline silicon in a PECVD deposition process. SiH_3 has been recognized as the key precursor for device-quality thin films in several studies. Micro/nanocrystalline film deposition is hindered by low lifetime radicals as well as higher silane radicals (Si_2H_5 , Si_3H_8 , etc.), and reactive radicals (SiH_2 , SiH , etc.). The ions are considered to determine the final film quality. The plasma electron temperature controls the kinetic energy of each ion reaching to the substrate, whereas the plasma density determines the ion flux density near the substrate. It is revealed that the presence or absence of ions (at the growth sites of the film) determines whether the film is amorphous or microcrystalline with the same nature of plasma. Even at lower substrate temperatures (T_s), the presence of ions in the high-frequency situation would result in higher surface diffusion of impinging molecules, which is essential for developing better nanocrystalline material [52]. Choice of the proper frequency of the exciting power source is essential to regulate beneficial ion bombardment. Because of the presence of high energy ions in the case of very high-frequency (VHF) PECVD, growth of higher crystalline material is found than that the sample prepared at conventional 13.56 MHz power source [52]. The energy of impinging elements on the developing surface should not surpass the threshold energy of defect development, according to the proposed model. The plasma contains silicon ions as well as hydrogen ions, although the former has a dominating influence in the plasma. The excitation frequency determines the peak of the ion energy distribution. Consequently, at frequencies 70 MHz and over, the peak ion energies for excitation are around 14 eV, which is less than the threshold energy of Si impact equals to 16 eV. Interestingly, the ion energy value for the 13.56 MHz case is about 45 eV. The use of deuterium as an alternative of hydrogen dilution is another way of controlling the ions and it increases crystallinity and lowers defect density. Deuterium dilution results in reduced ion bombardment because the plasma is produced at a lower electron temperature. This is due to the deuterium's heavier mass, which results in a lower electron loss rate [53]. Configuring the electrode arrangement accordingly is the second

approach to manipulate ion bombardment at the growth sites. As per Veprek *et al.* [54], by preventing Restricting the reactive ions from reaching the substrate surface yielded promising results at the attempts to create crystalline thin films. The usage of a triode technique, in which a negative-biased mesh electrode is present between plasma and the substrate, has recognized to be highly effective, as reported by Matsuda [55]. In the case of an electron cyclotron resonance (ECR) PECVD technique, the influence of ion bombardment on the film growth process is best realized, in which the advantages of improving the ion flux and their energy and without affecting the plasma might be used through remote deposition. It is observed that strong ion bombardment (by raising bias-voltage) produced a broadening of the Raman spectral line and a reduction in the electron mobility of the film, even in the growth of epitaxial layer on c-Si wafers. In the ECR PECVD, Nozawa *et al.* [56] discovered that increasing the positive DC bias towards the substrate increased the crystalline volume fraction in the deposited material, triggered by a decrease in ion flow towards the substrate.

3.8 References

- [1] C.N.R. Rao, S.R.C. Vivekchand, K. Biswas, A. Govindaraj, Dalton Trans. 34 (2007) 3728–3749.
- [2] V. Ramakrishna, A.S. Oberai, P.A. Farrar, D.W. Kemmer, P.A. Totta, N.G. Koopman, M.B. Small, Future Requirements for High Speed VLSI Interconnections, Proc. 4th IEEE VLSI Multilevel Interconnec. Conf. (1987) 27.
- [3] D.M. Mattox, Handbook of physical vapor deposition (PVD) processing: Film formation, Adhesion, surface preparation and contamination control, Noyes publications (1998) ISBN: 0-8155-1422-0.
- [4] J.H. Kim, K.A. Jeon, G.H. Kim, S.Y. Lee, Optical Materials 27 (2005) 991.
- [5] R. Okada, S. Ijima, Appl. Phys. Lett. 58/15 (1991) 1662.
- [6] W.A. Turner, G. Lucovsky, J. Non-Crys. Solids 164–166 (1993) 997–1000.
- [7] A. Rantzer, H. Arwin, J. Birch, B. Hjorvarsson, J.W.P. Bakker, K. Jarrendahl, Thin Solid Films 394 (2001) 256–263.
- [8] K. Fukaya, A. Tabata, T. Mizutani, Thin Solid Films 478 (2005) 132.
- [9] Y.C. Chu, G. Jiang, C. Chang, J.M. Ting, H.L. Lee, Y. Tzen, 11th IEEE International Conference on Nanotechnology, Portland Marriott, August 15–18, 2011, Portland, Oregon, USA, 2011.

- [10] V. Thaiyalnayaki, M.F. Cerqueira, J.A.Ferreira, J. Tovar, *Vacuum* 82/12 (2008) 1433.
- [11] R. Saleh, N Nickel, *Thin Solid Films* 427 (2003) 266.
- [12] A.J. Lewis, G.A.N. Connell, W. Paul, J.R. Pawlik, R.J. Temkin, *AIP Conference Proceedings* 20 (1974) 27.
- [13] A. Catalano, R.V.D. Aiello, J. Dresner, B. Faughnan, A.Firester, A.J.Kane, H.Schade, Z.E.Smith, G. Swartz, A. Triano, *Conf. Rec. IEEE Photovoltaic Spec. Conf.* 16 (1982) 1421.
- [14] W. Paul, A.J. Lewis, G.A.N. Connell, T.D. Moustakas, *Solid State Commun.* 20 (1976) 969.
- [15] T.D. Moustakas, *Solar Energy Materials* 8 (1982) 187.
- [16] R. Baghdad, D. Benlakehal, X. Portier, K. Zellama, S. Charvet, J.D. Sib, M. Clin, L. Chahed, *Thin Solid Films* 516 (2008) 3965–3970.
- [17] S.B. Hashim, N.H. Mahzan, S.H. Herman, M. Rusop, *Adv. Mater. Res.* 576 (2012) 543–547.
- [18] D. Adhikari, M.M. Junda, S.X. Marsillac, R.W. Collins, N.J. Podraza, *J. Appl. Phys.* 122 (2017) 075302.
- [19] R. Tiwari, S. Chandra, *Adv. Mater. Res.* 254 (2011) 187–190.
- [20] L. Yun, Y. Chen-Chen, J. Yun, S. Zhen-Liang, J. Cong-Hui, Y. Wei, L. Xiao Wei, *Chin. Phys. Lett.* 32 (2015) 046802.
- [21] D. Kar, D. Das, *J. Appl. Phys.* 121 (2017) 044305.
- [22] M.A. Signore, A. Sytchkova, D. Dimaio, A. Cappello, A. Rizzo, *Optical Materials* 34 (2012) 632–638.
- [23] Z. Ji-cheng, Z. Xu-qiang, *Trans. Nonferrous Met. Soc. China* 17 (2007) 373–377.
- [24] M.F. Cerqueira, M. Andritschky, L. Rebouta, J.A. Ferreira, M.F. da Silva, *Vacuum* 46 (1995) 1385–1390.
- [25] K.L. Chopra, “Thin Film Phenomena” Mc. Graw Hill (1969) ISBN: 978-0070107991.
- [26] T. Sato, *Jpn. J. Appl. Phys.* 6 (1967) 339–347.
- [27] Gemini 2 Product Brochure, Gemini Research, Inc. Fremont. CA.
- [28] D. Richman, *RCA Rev.* 41 (1997) 613.
- [29] R.C. Frieser, *J. Electrochem. Soc.* 115 (1968) 401.

- [30] A. Michelmore, J.D. Whittle, R.D. Short, *Frontier. Phys.* 3 (2015) 1.
- [31] D. Raha, D. Das, *J. Phys. D* 41 (2008) 085303.
- [32] G. Ganguly, T. Ikeda, T. Nishimiya, K. Saitoh, M. Kondo, A. Matsuda, *Appl. Phys. Lett.* 69 (1996) 4224–4226.
- [33] J. Ni, Q. Liu, J. Zhang, J. Ma, H. Wang, X.D. Zhang, Y. Zhao, *Sol. Energy Mater. Sol. Cells* 126 (2014) 6–10.
- [34] C. Dominguez, J.A. Rodriguez, M. Riera, A. Llobera, B. Diaz, *J. Appl. Phys.* 93 (2003) 5125.
- [35] B. Gorowitz, T.B. Gorczyca, R.J. Saia, *Solid State Technol.* 28 (1985) 19.
- [36] Q. Cheng, S. Xu, K. (Ken) Ostrikov, *J. Mat. Chem.* 20 (2010) 5853.
- [37] Q. Cheng, S. Xu, K. (Ken) Ostrikov, *Acta Materialia* 58 (2010) 560.
- [38] D. Raha, D. Das, *J. Phys. D* 41 (2008) 085303.
- [39] A.C. Adams, *Solid. State Technol.* 26 (1983) 135.
- [40] T.I. Kamins, K.L. Chiang, *J. Electrochem. Soc.* 129 (1982) 2326.
- [41] Y.X. Liu, Y.R. Zhang, A. Bogaerts, Y. N. wang, *J. Vac. Sci. Technol. A* 33 (2015) 020801.
- [42] T.E.F.M. Standaert, M. Schaepkens, N.R. Rueger, P.G.M. Sebel, G.S. Oehrlein, *J. Vac. Sci. Technol. A* 16 (1998) 239–249.
- [43] A.A. Warra, W.L.O. Jimoh, *Int. J. Chem. Res.* 3 (2011) 41.
- [44] P.M. Martin, *Handbook of Deposition Technologies for Films and Coatings: Science, application and technology*, Elsevier Inc., (2010), ISBN: 13:978-0-8155-2931-3.
- [45] K. Seshan, *Handbook of Thin Film Deposition Processes and Techniques: principles, method, equipment and applications*, Noyes publications, (2002) ISBN: 0-8155-1442-5.
- [46] M. Rand, *J. Vac. Sci. Technol.* 16 (1979) 420.
- [47] J.E. Greene, S.A. Barnett, *J. Vac. Sci. Technol.* 21 (1982) 285.
- [48] E.A.G. Hamers, A. Fontcuberta i Morral, C. Niikura, R. Brenot, P. Roca i Cabarrocas, *J. Appl. Phys.* 88 (2000) 3674.
- [49] M. Kondo, S. Yamasaki, A. Matsuda, *J. Non-Cryst. Solids* 266–269 (2000) 544.
- [50] M.R. Wertheimer, M. Moisan, *J. Vac. Sci. Technol. A* 3 (1985) 2643.

- [51] H. Keppner, U. Kroll, P. Torres, J. Meier, D. Fischer, M. Goetz, T. Tschärner, A. Shah, Proc. 25th IEEE PV Spec. Conf., p. 669 (1996).
- [52] M. Kondo, A. Matsuda, Thin Solid Films 1 (2001) 383.
- [53] S. Veprek, F.A. Sarrott, Z. Iqbal, Phys. Rev. B 36 (1987) 3344.
- [54] A. Matsuda, J. Non-Cryst. Solids 59-60 (1983) 767.
- [55] S. DeBoer, V.L. Dalal, R. Bartel, G. Chumanov, Appl. Phys. Lett. 66 (1995) 2528.
- [56] R. Nozawa, H. Takeda, M. Ito, M. Hori, T. Goto, J. Appl. Phys. 81 (1997) 8035.



Chapter 4

**Thin film characterization
techniques**

4.1 Introduction

Different techniques are used to characterize the material and its transient properties. The particular technique has a different role based on the evidence it provides. A thorough characterization of any material includes optoelectronic characterization, surface characterization, compositional characterization, and microstructural analysis that mainly gives the idea about the structural properties, film's composition, film's nature of morphology and transport phenomenon etc. This section deals with the experimental arrangement of different instruments used to characterise thin films in this thesis work, along with their theoretical background, the principle of operation and working mechanism.

4.2 Optical characterization and determination of thickness

4.2.1 Optical properties by UV-Vis-NIR spectroscopy

When light passes through a thin film sample, some part is reflected from the top surface of the sample, some part is absorbed in the sample, and the rest is transmitted. In this process, the photons with energy $h\nu \geq E_g$ are absorbed while those less than the band gap is transmitted. The ultraviolet-visible (UV-Vis) spectroscopy is based on the electronic transition from lower to higher energy levels due to absorbing energy from the incident light. Near-infrared (NIR) spectroscopy is based on the vibrational transition of the molecules. The ratio of the transmitted and the incident light depends on two parameters – the photon wavelength and the thickness travelled. According to Beer-Lambert law, if the intensity $I(x)$ of radiation at a specific depth x of the material does not depend on the incident radiation, but the change in the intensity is a function of the incremental change in distance, dx , which is described as [1]:

$$\frac{dI(x)}{dx} = -\alpha I(x) \quad (4.1)$$

The solution of the above differential equation is:

$$I(x) = I_0 \exp(-\alpha x) \quad (4.2)$$

where I_0 is the incident beam's intensity at $x = 0$, $I(x)$ is the intensity at $x = x$, and α is a constant, named as the absorption coefficient of the material in cm^{-1} .

The transmittance T is expressed as:

$$T = \frac{I}{I_0} \quad (4.3)$$

Furthermore, the absorbance A is related to transmission is given by:

$$A = \log_{10} \frac{1}{T} \quad (4.4)$$

Combining the Eqns. (4.2), (4.3) and (4.4), the absorption coefficient α can be expressed in terms of absorbance A as:

$$\alpha = \frac{A \ln 10}{d} \cong \frac{2.303 A}{d} \quad (4.5)$$

where the thickness of the thin film is 'd'.

The energy of the incident photon, $E = hv$ (in eV) can be calculated from the wavelength λ (in nm) of the light as:

$$E = hv = \frac{hc}{\lambda} = \frac{1242}{\lambda} \quad (4.6)$$

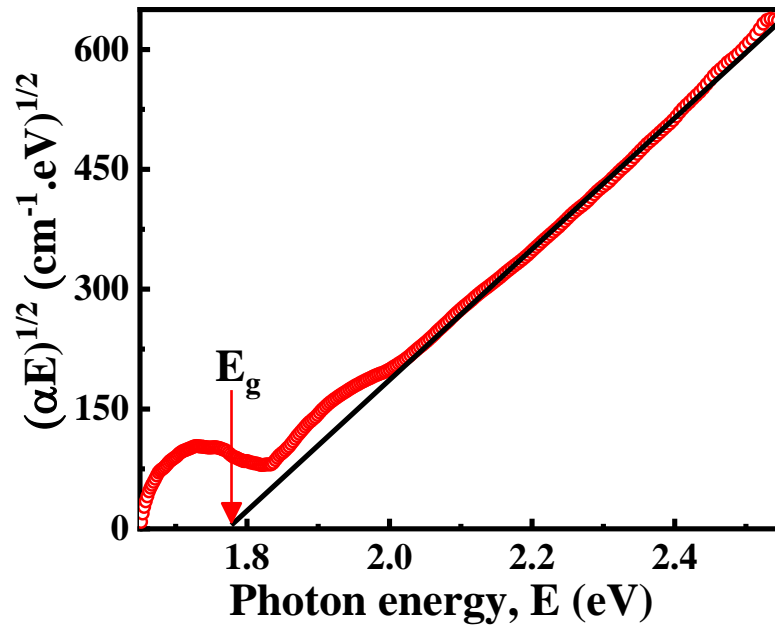


Fig. 4.1. Tauc plot of a 500 nm thick nc-Si:H/a-Si:H thin film on the glass substrates.

To estimate the optical band gap (E_g) of a material, Tauc has proposed a relation (based on the assumption that the density of states of the amorphous semiconductor material is parabolic near the band edges), as follows [2];

$$(\alpha hv)^{\frac{1}{2}} = B(hv - E_g) \quad (4.7)$$

Now, the extrapolation of the linear part at the intercept with the energy axis gives the optical band gap, E_g (as shown in **Fig. 4.1**). In general, The Tauc's plot ($(\alpha hv)^{\frac{1}{2}}$ vs $h\nu$ graph) follows a linear relationship for amorphous silicon materials. Furthermore, it is well-established in the literature that this approach is also valid in estimating the optical band gap of the mixed-phase nanocrystalline Si-alloy materials in which nanocrystalline nanocrystals are embedded within amorphous silicon matrix, as it holds good linearity at the higher photon energy region [3,4].

4.2.2 Spectroscopic ellipsometry

Spectroscopic ellipsometry (SE) is a non-destructive, non-contact optical measurement technique. SE is based on the change of the polarized state of light as it is reflected obliquely from a thin film sample and then is compared with a model [5,6]. It is used to determine different properties of thin film, substrates, the interface of single layers and multilayers of optically interactive materials along with solar cells. Ellipsometry measures the phase difference and the amplitude ratio in the changed polarization state when a linearly polarized light with both p- and s- components are reflected from the thin film samples. Two values define the change in polarization state, Δ and ψ , which describe the change of phase and amplitude of the incident light endured through reflection [**Fig. 4.2**]. The amplitude ratio represents the angle determined by the amplitude ratio between reflected p- and s-polarizations and can be defined as [6]:

$$\tan(\psi) = \frac{r_p}{r_s} = \frac{E_{rp}}{E_{ip}} / \frac{E_{rs}}{E_{is}} \quad (4.8)$$

The phase difference can be defined as:

$$\Delta = \delta_{rp} - \delta_{rs} \quad (4.9)$$

Using ψ and Δ , the change in polarization is described as:

$$\rho = \tan(\psi) e^{i\Delta} \quad (4.10)$$

The measured change in polarization is dependent on the optical properties and thickness of the material. Using a model representing thin film structure, the thickness and the optical parameters of the thin film are estimated from the collected ellipsometry data. The ellipsometer, as represented with a schematic diagram in **Fig. 4.3**, consists of – (1) a high-pressure xenon lamp as the light source, (2) a linear polarizer that transforms the

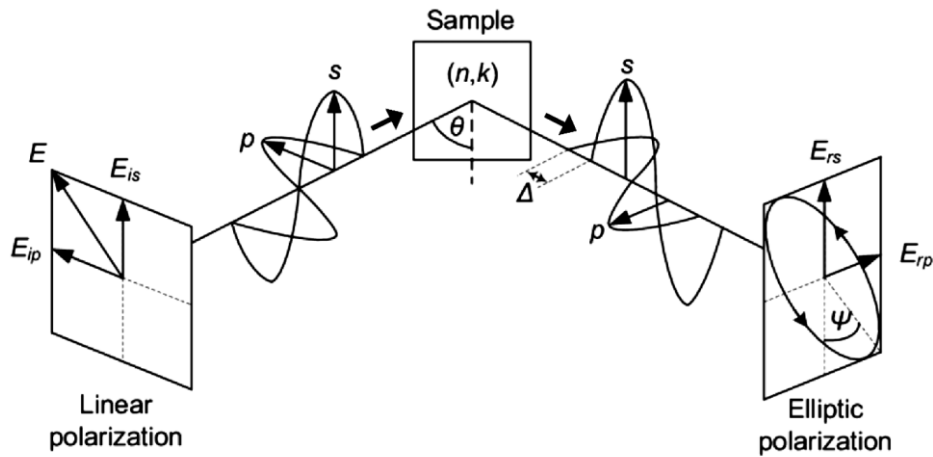


Fig. 4.2. The measurement principle of the ellipsometry.

unpolarized incident light into a linearly polarized light, (3) compensators which are used to displace the phase of one component of the incident light (which is optional), (4) analyzer, which determines the state of polarization of the beam of reflected light from the film deposited on the substrate (sample) and finally enters in (5) the detector, which receives the polarized light.

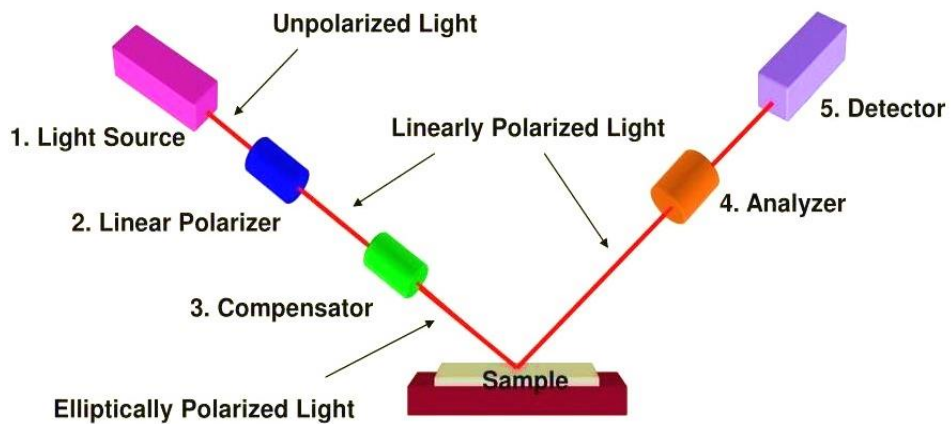


Fig. 4.3. Schematic diagram of a spectroscopic ellipsometer.

4.2.3 Experimental determination of thickness and refractive index

4.2.3.1 Thickness measurement by Quartz crystal thickness monitor

For determining the thickness of thin films, film thickness monitor (FTM) quartz crystals can be used [Fig. 4.4]. The quartz crystal is positioned within the vacuum chamber, facing towards deposition source for depositing materials on the crystal. This

crystal is a special piezoelectric crystal whose frequency of oscillation depends on the mass of the crystal. When the material is deposited on the crystal, then the oscillation of this crystal gets changed. By calculating the change of oscillation of this crystal, the thickness of the deposited films can be calculated by using the following relation [7].

$$t = \frac{N\rho_q}{\rho_f f^2} (f_q - f) \quad (4.11)$$

where, t = thickness of film,

$N = 16.68$ cm/sec for vibration of quartz crystal in the shear mode.

ρ_q = density of the quartz material (2.65 gm/cc)

ρ_f = density of the deposited film

f = resonance frequency of an uncoated crystal

f_q = resonance frequency of a coated crystal

The above equation would not be obeyed for the deposition of different materials together. The used relation for that case is [8],

$$t = \frac{\rho_q N}{\rho_f T R Z_f} \tan^{-1} \left(R Z \frac{T - T_q}{T} \tan \phi \right) \quad (4.12)$$

where R is the acoustic impedance ratio of the quartz and the deposited film. T and T_q are the oscillating periods of the uncoated and coated crystal. From the beginning of the

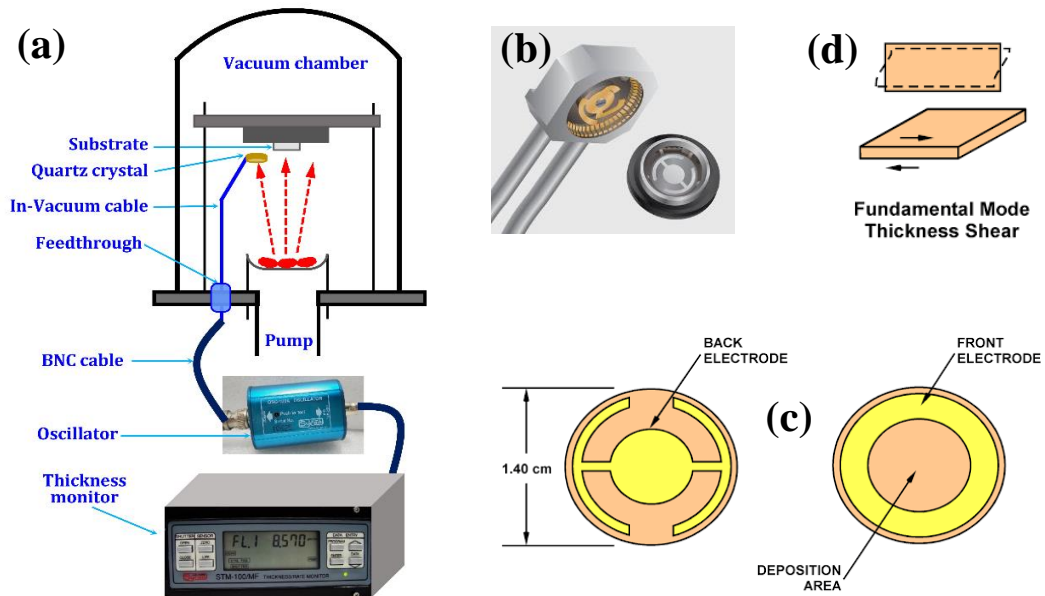


Fig. 4.4. (a) Block diagram of thin film thickness monitor connected within a vacuum chamber. (b) Photograph of a typical thickness monitor head. (c) The front and back contact of a thickness monitor head. (d) The schematic diagram of the fundamental shear mode used.

deposition, the mass of the quartz and the initial film was stored. The mass of new films can be obtained by subtracting the initial mass from the total mass of the deposited film and then the thickness of the newly deposited film is calculated. All the calculations related to film thickness are internally electronically done and the numerical value of thickness is displayed on the monitor.

4.2.3.2. Thickness measurement by profilometer

A thickness evaluation is essential to evaluate the deposition rate of the grown film (film thickness per unit time) for determining a few film properties dependent on the thickness parameter of the film and also to use it to estimate the growth time for device fabrication as well as to realize the suitability of a material for mass production. The Dektak 6M is a stylus profilometer that uses a step-height measurement mechanism to measure the thickness of the thin films. A diamond tip (radius 4mm) is used to quantify the thickness of the surface topology with surface roughness, with a range of several nanometers to hundreds of microns. This thickness calculation method is used for the relatively rigid films since the tip may physically destroy the film's top surface. The stylus may damage soft films, resulting in a distorted scan. The stylus on the profilometer

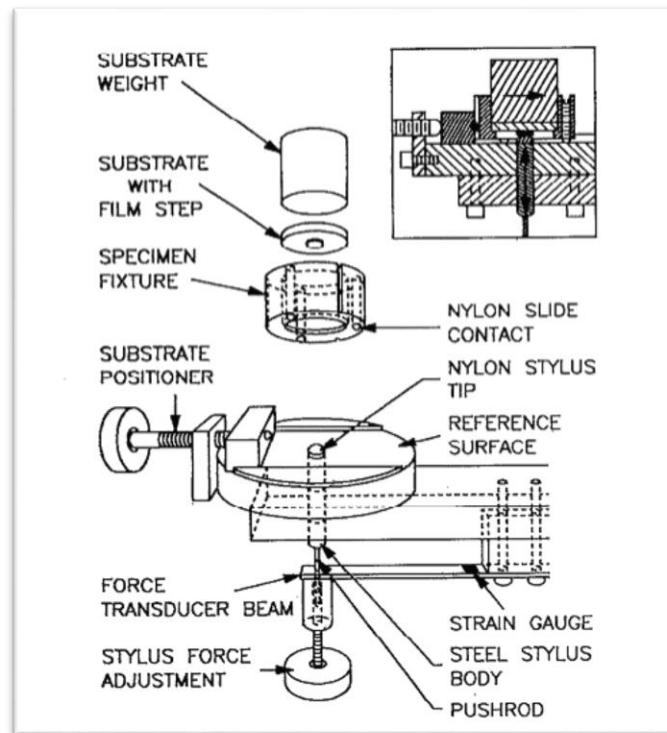


Fig. 4.5. Expanded view of the specimen, fixture, and profilometer.

is vertically pushed into contact with the sample and scans the sample surface laterally moved through the sample in the y-direction. Vertical translational motion provides an electrical signal as the stylus moves across the sample, estimating the approximate step height. Then, this vertical displacement is recorded by the tool for measurement purposes.

The schematic diagram of a stylus profilometer with step coverage is shown in Fig. 4.5 (adapted from Ref. [9]). The displacement is measured by a laser beam incident on the top of the diamond tip (radius 4 mm) as it moves laterally on the film surface. The vertical movement of the tip and thereby the thickness of the deposited film are measured by computing the displacement of the laser beam [10]. The displacement of the stylus tip is directly proportional to the voltage of the transducer. The proper thickness of the film is determined by calibrating the voltage with the thickness. The voltage to height calibration reference is 1.0 mV/m [11].

4.2.3.3. Thickness measurement by Swanepoel method

For the experimental determination of thickness (d) and optical parameters like refractive index (n) of the deposited silicon-germanium thin films, a method proposed by Swanepoel has been used. The optical parameters of a thin film deposited on a transparent substrate like corning glass are estimated from the transmission spectrum $T(\lambda)$ measured using a UV-VIS double-beam spectrometer [12,13].

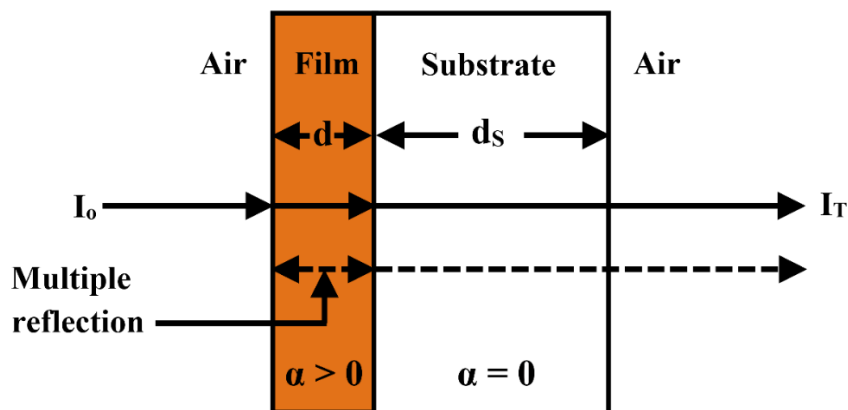


Fig. 4.6. Schematic illustration of transmission of light through a film/substrate system. Intensity of the ordinary incident beam has the intensity as I_0 . I_T is the intensity of the transmitted beams, which is the superposition of the straight transmitted light (solid line) and the beam transmitted after suffering the multiple reflections at the air/film and film/substrate interfaces (dashed line).

The optical transmission measurement on a thin film deposited on the substrate is shown schematically in **Fig. 4.6**. The substrate is transparent, the semi-transparent/transparent film on the transparent substrate, and the substrate's thickness d_s is some orders of magnitude larger than the thin film, having thickness d . Swanepoel has assumed that the incidence takes place in perpendicular direction and interference occurs via multiple refractions at the film/substrate and air/film interfaces, Swanepoel has expressed that transmission $T(\lambda)$ is provided by [12],

$$T(\lambda) = \frac{Ax}{B - Cx \cos \phi + Dx^2} \quad (4.13)$$

where,

$$A = 16n^2n_s \quad (4.14a)$$

$$B = (n + 1)^3(n + n_s^2) \quad (4.14b)$$

$$C = 2(n^2 - 1)(n^2 - n_s^2) \quad (4.14c)$$

$$D = (n - 1)^3(n - n_s^2) \quad (4.14d)$$

$$\phi = \frac{4\pi nd}{\lambda} \quad (4.14e)$$

$$x = \exp(-\alpha d) \quad (4.14f)$$

where refractive index of the film is n , n_s is the substrate's refractive index, film's thickness is d , x denotes the absorbance, the direct and the multiple reflected transmitted beams have phase difference ϕ , and α is the absorption coefficient.

The transmission spectrum of Si alloy thin films is shown in **Fig. 4.7**. Considering $\cos \phi = +1$ Eqn (4.13) takes form,

$$T_M = \frac{Ax}{B - Cx + Dx^2} \quad (4.15)$$

In the case of $\cos \phi = -1$, Eqn (4.13) becomes

$$T_m = \frac{Ax}{B + Cx + Dx^2} \quad (4.16)$$

The two specified boundary conditions defining the equations of smoothed envelopes surrounding the transmission spectrum are used to find Eqns (4.15) and (4.16).

$\cos \phi = 1$ implies from Eqn (4.14e)

$$\frac{4\pi nd}{\lambda} = m2\pi \Leftrightarrow 2nd = m\lambda \quad (4.17)$$

where, $m = 0, 1, 2, 3, \dots$

and $\cos\phi = -1$ implies from Eqn. (4.10e)

$$\frac{4\pi nd}{\lambda} = 2\pi m' \quad (4.18)$$

where $m' = 1/2, 3/2, 5/2, 7/2, \dots$

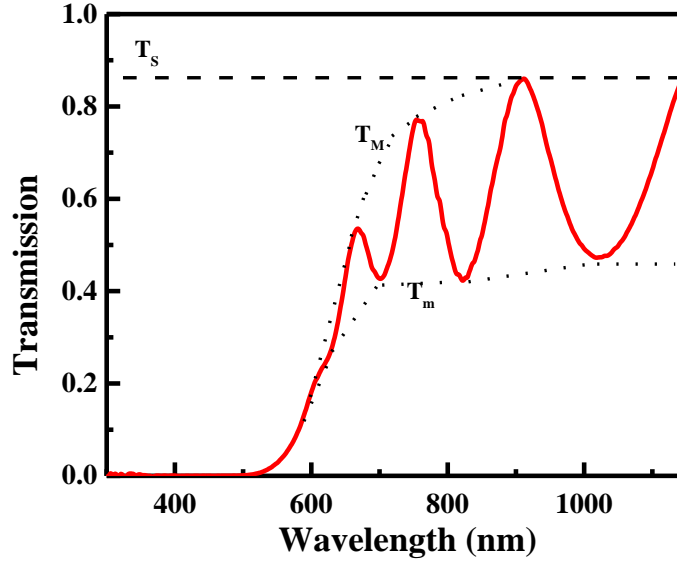


Fig. 4.7. Transmission spectrum of a 500 nm thick nc-SiGe film grown on a glass substrate.

In the region $\alpha \neq 0$ and $x < 1$, subtracting the reciprocal of Eqn (4.15) from the reciprocal of Eqn (4.16) follows an expression that does not depend on x

$$\frac{1}{T_m} - \frac{1}{T_M} = \frac{2C}{A} \quad (4.19)$$

Substituting the values of A and C on Eqn (4.15) and solving for n yields

$$n = [N + (N^2 - n_s^2)^{1/2}]^{1/2} \quad (4.20)$$

where

$$N = 2n_s \left(\frac{T_M - T_m}{T_M T_m} \right) + \frac{n_s^2 + 1}{2}. \quad (4.21)$$

For a transparent film α would have value as zero ($x=1$), Eqns. (4.13) and (4.14) become

$$T_M = \frac{2n_s}{n_s^2 + 1} \quad (4.22)$$

and

$$T_m = \frac{4n^2 n_s}{n^4 + n(n_s^2 + 1) + n_s^2} \quad (4.23)$$

Because T_M is only a function of n_s , it coincides with the transmission of the substrate alone. Eqn (4.17) yields the film's refractive index at the sampled λ . The thickness of the film can be deduced using the refractive indices obtained at the transmission spectrum's maxima and minima. If n_1 and n_2 are assumed to be refractive indices at two adjacent maxima (or minima) at λ_1 and λ_2 , $\lambda_1 > \lambda_2$, it gives Eqn. (4.17) and (4.18) that:

$$2n_1d = m\lambda_1 \quad (4.24)$$

$$2n_2d = (m+1)\lambda_2 \quad (4.25)$$

Solving Eqns (4.24) and (4.25), the film's thickness d is expressed as

$$d = \frac{\lambda_1\lambda_2}{2(\lambda_1n_2 - \lambda_2n_1)} \quad (4.26)$$

Since n_s is identified for a glass substrate, T_M and T_m are identified from the transmission spectra; the film's refractive index is estimated and subsequently, the thickness d is calculated from the Eqn. (4.26).

4.3 Structural characterization

4.3.1 Raman spectroscopy

Raman spectroscopy is a specialized non-destructive tool that provides a fast and straightforward way to determine the chemical composition of a thin film. It further offers both qualitative and quantitative ideas of the material phase, whether it is amorphous or nanocrystalline. **Fig. 4.8** represents a schematic of the micro-Raman spectrometer. In our work, Renishaw inVia micro-Raman spectrometer in a 180° backscattering geometry with a 514 nm Ar^+ Laser as the excitation source, operating with a laser power of ~ 2 mW/cm² is used. Raman spectroscopy reveals the nature of a molecule like the vibrational, rotational, and other low-frequency modes of the molecule based on the light scattering due to the inelastic interaction of light with the atom or molecules.

When an electromagnetic light of laser incident on a sample, it interacts with the molecules at the sample surface and scattering occurs. A more significant part of this scattering meets elastic scattering, with the total kinetic energy remaining conserved before and after the collision, known as Rayleigh scattering. The wavelength of scattered

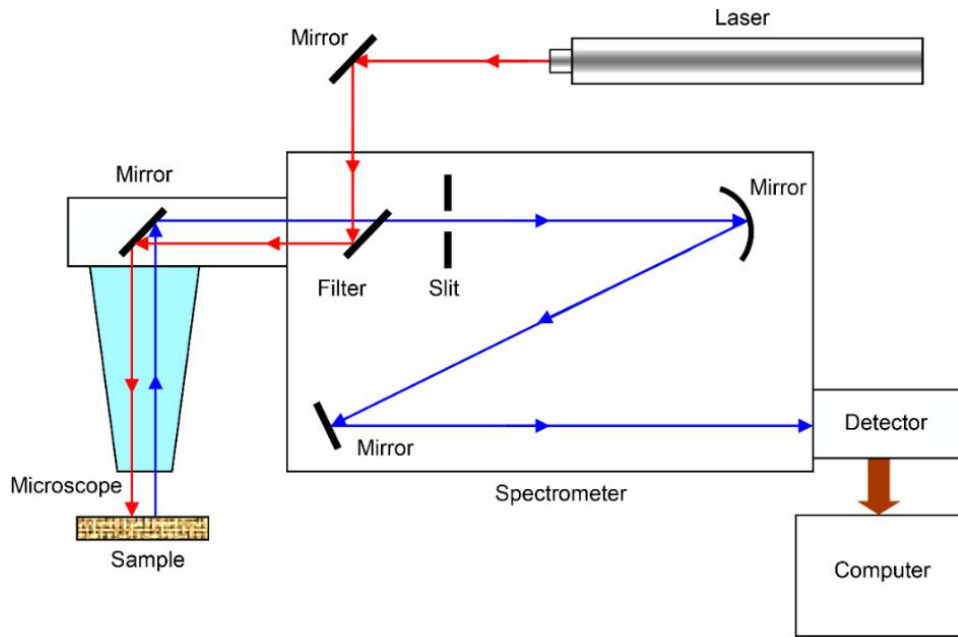


Fig. 4.8. Schematic diagram of the Raman microscope.

light is the same as the incident light. The little rest of the light is inelastically scattered, called the Raman scattering, in which the scattered light has a different frequency than the incident light. As a result, the energy levels in the irradiated sample are either greater or lower than the initial electronic state's energy level. The rotational and vibrational transitions in the sample are responsible for this difference in energy. This change in energy refers to phonons' energy that is created or annihilated [14]. Both energy and momentum remain conserved in the Raman scattering process according to following relations:

$$E_{\text{Incident}} = E_{\text{Raman}} + E_{\text{phonon}} \quad (4.27)$$

$$K_{\text{Incident}} = K_{\text{Raman}} + K_{\text{phonon}} \quad (4.28)$$

It is known as ‘Stokes scattering’, when a photon loses energy by producing a phonon and it is ‘anti-Stokes scattering’ when a photon gets energy by annihilating a phonon. **Fig. 4.9** demonstrates the processes involved in both Rayleigh and Raman scattering.

From the theoretical background, it is clear that for a molecule to be active in the Raman scattering, there should have a change in the molecular polarizability through the distortion in the shape of the molecules due to disturbance in the electron clouds of the molecules, in the presence of the oscillating electric field E of the incident

electromagnetic radiation. The observed change in frequency can be correlated to the vibrational excitations of the molecules in the sample under study by Eqn. (4.27) and (4.28). By examining the Raman spectra, properties like phase, degree of crystallinity, and crystal size can be estimated for SiGe nanocomposite thin films.

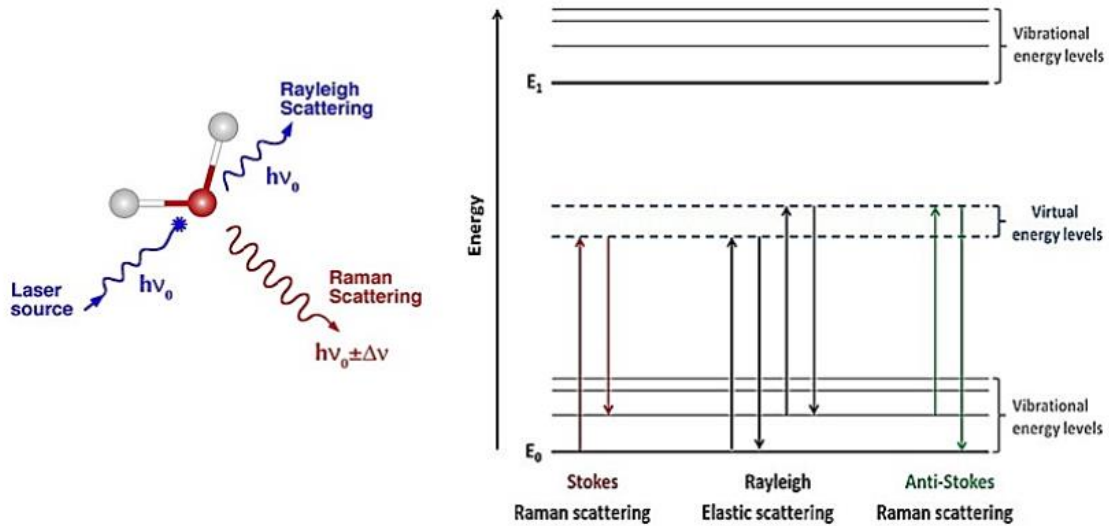


Fig. 4.9. Illustration of the formation of Stokes and anti-Stokes lines through Rayleigh and Raman scattering.

4.3.2 X-ray diffraction (XRD)

The X-ray diffraction (XRD) measurement is a widely used essential characterization tool to get structural insight and chemical composition of the materials, such as the presence of crystallites, their size, and the direction of the crystal planes. This measurement is based on the theory of constructive interference of X-rays (monochromatic), generated using a cathode ray tube. The X-Ray wavelength used in the present experiment is $\lambda = 0.154$ nm, where Cu is used as the cathode. The diffracted X-ray by the sample is detected by a detector and then proceeded in a counter. Here, the scanning is performed by changing 2θ angles and different peaks are obtained for all crystallographic planes present within the sample. As the inter-planar separation of the planes (d) is unique for a particular material, the material is recognised by calculating the d -spacing and using the Joint Committee for Powder Diffraction Standards (JCPDS) or American Standard Testing for Materials (ASTM) data cards. It is well-known that the diffraction happens when the incident light's wavelength and the path difference between

two scattering centers are about of the same order. **Fig. 4.10** demonstrates a schematic illustration of X-ray diffraction from the planes in samples.

According to the theory, the constructive interference occurs by the diffracted X rays, at the condition known as the Bragg's equation [15]:

$$n\lambda = 2 d_{hkl} \sin\theta \quad (4.29)$$

Where λ is the X-ray wavelength, d_{hkl} is the inter-planar spacing between the lattice planes, and Bragg's angle (diffraction angle) and $n = 1, 2, 3, \dots$

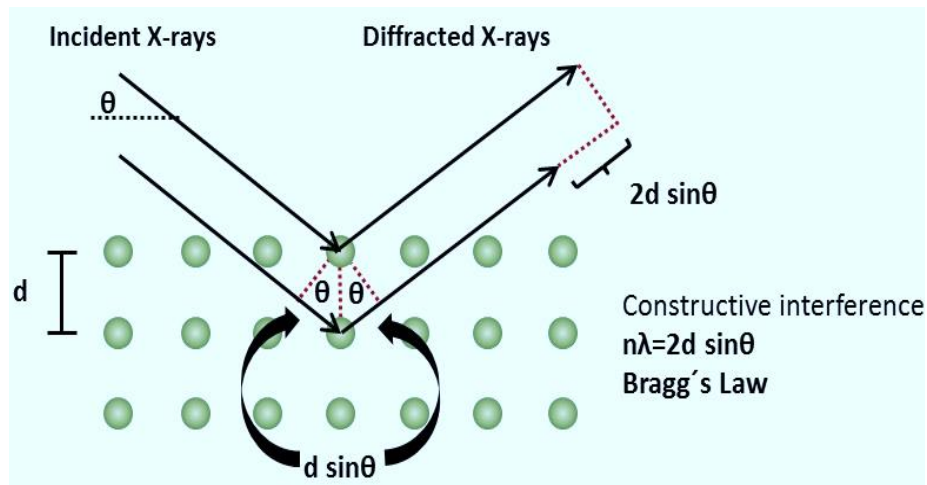


Fig. 4.10. A schematic illustration of the X-ray diffraction within a material.

The full width half maximum (FWHM) of the diffracted peak is represented by β , which is the width at an typical intensity level is expressed as

$$\beta = \frac{1}{2}(2\theta_1 - 2\theta_2) \quad (4.30)$$

where, $2\theta_1$ and $2\theta_2$ are two successive angular positions in units of 2θ where the intensity of the peak is zero, the Scherrer formula is specified by [15,16]:

$$D = \frac{K\lambda}{\beta \cos\theta} \quad (4.31)$$

where, θ is the Bragg angle, K is a dimensionless shape factor. For Si, the shape factor is used as 0.9 but changes with the actual shape and symmetry of the crystallite. Eqn. (4.29) estimates the average crystal size of the material and it is clear from the above Eqn. that larger crystallites produce minor diffracted peak widths. Due to the lack of long-range ordering in amorphous solids, the Bragg condition is not perfectly fulfilled, whereas one or two broad peaks identify the amorphous phase. On the other hand, XRD spectra for

crystalline samples show strong peaks due to positive interference caused by scattering from regularly spaced atoms. This XRD technique is also useful for determining miller indices, residual stresses, and other parameters.

4.3.3 Fourier transform infrared spectroscopy (FTIR)

The Fourier Transform infrared spectroscopy technique is quick, non-destructive, and economical, used for analysing chemical bonding configurations and their vibrational properties. This characterisation may be used to do both quantitative and

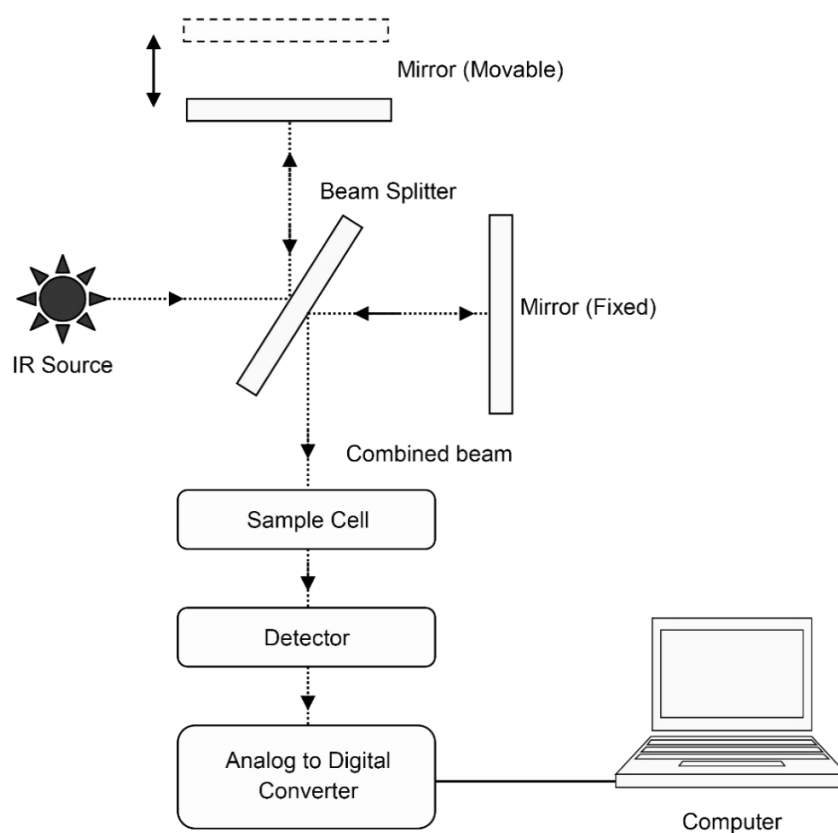


Fig. 4.11. Schematic diagram of the FTIR spectrophotometer with the main components.

qualitative investigation on a wide range of materials. The molecular bonds present in the materials vibrate at different frequencies with respect to the elements and bonds present in the material. It provides information on the atom-bonding vibration modes that occur in amorphous and microcrystalline silicon films and their alloy materials. In this technique, a long-wavelength infrared light beam passes through the film grown on a substrate. The substrate is partially transparent to infrared light to get the FTIR response.

The transmittance of a bare c-Si substrate and a coating on a comparable substrate are measured for the quantitative analysis. The ratio of the transmission spectrum of the thin film on a substrate and the transmission spectrum of the bare substrate was used to calculate the thin film's transmittance. A plot of transmittance (or absorbance) vs. wavenumber is the FTIR spectrum. The samples in our experiment are deposited on a c-Si substrate. An FTIR instrument's basic experimental set-up is schematically presented in **Fig. 4.11**. The force constant of bonds, the relative mass of the atoms, and the molecule's shape all influence the wavelength or frequency of absorption. As a result, any spectral characteristics observed are entirely related to the sample.

4.3.4 Transmission electron microscopy (TEM)

Transmission electron microscopy (TEM) is an exclusive structural characterization technology that gives accurate space imaging with 1-2 Å resolution and is an extraordinary tool to analyze the structure and chemical analysis of the material. For TEM measurement, the samples are deposited on a carbon-coated grid with a ~50-

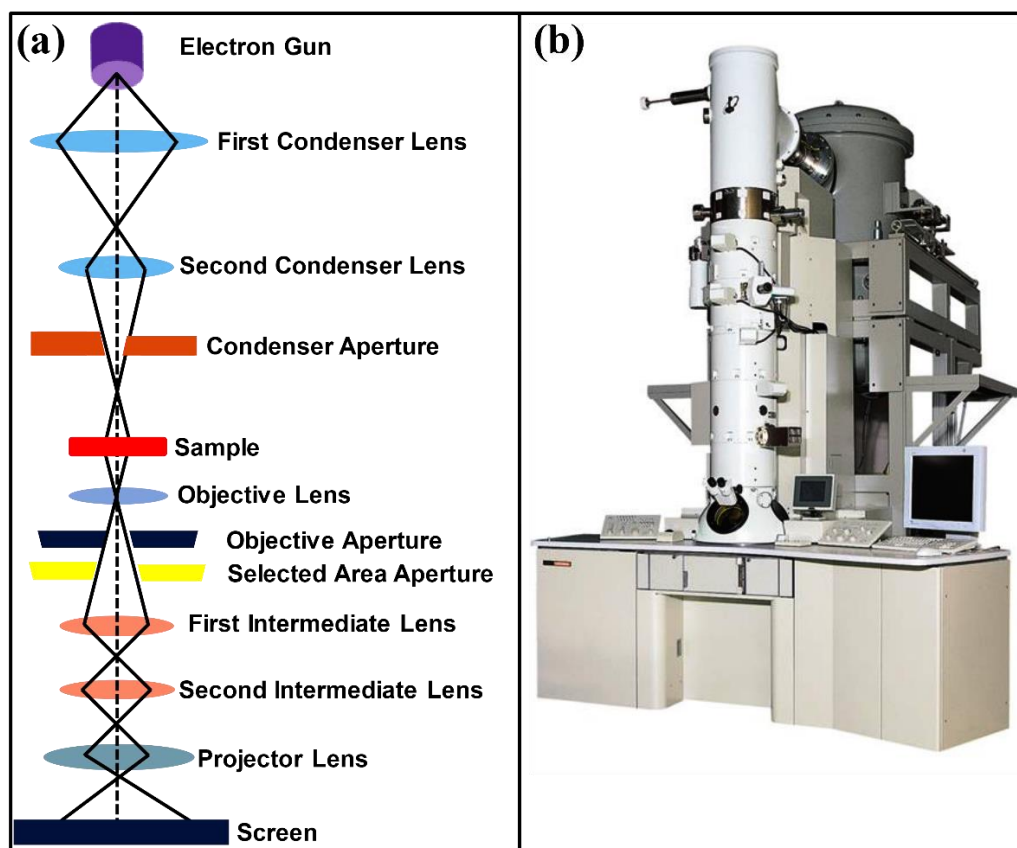


Fig. 4.12. (a) Schematic of the TEM showing the main components (b) TEM set-up.

60 nm thickness. This technique is named transmission electron microscopy. The final image is generated through employing multiple lenses in the arrangement just as done in a microscope with transmitting high-energy electron beam through ultra-thin samples. As the electron beam traverses through a material, it interacts with the atoms in the sample through elastic and non-elastic scattering. The electrons are transmitted through the sample from a picture on a fluorescent screen or a CCD camera, magnified and focussed by an objective lens. From the TEM micrographs (the images) and diffraction patterns (TED), detailed information about the material's microstructure like the distribution of micro-grains, the crystal shape, and the orientation and volume of the microcrystals can be derived. In the present research work, HRTEM Model JEOL 2010 has been used for structural characterization of silicon, germanium and silicon-germanium alloy thin films. In this instrument, the available energy of electrons ranges from 80 KeV to 200KeV. The JEOL JEM 2010 has a resolution of 0.194 nm, with magnification range varying between 50 and 1500000. The resolution of the present instrument is 0.1940 nm. The block diagram and real photograph of the TEM machine are presented in **Fig. 4.12**.

4.3.5 Atomic force microscopy (AFM)

One of the most useful scanning probe microscopy techniques is atomic force microscopy (AFM), a fantastic optics-mechanical instrument for measuring interaction forces on the nano-newton scale. The cantilever/tip assembly is like the heart of the AFM, referred as the probe, generally has a radius of curvature of 5–10 nm and a length of ~ 3-6 μm , made of silicon nitride (Si_3N_4) or silicon (Si). The AFM probe measures the interaction with the surface of the specimen through scanning motion. This interaction follows Hooke's law:

$$F = kx \quad (4.32)$$

where, F is the force of interaction on the cantilever, k is the spring constant, x is the deflection of the cantilever. The AFM's probe oscillates on the sample surface. It records the lateral and vertical deflection using the reflection of a laser beam incident on the top cantilever of the tip (**Fig. 4.13**).

As the reflected laser beam incidents into a position-sensitive photodetector, the piezoceramic remaining inside the contracts or expands in the presence of voltage

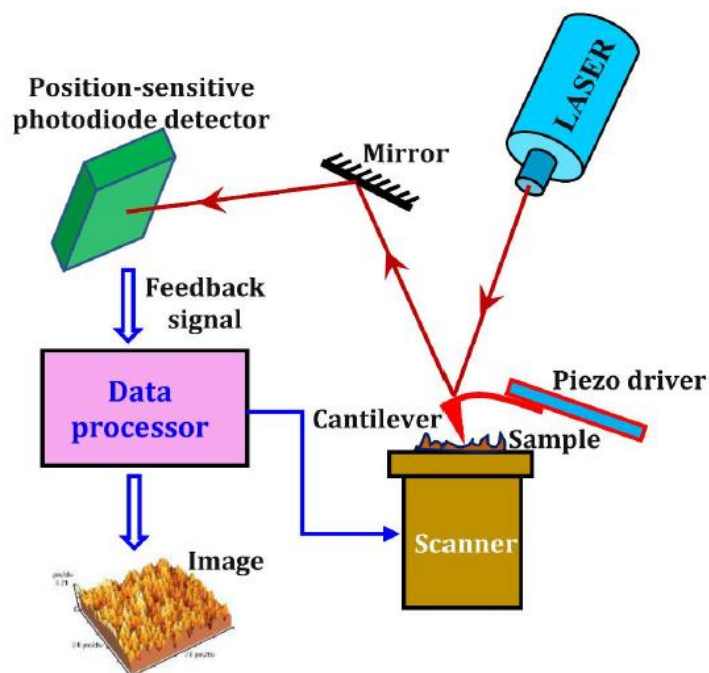


Fig. 4.13. The schematic diagram of the working principle of a typical AFM.

gradient, creating a 3D topographical image with high precision. Although the sample is generally moved in all three directions instead of the motion of the AFM probe, depending on the tip motion, three of the primary imaging modes of the AFM operation are discussed below with the schematic presentation in **Fig. 4.14**.

- **Contact mode of AFM:** The separation between AFM tip and sample is less than 0.5 nm and the tip remains in continuous contact with the film's surface. A 3D image of the surface is obtained using the feedback signal received by the tip from the sample's surface. The nature of force has repulsive nature here. Fast scanning of the rough surface can be gained in this mode of operation; however, physical contact between tip and sample's surface may damage the soft specimens, which is a drawback of this contact mode of AFM measurements.
- **Tapping mode of AFM:** The tip-sample separation is ~0.5–2 nm here. The cantilever of the tip oscillates with the resonant frequency in this imaging mode along with the similar methods adopted from the contact mode. The probe lightly taps on the surface of the sample. A constant tip-surface interaction is maintained by sustaining a constant oscillation amplitude to receive a 3-D image of the sample.
- **Non-contact mode of AFM:** It is defined as when the separation between tip and sample is ~ 0.1-10 nm in this mode of operation. During the scanning process,

the tip does not physically contact the sample surface but oscillates above an adsorbed fluid layer placed on the surface. As the force exerted between the tip and surface is lower than the other mode of AFM, the lifetime of the tip becomes higher relative to that in other modes. The main disadvantage of this mode is that it demands an ultra-high vacuum and the resolution in this operation is very poor

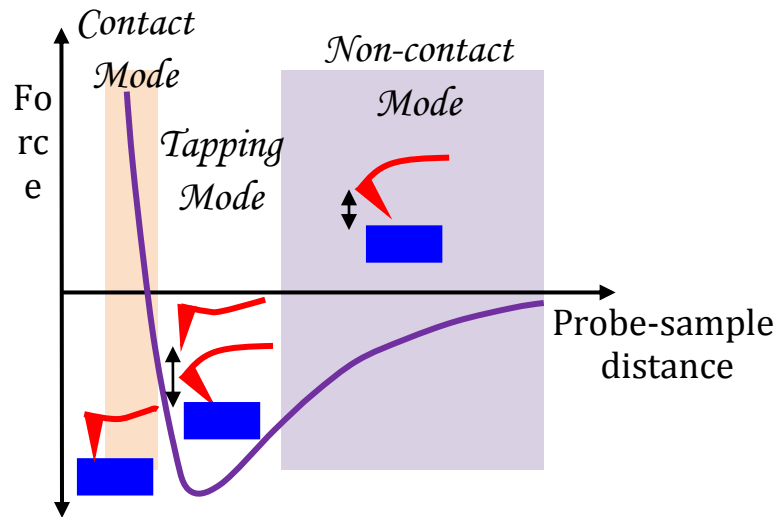


Fig. 4.14. Schematic diagram of tip action of different modes of operation of AFM operates in various regions of the force-distance curve.

4.3.6 Field emission scanning electron microscopy (FESEM)

The high-resolution image of the surface of the thin film can be obtained using a scanning electron microscope (SEM). The SEM was first developed in the early 1950s and opened a new learning area in the science communities about actual physical images [17]. Since the SEM measurements take place within a vacuum chamber using an electron gun, it demands the sample to be dry; otherwise, the moisture gets disturbed within the vacuum chamber and deflects the electrons. For a non-conducting sample, a metal coating on the sample is required to eliminate the accumulation of the electrons on the sample surface as it may lead to a non-clear surface. As shown in **Fig. 4.15(a)**, electrons are generated by heating a tungsten (high melting point in lower vapour pressure) filament in a typical SEM. Another filament, such as lanthanum hexaboride can be used for FE-SEM.

The energy of the emitted electrons (energy $\sim 0.2 - 40$ keV) is focused on one/two condenser lenses (diameter of spot ~ 0.4 to 5 nm). Then, the beam passes through

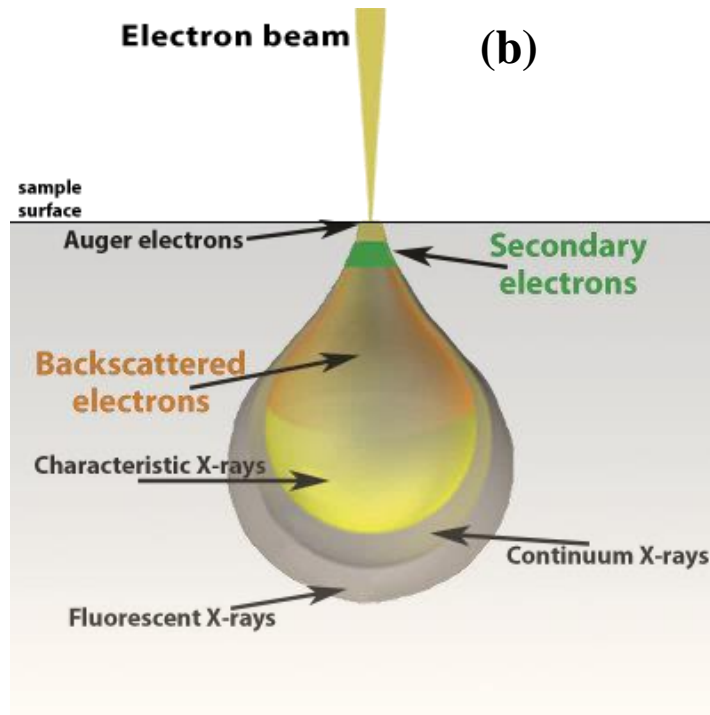
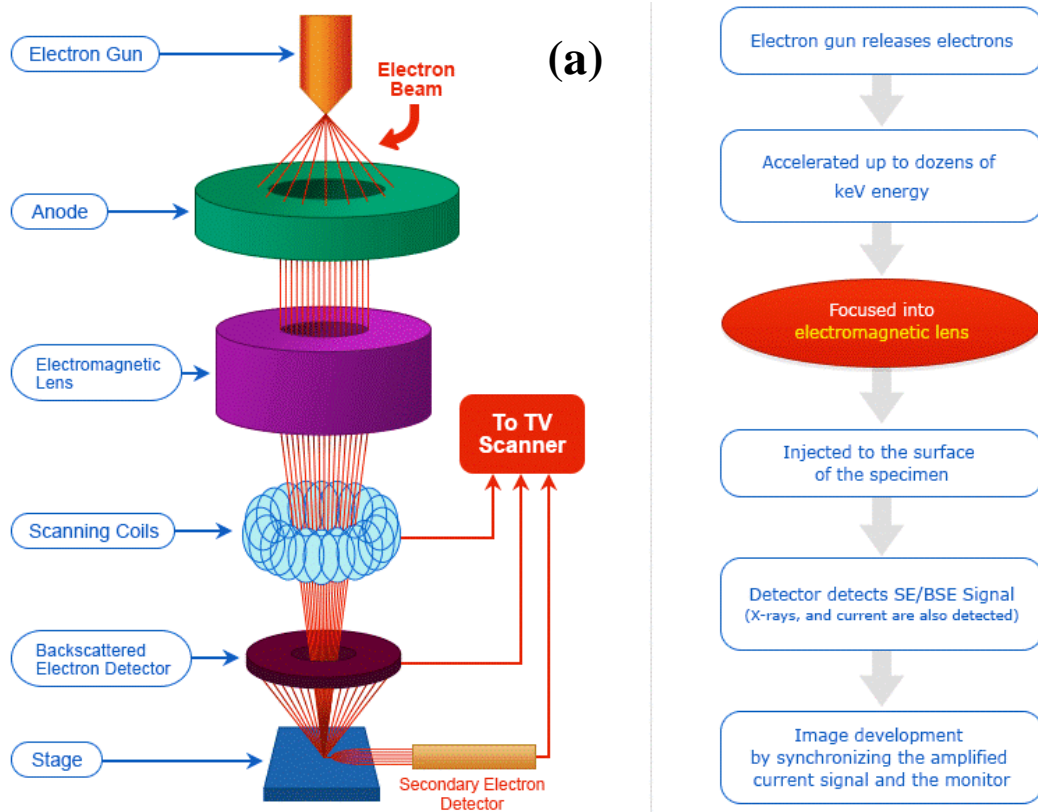


Fig. 4.15. (a) Schematic representation of the SEM instrument with an electron path diagram. (b) A schematic diagram of the different processes taking place during electron-solid interaction.

deflector plates or scanning coils to the final lens, which deflects the electron beams in the x-y direction for scanning in a rectangular area. The high energy of accelerated electrons is dissipated by the electron-sample interactions when the electrons are slow up on the sample's surface. It creates secondary electron signals and backscattered electrons (BSE), which are used for imaging of the sample, as shown in **Fig. 4.15(b)** [18]. The SEM is generally used for high-resolution 2-D images of the sample.

Additionally, it also gives information about the chemical compositions such as chemical analysis. The elemental map is obtained using EDS, estimation of mean atomic number by the phase-based method using BSE, etc. The electron probe size, current and convergence angle control the depth of field and finally determine the contrast and sharpness of any SEM images.

4.4 Compositional characterization

4.4.1 X-ray photoelectron spectroscopy (XPS)

X-ray photoelectron spectroscopy (XPS) or electron spectroscopy for chemical analysis (ESCA) is an extensively used characterization technique to investigate the chemical composition, chemical bonding configuration, and material's electronic structure. A schematic representation of the working principle of the XPS is shown in

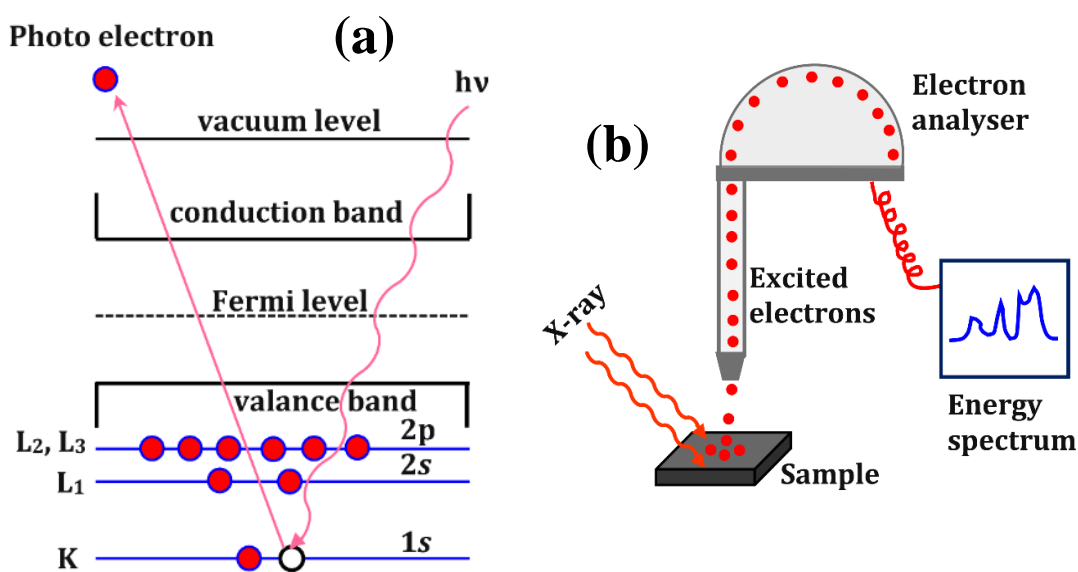


Fig. 4.16. Schematic diagram of (a) the production of photoelectron and (b) the working mechanism of XPS.

Fig. 4.16(a) and **Fig. 4.16(b)**. The XPS provides the evidence from the top surface of the sample within 10 nm depth, such as the composition of the elements up to 0.1% sensitivity, information of the chemical states and depth distribution profile of the chemical species. However, it cannot detect hydrogen and helium due to the absence of their core electrons [19].

In a high-vacuum chamber, when the sample's surface is irradiated by the X-rays produced from Al K_{α} or Mg K_{α} , the X-ray photon hits a valence electron or core-level electron and transfers its energy. This electron is ejected from the material with kinetic energy, which is determined by the binding energy of the atomic orbital and the energy of the incident X-ray. The concentrations of the elements can be obtained by calculating the energy and intensity of the emitted photoelectrons. Using the Einstein equation, the relation between binding energy and the kinetic energy of the core-shell electron can be determined, as [20];

$$h\nu = E_b + E_k + \phi \quad (4.33)$$

where $h\nu$ is the X-ray photon's energy, E_k is the photoelectron's kinetic energy, E_b represents the binding energy of the core-shell electron, and ϕ is the work function. The ϕ can be calibrated and eliminated. So, the above relation takes the form,

$$E_b = h\nu - E_k \quad (4.34)$$

So, the binding energy of the core-level electron can be measured directly by removing the electron from the core level to the vacuum/Fermi level of free molecules/atoms. XPS measurement gathers the basic information (from the peak position of XPS spectra) but also provides the idea about the percentage of an element within the sample from the peak intensity of the XPS spectra; that is why it is termed Electron Spectroscopy for Chemical Analysis (ESCA). A generalized expression for determining the atomic percentage. Alternatively, the atomic percentage of any component element from the sum of the peak intensities from all the elements in the specimen being investigated:

$$C_x = \frac{n_x}{\sum_i n_i} = \frac{\frac{I_x}{S_x}}{\sum_i \frac{I_i}{S_i}} \quad (4.35)$$

where C is the analyte concentration, x [21]. This formula is applicable for the specimens assuming a uniform distribution of elements throughout the material. The atomic sensitivity factor (S) differs for different elemental photoelectric transitions.

4.5 Electrical characterization

4.5.1 Temperature dependent dark conductivity

The electrical characterization of the nanocrystalline silicon-germanium alloy thin film involves determining the film's dark-conductivity and activation energy. Before the measurement, two Al electrodes of length (l) 1.0 cm and a distance of separation (w) 1.0 mm are deposited on the film surface in a thermal evaporation unit at room temperature at a vacuum of $\sim 10^{-6}$ Torr. **Fig. 4.17** shows the schematic diagram of the dark-conductivity measurement set-up. In our experiments, a 6517A Keithley electrometer is used to measure the current (I) through the sample, applying a voltage across it., The electrical conductivity of the thin film with thickness d at a given temperature is determined using the I–V characteristics curve following the relation:

$$\sigma = \frac{Iw}{Vld} \quad (4.36)$$

To understand the transport phenomena in the SiGe alloy thin films, temperature-dependent dark conductivity is measured in a high vacuum chamber with the sample heated from room temperature to the temperature 170 °C at a rate of heating as 3°C/min.

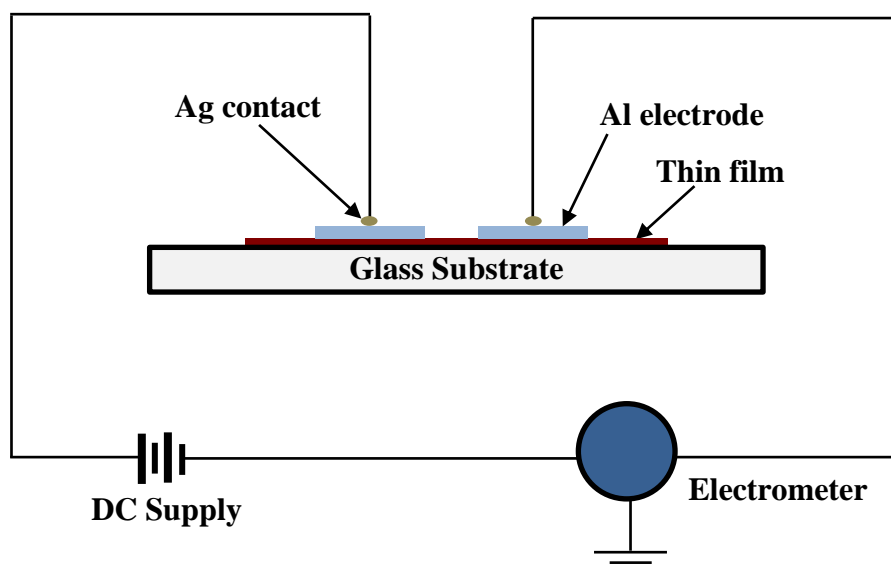


Fig. 4.17. Schematic diagram of the electrical conductivity measurement set-up.

Subsequently, it is cooled down to -30 °C at a 0.5°C/min cooling rate. The current flowing between the electrodes through the sample layer is measured as a function of temperature by applying a fixed voltage across the sample electrodes during the cooling

of the sample. The activation energy (E_a) is determined through the linear fitting of temperature-dependent dark conductivity ($\ln\sigma_D$ vs $1000/T$ plot) using the following relation:

$$\sigma_D = \sigma_0 \exp^{-E_a/k_B T} \quad (4.37)$$

where σ_0 is a constant and k_B is the Boltzmann constant.

4.5.2 Hall Measurement

The Hall measurement can obtain the electrical type and concentration of charge carriers and their mobility. Based on the basic principle of Lorentz force, when a current perpendicular to the magnetic field passes through the ends of a conductor or semiconductor, an electric field is produced perpendicular to both the magnetic field and the current flow [22]. A voltmeter is used to measure the produced electric field, which is linearly dependent on the magnetic field and current. This phenomenon is known as the Hall effect. The schematic diagram for Hall effect measurement is shown in **Fig. 4.18**.

Let us consider a rectangular sample with length, L and cross-sectional area, A . If a voltage V is applied transversely along the sample and the magnetic field, B along z -direction. The Lorentz force acting on the free carriers:

$$\vec{F} = q(\vec{E} + \vec{v} \times \vec{B}) \quad (4.38)$$

Taking a flow of charge along z -direction,

$$\vec{F} = q\vec{E} + q \begin{vmatrix} \hat{e}_x & \hat{e}_y & \hat{e}_z \\ v_x & 0 & 0 \\ 0 & 0 & B_z \end{vmatrix} = qE_x\hat{e}_x + q(E_y - v_x B_z)\hat{e}_y + qE_z\hat{e}_z \quad (4.39)$$

The net force must be zero along y - and z -direction. As a result, the electric field is zero along the z -direction and,

$$F_y = q(E_y - v_x B_z) = 0 \quad (4.40)$$

which can be rewritten as,

$$E_y = v_x B_z = \frac{J_x}{qn} B_z \quad (4.41)$$

where q and n are the charge and density of carriers. This electric field is known as the Hall field. The Hall field produced per unit current density and unit applied magnetic field termed as Hall coefficient (R_H). Hence,

$$R_H = \frac{E_y}{J_x B_z} = \frac{1}{qn} \quad (4.42)$$

So, the Hall resistivity,

$$\rho_H = \frac{E_y}{J_x} = H_z R_H \quad (4.43)$$

Also, the Hall mobility can be obtained from the relation,

$$\mu_H = \frac{R_H}{\rho_H} \quad (4.44)$$

The applied voltage per applied current is the average resistance, but the generated hall voltage per applied current is the Hall resistance. In most cases, the Hall resistance is proportional to the applied magnetic field. However, at low temperature and high field, Hall resistance in the two-dimensional (2D) system is step-like rather than linear. This

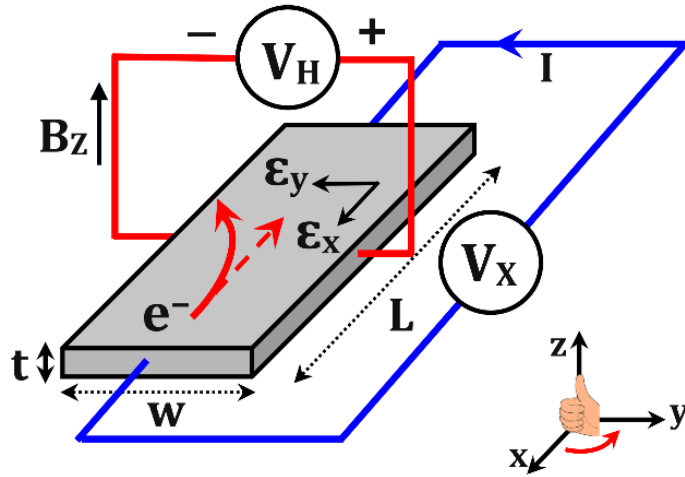


Fig. 4.18. The schematic diagram of the Hall measurement configuration.

step's value is h/me^2 , which does not depend on the nature of the material, is known as the Quantum Hall Effect [23].

Hall measurement gives the information of the nature and concentration of charge carriers with the mobility of a single dopant case. But in the case of multiple impurities with free holes and electrons [24]. In the case of a low carrier concentration, the produced

Hall voltage is minimal, which can be measured by a very precise digital voltmeter. The other problems arise because of sample shape contacts placed at non-symmetric positions [25].

4.6 Measurement of I-V characteristics of solar cell

The fundamental characteristic of a solar cell is identified from the current density (J)-voltage (V) measurement to understand the process of light conversion directly into electricity. The functioning of a solar cell is determined by three major parameters: short circuit current density (J_{SC}), open-circuit voltage (V_{OC}), and fill factor (FF) of the solar cell. The short circuit current (I_{SC}) is defined as the current created due to the generation of charge carriers under light exposure. Ideally, this current is equivalent to the load current, at zero bias. However, conventionally, to eliminate the dependency of solar cell area (A), the short-circuit current density, defined as $J_{SC} = \frac{I_{SC}}{A}$ is used. Further, open circuit voltage is denoted as the voltage when no current passes through the cell and it is equal to the potential difference at the junction of the solar cell. However, at the point of V_{OC} and I_{SC} , the power from the solar cell is zero. The fill factor (FF) is a parameter that defines the maximum power output (P_{max}) of a solar cell in conjunction with V_{OC} and I_{SC} and it is written as

$$FF = \frac{P_{max}}{J_{SC}V_{oc}} = \frac{J_{mp}V_{mp}}{J_{SC}V_{oc}} \quad (4.45)$$

The power conversion efficiency (PCE) of such a device is defined as the ratio of output electrical power (P_{out}) to input sunlight power (P_{in}), as follows,

$$PCE = \eta = \frac{P_{out}}{P_{in}} = \frac{J_{sc}V_{oc}FF}{P_{in}} \quad (4.46)$$

J_{SC} , V_{oc} , and FF are short-circuited current density, open-circuit voltage and fill factor of the solar cell respectively.

To measure the illuminated I-V curve of a solar cell, the measuring conditions are under the standard AM1.5G spectrum (100 mW/cm^2 , $25 \text{ }^\circ\text{C}$). The intensity of the 1-Sun light is calibrated by a standard reference silicon cell and is kept constant through the measurement. This calibration is based on the assumption that the light spectrum of

the sun simulator in Dark-Star is identical to the light spectrum used for the calibration of the reference cell. The illuminated I-V measurement gives open-circuit voltage (V_{OC}),

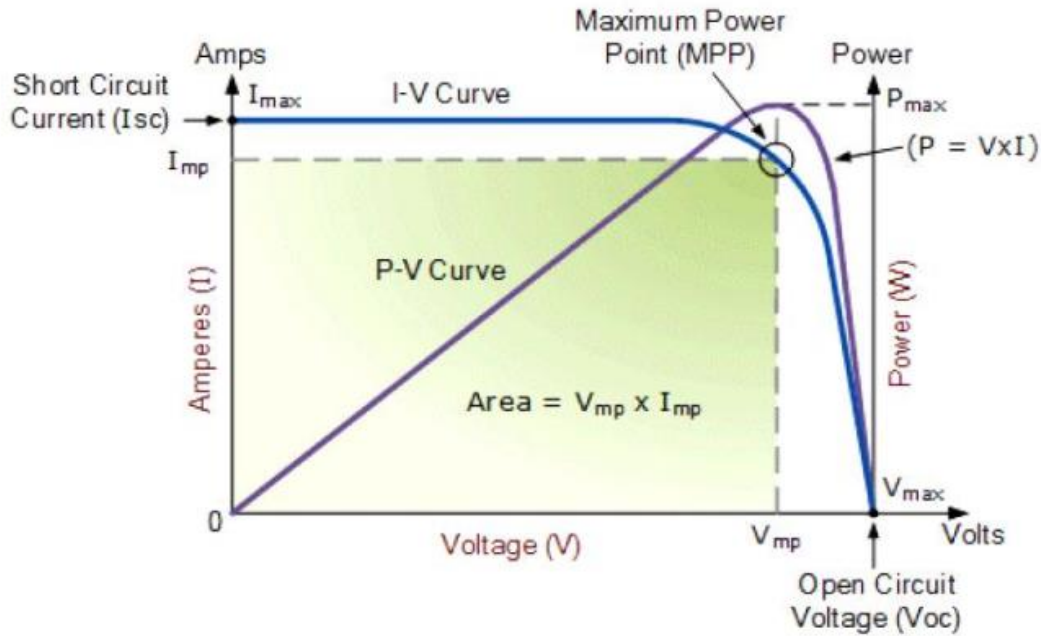


Fig. 4.19. Solar cell I-V characteristic curve.

short circuit current (I_{SC}), short circuit current density (J_{SC}), maximum voltage (V_{mp}), maximum power (P_{max}), current at maximum power point (I_{mp}), fill factor (FF) and conversion efficiency (η) of the measured cell [Fig. 4.19].

A set of filters with different transmissions is needed to be placed between the measuring cell and the light source of the sun simulator before measurements. Dark IV measurement is performed using a sample holder covered by a copper casing to impede the environmental light from interfering with the collection of dark I-V data. Before the I-V measurement, the program menu must define the measured current range and conduction type of the cell's substrates (*n*-type or *p*-type).

4.7 References

- [1] K.J. Laidler, J.H. Meiser, Physical Chemistry, 2nd edition (1995).
- [2] J. Tauc, Optical Properties of Solids, edited by F. Abelès (North-Holland, Amsterdam, the Netherlands) p.277 (1972).
- [3] D. Das, Jpn. J. Appl. Phys. 33 (1994) 571–574.
- [4] A. Samanta, D. Das, J. Electrochem. Soc. 158 (2011) H1138–H1144.

- [5] T. Tsuru, *Compendium of Surface and Interface Analysis* Anonymous, chapter-Ellipsometry, Springer, pp. 155–164 (2018).
- [6] H. Fujiwara, *Spectroscopic Ellipsometry: Principles and Applications*. John Wiley and Sons (2007).
- [7] C.S. Lu, O. Lewis, *J. Appl. Phys.* 43 (1972) 4385.
- [8] Instruction manual for Vacuum Coating Unit Model-15F6-D, Hindhead Pvt. Ltd., Bangalore.
- [9] J.W. Wood, R.D. Redin, *Rev. Sci. Instrum.* 64 (1993) 2405.
- [10] T. Kanada, T. Kubota, A. Suzuki, *Meas. Sci. Technol.* 2 (1991) 191–197.
- [11] R.E. Evans, *Rev. Sci. Instrum.* 43 (1972) 806–810.
- [12] R Swanepoel, *J. Phys. E: Sci. Instrum.* 17 (1984) 896.
- [13] R Swanepoel, *J. Phys. E: Sci. Instrum.* 16 (1984) 1214.
- [14] P.E.J. Flewitt, R.K. Wild, *Physical methods for materials characterization*, IOP Publishing Ltd. (1994).
- [15] P. Scherrer, *Göttinger Nachrichten Gesell.* 2 (1918) 98.
- [16] B.D. Cullity, S.R. Stock, *Elements of X-Ray Diffraction*, 3rd Ed., Prentice-Hall Inc., p 167–171, ISBN: 0-201-61091-4, (2001).
- [17] https://www.nanoimages.com/sem-technology-overview/sem_img2/.
- [18] <https://www.nanoscience.com/techniques/scanning-electron-microscopy/>.
- [19] N. Stojilovic, *J. Chem. Educ.* 89 (2012) 1331–1332.
- [20] S. Hufner, *Photoelectron Spectroscopy: Principles and Applications*, 3rd Ed., Springer Verlag Berlin Heidelberg, Germany (2003) ISBN: 978-3-642-07520-9.
- [21] U. Vohrer, C. Blomfield, S. Page, A. Roberts, *Appl. Surf. Sci.* 252 (2005) 61–65.
- [22] E. Hall, *American J. Mathemat.* 2 (1879) 287–292.
- [23] F.D.M. Haldane, *Phys. Rev. Lett.* 61 (1988) 2015–2018.
- [24] C.M. Hurd, *The Hall effect in metals and alloys*, Plenum Press (1972).
- [25] A. Beer, *Solid State Electron* 9 (1966) 339–351.



Chapter 5

Effect of RF power in opto-electronic and structural properties of hydrogenated nanocrystalline SiGe thin film in RF-PECVD

5.1 Introduction

The benefits of low material cost and large module manufacturing flexibility has made thin film silicon based solar cells largely commercialized [1,2]. Tandem-type design has been employed in the production of thin film silicon solar cells to obtain efficient spectral utility and long-term stability against light induced degradation [3–5]. In the past years, nc-Si and a-SiGe had been used at the middle and bottom sub-cells in its tandem structure multi band-gap scheme [6–8]. However, use of a-SiGe does not match with the reduced light induced degradation strategy [9], while nc-Si requires an increased layer thickness due to its reduced optical absorption co-efficient [10] that does not comply with the stringent cost requirements. In this context, nanocrystalline silicon–germanium alloy (nc-Si_{1-x}Ge_x) has been envisaged as an ideal absorber material at the bottom-cell in multi junction Si thin film solar cells because of its simultaneous spectral sensitivity in the infrared range and good stability against light exposure [11–16]. The optical absorption co-efficient of SiGe:H alloy increases with the inclusion of Ge atoms into the network; however, its larger dimension (dia: 250 pm) to that of Si (dia: 220 pm) introduces additional defects [8,17,18] which initiates sharp deterioration of electrical properties. It is quite challenging to produce good quality SiGe thin films with sustained nanocrystallinity, particularly at low growth temperature. The nc-SiGe thin films have been reported mainly using variations of different flow ratio of source gases (e.g., SiH₄, GeH₄, etc.) [11,17–28], different nature of diluent gases (e.g., H₂, He, Ar) in various proportions [29–33], including changes in the physical plasma parameters [34]. All of those have very strong influence on the growth prospect of the SiGe alloy network. However, the deposition conditions in the preparation of nc-Si_{1-x}Ge_x network are very complex because the major precursors produced from two frequently used source gases, e.g., SiH₄ and GeH₄ are very different in their chemical reaction behaviors, controlled via different energy requirements [35]. Ge atoms are promptly combined to the network and facilitate band gap narrowing; however, additional defects arising out of its larger dimension led to inevitable amorphization of the network. Accordingly, in order to maintain stringent nanocrystallinity in the nc-Si_{1-x}Ge_x:H network and retain the desired optoelectronic properties of the films, optimization in the electrical excitation to the mixture of source gases present at specific proportion in the plasma appears to have the most sensitive control.

The present investigation involves the optimized growth of nc-Si_{1-x}Ge_x:H absorber layers using (SiH₄+GeH₄) precursor gases diluted by H₂, in particular at low temperature (~220 °C), through delicate control of the plasma by precisely varying the RF power applied to the parallel plate capacitively coupled electrodes of the PECVD reactor. The optoelectronic properties of the nc-Si_{1-x}Ge_x:H films have been correlated with their structural characteristics, towards tailoring those for future applications in tandem structure nc-Si solar cells. Towards this objective, the variations of the chemical bonding configuration, microstructural organisation, the micro-voids, defect densities with bonded hydrogen content and the nanostructural evolution as a function of the intake of germanium on film's crystallinity, grain size, strain of complex nc-SiGe system are explicitly studied systematically. In this way, the explored chemical insights of the SiGe network related to its microstructure would help in its further utilization for a better control of its microstructural construction on specialized need-based applications.

5.2 Experimental details

The nc-Si_{1-x}Ge_x:H thin films were grown from the gaseous mixtures of hydrogen (H₂), silane (SiH₄) and germane (GeH₄) in a 13.56 MHz conventional capacitively coupled RF-PECVD system maintained at a high base vacuum of ~10⁻⁷ Torr, using a turbo pump backed by a rotary pump. Films of thickness ~800 nm were grown on glass substrates for different optoelectronic and structural measurements and about 40 nm thick films grown on carbon coated Cu microscopic grids were used for transmission electron microscopy studies. A set of samples were grown by varying the RF power in the range 50 – 150 W applied to the (12x12) cm² area parallel plate electrodes, while the substrate temperature (T_s) was fixed at 220 °C and a fixed chamber pressure was maintained at 1.2 Torr. The flow rates of precursor gases GeH₄ and SiH₄ were fixed as 0.2 sccm and 1.8 sccm, respectively, while a constant flow of the diluent gas H₂ was maintained at 50 sccm.

The optical characterization of the nc-Si_{1-x}Ge_x:H films was done using a double-beam spectrophotometer (Hitachi 330, Japan). The Raman backscattering data was obtained from a Renishaw inVia Raman microscope, using an air-cooled Ar⁺ laser with wavelength 514 nm as excitation source operated at ~2 mW/cm² of power density. Different structural orientation of the nanocrystals and their average size were studied by the X-ray diffraction analysis, applying Cu-K_α X-ray (λ = 1.5418 Å) radiation in a Seifert

3000P Bragg diffraction set-up. The chemical bonding configuration of the samples was analysed using the infrared vibrational spectra taken from Fourier transformed infrared spectrometer (Nicolet Magna-IR 750). The electrical conductivity of the films deposited on glass substrate was measured in a cryostat at a high vacuum level of $\sim 10^{-7}$ Torr, by a Keithley 6517A electrometer with dc voltage applied to the Ohmic resistance across the coplanar Al electrodes with 1 mm separation. The microstructural network was studied by high-resolution transmission electron microscopy (JEOL-JSM 2010) operated at 200 kV. The surface features of nc-Si_{1-x}Ge_x:H samples were analysed using Veeco dI CP II atomic force microscope (AFM) (Model no: 0100). Omicron X-ray photoelectron spectrometer with Mg K_α X-ray source was used to get the XPS data, without any surface etching of the sample deposited on glass substrate.

5.3 Results

Fig. 5.1(a) presents the Raman spectra of a set of Si_{1-x}Ge_x:H thin films prepared at different RF power applied to the (SiH₄ + GeH₄) plasma, varying from 50 to 150 W. Three distinct spectral regions within specific spans of wave number 185–310, 310–440 and 440–550 cm⁻¹ are distinctly identified, which are categorized with the vibrational response from Ge–Ge, Si–Ge and Si–Si bonds, respectively [11]. It has been noted that for the a-SiGe film deposited at P = 50 W, the peak positions corresponding to the above three spectral regions are centred at ~ 255 , ~ 382 and ~ 450 cm⁻¹, which abruptly shift to ~ 282 , ~ 404 and ~ 497 cm⁻¹, respectively, for an increase in RF power to 75 W. For further elevation of RF power, however, the lower wave number components corresponding to Ge–Ge and Si–Ge bonds gradually reduce in intensity and on the contrary, the higher wave number Si–Si components become the most dominant one with its gradually sharper characteristics. Accordingly, a gradual dominance from the Ge–Ge towards a Si–Si network has been ascertained in the Si_{1-x}Ge_x:H hetero-structured system on increasing applied RF power to the plasma ensemble. The film prepared at the highest RF power, P = 150 W, has been deconvoluted with all possible satellite components marked by different colors and labelled by corresponding amorphous as well as crystalline counterparts of all possible (Si,Ge)–(Si,Ge) bonding configurations, as shown in **Fig. 5.1(b)**. In general, the Ge dominated as well as amorphous populated components appear at lower wave numbers and the Si dominated as well as their crystalline populated counterparts emerge at higher wave numbers. Accordingly, it can be evident from the

Raman spectra for $75 < P \text{ (W)} < 150$ that in the lower wave number ($185\text{--}310 \text{ cm}^{-1}$) Ge–Ge band the c-(Ge–Ge) component around 280 cm^{-1} significantly reduce in intensity at higher P. In the intermediate wave number ($310\text{--}440 \text{ cm}^{-1}$) Si–Si_n–Ge_{4-n} band the intensity of its dominant Si–SiGe₃ component decrease promptly, whereas the nc-(Si–Si) component at the largest wave number ($440\text{--}550 \text{ cm}^{-1}$) region enhances rapidly at elevated RF power (P). Particularly, probing at the $440\text{--}550 \text{ cm}^{-1}$ Si–Si region, it may be

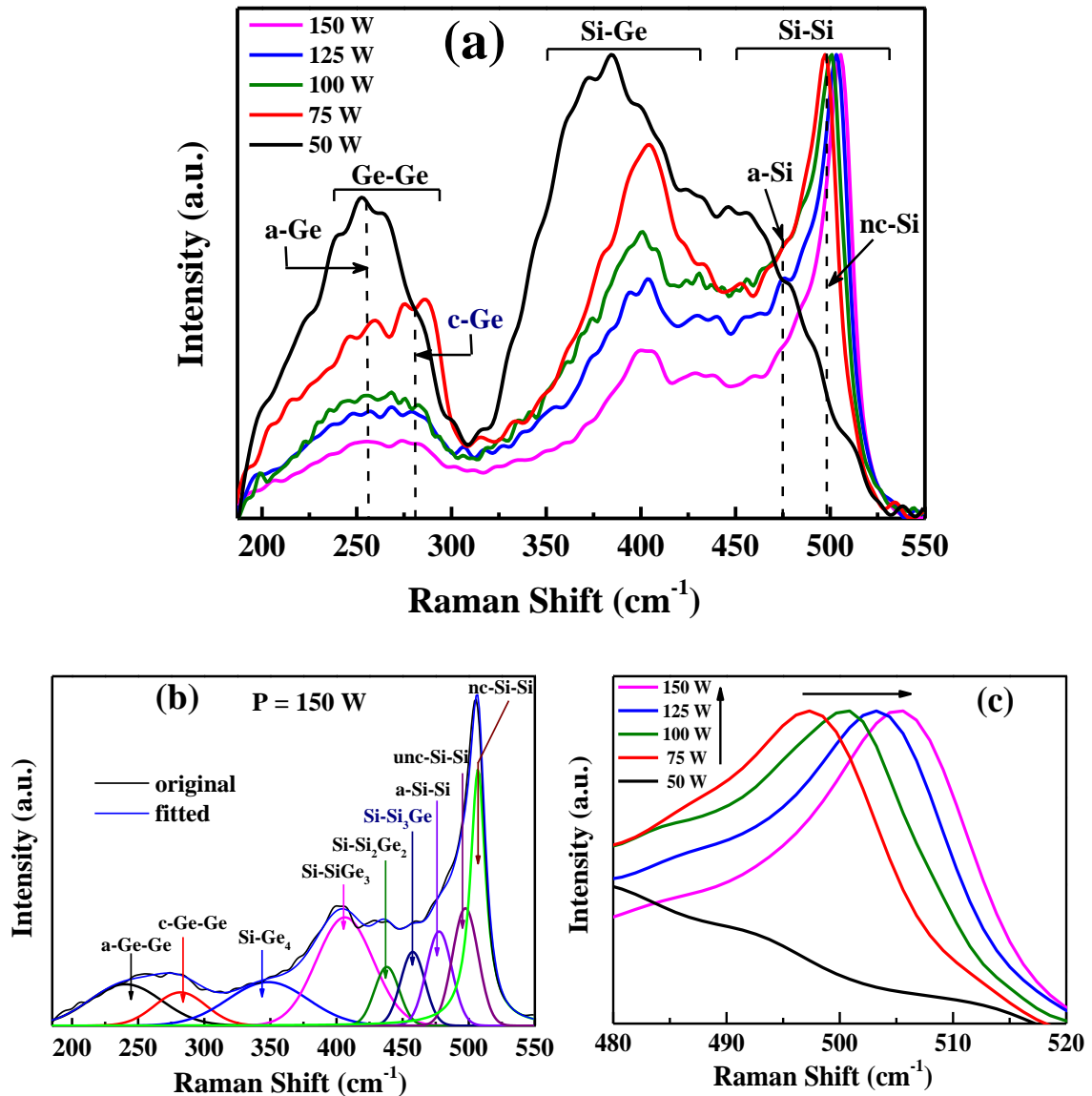


Fig. 5.1. (a) Raman spectra for Si_{1-x}Ge_x:H films prepared at different RF powers, P = 50 to 150 W; (b) Deconvolution of Raman Spectra of the film grown at P = 150 W; (c) Blue shift of Si–Si TO peak with increasing RF power.

noted from **Fig. 5.1(c)** that the sharp peak position systematically shifts towards a higher wave number at increased RF power. The Si–Si vibrational spectra are decomposed into

three sections; two Gaussian components at $\sim 465\text{--}470\text{ cm}^{-1}$ and $\sim 485\text{--}490\text{ cm}^{-1}$, and one Lorentzian component at $\sim 500\text{ cm}^{-1}$ which signify the amorphous, ultra-nanocrystalline and nanocrystalline counterparts of Si–Si network, respectively. The individual peak positions of the satellite components in the nc-SiGe:H network are different from those of nc-Si:H system because of the presence of Ge influencing the vibrational characteristics. Gradually reduced population of the amorphous and ultra-nanocrystalline components and the dominance of the nanocrystalline fragment are mostly responsible for systematic blue-shift of this sharp peak position from ~ 497.3 to $\sim 505.6\text{ cm}^{-1}$ on systematic increase of RF power from 75 to 150 W [36]. There is, however, another important reason for the observed shift in the Si–Si peak position. The size of Ge atom being bigger than that of Si atom, its presence in larger amount at lower RF power causes significant lattice mismatch and induces strain into the alloy network. At increased RF power, Si-dominated alloy network rapidly counterbalances the lattice mismatch related bond strain in proportion to reducing Ge content. Accordingly, the observed blue shift of the sharp Raman peak corresponding to the nc-Si–Si component towards around 505.6 cm^{-1} is a resultant effect of reduced Ge content as well as increased Si–Si crystallization of the network, together. The nc-Si_{1-x}Ge_x:H alloy is a complex hetero-structured material with its amorphous and crystalline mixed phases. Accordingly, the systematic shift of the peak position shown in **Fig. 5.1(c)** cannot make any estimate of incorporated Ge component in the a-/nc-(Si–Ge) hetero-structured system, although some authors have already tried in this regard [15,37–39].

Fig. 5.2 shows the changes in deposition rate of the nc-Si_{1-x}Ge_x:H alloy films as a variable of the RF power applied to the plasma. At the lowest applied power of 50 W, the growth rate is $\sim 7.56\text{ nm/min}$, corresponding to the overall amorphous structure of the network identified from the Raman studies. The deposition rate attains its maximum magnitude of $\sim 9.51\text{ nm/min}$ when the RF power is raised to 100 W. However, on further increase in RF power the growth rate reduces monotonically and attains $\sim 8.5\text{ nm/min}$ at $P=150\text{ W}$. The corresponding Raman analysis, however, identifies an upgraded crystallinity of the Si–Si network developed at $P \geq 75\text{ W}$ and the fraction of the average growth rate appears to be contributed by the simultaneous moderately high volume fraction of the growing Ge–Ge and Si–Ge network. For further elevation of RF power beyond 100 W, however, the Ge–Ge and Si–Ge networks significantly reduce in volume

fraction, simultaneous to the significant reduction of the Si–Si amorphous volume fraction too, and those together lead to the notable reduction in the overall deposition rate

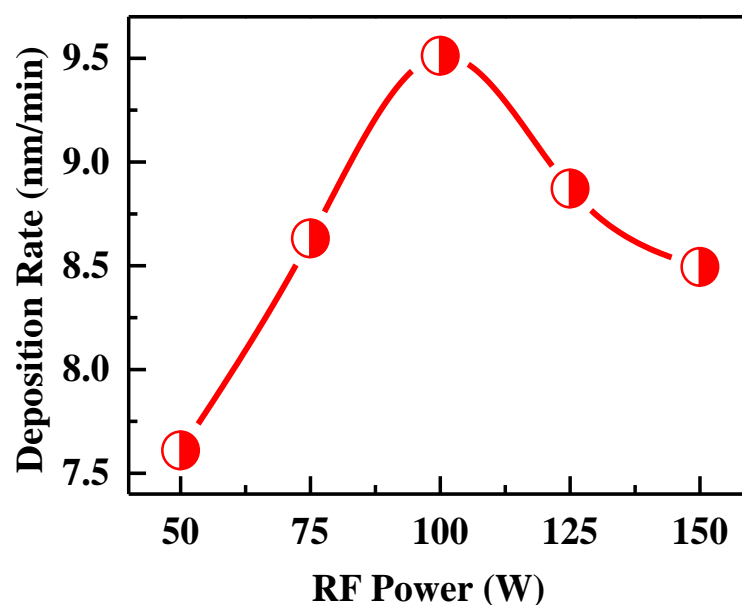


Fig. 5.2. Deposition rate of the SiGe films at different applied RF power.

of the nc-Si_{1-x}Ge_x:H alloy network. Accordingly, the sample prepared at P =100 W has been found to possess optimum presence of the Ge–Ge and Si–Ge matrix as well as Si–Si network with significant fraction of its both amorphous and nano-crystalline components.

Fig. 5.3(a) depicts the X-ray diffraction spectra of a set of silicon germanium (Si_{1-x}Ge_x:H) thin films prepared by using a fixed GeH₄ fraction of the precursor gases $R = \text{GeH}_4 / (\text{SiH}_4 + \text{GeH}_4) = 0.1$, at applied RF powers (P) varying from 50 to 150 W. The corresponding spectrum for P =50 W shows only a broad hump over a 2θ range $\sim 20\text{-}35^\circ$ which arises typically from the glass substrate and the absence of any crystallographic peak demonstrates mostly the amorphous network of the grown material. At P =75 W, three discrete peaks are identified at $2\theta \sim 27.9^\circ$, 47.6° and 55.7° which are associated with the $\langle 111 \rangle$, $\langle 220 \rangle$ and $\langle 311 \rangle$ crystallographic planes of the Si-Ge network, respectively. With P =100 W, all the XRD peaks become more intense as well as sharper, however, $\langle 111 \rangle$ peak appears as the most dominant one. On further increase in P, however, a declining intensity of all the peaks demonstrates a reducing crystallinity of the network. All the films show a common nature of preferential crystalline orientation along the $\langle 111 \rangle$ direction, although a good fraction of $\langle 220 \rangle$ oriented crystallites are present in every nc-SiGe films. It has been reported in the literature that the $\langle 111 \rangle$

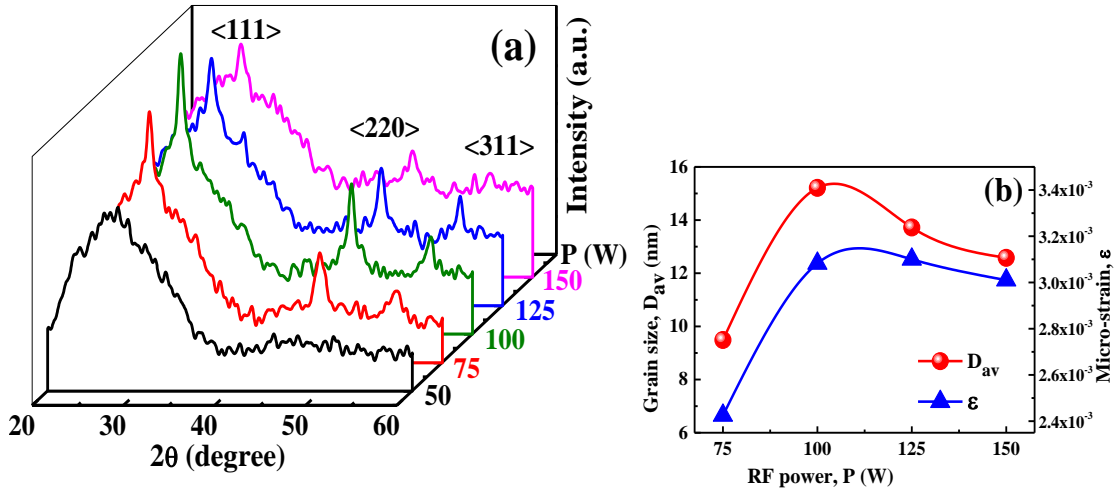


Fig 5.3. (a) X-ray diffraction spectra of SiGe films grown at different RF power. (b) Changes in the average grain size and micro-strain in the film network, as a function of applied RF power.

orientation arises from random crystalline growth, whereas, more ordered growth kinetics are required for attaining <220> crystallographic orientation [36]. In the present case a maximum crystalline network has been evident by the most intense XRD peaks at $P = 100$ W where a preferential orientation along the <220> direction, $I_{<220>}/I_{<111>} \sim 0.68$ has been attained. XRD peaks clearly demonstrate a continuous change in the morphological configuration from dominant amorphous to highly crystalline and then towards a less crystalline network structure of the films on gradual increase in the applied RF power. Further, in view of the source gases GeH_4 and SiH_4 having different dissociation energies the film forming elements Ge and Si contribute continuous variations in their relative composition in complex network grown at increased RF power. Altogether, a good degree of micro-strain develops in the network that influences on the line width of each crystalline peak, while generally a narrow line width signifies a larger dimension of the crystallites. Peak broadening due to increased strain and peak narrowing due to increased grain size together have been combined in Williamson-Hall approach [40]. Broadening of the line-width due to size enhancement has been related by Debye-Scherer formula as,

$$\beta_{DS} = \frac{0.9\lambda}{D_{av} \cos\theta} \quad (5.1)$$

while the strain induced broadening arising from crystal defects and distortions has been related to the Bragg angle θ as:

$$\beta_{\epsilon} = 4\epsilon \tan \theta \quad (5.2)$$

where, ε is the maximum tensile or compressive strain and D_{av} is the average grain size. In Williamson-Hall approach, effects of the independent contribution of size of the crystallites and the network strain have been simply combined in the ultimate peak broadening, as:

$$\beta = \beta_{DS} + \beta_{\varepsilon} \quad (5.3)$$

which finally leads to a relation:

$$\beta \cos\theta = \frac{0.9 \lambda}{D_{av}} + 4\varepsilon \sin \theta \quad (5.4)$$

Now, from the straight-line fitting of $(\beta \cos\theta)$ vs. $\sin \theta$ plot for the XRD peaks and the corresponding slope and intercept, the average grain size (D_{av}) and the micro-strain (ε) are extracted for each individual sample. **Fig. 5.3(b)** shows the nature of variations of both D_{av} and ε in the SiGe thin films grown as a function of increased applied RF power. Major changes in crystallinity and simultaneous increase in the grain size as well as the strain in the network occurred when the applied RF power increased from 75 to 100 W; however, on further increase in power the grain size reduced notably and the stress only marginally, leading to a typical size of the SiGe nanocrystals $\sim 15\text{--}13$ nm with characteristic micro-strain in the matrix $\geq 3.1 \times 10^{-3}$.

In order to have a deeper insight into the structural aspect of the nc-Si_{1-x}Ge_x:H alloy and systematic evolution of the silicon-nanocrystals embedded in amorphous tissue, high resolution transmission electron microscope (HR-TEM) study has been carried out. A typical plain view HRTEM micrograph of the nc-Si_{1-x}Ge_x:H thin film prepared at 100 W has been shown in **Fig. 5.4(a)** in which the physical evidence of the dispersion of spherical Si-nanocrystals within amorphous matrix is evident. In the micrograph, the bright and dark segments identify the density difference between the amorphous and crystalline regions. The magnified view of transmission electron micrograph in **Fig. 5.4(b)** demonstrates, by the marked circular area, one of the Si-ncs having size ~ 6.19 nm with $\langle 220 \rangle$ crystallographic orientation, as embedded within the amorphous network. The corresponding FFT image is shown in **Fig. 5.4(c)** which detects a specific $\langle 220 \rangle$ crystallographic orientation with corresponding inter-planar spacing of 0.193 nm of the nanocrystals, as shown in **Fig. 5.4(d)**. The selected area electron diffraction (SAED) pattern in **Fig. 5.4(e)** exhibits the sharp characteristic rings due to $\langle 111 \rangle$, $\langle 220 \rangle$ and $\langle 311 \rangle$ major crystallographic planes in nc-Si-QDs distributed over

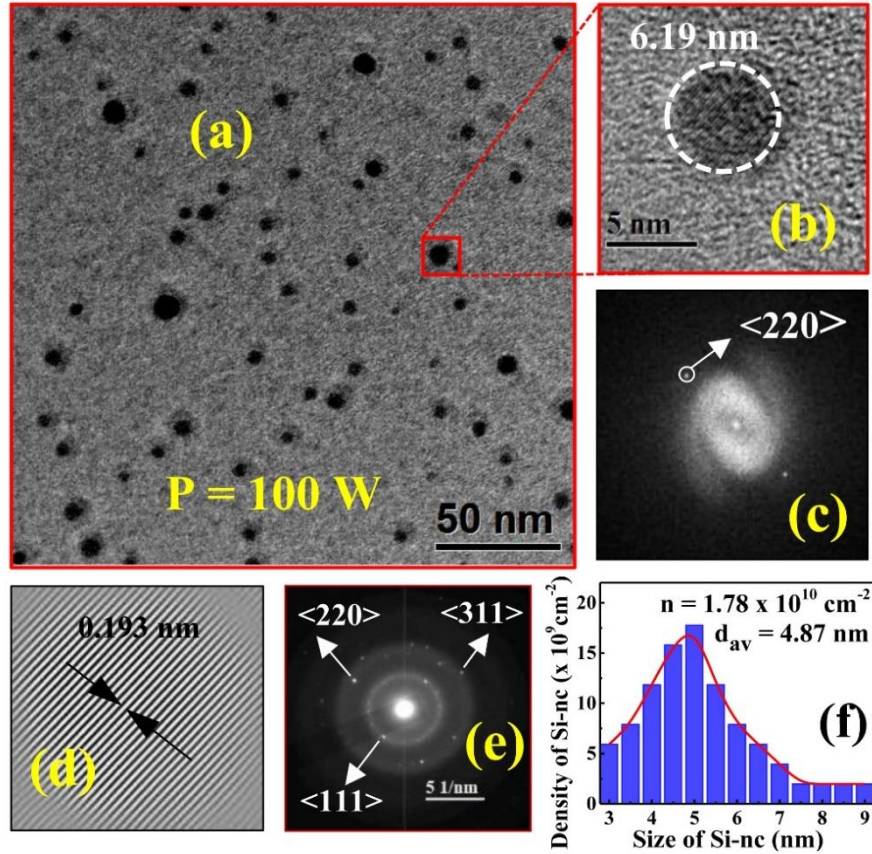


Fig. 5.4. (a) TEM micrograph of nc-Si_{1-x}Ge_x film representing the growth of silicon nanocrystals embedded in amorphous matrix, (b) HRTEM image of arbitrarily chosen Si-nano-crystal of <220> crystallographic orientation, corresponding (c) FFT image, (d) inter-planar spacing, (e) SAED pattern showing different crystal orientations and (f) size distribution of Si-ncs.

the amorphous silicon germanium network. The size distribution of Si-ncs has been assessed from the statistical data analysis on the number density of Si-ncs vs size of the nanocrystals plot, as shown in the corresponding histograms shown in **Fig. 5.4(f)** [41]. The sample matrix possesses Si-ncs of average particle size (d) of ~4.87 nm with number density (n) ~ $1.78 \times 10^{10} \text{ cm}^{-2}$.

The optical characterization of the nc-Si_{1-x}Ge_x:H alloy films has been carried out using the absorption and the reflection spectra in the UV-visible region. The absorption co-efficient spectra are found to enhance in intensity for the films grown at lower RF power where Ge incorporation is favorable. Being an indirect-band gap alloy, the optical band gaps of the samples are estimated following Tauc's equation [42,43]:

$$\sqrt{\alpha h\nu} = B(h\nu - E_g) \quad (5.5)$$

where α is the absorption coefficient, $h\nu$ is the photon energy and E_g is the optical band gap and B is a constant known as the Tauc's constant or the edge width parameter, associated to the degree of disorder in the matrix. The optical band gaps have been obtained from the straight-line extrapolation of the $\sqrt{\alpha h\nu}$ vs. $h\nu$ plot to $\alpha = 0$, as demonstrated in **Fig. 5.5(a)**.

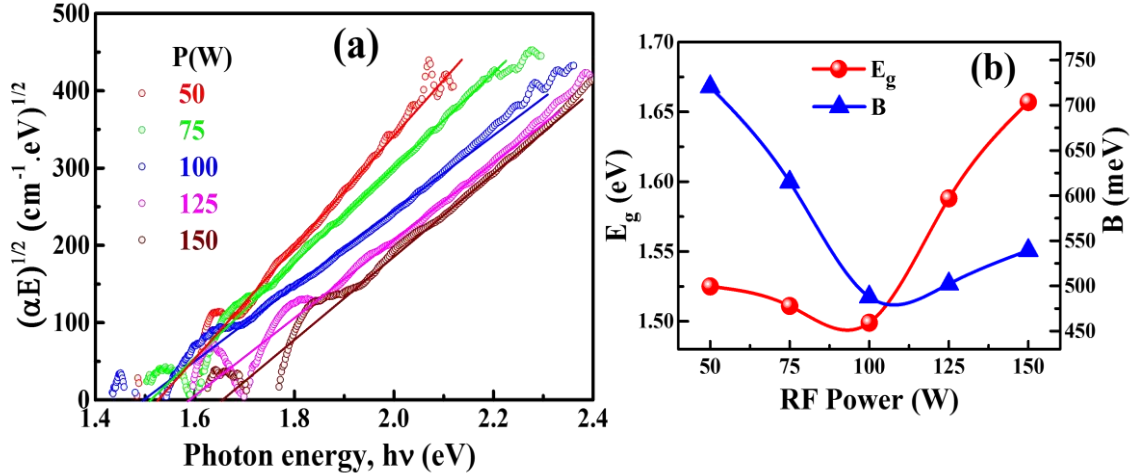


Fig. 5.5. (a) Absorption co-efficient spectra of the SiGe thin films in the Tauc's plot, (b) presents the variations of optical band gap (E_g) and Tauc's constant (B) on increasing RF power.

At the lowest applied RF power of 50 W, the optical band gap of the SiGe film has been estimated as 1.525 eV along with a corresponding high magnitude of the Tauc's constant (B) ~720 meV, characteristic of its amorphous dominated network. Tauc's constant sharply reduces to a low magnitude of ~615 meV for increasing the RF power to $P = 75$ W and ~488 meV for $P = 100$ W, identifying gradual transition from an amorphous to a reasonably nanocrystalline $\text{Si}_{1-x}\text{Ge}_x\text{:H}$ alloy network with steadily reducing Ge content, as envisaged from the Raman data. It has been carefully noted that the corresponding Si-dominated nanocrystalline network with a moderate Ge content narrows in its optical band gap to $E_g \sim 1.511$ eV for $P = 75$ W and $E_g \sim 1.499$ eV for $P = 100$ W. Further increase of power to 150 W, however, introduces little increase in Tauc's constant (B) originating probably by virtue of grain boundary defects from considerably increased crystallinity. Significant reduction in the Ge content from the Si dominated intense nanocrystalline network leads to its wider optical band gap to a relatively high magnitude of ~1.588 eV at $P = 125$ W and ~1.657 eV at $P = 150$ W, as shown in **Fig. 5.5(b)**. In such state of affairs reduced Ge content plays leading role in determining the optical band gap than the effect on its narrowing due to nanocrystallization in the network.

The three dimensional surface topography studied by atomic force microscopy (AFM) on $5 \times 5 \mu\text{m}^2$ surface area of the films prepared at $P = 50 \text{ W}$, 100 W , 150 W are demonstrated in **Fig. 5.6(a)**. The surface morphology and roughness are inherent functions of the film microstructure [44]. The notable difference in the surface morphology for the films grown at $P = 50 \text{ W}$ and 100 W can be easily correlated with the transition from its amorphous dominated to nanocrystals populated structure, as

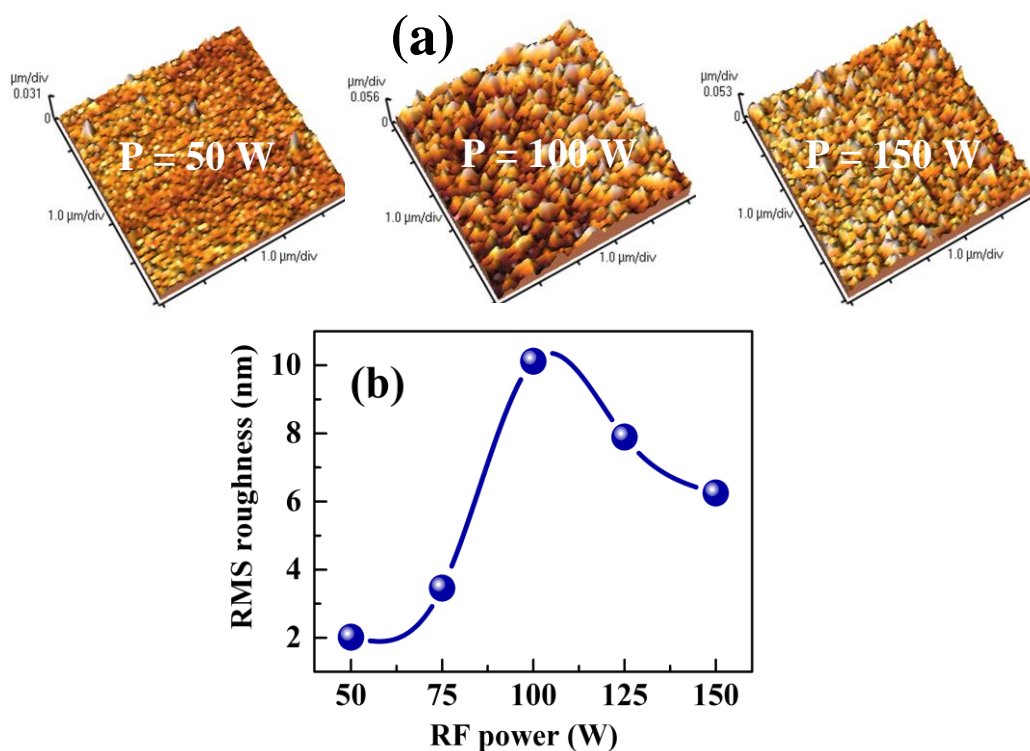


Fig. 5.6. (a) AFM 3D surface morphologies of $\text{Si}_{1-x}\text{Ge}_x:\text{H}$ thin films deposited at $P = 50 \text{ W}$, 100 W and 150 W . (b) RMS roughness of the films grown at various RF power.

identified from the XRD studies [45]. The presence of larger clusters closely packed with each other on the surface along with notably increased voids corroborate with the significant crystallinity of the film network grown at a higher RF power, $P = 100 \text{ W}$, under current parametric conditions. However, further increase in RF power results in film surfaces with diminished size of the clusters and comparable voids between the clusters, consequent to reduced overall crystallinity. A regular variation in RMS roughness at the film surface on increase in the RF power, as estimated from 3D images and depicted in **Fig. 5.6(b)**, resembles closely to the nature of variations in crystallinity as well as size of nanocrystals with changes of RF power, as obtained from the XRD studies.

High-resolution XPS analysis has been performed to investigate on the chemical composition and bonding configuration in nc- $\text{Si}_{1-x}\text{Ge}_x:\text{H}$ films. The XPS survey scan

spectrum of sample grown at $P = 100$ W, presented in **Fig. 5.7(a)**, identifies five strong signals located at about 29 eV, 100 eV, 122 eV, 150 eV and 180 eV, corresponding to Ge-3d, Si-2p, Ge-3p, Si-2s and Ge-1s, respectively. Gaussian deconvolution of the Ge 3d peak in **Fig. 5.7(b)** identifies Ge 3d_{5/2} and Ge 3d_{3/2} sublevels at 28.9 eV and 29.5 eV, respectively [46]. Similarly, the Si 2p core level peak has been deconvoluted into two

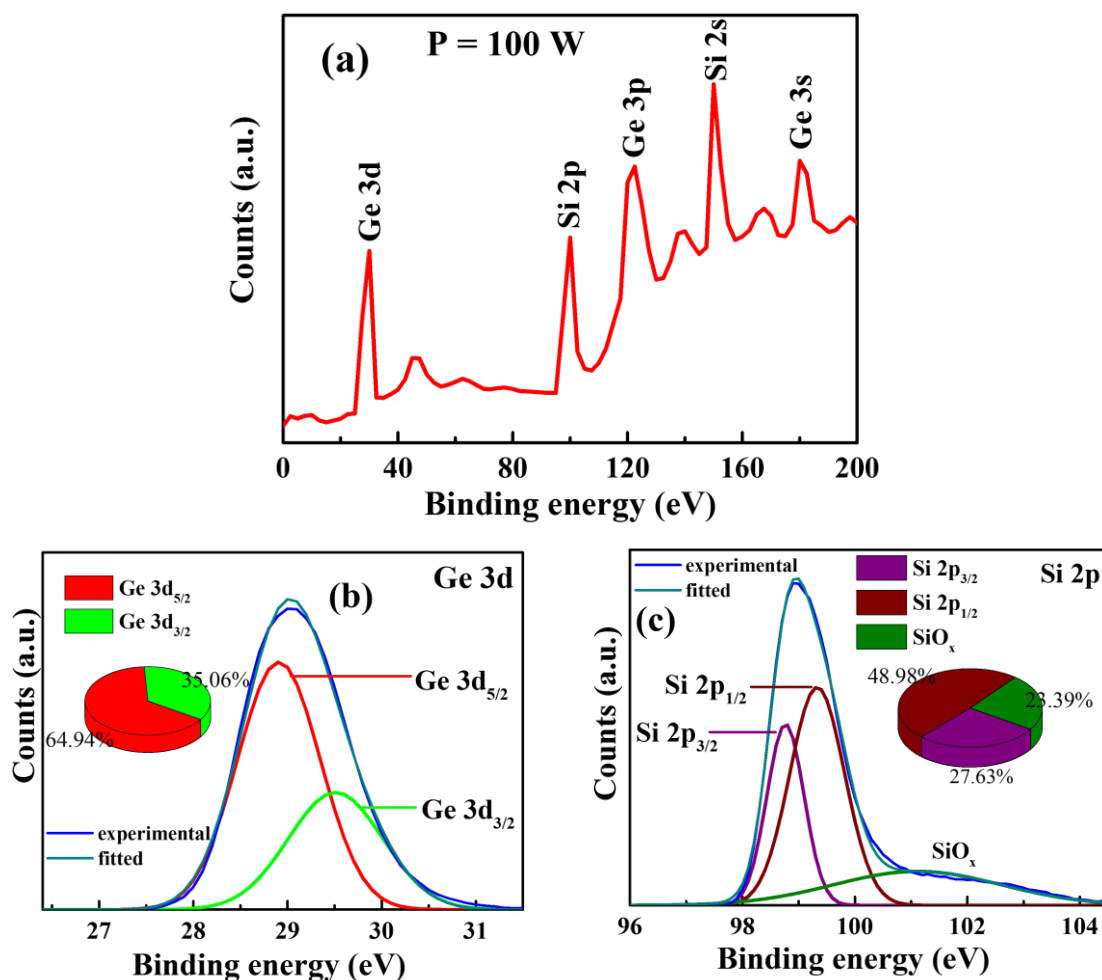


Fig. 5.7. (a) The wide scan XPS spectrum for the nc-Si_{1-x}Ge_x:H film prepared at $P=100$ W. Deconvoluted spectrum into possible satellite components for (b) Ge 3d and (c) Si 2p; Pie chart at the Inset demonstrates the relative intensity of different sub-levels of the orbital.

sub-levels: Si 2p_{3/2} and Si 2p_{1/2} at 98.8 and 99.3 eV, respectively, as shown in **Fig. 5.7(c)**, along with a broad SiO_x flat peak at higher energy side. The individual % composition of each of the Ge 3d and Si 2p components are presented in corresponding pie charts in **Fig. 5.7(b)** and **Fig. 5.7(c)**.

Various chemical bonding configurations between silicon, germanium and hydrogen have been thoroughly investigated via Fourier transformed infrared absorption studies of the samples deposited on c-Si wafer substrates. **Fig. 5.8** presents the FTIR

absorption co-efficient spectrum of the nc-Si_{1-x}Ge_x:H sample grown at P =100 W that typically identifies three prime absorption peaks at spectral ranges over 525–720 cm⁻¹, 750– 925 cm⁻¹ and 1800–2200 cm⁻¹ [19,41,47]. The absorption bands around 525–720 cm⁻¹, shown in **Fig. 5.9**, are deconvoluted into three well-distinguished peaks with centres at ~570 cm⁻¹, ~630 cm⁻¹ and 670 cm⁻¹, associated to the Ge-H wagging mode,

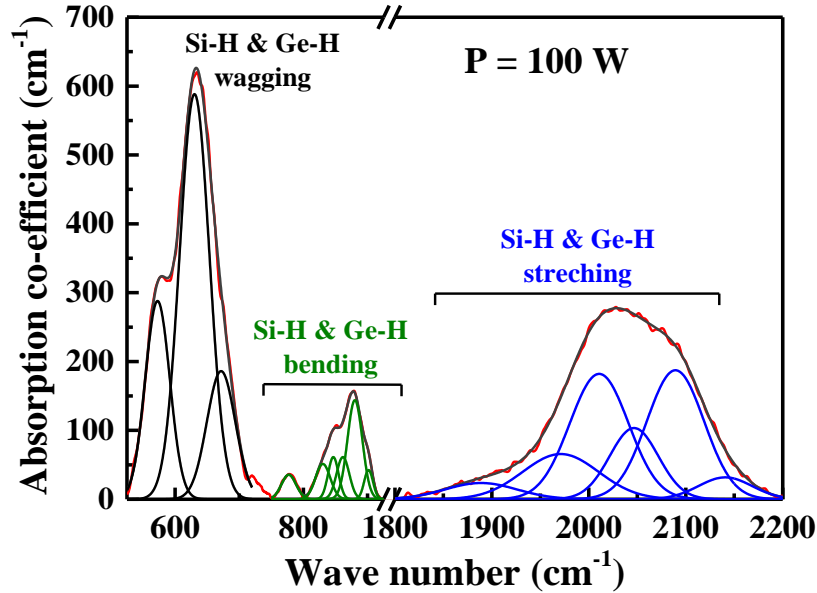


Fig. 5.8. The FTIR absorption spectra with corresponding deconvoluted components for the nc-Si_{1-x}Ge_x:H sample grown at P =100 W.

Si-H wagging mode and SiH_x (x≥2) rocking vibrational modes, respectively. The content of bonded hydrogen (C_H) in individual film has been evaluated using integrated areas under absorption co-efficient components of the Ge-H wagging and Si-H wagging modes at 570 cm⁻¹ and 630 cm⁻¹, respectively, following:

$$C_H = (A_\omega / N_{Si}) \int \alpha d\omega / \omega \times 100 \text{ at. \%} \quad (5.6)$$

where $A_\omega = 1.1 \times 10^{19} \text{ cm}^{-2}$ and $A_\omega = 1.6 \times 10^{19} \text{ cm}^{-2}$ are the related oscillator strengths for Ge and Si, respectively and $N_{Si} = 5 \times 10^{22} \text{ cm}^{-3}$ is the crystalline silicon atomic density [47–49]. The total bonded H-content, C_H, of the material comes from the summation of two individual components from Ge and Si. The relative integrated intensity of the SiH_n (n≥2) rocking mode component of absorption with respect to the total integrated intensity of the wagging and rocking modes of SiH_n (n=1 or ≥2) can be shown as,

$$\Delta I_{670} = \frac{I_{670}}{I_{630} + I_{670}} \quad (5.7)$$

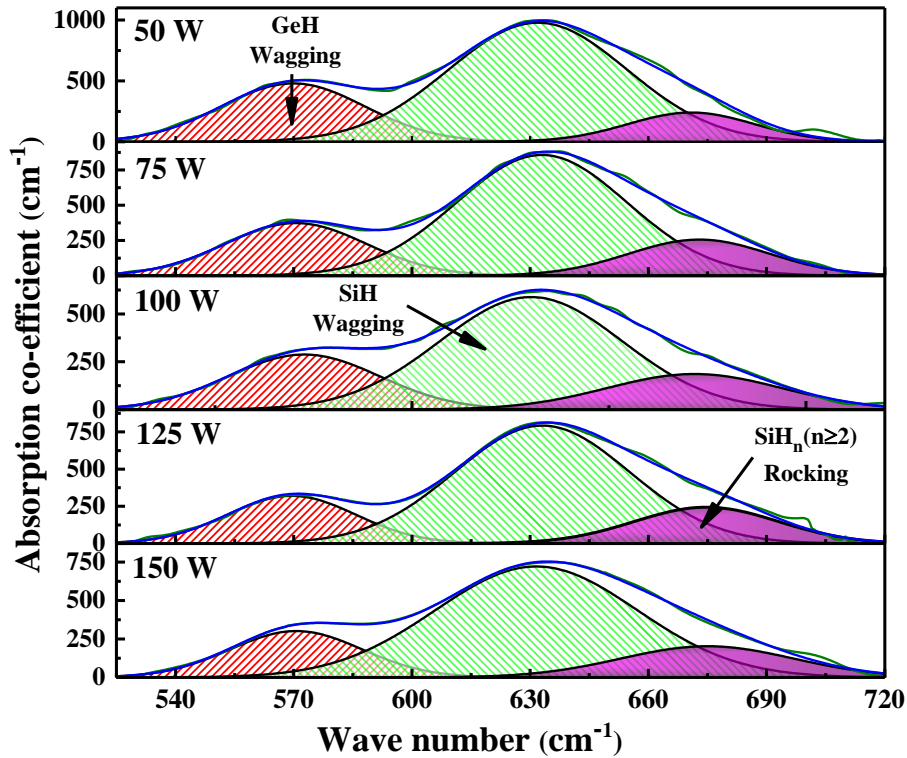


Fig. 5.9. Deconvoluted GeH and SiH wagging modes and SiH_n rocking mode components of IR absorption.

which ultimately depicts the relative strength of Si-polyhydride fraction in the film [50]. The changes in the magnitude of C_H and ΔI_{670} with the applied RF power are plotted in **Fig. 5.10**, which reveal that the bonded H-content reduces from 3.68 at.% to a minimum of 2.32 at.% at remains exactly reciprocal to the nature of variation of C_H , i.e., in other words, in the most crystalline network H is bonded at its lowest population, however, mostly in polyhydride configuration.

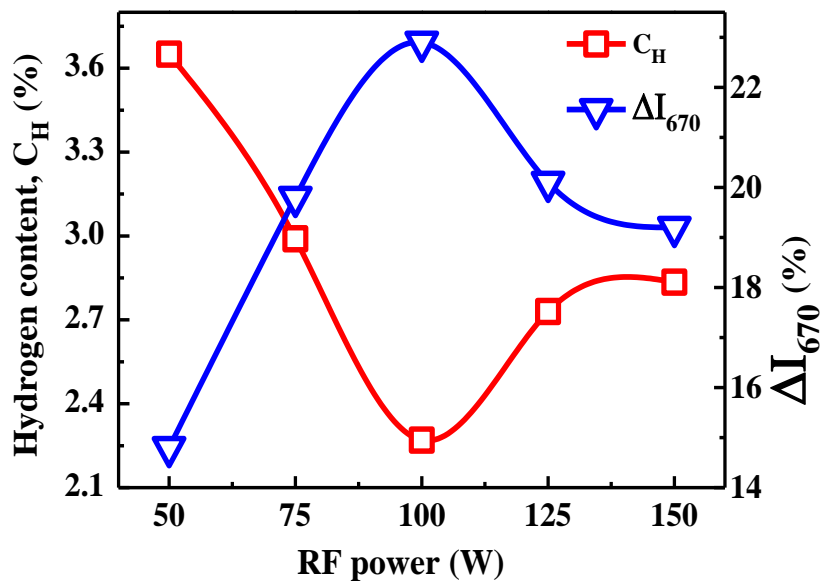


Fig. 5.10. Bonded H-content, C_H , and the relative strength of SiH_n ($n \geq 2$) rocking mode, ΔI_{670} , as a function of RF power.

Deconvolution of the absorption co-efficient spectra over $750\text{--}925\text{ cm}^{-1}$ presented in **Fig. 5.11** identifies six individual bands: $(\text{GeH}_2)_n$ poly-hydride wagging mode at $\sim 775\text{ cm}^{-1}$, GeH_2 di-hydride bending mode at $\sim 832\text{ cm}^{-1}$, $(\text{SiH}_2)_n$ poly-hydride wagging component at $\sim 845\text{--}850\text{ cm}^{-1}$, isolated SiH_2 di-hydrides around $\sim 880\text{ cm}^{-1}$ as well as SiH_3 doublets at $\sim 862\text{ cm}^{-1}$ and $\sim 905\text{ cm}^{-1}$, respectively. The relative strengths of the polyhydride wagging mode components $(\text{XH}_2)_n$ ($\text{X} = \text{Si}, \text{Ge}$), with corresponding di-hydrides, XH_2 ($\text{X} = \text{Si}, \text{Ge}$), are separately estimated and plotted in **Fig. 5.12** which identify the maxima for both of Si and Ge appearing at around applied RF power of $P = 100\text{ W}$. For further increase in P beyond 100 W , however, the network becomes less populated with polyhydrides, though the hydrogen content of the films increases.

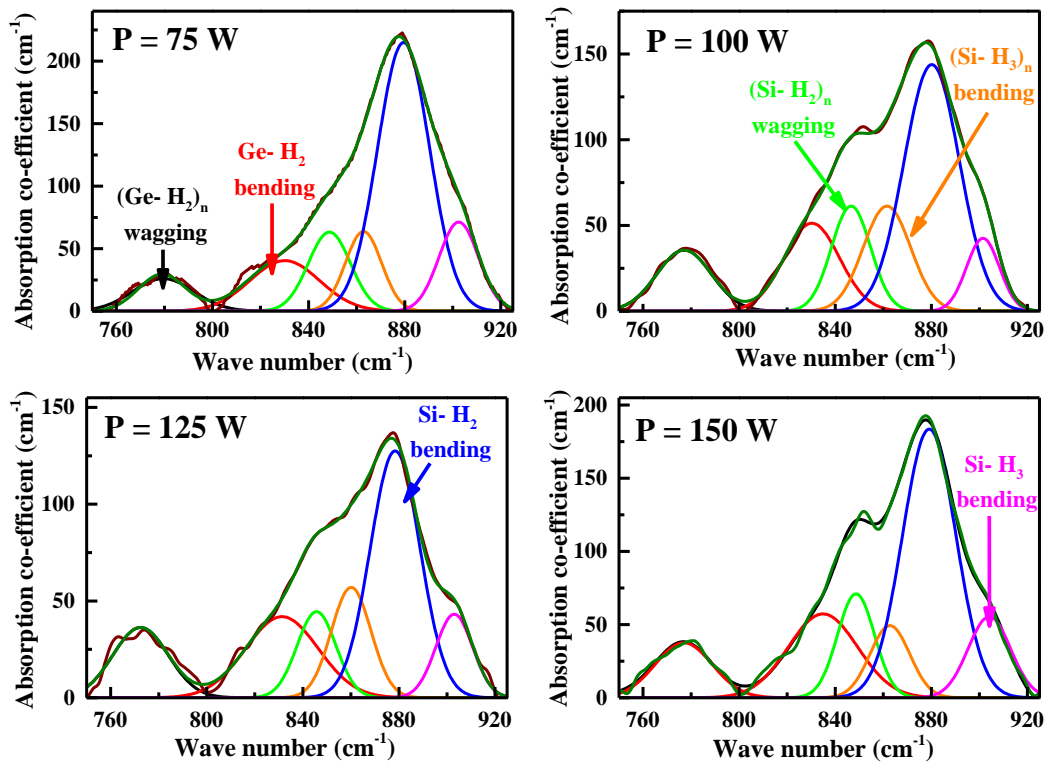


Fig. 5.11. (a) IR absorption spectra around wave number range of $750\text{--}925\text{ cm}^{-1}$, accommodating di-hydride bending and poly-hydride wagging modes.

Fig. 5.13 shows the absorption peaks of Ge-H and Si-H stretching vibrations at wave number range $1800\text{--}2200\text{ cm}^{-1}$ which can be fitted with six well-resolved Gaussian components, which are very useful to have detail microstructural insight of the grown $\text{nc-Si}_{1-x}\text{Ge}_x\text{:H}$ network. The Gaussian components peaked at $\sim 1885\text{ cm}^{-1}$ and $\sim 1970\text{ cm}^{-1}$ are related to stretching modes of mono-hydride GeH vibration and the di-hydride GeH_2 vibration, respectively [7]. Similar pair of Gaussian peaks at $\sim 2005\text{ cm}^{-1}$ and $\sim 2080\text{--}2090\text{ cm}^{-1}$ are correlated to vibrational absorptions of monohydride SiH and dihydride

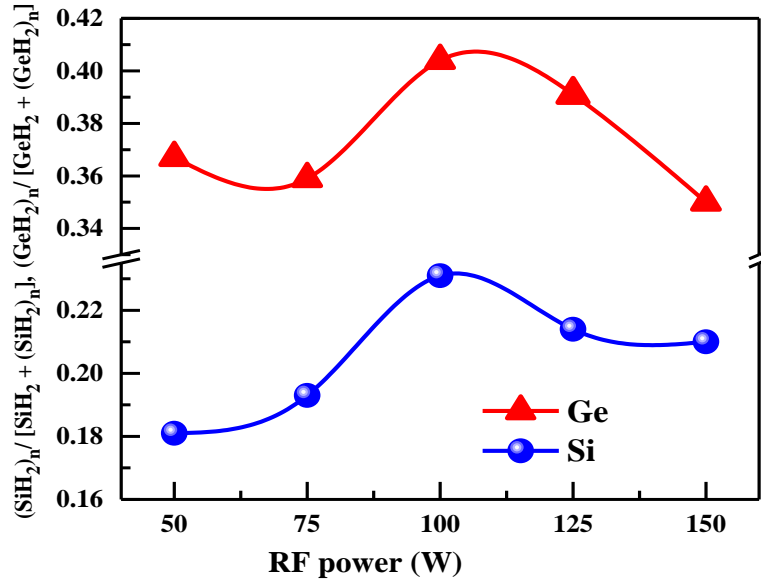


Fig. 5.12. Changes in the relative strength of poly-hydride wagging mode components for both Ge and Si, $(\text{GeH}_2)_n$ and $(\text{SiH}_2)_n$, at elevated RF powers.

SiH_2 stretching modes, respectively [51]. In addition to the above said pairs of components a peak at $\sim 2040\text{-}2050\text{ cm}^{-1}$ is recognized to be related to the bond-centred hydrogen with Si-H-Si structure, in addition to another tri-hydride SiH_3 stretching mode peak between $2135\text{-}2140\text{ cm}^{-1}$ [52]. The Si-H-Si silicon hydride platelet-like configuration is not normally manifested in nc-Si thin films. In $\text{Si}_{1-x}\text{Ge}_x\text{:H}$ alloys, the film quality strongly depends on the hydrogen passivation in Ge and Si related dangling bonds between which Si related dangling bonds are preferentially passivated.

A monotonic decrease of GeH stretching mode absorption at 1880 cm^{-1} has been observed at elevated RF powers and that becomes almost insignificant in case of the films grown at $P > 100\text{ W}$, while the GeH_2 component in general increases with applied power. Simultaneously, at elevated RF power the Si related vibrational peaks gradually increase in intensity; moreover, the di-hydride and poly-hydride Si components, SiH_2 and SiH_3 , dominate over the SiH counterpart in Si-network. Generally, an increased crystallinity and a Si-dominated Si-Ge network result from an elevated RF power.

A quantitative measure on the nature of $\text{Si}_{1-x}\text{Ge}_x\text{:H}$ alloy films can be obtained from estimation of its Si-structure factor, R_{Si} , and Ge-structure factor, R_{Ge} , defined as the polyhydride fraction in related matrix and presented as:

$$R_{\text{Ge}} = \frac{[\text{GeH}_2]}{[\text{GeH}] + [\text{GeH}_2]} \quad (5.8)$$

$$R_{Si} = \frac{[SiH_2]+[SiH_3]}{[SiH]+[Si-H-Si]+[SiH_2]+[SiH_3]} \quad (5.9)$$

where [SiH], [Si-H-Si], [SiH₂], [GeH], [GeH₂] and [SiH₃] are the integrated areas under respective stretching mode absorption components. Similarly, the surface passivation index (S) is defined by the fraction of Si-H-Si component in the Si-network as [53],

$$S = \frac{[Si-H-Si]}{[SiH]+[Si-H-Si]+[SiH_2]+[SiH_3]} \quad (5.10)$$

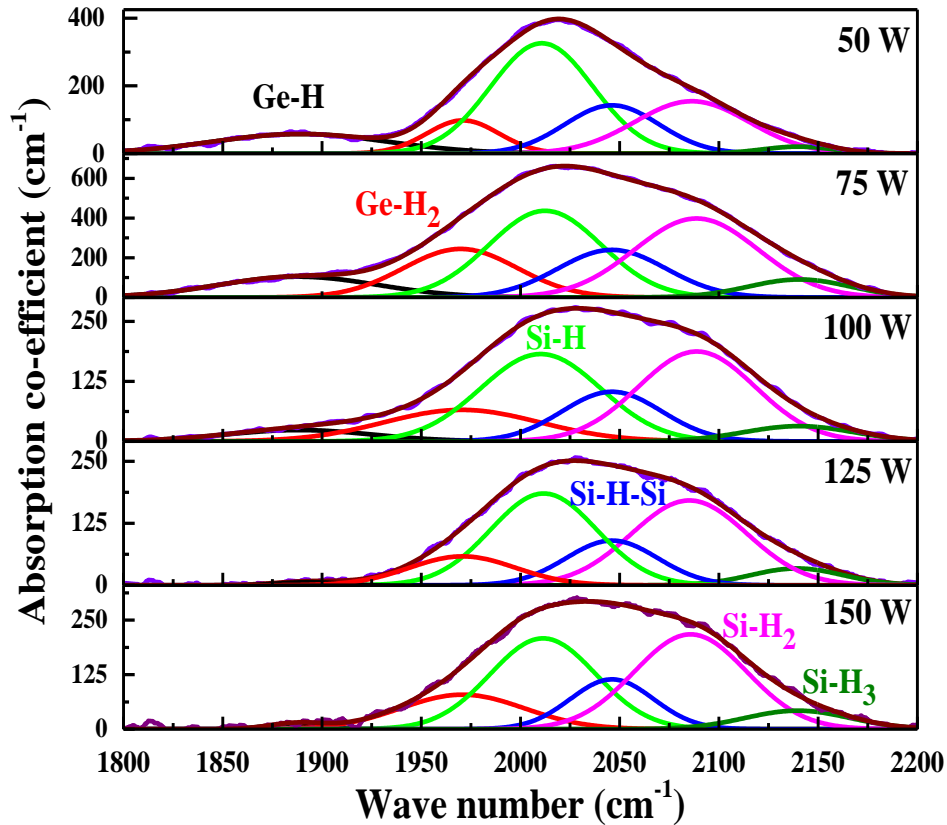


Fig. 5.13. IR absorption spectrum deconvoluted into Ge and Si monohydride and dihydride along with the bond-centred hydrogen, Si-H-Si, components with increase of RF power.

In **Fig. 5.14**, it is well observed that the Ge-structure factor, R_{Ge} , as well as Si-structure factor, R_{Si} , both have increased monotonically at elevated RF power. It is believed that lower structure factor i.e., lesser poly-hydride contribution implies lower defect density and voids in the film network. Very rapid and nearly linear increase in the magnitude of R_{Ge} identify over population of the network by poly-hydrides of Ge at elevated RF power. The R_{Si} on the other hand increases very fast corresponding to the initial crystallization in Si network at an increase in RF power from 50 to 75 W. However, increased dissociation of SiH₄ precursors at power ≥ 75 W facilitates enhanced

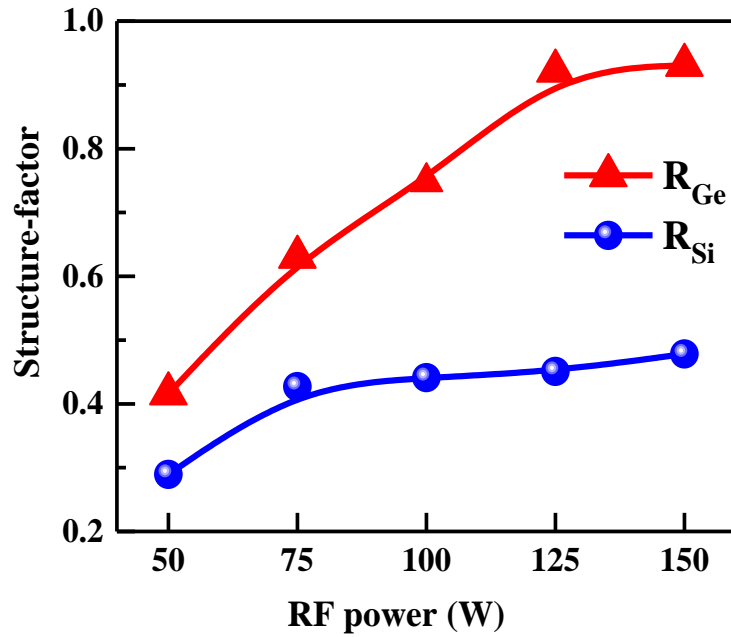


Fig. 5.14. Effect of varying RF powers changing the structure factors, R_{Si} and R_{Ge} , of the nc- $Si_{1-x}Ge_x:H$ films.

crystallization, maintaining R_{Si} virtually unchanged at a low magnitude around 0.43 ± 0.02 over a relatively large span of RF power up to 125 W. Corresponding linear reduction in the surface passivation index, S , in **Fig. 5.15** implies a better Si-crystallinity; however, the overall Si-Ge network deviates from recovering crystallinity because of the extremely high magnitude of R_{Ge} to 0.92 and above. The Ge-related radicals hold intense reactivity on the growing surface, however lower mobility compared to Si-related radicals which induce more inhomogeneity in the growth mechanism of SiGe alloy thin

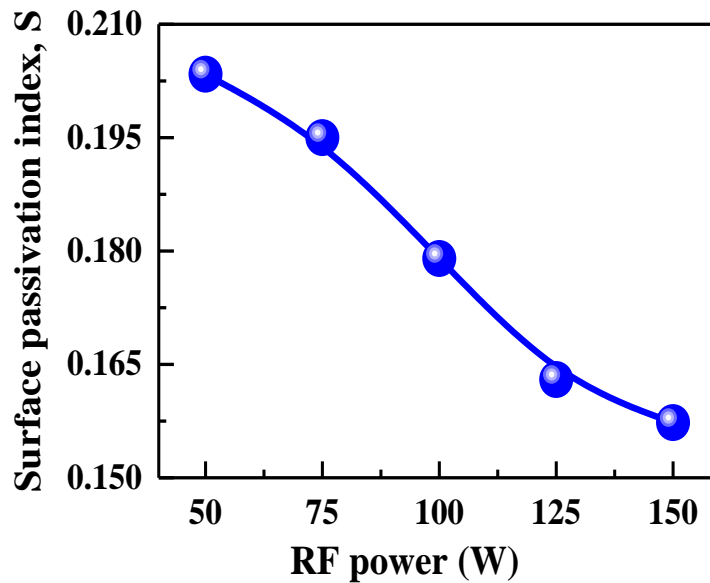


Fig. 5.15. Effect of applied RF powers changing the surface passivation index, S , in nc- $Si_{1-x}Ge_x:H$ network.

film with high Ge content in the grown film [54]. Accordingly, a moderate RF power is needed to attain an optimum nc-SiGe:H network at which moderate amount of Ge could be into the Si dominated network, organized in crystalline configuration with controlled amount of poly-hydrogenation.

The electrical characteristics of the nc-Si_{1-x}Ge_x:H alloy thin films have been studied with the temperature variable dc conductivity measurement with co-planar aluminum electrodes configuration. The temperature dependent dark conductivity $\sigma_D(T)$ data in **Fig. 5.16** follow the Arrhenius relationship [49,55]:

$$\sigma_D(T) = \sigma_0 \exp\left(\frac{-\Delta E}{K_B T}\right) \quad (5.11)$$

where ΔE remains the activation energy for electron conduction, K is the Boltzmann constant and σ_0 is the pre-exponential factor. Two distinct straight line plots of the data points identify lower and higher temperature regimes, respectively. Furthermore, typically the dominant amorphous and crystalline phases are contributed mostly by the where ΔE remains the activation energy for electron conduction, K is the Boltzmann constant and σ_0 is the pre-exponential factor. Two distinct straight line plots of the data points identify lower and higher temperature regimes, respectively. Furthermore, typically the dominant amorphous and crystalline phases are contributed mostly by the Ge-Ge and Si-Si network, respectively in the nc-SiGe:H ensemble. The variations in

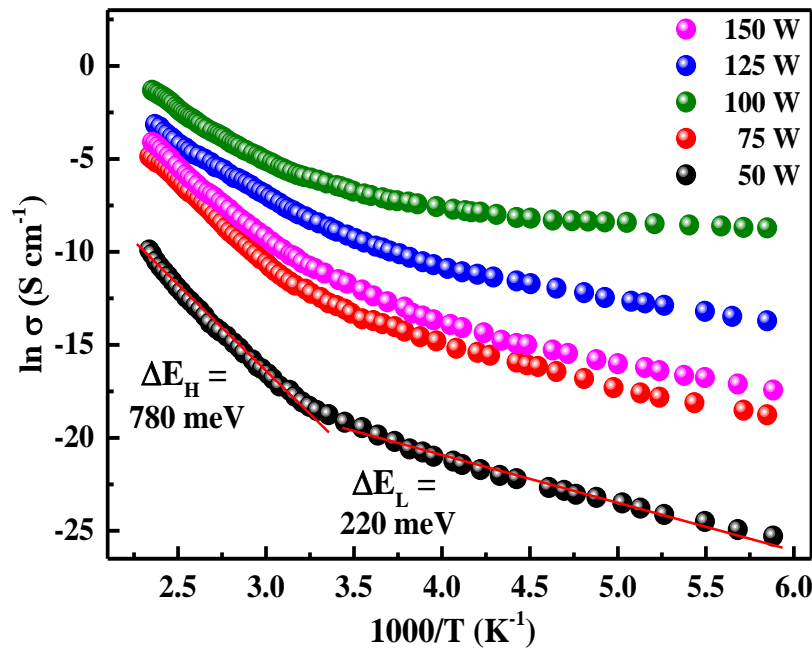


Fig. 5.16. Arrhenius plots of the dark conductivity (σ_D) of nc-Si_{1-x}Ge_x films deposited at different RF powers.

the activation energies corresponding to both the high-temperature and low-temperature regimes, ΔE_H and ΔE_L , respectively, are plotted with changes in the applied RF power, in **Fig. 5.17**. A sharp minimum attained in both ΔE_H and ΔE_L observed around $P=100$ W identify optimum crystallization in two different types of carrier activation at two separate temperature zones across around room temperature identifying a two-phase structure of the material e.g., amorphous and crystalline phases which make dominant contribution to the electrical conductivity of the ensemble in the network, accommodating substantial amount of Ge, occurring at 100 W of the applied RF power.

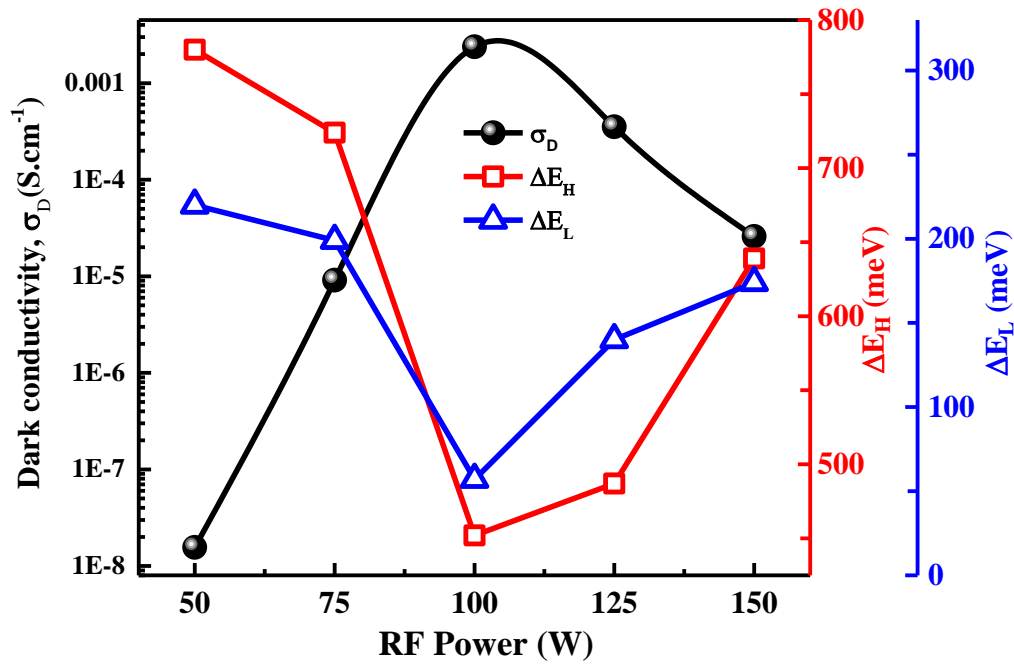


Fig. 5.17. Variation of the room temperature dark conductivity (σ_D) and changes in its activation energies at high temperature (ΔE_H) and low temperature (ΔE_L) regions, with applied RF power.

regimes, ΔE_H and ΔE_L , respectively, are plotted with changes in the applied RF power, in **Fig. 5.17**. A sharp minimum attained in both ΔE_H and ΔE_L observed around $P=100$ W identify optimum crystallization in two different types of carrier activation at two separate temperature zones across around room temperature identifying a two-phase structure of the material e.g., amorphous and crystalline phases which make dominant contribution to the electrical conductivity of the ensemble in the network, accommodating substantial amount of Ge, occurring at 100 W of the applied RF power. Corresponding to the systematic lowering in the activation energy, the room temperature dark conductivity of the films increased monotonically from $\sigma_D \sim 1.6 \times 10^{-8} S cm^{-1}$ for $P = 50$ W by several orders of magnitude to $\sigma_D \sim 2.38 \times 10^{-3} S cm^{-1}$ for $P = 100$ W. However,

on further increase in applied RF power, σ_D gradually decreased to $\sim 2.59 \times 10^{-5} \text{ S cm}^{-1}$ at $P = 150 \text{ W}$. Controlling the individual contribution of Si and Ge precursors influencing the structural changes and thereby improving the crystallinity of the SiGe alloy material and obtaining a reasonably high conductivity nc-SiGe network is a challenging task that has been attained on tuning the applied RF power at 100 W.

The pre-exponential factor for conductivity, σ_{0H} , estimated for the high temperature regime, has been plotted in a logarithmic scale against the corresponding activation energy ΔE_H , for the nc-SiGe:H films prepared at RF powers varying from 75

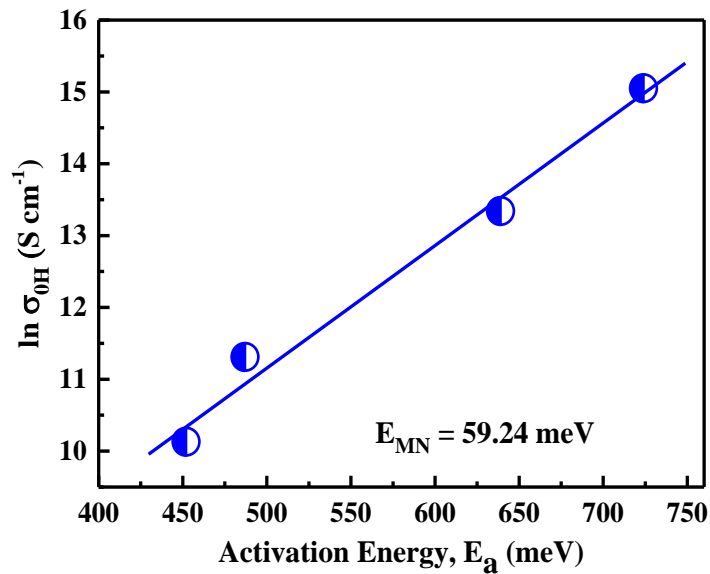


Fig. 5.18. Pre-exponential factor (σ_{0H}) of dark conductivity as function of high temperature activation energy ΔE_H .

to 150 W. **Fig. 5.18** shows the linear plot of the data points following the Meyer–Neldel rule (MNR) [45,56]:

$$\sigma_{0H} = \sigma_{00} \exp(\Delta E_H / E_{MN}) \quad (5.12)$$

The Meyer–Neldel characteristic energy, E_{MN} , has been estimated as $\sim 59.24 \text{ meV}$ and the good linearity obtained in the data points signifies maintaining a specific category of alloy network grown from the $(\text{SiH}_4 + \text{GeH}_4)$ plasma in RF-PECVD.

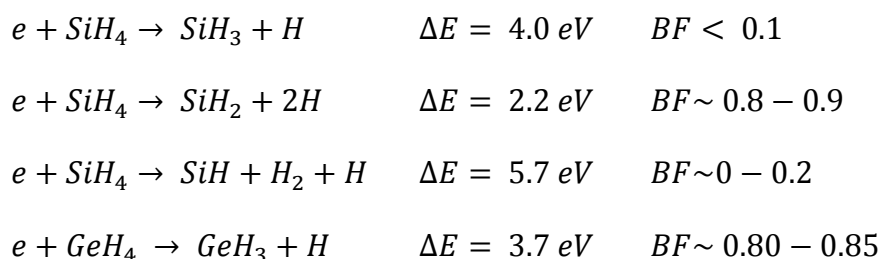
5.4 Discussion

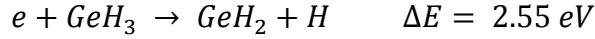
The overall growth of the nc-Si_{1-x}Ge_x:H alloy network is actually controlled by two simultaneous processes; physical deposition and the chemical etching of the weak bonds, which simultaneously proceed within the growth zone. The physical deposition

rate depends on few active parameters within the plasma, e.g., the amount of incident flux of active radicals near the substrate, availability of more sites for incident active radicals at the growing film surface as well as the probability of occupancy of the active radicals at the growth site [57]. The amount of incident flux of active radicals normally increases with increasing applied RF power which simultaneously enhances the atomic H density in the plasma that introduces the chemical etching of the weak bonds [58]. Moreover, chemical etching happens to be more effective on the amorphous dominated structures, along with concurrent development of crystallinity. At $P > 100$ W, atomic H, with its significantly high density available in the plasma, interacts with the loosely bonded amorphous component, eliminates those from the network and plays significantly in the structural orientation towards crystallization, leading to a lowering in the growth rate. At very high RF power, saturation of incident precursors and simultaneous increase in the atomic H etchants generated from the conversion of the precursors towards lower hydrides lead to significant etching of the network and a consequent lower growth rate of the material, as obtained in Fig. 5.2 [44].

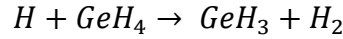
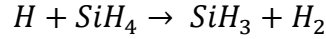
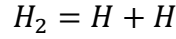
It is evident from the Raman study that the films gradually become more Si–Si populated from Ge–Ge dominated network on elevation of the applied RF power. The lower dissociation energy of GeH_4 than SiH_4 makes the Ge precursors to be dominant over Si precursors within the plasma at lower applied RF power. Accordingly, the Ge atoms preferentially incorporate into the alloy network in large proportion at very low power as $P = 50$ W. The films grown at RF power $P \geq 75$ W are basically a mixed-phase material wherein the Si-ncs are developed in the a-SiGe matrix. The gradual decrease in the FWHM (full width half maximum) of the Si–Si TO (transverse optical) peak with increasing RF power witnesses the decrease of amorphous content of the film with simultaneous development of the crystalline fraction.

Applied RF power has dramatic impact on nano-crystallization of the film network. The primary growth kinetics in $\text{SiH}_4/\text{GeH}_4$ mixed plasma is constituted by the dissociation of the source gases via following route [35, 59–61]:

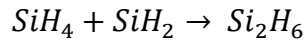
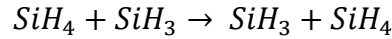




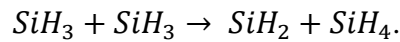
where ΔE presents the threshold energy and BF is the branching fractions of respective dissociation reactions. The dissociation also takes place via a second channel as:



The diluent H_2 gas creates the surface coverage by supplying atomic hydrogen [62]. In presence of adequate atomic H, the second channel becomes the dominant path for generation of tri-hydride radicals of both Si and Ge due to their lower threshold energy of reaction (-0.5 eV). When the atomic hydrogen (H) present in the plasma is not enough SiH_4 mainly dissociates via the first route; subsequently the SiH_2 and SiH_3 radicals would be dominantly available in the plasma as the threshold energy for the reactions producing SiH is larger. The reaction-lifetime of SiH_3 is longer than that of SiH_2 because SiH_3 itself forms SiH_3 reacting with SiH_4 again, while SiH_2 produce non-reactive Si_2H_6 by similar secondary reactions:



However, the density and flux of SiH_3 is self-controlled upon increasing RF power due to the fast radical recombination reaction:



At very low RF power of 50 W, the radicals generated in the plasma are dominated by GeH_3^+/GeH_3 compared to the SiH_3^+/SiH_3 species. Thus, the growing surface is accommodated mainly with GeH_3 radicals due to its higher growth rate within plasma and lower mobility compared to SiH_3 . Accordingly, the film grown at RF power 50 W happens to possess a Ge-dominated amorphous alloy network. At an increased applied RF power beyond a certain optimum, proportionate dissociation of the SiH_4 along with GeH_4 source gases into different chemical species within the plasma promotes the growth of Si-Ge network. The rates of reactions depend on the concentration of fragments and their energy distribution. Application of an optimized (minimum) RF

power changes the ion bombardment at the growth surface which increases surface diffusion length of the incident radicals leading to a homogeneous accumulation of Ge and Si related radicals near the growing surface. At different RF power, the interaction of the species reaching the substrate gets transformed due to their smaller mean free path within the plasma region. It is well understood that SiH_3 and GeH_3 are the main precursors in a hydrogen diluted silane-germane plasma which are mostly liable for the film growth [63], while lower hydride precursors like GeH_x and SiH_x ($1 \leq x \leq 2$) and ions, which are more reactive, contribute to the properties of the material [64,65]. SiH_x or GeH_x ($1 \leq n \leq 2$) have shorter lifetime than SiH_3 and GeH_3 , respectively and both these species possess shorter diffusion length on absorption surface of the growing network [66]. At RF power of 100 W, the radicals diffusing in the growing surface are mainly GeH_3^+ , SiH_3^+ and H which plausibly result in the growth of nanocrystalline network. A critical balance of available SiH_3 precursors to its lower hydride components, with the simultaneous presence of equivalent Ge-hydrides has promoted towards highest crystalline volume fraction with the largest grain size at this moderate RF power. At further elevated RF power, the population of lower hydride precursors, mainly of Ge, increases enormously. At high RF power Si-Si network becomes dominant, maintaining reasonable crystallinity; however, Ge content reduces drastically and breaking of weaker Ge-Ge bonds produces plenty of defects via creating dangling bonds and/or polyhydrides of Ge that hamper the growth of the nano-crystallites which ultimately induce lowering in the crystallinity with reduced average size of the nanocrystals.

High magnitude of the Ge content in the network in forms of both Ge-Ge and Si-Ge bands along with the significant presence of the Si-Si TO band at low RF power of 50 W is responsible for the significantly high optical absorption and narrow optical band gap. Crystallization in the Ge-Ge network at moderate RF power of 75 W and increased crystallinity in the Si-Si network at higher RF power of 100 W leads to further narrowing of the optical band gaps. Cao *et al.* inferred that the optical band gap of the nc-SiGe film reduces to a good extent with the presence of crystalline phase of Ge-associated network within the material [19]. However, deconvolution of the Ge-Ge as well as the Si-Ge modes in Raman spectra into their corresponding crystalline and amorphous counterparts appears to be extremely speculative and is virtually absent in the literature. Presently, the systematic widening of optical band gap for the films prepared at $P > 100$ W, results from the increasing relative population of Si bonds to Ge bonds in the Si-Ge alloy network

and hydrogen attachment to the Ge dangling bonds after breaking of the Ge–Ge bonds as well as poly-hydrogenation at the increased grain boundary of the highly crystallized Si–Si component of the network at elevated RF power [67].

The electronic transport of the charge carriers in nc-Si_{1-x}Ge_x:H films at room temperature happens to take place via the Si and Ge nanocrystals embedded in the amorphous SiGe:H matrix. At moderately increased RF power around 75 W and 100 W, increasing crystalline volume fraction, by virtue of either increased grain size or increasing number density of grains, reduces the average distance (L) between two adjacent crystallites and makes the percolation of carriers through the amorphous phase easier, leading to high electrical conductivity [68]. At very high RF power above 100 W defect formation due to Ge–Ge bond breaking may hamper transport of the charge carriers. In addition, increased amount of disordered grain boundary regions around the enhanced crystallinity functions like the charge carrier trapping centers and retards their motion during the tunneling transport, altogether leading to reduced electrical conductivity [69].

Cao *et al.* [19] reported the growth of $\mu\text{c-Si}_{1-x}\text{Ge}_x\text{:H}$ films with accompanying conductivity varying over the range $10^{-8} - 10^{-5} \text{ S cm}^{-1}$, however, surprisingly the conductivity of their films was identified to increase continuously with the increase in Ge content from 0 to a high magnitude of 60%. In addition, they could not report on the corresponding changes in the optical band gap of the material. Xu *et al.* [32] reported on the nanocrystallization of a-Si_{1-x}Ge_x:H thin films by the Ar plasma processing and demonstrated conductivity $\sim 4.3 \times 10^{-6} \text{ S cm}^{-1}$ for an optical band gap $\sim 1.06 \text{ eV}$ of the material. However, it was not a direct growth of the material, rather a two-step process wherein easier nanocrystallization was observed in a-Si_{1-x}Ge_x:H samples with higher germanium content. Tang *et al.* [31] reported the growth of $\mu\text{c-SiGe:H}$ films using increasing H₂/Ar ratio as the diluent to the (SiH₄ + GeH₄) plasma in PECVD and reported on conductivity varying over the range $1 \times 10^{-3} - 5 \times 10^{-4} \text{ S cm}^{-1}$ for changing optical band gap over 1.42 – 1.55 eV range, corresponding to decreasing Ge content from 0.53 to 0.28. It is interesting to note that while reducing Ge content and subsequently increasing optical band gap, the grossly enhanced crystallinity was accompanied by reduced electrical conductivity and associated increase in the activation energy which is exactly similar to that obtained in the present case while applying an RF power $\geq 125 \text{ W}$.

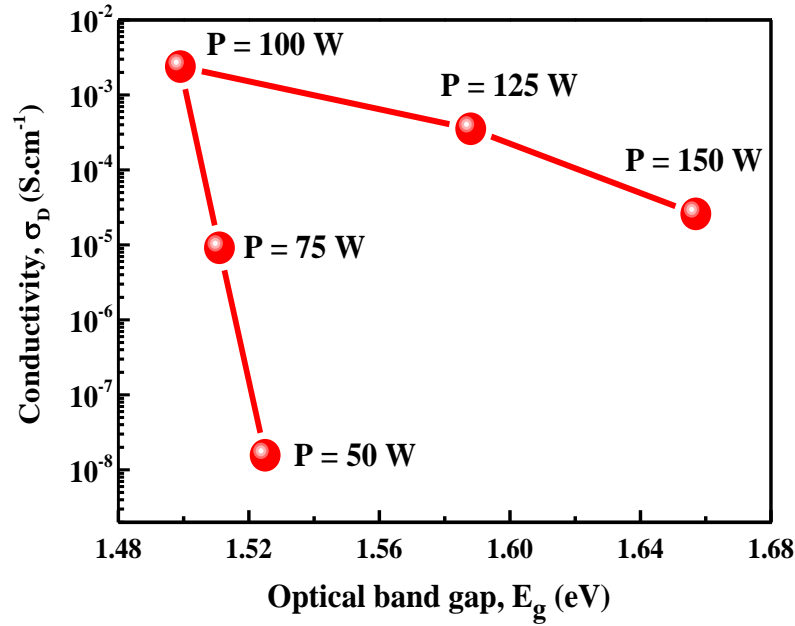


Fig. 5.19. Variations of the dark conductivity (σ_D) as function of the changing optical band gap of the SiGe:H network.

However, the most interesting feature realized in the present investigation is the narrowing of the optical band gap even at lower Ge content through moderate crystallization in the SiGe network and a simultaneous high electrical conductivity of the nc-SiGe:H films obtained at a high growth rate, via optimization of RF power applied to the capacitively coupled plasma (**Fig. 5.19**). The nc-SiGe:H films with a low $E_g = 1.499$ eV and a high $\sigma_D \sim 2.38 \times 10^{-3}$ S cm $^{-1}$ has been grown at a deposition rate ~ 9.5 nm/min from H $_2$ -diluted (SiH $_4$ + GeH $_4$) plasma in PECVD operated at an optimum RF power of 100 W at a growth temperature of 220 °C. A comparison of the available data on nanocrystallization in SiGe:H network grown by PECVD is presented in Table-4.1.

Table-5.1: Optoelectronic properties of μ c/nc-Si $_{1-x}$ Ge $_x$:H thin films:

Ref.	Dark conductivity (S cm $^{-1}$)	Optical band gap (eV)	Deposition rate (nm/min)	T $_s$ (°C)	Diluent gas
Ref. [19]	10 $^{-8}$ – 10 $^{-5}$	–	–	180 – 260	H $_2$
Ref. [32]	4.3 \times 10 $^{-6}$	1.06	–	230	Ar
Ref. [31]	1 \times 10 $^{-3}$ – 5 \times 10 $^{-4}$	1.42 – 1.55	3.2	250	H $_2$ /Ar
Present work	2.4 \times 10 $^{-3}$	1.499	9.5	220	H $_2$

5.5 Conclusion

Low temperature ($T_S \sim 220^\circ\text{C}$) growth of nc-SiGe:H thin films have been pursued using H_2 -diluted (by $\sim 96\%$) ($\text{SiH}_4 + \text{GeH}_4$) plasma in 13.56 MHz RF-PECVD, by varying the RF power applied to the parallel plate capacitively coupled electrodes of the reactor. It has been demonstrated that lower RF power produces Ge-dominated low band gap SiGe network with Si component in mostly amorphous configuration that leads to a low electrical conductivity. At high RF power Si-Si network becomes highly crystalline, however, Ge content reduces drastically; breaking of weaker Ge-Ge bonds creates defects via dangling bonds and increased grain boundary defects around Si nanocrystals together produce relatively wider band gap SiGe network with degraded electrical conductivity. However, the most interesting feature realized in the present investigation is the narrowing of the optical band gap even at lower Ge content through moderate crystallization in the SiGe network and a simultaneous high electrical conductivity of the nc-SiGe:H films obtained at a high growth rate, via optimization of the applied RF power to a moderate level. In such circumstances nanocrystallization of the network plays leading role in narrowing the optical band gap, overriding the effect arising out of the restricted presence of Ge. Under present parametric condition, a moderate RF power (100 W) is needed to attain an optimum configuration at which adequate amount of Ge could be accommodated to Si in its fairly crystalline structure, providing a narrow band gap ($E_g \sim 1.499\text{ eV}$) and highly conducting ($\sigma_D \sim 2.38 \times 10^{-3}\text{ S cm}^{-1}$) nc-SiGe:H alloy network at a growth rate $\sim 9.5\text{ nm/min}$, altogether appropriate for device applications, e.g., as an absorber layer at the middle or bottom sub-cell of tandem-structure nc-Si solar cells.

5.6 References

- [1] J. Yang, A. Banerjee, S. Guha, Sol. Energy Mater. Sol. Cells 78 (2003) 597–612.
- [2] F. Schindler, A. Fell, R. Müller, J. Benick, A. Richter, F. Feldmann, P. Krenckel, S. Riepe, M.C. Schubert, S.W. Glunz, Sol. Energy Mater. Sol. Cells 185 (2018) 198–204.
- [3] T. Yoshida, K. Maruyama, O. Nabeta, Y. Ichikawa, H. Sakai, Y. Uchida, Proceedings of the 19th IEEE Photovoltaics Specialists Conference, (1987) pp. 1095–1000.

- [4] A.K. Barua, A. Sarker, A.K. Bandyopadhyay, D. Das, S. Ray, Proc. of 28th IEEE PV Specialists Conf., (Anchorage Alaska, USA, September 17-22, 2000) pp. 829–832.
- [5] Q. Ren, S. Li, S. Zhu, H. Ren, X. Yao, C. Wei, B. Yan, Y. Zhao, X. Zhang, Sol. Energy Mater. Sol. Cells 185 (2018) 124–129.
- [6] J. Yang, A. Banerjee, S. Guha, Appl. Phys. Lett. 70 (1997) 2975–2977.
- [7] D. Das, S.C. De, S. Ray, A.K. Batabyal, A.K. Barua, J. Non-Cryst. Solids 114 (1989) 552–554.
- [8] D. Das, S.C. De, S. Ray, A.K. Barua, J. Non-Cryst. Solids 128 (1991) 172–182.
- [9] H. Keppner, J. Meier, P. Torres, D. Fischer, A. Shah, Appl. Phys. A 69 (1999) 169–177.
- [10] M. Berginski, B. Rech, J. Hupkes, G. Schope, M.N. van den Donker, W. Reetz, T. Kilper, M. Wuttig, in 21st European Photovoltaic Solar Energy Conference, 2006, pp. 1539.
- [11] G. Ganguly, T. Ikeda, T. Nishimiya, K. Saitoh, M. Kondo, A. Matsuda, Appl. Phys. Lett. 69 (1996) 4224–4226.
- [12] T. Matsui, H. Jia, M. Kondo, Progress in Photovoltaics: Research and Applications 18 (2010) 48–53.
- [13] T. Matsui, C.W. Chang, M. Kondo, K. Ogata, M. Isomura, Appl. Phys. Lett. 91 (2007) 10211.
- [14] T. Matsui, C.W. Chang, T. Takada, M. Isomura, H. Fujiwara, M. Kondo, Applied Physics Express 1 (2008) 031501.
- [15] A. Fedala, C. Simon, N. Coulon, T. Mohammed-Brahim, M. Abdeslam, A.C. Chami, Phys. Status Solidi C 7 (2010) 762–765.
- [16] J. Ni, Q. Liu, J. Zhang, J. Ma, H. Wang, X.D. Zhang, Y. Zhao, Sol. Energy Mater. Sol. Cells 126 (2014) 6–10.
- [17] C.W. Chang, T. Matsui, M. Kondo, J. Non-Cryst. Solids 354 (2008) 2365–2368.
- [18] T. Matsui, K. Ogata, C.W. Chang, M. Isomura, M. Kondo, J. Non-Cryst. Solids 354 (2008) 2468.
- [19] Y. Cao, Y. Liu, J. Zhou, Y. Wang, J. Ni, J. Zhang, Sol. Energy Mater. Sol. Cells 151 (2016) 1–6.
- [20] T. Matsui, K. Ogata, M. Isomura, M. Kondo, J. Non-Cryst. Solids 352 (2006) 1255–1258.

- [21] T. Matsui, M. Kondo, *Appl. Phys. Lett.* 89 (2006) 142115.
- [22] G.H. Bauer, F. Voigt, R. Carius, M. Krause, R. Bruggemann, T. Unold, *J. Non-Cryst. Solids* 299–302 (2002) 153–157.
- [23] S. Miyazaki, H. Takahashi, H. Yamashita, M. Narasaki, M. Hirose, *J. Non-Cryst. Solids* 148 (2002) 299-302.
- [24] L. Zhang, J. Zhang, Z. Shang, Z. Hu, X. Geng, Y. Zhao, *Chin. Phys. B* 17 (2008) 3448–3452.
- [25] H. Shirai, Y. Fukuda, T. Nakamura, K. Azuma, *Thin Solid Films* 350 (1999) 38–43.
- [26] M. Krause, H. Stiebig, R. Carius, U. Zastrow, H. Bay, H. Wagner, *J. Non-Cryst. Solids* 299–302 (2002) 158–162.
- [27] Y. Huang, H. Hsu, S. Liang, C. Hsu, C. Tsai, *Int. J. Photoenergy* 2014 (2014) 579176.
- [28] M. Isomura, K. Nakahata, M. Shima, S. Taira, K. Wakisaka, M. Tanaka, S. Kiyama, *Sol. Energy Mater. Sol. Cells* 74 (2002) 519–524.
- [29] S. Kim, C. Park, J.C. Lee, J.S. Cho, Y. Kim, *C. Appl. Phys.* 13 (2013) 457–460.
- [30] L. Zhang, J. Zhang, X. Zhang, Y. Cao, Y. Zhao, *Thin Solid Films* 520 (2012) 5940–5945.
- [31] Z. Tang, W. Wang, D. Wang, D. Liu, Q. Liu, D. He, *J. Alloys Compd.* 504 (2010) 403–406.
- [32] R. Xu, W. Li, J. He, Y. Sun, Y.D. Jiang, *J. Non-Cryst. Solids* 365 (2013) 37–41.
- [33] S. Fan, Q. Guo, X. Wang, W. Yu, G. Fu, *Cryst. Res. Technol.* 53 (2018), 1700141.
- [34] J.K. Rath, F.D. Tichelaar, R.E.I. Schropp, *Sol. Energy Mater. Sol. Cells* 74 (2002) 553–560.
- [35] D. Das, *Solid State Phenomena (Special Volume on Hydrogenated Amorphous Silicon)* (Scitech Publication, Switzerland, 1995) pp.227–258.
- [36] B. Sain, D. Das, *Sci. Adv. Matter.* 5 (2013) 188–198.
- [37] S. Kim, C. Park, J.C. Lee, J.S. Cho, Y. Kim, *Thin Solid Films* 534 (2013) 214–217.
- [38] R. Cariou, J. Tang, N. Ramay, R. Ruggeri, P. Roca i Cabarrocas, *Sol. Energy Mater. Sol. Cells* 134 (2015) 15–21.

- [39] N. Reininghaus, M. Kellermann, K. von Maydell, C. Agert, *EPJ Photovoltaics* 6 (2015) 65301.
- [40] G.K. Williamson, W.H. Hall, *Acta Metall.* 1 (1953) 22–31.
- [41] D. Kar, D. Das, *J. Mater. Chem. A* 1 (2013) 14744–14753.
- [42] J. Tauc, R. Grigorovici, A. Vancu, *Phys. Status Solidi (b)* 15 (1966) 627–637.
- [43] K. Bhattacharya, D. Das, *J. Phys. D: Appl. Phys.* 41 (2008) 155420.
- [44] D. Raha, D. Das, *Appl. Surf. Sci.* 276 (2013) 249–257.
- [45] D. Das, B. Sain, *J. Appl. Phys.* 114 (2013) 073708.
- [46] J.A.P. Taborda, J.J. Romero, B. Abad, M. Muñoz-Rojo, A. Mello, F. Briones, M.S. Martin Gonzalez, *Nanotechnology* 27 (2016) 175401.
- [47] C.J. Fang, K.J. Gruntz, L. Ley, M. Cardona, F.J. Demond, G. Muller, S. Kalbitzer, *J. Non-Cryst. Solids* 35-36 (1980) 255–260.
- [48] M. Cardona, *Phys. Status Solidi B* 118 (1983) 463.
- [49] D. Das, *J. Phys. D: Appl. Phys.* 36 (2003) 2335.
- [50] S. Samanta, D. Das, *Physica E: Low-dimensional Systems and Nanostructures* 103 (2018) 99–109.
- [51] G. Lucovsky, *J. Non-Cryst. Solids* 76 (1985) 173.
- [52] P. Mondal, D. Das, *RSC Adv.* 5 (2015) 54011–54018.
- [53] S. Samanta, D. Das, *J. Phys. Chem. Solids* 105 (2017) 90–98.
- [54] A. Matsuda, M. Koyama, N. Ikuchi, Y. Imanishu, K. Tanaka, *Jpn J. Appl. Phys.* 25 (1986) L54–L56.
- [55] K.D. Mackenzie, J.R. Eggert, D.J. Leopold, Y.M. Li, S. Lin, W. Paul, *Phys. Rev. B* 31 (1985) 2198.
- [56] R.W. Lof, R.E.I. Schropp, *J. Appl. Phys.* 108 (2010) 063714.
- [57] Y.P. Chou, S.C. Lee, *J. Appl. Phys.* 83 (1998) 4111-4123.
- [58] D. Das, *Sol. Energy Mater. Sol. Cells* 81 (2004) 155-168.
- [59] S. Hazra, A.R. Middy, S. Ray, *J. Phys. D: Appl. Phys.* 29 (1996) 1666–1674.
- [60] F.J. Kampas, *Semiconductors Semimetals A* 21 (1984) 153–177.
- [61] J.R. Doyle, D.A. Doughty, A. Gallagher, *J. Appl. Phys.* 71 (1992) 4727.
- [62] D. Raha, D. Das, *J. Phys. D: Appl. Phys.* 41 (2008) 085303.

- [63] M. Chakraborty, A. Banerjee, D. Das, *Physica E* 61 (2014) 95–100.
- [64] A. Matsuda, *Jpn. J. Appl. Phys.* 43 (2004) 7909.
- [65] J. Perrin, T. Broekhuizen, *Appl. Phys. Lett.* 50 (1987) 433.
- [66] J.P.M. Schmitt, *J. Non-Cryst. Solids* 59–60 (1983) 649.
- [67] P. Roca i Cabarrocas, *Phys. Stat. Sol. (c)* 1 (2004) 1115–1130.
- [68] M. Jana, D. Das, S.T. Kshirsagar, A.K. Barua, *Jpn. J. Appl. Phys.* 38 (1999) L1087.
- [69] P. Dutta, M. Kumar, M. Rathi, S. P. Ahrenkiel, S. Paul, D. Galipeau, V. Bommisetty, *J. Nanosci. Nanotech.* 13, (2013) 1-10.



Chapter 6

Optimal H₂-dilution playing key role in accomplishing significant nanocrystallinity with both Si and Ge moieties in SiGe nanocomposite thin film network

6.1 Introduction

Silicon-based thin films are widely commercialized since their matured cost-effective and large-module production technology [1,2]. The tactical use of different Si-alloy thin films with different optical band gaps in the tandem-structure multi-junction nanocrystalline silicon (nc-Si) thin film solar cells has enabled the efficient utilization of a wider range of the solar spectrum, as well as in improving the device performance, stabilizing the light-induced degradation [3–5]. Intrinsic nc-Si and amorphous silicon germanium (a-SiGe) thin films have been used for many years at the bottom layer of the tandem solar cells [6–9]. However, nc-Si possesses a poor optical absorption coefficient in the infrared part of the solar radiation [10], and a-SiGe has poor stability against exposure to light [11]. With time, nanocrystalline silicon–germanium (nc–SiGe:H) alloy thin film has come up as a suitable alternate material for the bottom-cell absorber-layer in multi-junction nc-Si solar cells, as it meets the optimal requirement of improved infrared absorption and good stability under light exposure [12–16]. Eventually, Si-Ge alloy films are in potential use in infrared detectors [17], biomedical applications [18], micro-electromechanical systems (MEMS) [19], near-infrared light-emitters [20], and devices with 3D structures [21–24]. However, the major limitation in this binary mixed-phase alloy lies in its rapid deterioration of the optoelectronic qualities at an increased amount of Ge-inclusion. Overpopulation of dangling bonds and the non-uniform distribution of H-bonding to a fraction of its two-phase heterostructure that involves two separate transport paths, and ultimately the dominant amorphization of the film network are the factors responsible for weakening the optoelectronic properties [25,26].

In the process of film's growth in PECVD, rapid accumulation of Ge-hydrides at the film growth sites causes the extensive residence of Ge atoms in the film through the rapid dissociation of the precursor gas GeH₄ because of its lower dissociation energy over SiH₄ [27–29]. In the literature, it has been deliberated that the H₂ dilution method is adopted as one of the finest techniques to improve the film quality in the plasma synthesis of the a-SiGe [30–32], nc-Si:H [33–35], and other nc-Si-alloys [36–39]. Several investigations have reported that significant H₂ dilution acts beneficially in sustaining the nanocrystalline phase in the SiGe alloy network [40–42]. Furthermore, an increase in atomic H in the plasma with additional H₂ dilution is expected to enhance the atomic H coverage at the vicinity of the growth surface that helps to enhance the surface diffusion

lengths of the adsorbed precursors and facilitate those reaching the favorable growth sites at lower energy configurational positions in the film network. [43]. In addition, atomic H can etch out the weak and strained bonds in the Si alloy network, improving its stability [44].

The purpose of the present study concerns the investigation on the impact of H₂ dilution in the (SiH₄ + GeH₄)-plasma in PECVD on the low-temperature growth of Si_{1-x}Ge_x thin films via a detailed characterization of their structural and optoelectronic properties. The variations of the bonding configuration, composition, and microstructures of the Si_{1-x}Ge_x films have been studied systematically. Their interrelationships with the optical and electrical properties in changing the crystallization behavior, as influenced by the varying H₂ dilution during growth, are investigated.

6.2 Experimental details

A set of Si_xGe_{1-x} films were prepared using silane (SiH₄), germane (GeH₄) and hydrogen (H₂) gases in a capacitively-coupled PECVD (13.56 MHz) system, maintaining a working pressure of 1.2 Torr. The films were grown on glass, carbon-coated copper TEM grid (Pacific Grid-Tech, USA) and *p*-type *c*-Si substrates, using applied RF power of 100 W, at a low growth temperature (T_S) ~220 °C. The samples were grown with the individual flow rates of SiH₄ ~1.8 sccm, GeH₄ ~0.2 sccm, and varying the hydrogen dilution ratio $R(\text{H}_2) = [\text{H}_2] / [\text{GeH}_4 + \text{SiH}_4]$ from 12.5 to 50. The initial base vacuum in the PECVD reactor before plasma ignition was retained at ~10⁻⁶ Torr.

The crystallinity of the grown film network was estimated using a Raman spectrometer (Renishaw inVia) with an Ar⁺ laser (wavelength ~514 nm) at a low power density of ~2 mW/cm². The crystallographic orientations of the films were determined using a high-resolution X-ray Bragg diffraction set-up (Rich Seifert 3000P) and Cu-K_α radiation of wavelength 1.541 Å. The film's chemical bonding configurations and microstructures were investigated using Nicolet Magna-IR 750 FTIR spectrometer. The optical absorption and transmission data were recorded using a Hitachi 330, Japan UV-VIS-NIR double-beam spectrophotometer. The film's microstructures were obtained using JEOL JSM 2010 UHR-FEG high-resolution transmission electron microscope, operating at 200 kV. The dark conductivity of the films at different temperatures was measured within a cryostat with its base vacuum of ~10⁻⁶ Torr, using coplanar parallel Al electrodes with an inter-electrode gap of 1.0 mm and a Keithley 6517A electrometer.

6.3 Results

6.3.1 Raman analysis

The Raman spectra of the SiGe thin films, prepared at various H₂-dilution ratios, $R(\text{H}_2) = 12.5 - 50$, at fixed flow rates of SiH₄ (1.8 sccm) and GeH₄ (0.2 sccm), are presented in **Fig. 6.1(a)**. Each spectrum identifies three significant peaks at $\sim 260 \text{ cm}^{-1}$, 400 cm^{-1} and 500 cm^{-1} , which correspond to the Ge-Ge, Si-Ge and Si-Si bond-vibrations, respectively [25,45].

The presence of Ge-Ge broad peaks with modest intensity and the corresponding much sharper and intense Si-Si peaks identifies that the prepared Si_{1-x}Ge_x films are primarily composed of mostly the Si-dominated networks. In **Fig. 6.1(b)**, the Raman spectrum of the film prepared at $R(\text{H}_2) = 50$ has been deconvoluted into several satellite

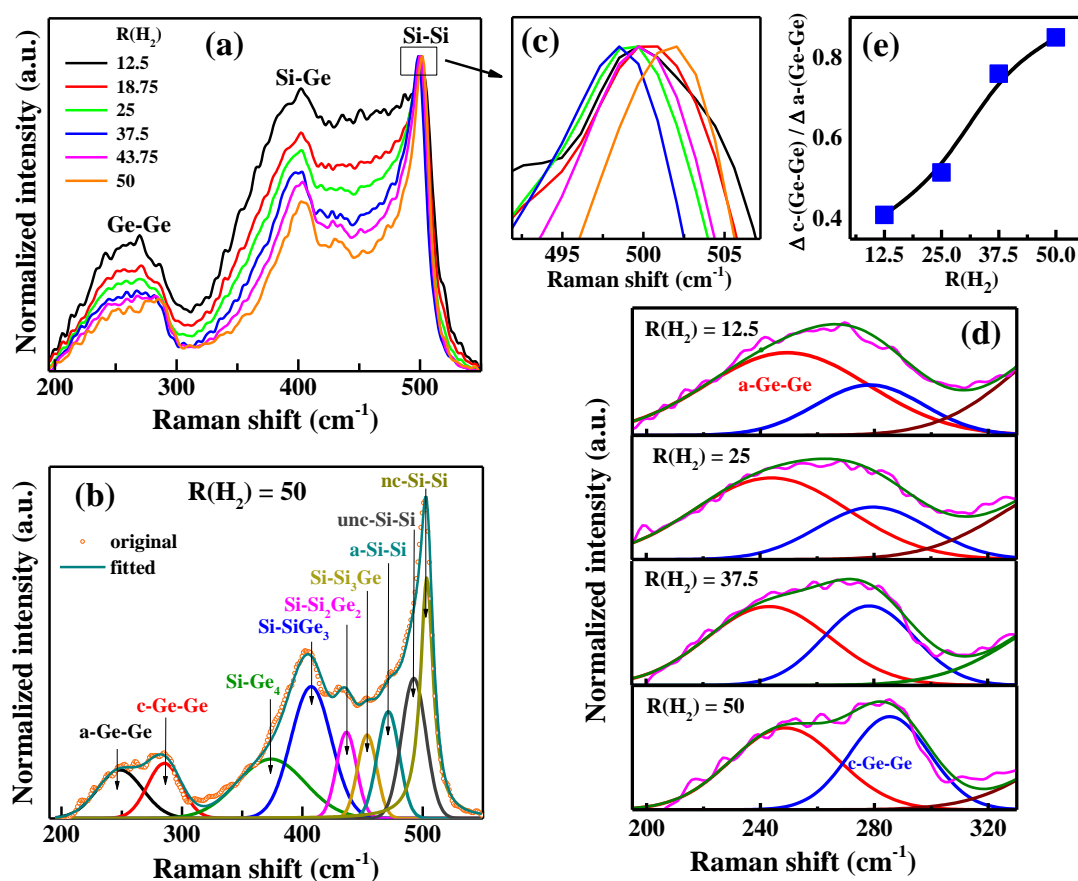


Fig. 6.1. (a) Raman spectra of the SiGe thin films prepared at different hydrogen dilution, $R(\text{H}_2)$. (b) Deconvoluted Raman spectrum of the sample grown at $R(\text{H}_2) = 50$, into satellite components. (c) Magnified view of (494-506) cm^{-1} Raman peaks. (d) Deconvolution of the (195-325) cm^{-1} Raman peaks, showing the crystalline and amorphous Ge-Ge components. (e) Variations in the integrated area ratios of the c-(Ge-Ge) to a-(Ge-Ge) components.

components. In the lower wavenumber range, the Ge-Ge band identifies the a-Ge-Ge component at $\sim 249\text{ cm}^{-1}$ and the nc-Ge-Ge component at $\sim 285\text{ cm}^{-1}$. In the higher wavenumber range, the Si-Si band identifies the a-Si-Si component at $\sim 471\text{ cm}^{-1}$, the nc-Si-Si component at $\sim 503\text{ cm}^{-1}$ and an intermediate component at $\sim 493\text{ cm}^{-1}$ corresponding to its ultra-nanocrystalline (unc-Si) component [46,47]. While at an intermediate wavenumber range the Si-Ge band is comprised of different Si-Si_nGe_{4-n} bonding configurations, where components with increasing n-values correspond to the Si-rich constituents and those have their vibrational positions at relatively higher wavenumbers [28]. The Si-Ge₄ and Si-SiGe₃ bonding configurations, respectively at $\sim 375\text{ cm}^{-1}$ and $\sim 398\text{ cm}^{-1}$, have contributed mainly to the Si-Ge band at the intermediate wavenumber range [48]. The gradual peak shift in the corresponding satellite components in the asymmetric Si-Ge band occurs due to differences in the behavior of Si-Ge clusters present in the film matrix with Si at the center (Si-Ge₄, Si-SiGe₃, Si-Si₂Ge₂, Si-Si₃Ge) [49].

Looking at the extension of the lower wavenumber section of the Si-Si peak it is evident that the intensity reduced monotonically on increased R(H₂). However, the tips of the spectra, presented with an enlarged view in **Fig. 6.1(c)**, demonstrate that its width narrowed down significantly and the peak position initially red-shifted for the initial increase in R(H₂), while it ultimately blue-shifted along with a gradual narrowing of its width for R(H₂) above 37.5. Significant narrowing and the red-shift signify a rapid elimination of the a-Si component and growth of the ultra-nanocrystalline (unc-Si) fraction around 493 cm^{-1} , while further gradual narrowing and the corresponding blue-shift attributes the growth of prominent nanocrystalline (nc-Si) fraction around 503 cm^{-1} at an elevated R(H₂) above 37.5. The corresponding positions are different (at lower wavenumbers) from the regular sites because of the influence of the Ge atoms as the nearest neighbor. Careful observation similarly identifies that the Si-Ge and Ge-Ge peaks also systematically blue shifted along with steadily reducing in intensity as well as peak-width, with the gradual increase in R(H₂), because of consistent nanocrystallization.

Fig. 6.1(d) demonstrates a comparison between films prepared at different R(H₂), in terms of relative strengths of the deconvoluted satellite components signifying the c-(Ge-Ge) and a-(Ge-Ge) bonding vibrations. The variations in the ratios of the integrated areas under individual components, $\Delta\text{c-(Ge-Ge)} / \Delta\text{a-(Ge-Ge)}$, as plotted in **Fig. 6.1(e)**, clearly demonstrates a gradual and significant increase of the crystalline fraction in the

Ge component of the Si-Ge alloy network from 0.41 to 0.85, with the increase in R(H₂) from 12.5 to 50 in the plasma.

6.3.2 XRD analysis

The X-ray diffraction pattern of the Si_{1-x}Ge_x:H films are presented in **Fig. 6.2(a)** that detects a systematic modification of the structural network from purely amorphous to highly crystalline configuration with the gradual increase in R(H₂). There was hardly any sign of crystallinity in the films prepared with low H₂-dilution ratio, R(H₂) = 12.5. Very tiny peaks at 2θ ~ 27.9° and 46.5° were appeared with the increase in R(H₂) to 18.75. With further increase in R(H₂) to 25, strong XRD peaks were appeared at 2θ ~ 28.1°, 46.7° and 55.5°, which are associated to the <111>, <220>, and <311> crystallographic orientations of Si, respectively. The intensity and sharpness of all the

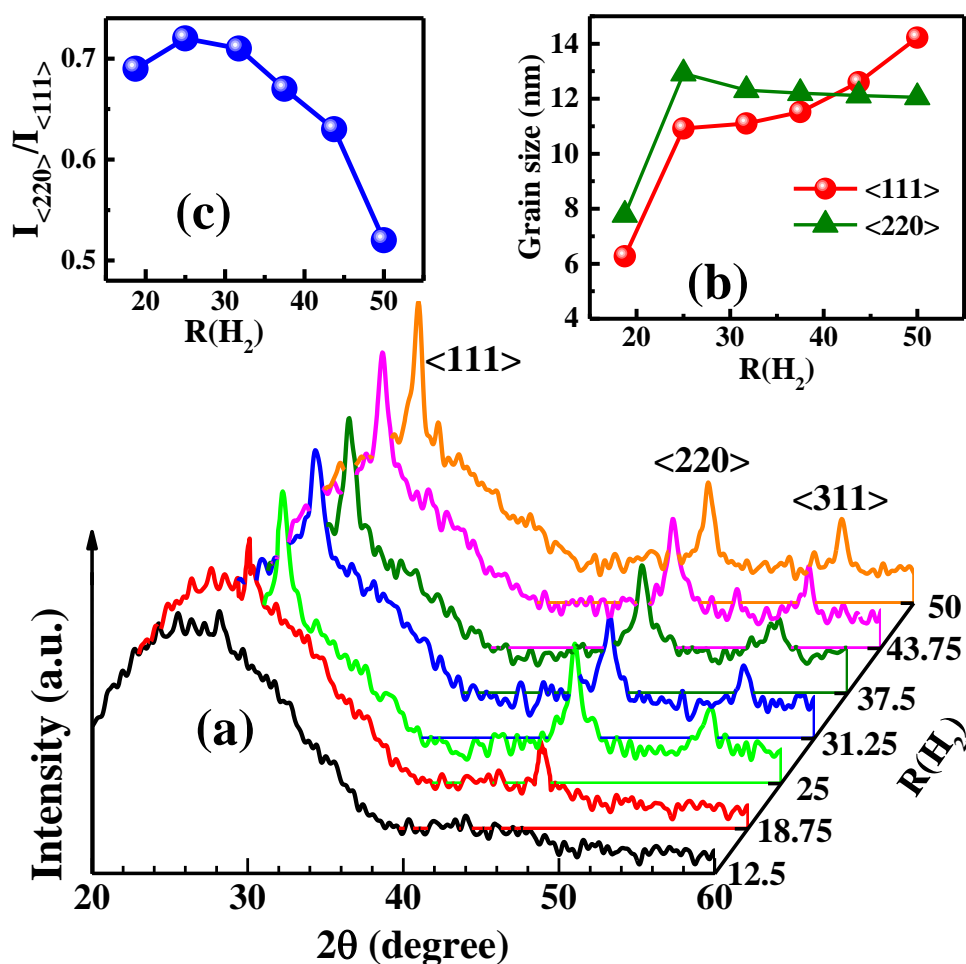


Fig. 6.2. (a) XRD pattern of the SiGe films prepared at different hydrogen dilution, R(H₂). (b) Changes in the grain size of the Si-ncs in <111> and <220> orientations and (c) $I_{\langle 220 \rangle} / I_{\langle 111 \rangle}$ ratio, with the change in R(H₂).

peaks increased on the sequential escalation in R(H₂), signifying perpetual crystallization of the network induced by the prevailing association of atomic H in the plasma. All the XRD peaks were found to systematically shift towards a higher 2 Θ value at increased R(H₂). The average size of the crystalline grains of different orientations were calculated from the corresponding peak positions and their full width at half maxima (FWHM), using Debye-Scherrer's formula [47]:

$$d = \frac{0.9\lambda}{\beta \cos\theta} \quad (6.1)$$

The crystalline grains of <111> orientation increased from 6.3 nm to 14.2 nm with increase in the R(H₂) from 18.75 to 50, while that of <220> orientation changed sharply from 7.8 nm to 12.9 nm, for increasing R(H₂) from 18.7 to 25, after which it decreased marginally and attained a virtual saturation at increased R(H₂), as observed in **Fig. 6.2(b)**. **Fig. 6.2(c)** shows that the intensity ratios of <220> and <111> become maximum for R(H₂) = 25, and then decreased with increase in R(H₂).

6.3.3 TEM analysis

The detailed microstructural characteristics of the prepared nc-SiGe thin films were explored via the ultra-high-resolution transmission electron microscopy (UHR-TEM). The HR-TEM image of the film prepared at R(H₂) = 25, shown in **Fig. 6.3(a-i)**, identifies a homogeneous distribution of tiny nanocrystals dispersed in the amorphous matrix. The transmission electron diffraction (TED) pattern in the inset of **Fig. 6.3(a-i)** reveals distinguished bright rings signifying the growth of a substantial volume fraction of nanocrystals with <111>, <220>, and <311> crystallographic orientations in the film [50,51]. **Fig. 6.3(a-ii)** shows the UHR-TEM image, identifying an isolated Si-nanocrystal of <220> orientation with interplanar separation of ~ 0.193 nm. Elemental mapping by energy-dispersive X-ray spectroscopy shows in **Fig. 6.3(a-iii)** the peaks with different intensities, associated to Si of ~95.97 at.% and Ge of ~4.03 at.%, and signifying the growth of a Si-rich nc-Si_{1-x}Ge_x alloy film network. The TEM micrograph of film prepared at R(H₂) = 50, presented in **Fig. 6.3(b-i)**, reveals a relatively dense nc-SiGe network, with its TED pattern at the inset identifying more prominent circular rings, principally with <111> orientation of c-Si. In **Fig. 6.3(b-ii)**, the micrograph in higher magnification identifies the Si-nanocrystals dispersed within an amorphous tissue. The corresponding inter-planar separation of ~0.247 nm corresponds to the <111>

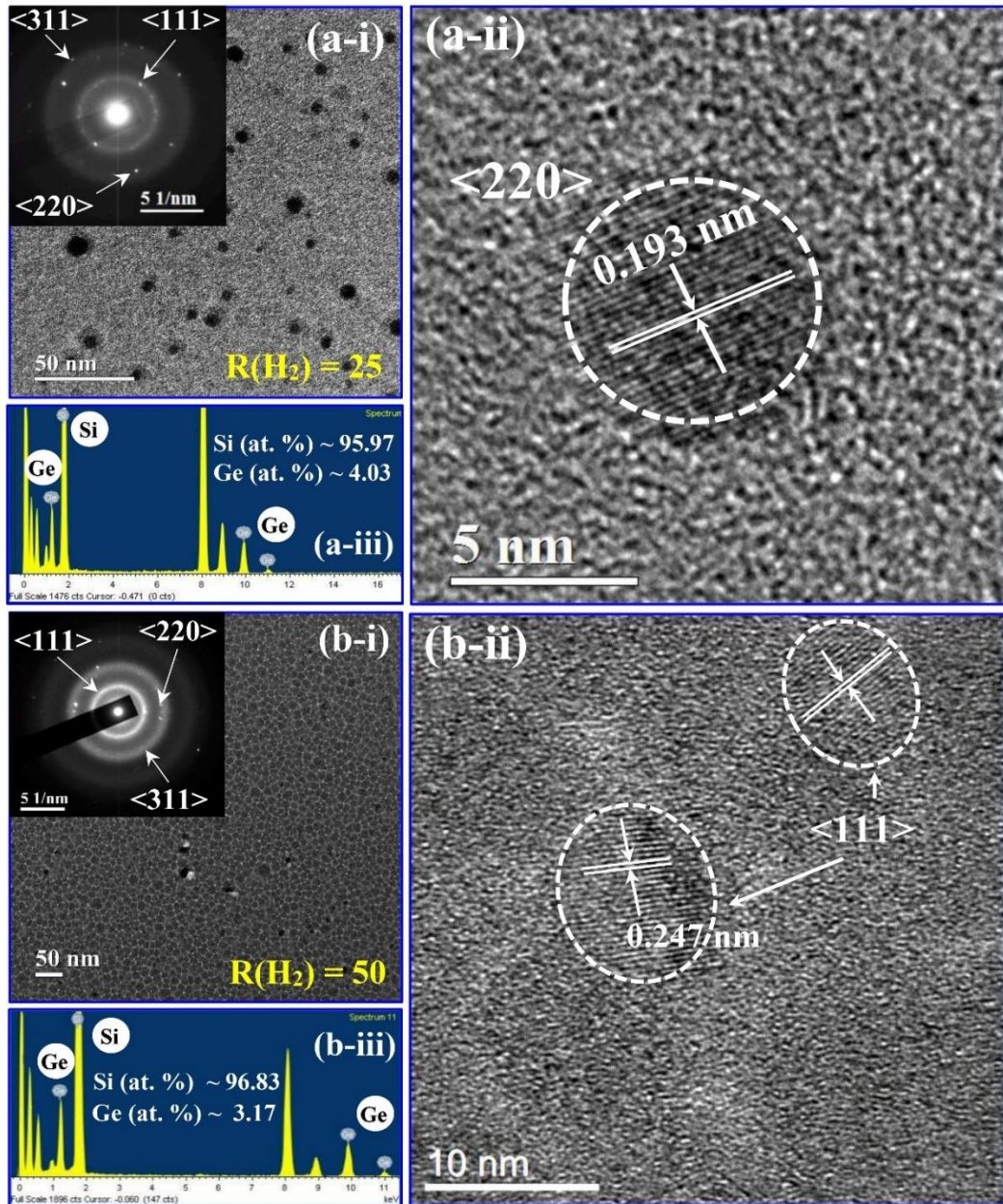


Fig. 6.3. The TEM image of the nc-SiGe thin film deposited at (a-i) $R(H_2) = 25$ and (b-i) $R(H_2) = 50$ with the corresponding transmission electron diffraction (TED) pattern at the inset. (a-ii) and (b-ii) are the corresponding HR-TEM image showing well-defined c-Si nanocrystals in different orientations. (a-iii) and (b-iii) are the corresponding EDAX spectra, identifying the presence of Si and Ge with individual intensities.

crystallographic planes of the Si nanocrystals of larger size and higher density, as also supported by the relatively bright circle in the related TED pattern in the inset of **Fig. 6.3(b-i)**. Corresponding elemental mapping of the EDX data in **Fig. 6.3(b-iii)** shows the peaks with different intensities, associated to Si of ~96.83 at.% and Ge of ~3.17 at.%,

signifying the growth of the Si-rich nc-Si_{1-x}Ge_x alloy film network with relatively less amount of Ge-content at higher R(H₂).

6.3.4 Electrical Properties

The impact of increasing the H₂-dilution on the electrical transport mechanism of the nc-SiGe thin films was studied via measuring the dark conductivity (σ_D) at different temperatures. The activation energies (E_a) were estimated from the slopes in the Arrhenius-plots, presented at the inset of **Fig. 6.4**, following the relation [36]:

$$\sigma_D = \sigma_0 \exp\left(\frac{-E_a}{KT}\right) \quad (6.2)$$

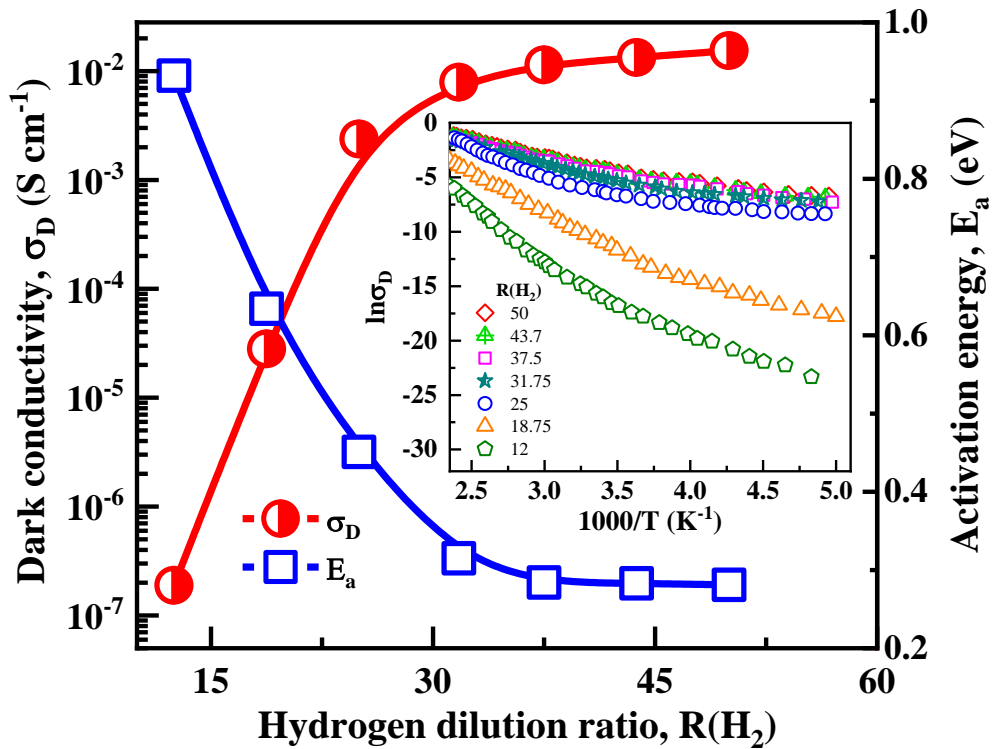


Fig. 6.4. Variation of dark conductivity (σ_D) and activation energy (E_a) of the SiGe films prepared with different H₂-dilution ratios, $R(H_2)$, along with the plot of $\ln(\sigma_D)$ as a function of $1000/T$ in the inset.

Fig. 6.4 demonstrates that the room-temperature dark conductivity (σ_D) and the activation energy (E_a) of the mixed-phase binary SiGe alloy thin films strongly depends on the variations of H₂-dilution in the rf-plasma, which in turn depends on the relative composition of Si/Ge and the relative residence of the amorphous and nanocrystalline phases in the film network. The film deposited at $R(H_2) = 12.5$ with its predominantly amorphous SiGe:H network possessed a low $\sigma_D \sim 1.89 \times 10^{-7}$ S cm⁻¹ and relatively high $E_a \sim 0.93$ eV. The σ_D increased significantly by about three orders of magnitude, along

with a sharp decrease in the corresponding E_a on increasing the $R(H_2)$ from 12.5 to 25, relating to a rapid transformation of the network towards its nanocrystalline structure with elevated average grain size. Further increase in $R(H_2)$, however, prompted a gradual elevation in σ_D to its maximum of $\sim 1.54 \times 10^{-2} \text{ S cm}^{-1}$ and the associated minimum in E_a $\sim 0.28 \text{ eV}$, for the film prepared with $R(H_2) = 50$.

6.3.5 Optical band gap

The changes in optical properties of the nc-Si_{1-x}Ge_x films with increase in $R(H_2)$ was carried out using the transmission and reflection data in the UV-VIS-NIR range. As the SiGe alloy is an indirect band-gap material, the optical band gaps of the films were estimated using Tauc's relation as follows:

$$\sqrt{\alpha h\nu} = B(h\nu - E_g) \quad (6.3)$$

where, α is the absorption coefficient, $h\nu$ is the corresponding photon's energy, E_g represents Tauc's optical band gap, and B is the slope of the plot that corresponds to the inverse of band edge width [52,53]. The Tauc's band gap is obtained from the intercept of extension of the linear part of $(\alpha h\nu)^{1/2}$ vs $h\nu$ plot at higher α values with the X-axis at $\alpha = 0$, as presented in Fig. 6.5(a)

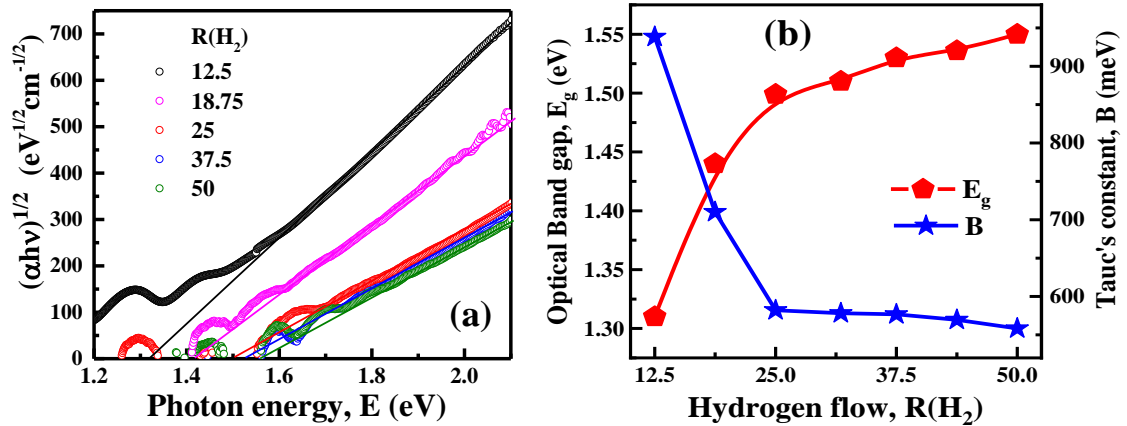


Fig 6.5. (a) Tauc's plot of the SiGe thin film prepared at different hydrogen dilutions, $R(H_2)$. (b) Variation in the optical band gap (E_g) and Tauc constant (B) with $R(H_2)$.

[54,55]. Fig. 6.5(b) demonstrates a sharp elevation in the film's optical band gap (E_g) from 1.31 eV to 1.56 eV with an increase in $R(H_2)$ from 12.5 to 50. The band edge width parameter 'B' decreased very rapidly from a high magnitude of 938.4 meV to 582.1 meV initially for varying H_2 dilution in the range $12.5 \leq R(H_2) \leq 25$, however, for further

increase in R(H₂) upto 50, the values of B attained a virtual saturation within ~(582.1–555) meV.

6.3.6 Deposition rate

Fig. 6.6 shows the change in the film deposition rate that decreased sharply from ~15.29 nm/min at R(H₂) = 12.5 to ~9.51 nm/min at R(H₂) = 25, after which it reduced gradually and attained a virtual saturation with ~6.74 nm/min at R(H₂) = 50.

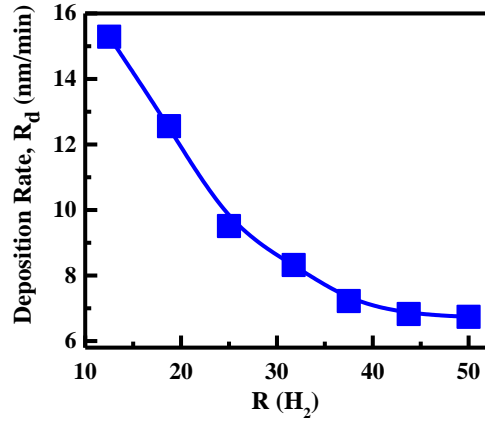


Fig. 6.6. Variation in the deposition rate of SiGe thin films with hydrogen dilution ratio, R(H₂).

6.3.7 FTIR spectroscopy analysis

The changes in chemical bonding configuration of the film network were studied via the Fourier transformed infrared vibrational spectroscopy on films deposited on c-Si wafers [56]. **Fig. 6.7(a)** presents the absorption co-efficient spectra in the range 525-720 cm⁻¹, deconvoluted into three distinguished components as Ge-H wagging mode with peak at ~570 cm⁻¹, Si-H wagging mode at ~625-630 cm⁻¹, and SiH_n (n ≥ 2) stretching mode at ~670 cm⁻¹. Using the integrated area under the absorption peaks of the wagging mode vibrations related to Ge and Si, the H content (C_H) within the film network was calculated from the following equation [57–59]:

$$C_H = \left(\frac{A_\omega}{N_{Si}} \right) \int \frac{\alpha d\omega}{\omega} \times 100 \text{ at. \%} \quad (6.4)$$

where N_{Si} = 5 × 10²² cm⁻³ denotes the atomic density of c-Si, the corresponding oscillator strengths for Ge and Si are A_w = 1.1 × 10¹⁹ cm⁻² and A_w = 1.6 × 10¹⁹ cm⁻², respectively and ∫α(dω/ω) denotes the integrated area under individual absorption peak. The H content (C_H), as plotted in **Fig. 6.7(b)**, was found to reduce sharply from 7.02 at.% to 2.3 at.% for an increase in R(H₂) from 12.5 to 25, where a sharp gradual transition from

amorphous to nanocrystalline network was identified from the Raman as well as the XRD data. However, once the nanocrystallization was attained in the network with a specific minimum C_H, further increase in R(H₂) from 25 to 50, resulted in gradual decrease in C_H from 2.3 at.% to 1.8 at.%, corresponding to its increased crystallinity and reduced Ge-content.

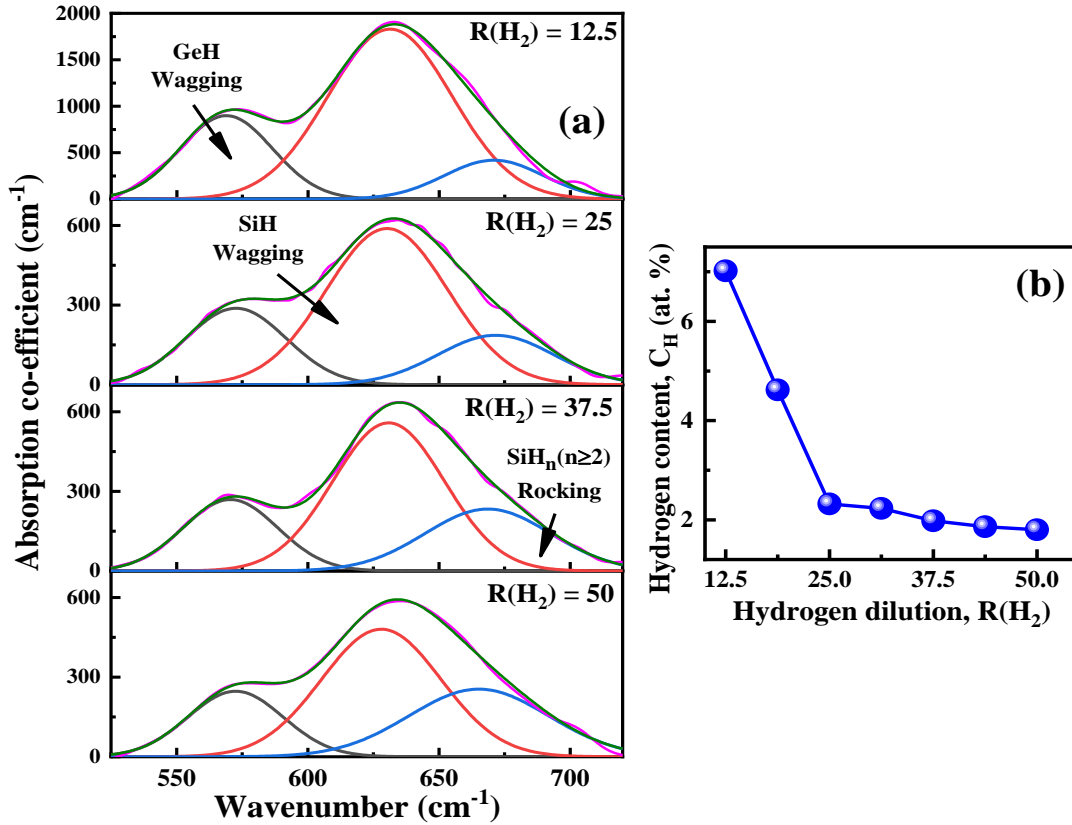


Fig. 6.7. (a) The deconvolution of the vibrational spectra into Si and Ge wagging modes. (b) Changes in hydrogen content (C_H) with hydrogen dilution ratio, R(H₂).

The absorption coefficient spectra within 1800-2200 cm⁻¹ region were deconvoluted into several Gaussian satellite components corresponding to the mono-, di-, tri-hydride stretching modes of Si and Ge and the platelet-like configuration of Si in the form of Si-H-Si present in the film matrix, as shown in **Fig. 6.8(a)**. The intensity of the Ge-H mono-hydride stretching absorption peak showed a decreasing trend with the increase in R(H₂). Using the deconvoluted stretching mode absorption co-efficient components, the Ge-structure factor (R_{Ge}) and the Si-structure factor (R_{Si}) of the film matrix, which quantify the individual relative fraction of the poly-hydride component in the matrix, were estimated following the relations:

$$R_{Ge} = \frac{I_{GeH_2}}{I_{GeH_2} + I_{GeH}} \quad (6.5)$$

$$R_{Si} = \frac{I_{SiH_2} + I_{SiH_3}}{I_{SiH} + I_{Si-H-Si} + I_{SiH_2} + I_{SiH_3}} \quad (6.6)$$

where I_x represents the integrated area under the respective absorption peaks associated with the GeH, GeH₂, SiH, Si-H-Si, SiH₂ and SiH₃, and presented in Fig. 6.8(a).

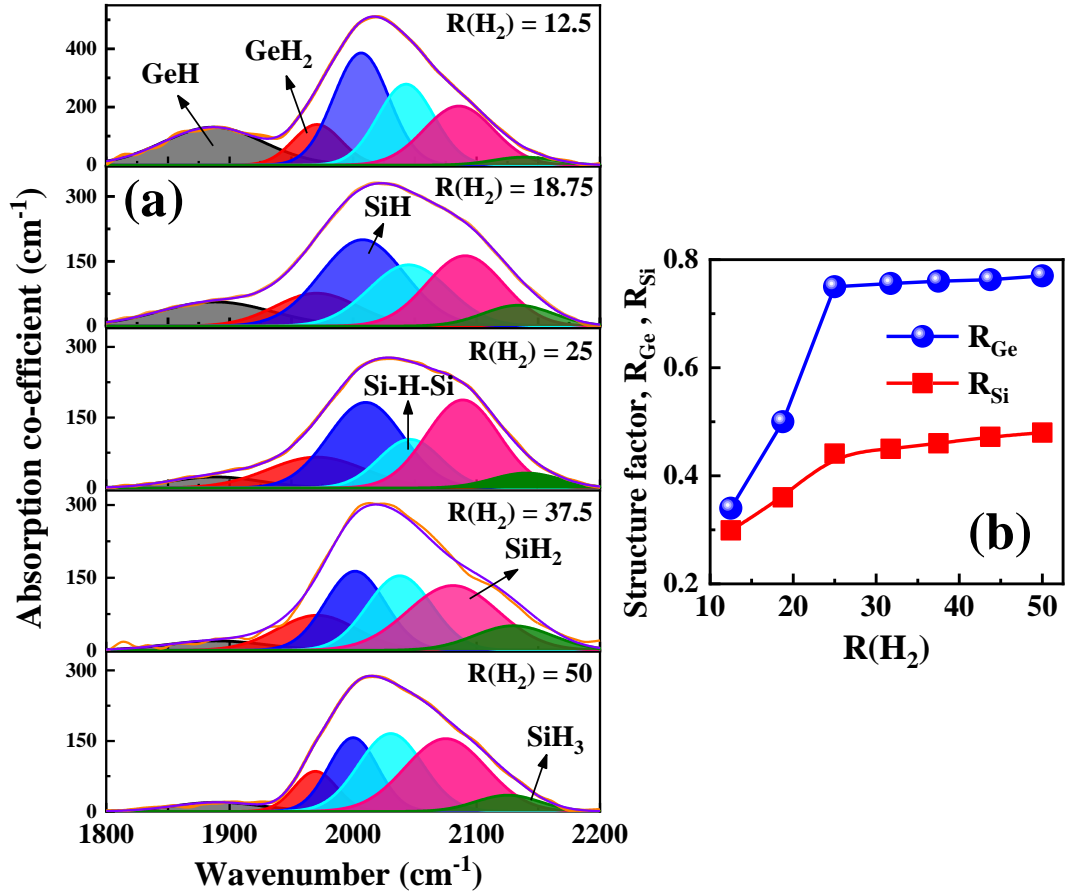


Fig. 6.8. (a) Changes in the deconvoluted vibrational spectra in stretching mode with the increase in hydrogen dilution ratio, $R(H_2)$. (b) Effect of variation in $R(H_2)$ on the structure factors of Ge (R_{Ge}) and of Si (R_{Si}) in nc-Si_{1-x}Ge_x:H films.

In Fig. 6.8(b), two distinguished slopes in the changes of R_{Ge} across the $R(H_2)$ ~25 was observed. R_{Ge} sharply enhanced from 0.34 to 0.75 with an initial increase in $R(H_2)$ to 25, however, on further increase in $R(H_2)$ to 50, R_{Ge} attains a virtual saturation with a maximum magnitude of ~0.76. Interestingly, the Si-structure factor (R_{Si}) also followed a similar trend showing a relatively feeble slope till $R(H_2)$ =25, increasing slowly from 0.3 to 0.44, above which approaching a virtual saturation, R_{Si} attained a magnitude ~0.48 at $R(H_2)$ =50. Higher structure factors, i.e., more poly-hydride contributions signify higher defect density and voids in the respective film matrices at increased H₂-dilution, $R(H_2)$, in the plasma. Furthermore, a higher magnitude of R_{Ge} than R_{Si} identifies that the relative presence of poly-hydrides over its mono-hydride

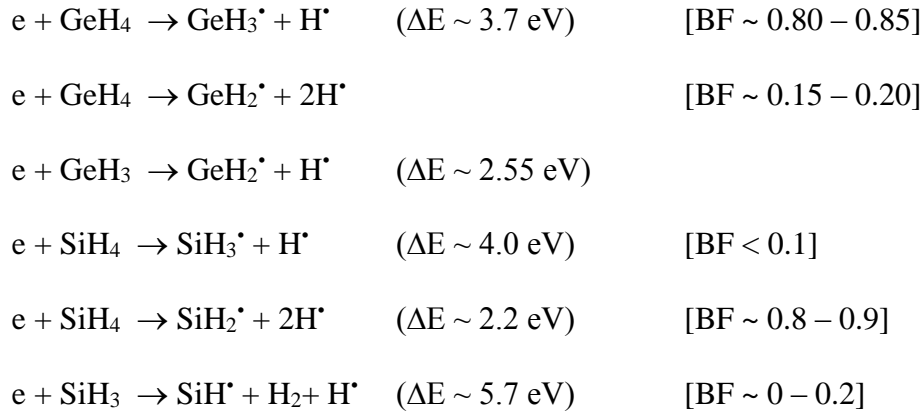
counterpart in the network is dominant for the Ge atoms compared to that for Si atoms, in the mixed-phase network of the nc-Si_{1-x}Ge_x film.

6.4 Discussion

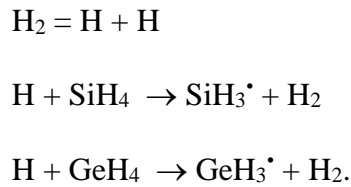
The present investigation mainly focuses on comprehending the modifications in the structural and optoelectronic properties of the SiGe thin films due to the gradual increase in the atomic H density in the plasma through the increase in H₂-dilution ratios at low temperatures.

The Raman study demonstrates that the higher H₂-dilution ratio facilitates an easier nanocrystallization in the film matrix, preferentially in the Si-Si network, along with a gradual reduction in the relative intensities of the Si-Ge and Ge-Ge peaks, signifying the lowering of the residence of Ge atoms with respect to Si atoms in the SiGe network. A similar decrease in the relative intensities of Ge-Ge and Si-Ge peaks with the simultaneous increase in the sharpness of the Si-Si peak at an elevated H₂-dilution in the (SiH₄ + GeH₄ + H₂) plasma, was reported by Cao *et al.* [26]. The XRD spectra identify that the SiGe film prepared at R(H₂) = 12.5 was primarily amorphous in nature and an increase in R(H₂) to 25 resulted in the prominent structural transformation of the film matrix from amorphous to nanocrystalline one. It is evident from the XRD studies that the crystallinity of the films has monotonically increased with the increase in R(H₂) and the average grain size of the Si-ncs attained its maximum of ~14.2 nm (for <111> orientation) for the film prepared at R(H₂) = 50. The gradual increase in crystallinity in the film network with an increase in H₂-dilution ratio R(H₂) resulted in the increase in dark conductivity (σ_D) from $\sim 1.89 \times 10^{-7}$ S cm⁻¹ to $\sim 1.54 \times 10^{-2}$ S cm⁻¹.

In general, the optical band gap of a two-phase network in nc-SiGe thin film is determined through the relative residence of Ge atoms compared to Si atoms within the film and its network's crystalline configuration is influenced by the Si/Ge bonding configurations. In the present study, the band gap of the films has been increased with increase in the H₂-dilution ratio due to the decrease in the relative population in Ge-bonds to Si-bonds in the film matrix. The growth kinetics involved in the plasma synthesis of nanocrystalline SiGe films can help in explaining the evolution in the network structure by enhancing the H₂-dilution ratio R(H₂). The precursor gases GeH₄ and SiH₄ dissociate into ions and plasma radicals with different masses. Some of the main reactions proceed via the following reaction channels [60–63]:



where ΔE represents the threshold energy and BF is the branching fraction of respective reaction channels. There are some secondary channels via which the dissociation takes place:



The H₂-molecules have higher dissociation energy (436 kJ/mol) than that of GeH₄ (164.5 kJ/mol) and SiH₄ molecules (299.2 kJ/mol), and the Ge-based radicals have a much higher sticking coefficient compared to the Si-based radicals [64]. So, the faster dissociation rate of GeH₄ than SiH₄ and the larger mass of Ge atoms induce a smaller mobility of the gas-phase GeH_x precursors than that of SiH_x, which leads the plasma with an overpopulation in Ge-radicals, with simultaneous increase in its lower-hydride component fraction [65]. At R(H₂) of 12.5, the higher density of GeH₄ component in the source gas and its lower dissociation energy induct the escalated decomposition of GeH₄ over SiH₄, making the plasma dominated by the Ge-hydrides over Si-hydrides, which consequences the amorphization of the SiGe network with high Ge content. The weaker bond strength of Ge-H compared to Si-H enables the growing surface crowded by Ge-H bonds even at low H₂-dilution [66]. In general, the bonded H-content (C_H) tends to increase with a decrease in the Ge-content in SiGe alloy film because of the preferential attachment of H with Si than Ge [67]. Here, the regression in C_H with the rise in R(H₂) from 12.5 up to 25 can be accounted for the gross structural transformation through nanocrystallization of the film matrix. However, a further increase in R(H₂) resulted in an associated further decrease in the C_H with increase in nanocrystallization in the Si-Si network as well as Ge-Ge network. Additional atomic H in the plasma stimulates the

formation of tri-hydride radicals (SiH₃ and GeH₃) via the dissociations mentioned in the secondary channels at high R(H₂) and these radicals have shorter diffusion lengths at the growth-sites and longer lifetimes than the lower-hydride precursors as GeH_x or SiH_x ($1 \leq x \leq 2$) [68]. Thus, reasonably at an optimized H₂-dilution ratio, R(H₂) ~25, diffusion of SiH₃ and GeH₃ radicals at the active growth site in the film stimulated the nanocrystallization process in the film matrix, accompanying very low bonded H-content, C_H < 3 at.%. Although, the high magnitudes of Ge- and Si-structure factors signify a surplus poly-hydrogenation in the film along with high defect density and micro-voids. A more intense flux of impacting atomic-H enhanced the surface mobility of the arriving radicals at the growth sites, which played an important role in further reinforcing the nanocrystallinity in the alloy network through the preferential etching of the weak Ge-Ge bonds in the film. Furthermore, H-etching facilitated in the reconstruction of the network to a more compact microstructure, via the relaxation of the network through a slower deposition rate.

6.5 Conclusion

Detailed analysis on the evolution of the silicon-germanium alloy's structural and optoelectronic properties, due to change in H₂-dilution of the (SiH₄ + GeH₄) precursor gases in the PECVD system has been presented. On increasing the H₂ dilution ratio from 12.5 to 50, the nc-SiGe thin films are obtained with an elevated nanocrystallinity and improved microstructural configuration.

The SiGe film prepared at very low H₂-dilution ratio of 12.5 is amorphous in nature with a high Ge-content. At an elevated R(H₂) = 25, highly nanocrystalline SiGe film with grains of average size ~11 nm, bonded H-content of <3%, an optical band gap ~1.5 eV and dark conductivity ~2.38 × 10⁻³ S cm⁻¹ has been produced, while the H-bonding is mostly in poly-hydride configuration that delivers elevated Ge- and Si-structure factors. With further increase of the H₂-dilution ratio, the nc-SiGe thin film prepared at R(H₂) = 50 possesses superior crystallinity in both Si-Si and Ge-Ge network with associated increased dark conductivity ~1.54 × 10⁻² S cm⁻¹. In the improved nanocrystalline network containing reduced H-content, however, optical band gap widens to ~1.56 eV due to increased poly-hydrogenation as indicated by the gradually increased structure factors of both Si and Ge, and most importantly, by the reduced Ge-content in the network. An adequate amount of atomic H at a higher H₂-dilution

facilitates nanocrystallization in the binary alloy network via changing the growth kinetics by providing better mobility to the precursors and chemical potential to the growing surface.

The dissociation energy of GeH₄ being much lower than that of SiH₄, the plasma parameters required for initiating crystallization are grossly different in Ge-Ge and Si-Si network. Inclusion of adequate amount of Ge and maintaining an optimum crystallinity in both Ge-Ge and Si-Si moieties for attaining an amply narrow band gap and sufficiently electrically conducting nanostructured SiGe binary alloy network has been accomplished via studying the growth characteristic by changing H₂-dilution to the (SiH₄ + GeH₄) plasma in RF PECVD. The nc-SiGe film prepared at a low substrate temperature of T_S ~220°C and at an optimum R(H₂) = 25, possess a narrow optical band E_g ~1.5 eV by virtue of substantial amount of Ge present in the network and significant dark conductivity ($\sigma_D \sim 2.38 \times 10^{-3} \text{ S cm}^{-1}$) due to substantial crystallinity in both Ge-Ge and Si-Si moieties, with altogether it appears appropriate for an ideal absorber layer in the bottom sub-cell in tandem-structured nc-Si solar cells.

6.6 References

- [1] A. Shah, P. Torres, R. Tscharnner, N. Wyrsh, H. Keppner, *Science* 285 (1999) 692–698.
- [2] S. Guha, J. Yang, B. Yan, *Sol. Energy Mater. Sol. Cells* 119 (2013) 1–11.
- [3] B. Yan, G. Yue, X. Xu, J. Yang, S. Guha, *Phys. Status Solidi* 207 (2010) 671.
- [4] D. Das, *J. Phys. D: Appl. Phys.* **36** (2003) 2335–2346.
- [5] D. Das, P. Mondal, *Appl. Surf. Sci.* 416 (2017) 980–987.
- [6] J. Yang, A. Banerjee, S. Guha, *Appl. Phys. Lett.* 70 (1997) 2975–2977.
- [7] D. Das, *Solid State Commun.* 108 (1998) 983–987.
- [8] M. Deng, X.M. Cao, Y. Ishikawa, W. Du, X. Yang, C. Das, A. Vijn, *Conference Record of the 2006 IEEE 4th World Conference on Photovoltaic Energy Conversion, Waikoloa, Hawaii* (2006) 1461–1464.
- [9] D. Das, S.C. De, S. Ray, A.K. Barua, *J. Non-Cryst. Solids* 128 (1991) 172–182.
- [10] H. Keppner, J. Meier, P. Torres, D. Fischer, A. Shah, *Appl. Phys. A* 69 (1999) 169–177.

- [11] S. Schicho, D. Hrunski, R. van Aabel, A. Gordijn, *Prog. Photovoltaics Res. Appl.* 18 (2010) 83–89.
- [12] G. Ganguly, T. Ikeda, T. Nishimiya, K. Saitoh, M. Kondo, A. Matsuda, *Appl. Phys. Lett.* 69 (1996) 4224–4226.
- [13] T. Matsui, H. Jia, M. Kondo, *Prog. Photovolt. Res. Appl.* 18 (2010) 48–53.
- [14] A. Dey, D. Das, *J. Phys. Chem. Solids* 154 (2021) 110055.
- [15] T. Matsui, C.W. Chang, M. Kondo, K. Ogata, M. Isomura, Effect of illumination induced space charge on photocarrier transport in hydrogenated microcrystalline Si_{1-x}Ge_x p-i-n solar cells, *Appl. Phys. Lett.* 91 (2007) 10211.
- [16] J. Ni, Q. Liu, J. Zhang, J. Ma, H. Wang, X.D. Zhang, Y. Zhao, Microcrystalline silicon-germanium solar cells with spectral sensitivities extending into 1300 nm, *Sol. Energy Mater. Sol. Cells* 126 (2014) 6–10.
- [17] R. Jiménez, M. Moreno, A. Torres P. Rosales, M.T. Sanz, R. Ambrosio, *Phys. Status Solidi* 215 (2018) 1700736.
- [18] Q. Wang, H. Vogt, *J. Electron. Mater.* 48 (2019) 7360–7365.
- [19] F.L. Huerta, R.M.W. García, L.G. González, A.L.H. May, W.C. Arriaga, R. Vega, E. Soto, *IOP Conf. Ser. Mater. Sci. Eng.* 628 (2019) 012003.
- [20] L. Tsybeskov, D. J. Lockwood, *Proc. IEEE* 97 (2009) 1284.
- [21] Z. Yu, X. Zhang, H. Zhang, Y. Huang, Y. Li, X. Zhang, Z. Gan, *J. Alloys Compd.* 803 (2019) 260–264.
- [22] X. Ji, H.Y. Cheng, A.J. Grede, A. Molina, D. Talreja, S.E. Mohny, N.C. Giebink, J.V. Badding, V. Gopalan, *APL Mater.* 6 (2018) 046105.
- [23] M. Shima, A. Terakawa, M. Isomura, H. Haku, M. Tanaka, K. Wakisaka, S. Kiyama, S. Tsuda, *J. Non-Cryst. Solids* 442 (1998) 227–230.
- [24] D.J. Paul, *Semicond. Sci. Technol.* 19 (2004) R75.
- [25] D. Das, A. Dey, *Physica E: Low-dimensional Systems and Nanostructures* 111 (2019) 20–28.
- [26] Y. Cao, Y. Liu, J. Zhou, Y. Wang, J. Ni, J. Zhang, *Sol. Energy Mater. Sol. Cells* 151 (2016) 1–6.
- [27] Y.H. Shing, J.W. Perry, C.E. Allevato, *Sol. Cells* 24 (1988) 353.
- [28] A. Dey, D. Das, *J. Alloys Compd.* 806 (2019) 1529–1535.
- [29] M. Stutzmann, R.A. Street, C.C. Tsai, J.B. Boyce, S.E. Ready, *J. Appl. Phys.* 66 (1989) 569.

- [30] M. Shima, A. Terakawa, M. Isomura, H. Haku, M. Tanaka, Kenichiro W.S. Kiyama, S. Tsuda, *J. Non-Cryst. Solids* 227–230 (1998) 442–446.
- [31] A.R. Middy, S. Ray, S.J. Jones, D.L. Williamson, *J. Appl. Phys.* 78 (1995) 4966.
- [32] M.E. Gueunier, J.P. Kleider, R. Brüggemann, S. Lebib, P. Roca i Cabarrocas, R. Meaudre, B. Canut, *J. Appl. Phys.* 92 (2002) 4959.
- [33] A.M. Funde, N.A. Bakr, D.K. Kamble, R.R. Hawaldar, D.P. Amalnerkar, S.R. Jadkar, *Sol. Energy Mater. Sol. Cells* 92 (2008) 1217–1223.
- [34] D. Das, M. Jana, *Sol. Energy Mater. Sol. Cells* 81 (2004) 169–181.
- [35] J. Mullerova, P. Sutta, G. van Elzakker, M. Zeman, M. Mikula, *Appl. Surf. Sci.* 254 (2008) 3690–3695.
- [36] D. Das, B. Sain, *J. Appl. Phys.* 114 (2013) 073708.
- [37] S.Y. Myong, K.S. Lim, M Konagai, *Appl. Phys. Lett.* 88 (2006) 103120.
- [38] D. Das, S. Samanta, *Mater. Chem. Phys.* 243 (2020) 122628.
- [39] D. Wenge, Z. Lanfang, Z. Jiangyong, L. Yachao, Y. Wei, F. Guangsheng, *Plasma Sci. Technol.* 9 (2007) 599.
- [40] T. Li, J. Zhang, Y. Ma, Y. Yu, Y. Zhao, *Mod. Phys. Lett. B* 31 (2017) 1740010.
- [41] S. Kim, C. Park, J. Lee, J. Cho, Y. Kim, *Curr. Appl. Phys.* 13 (2013) 457–460.
- [42] A. Fedala, C. Simon, N. Coulon, T. Mohammed-Brahim, M. Abdeslam, A.C. Chami, *Phys. Status Solidi C* 7 (2010) 762–765.
- [43] A. Matsuda, G. Ganguly, *Appl. Phys. Lett.* 67 (1995) 1274–1276.
- [44] D.V. Tsu, B.S. Chao, S.R. Ovshinsky, S. Guha, J. Yang, *Appl. Phys. Lett.* 71 (1997) 1317–1319.
- [45] J.B. Renucci, M.A. Renucci, M. Cardona, *Solid State Commun.* 9 (1971) 1651.
- [46] D. Raha, D. Das, *Sol. Energy Mater. Sol. Cells* 95 (2011) 3181–3188.
- [47] B. Sain, D. Das, *Sci. Adv. Mater.* 5 (2013) 188–198.
- [48] T. Tah, C.K. Singh, S. Amirthapandian, K.K. Madapu, A. Sagdeo, S. Ilango, T. Mathews, S. Dash, *Mater. Sci. Semicond. Process.* 80 (2018) 31–37.
- [49] S.F. Ren, W. Cheng, P.Y. Yu, *Phys. Rev. B* 69 (2004) 235327.
- [50] D. Das, C. Patra, *Mater. Adv.* 2 (2021) 2055.
- [51] D. Das, D. Kar, *J. Phys. Chem. Solids* 111 (2017) 115–122.

- [52] A.M. Funde, N. Ali, D.K. Kamble, R.R. Hawaldar, D.P. Amalnerkar, S.R. Jadkar, *Sol. Energy Mater. Sol. Cells* 92 (2008) 1217–1223.
- [53] J. Tauc, R. Grigorovici, A. Vancu, *Phys. Status Solidi (b)* 15 (1966) 627–637.
- [54] D. Kar, D. Das, *J. Appl. Phys.* 120 (2016) 025102.
- [55] G.B. Tong, Z. Aspanut, M.R. Muhamad, S.A. Rahman, *Vacuum* 86 (2012) 1195–1202.
- [56] D. Das, A.K. Barua, *Sol. Energy Mater. Sol. Cells* 60 (2000) 167–179.
- [57] C.J. Fang, K.J. Gruntz, L. Ley, M. Cardona, F.J. Demond, G. Muller, S. Kalbitzer, *J. Non-Cryst. Solids* 35–36 (1980) 255–260.
- [58] G. Lucovsky, *Sol. Cells* 2 (1980) 431–442.
- [59] M. Jana, D. Das, A.K. Barua, *J. Appl. Phys.* 91 (2002) 5442–5448.
- [60] F.J. Kampas, *Semiconduct. Semimet.* 21 (1984) 153–177.
- [61] S. Hazra, A.R. Middy, S. Ray, *J. Phys. D: Appl. Phys.* 29 (1996) 1666–1674.
- [62] J.R. Doyle, D.A. Doughty, A. Gallagher, *J. Appl. Phys.* 71 (1992) 4727.
- [63] D. Das, *Solid State Phenomena* (Special Volume on Hydrogenated Amorphous Silicon), Scitec Publication, Switzerland, 1995, pp. 227–258.
- [64] D. Polino, A. Barbato, C. Cavallotti, *Phys. Chem. Chem. Phys.* 12 (2010) 10622–10632.
- [65] Y.P. Chou, S.C. Lee, *J. Appl. Phys.* 83 (1998) 4111.
- [66] K. Tanaka, A. Matsuda, *Thin Solid Films* 163 (1988) 123.
- [67] M. Stutzmann, R.A. Street, C.C. Tsai, J.B. Boyce, S.E. Ready, *J. Appl. Phys.* 66 (1989) 569–592.
- [68] J.P.M. Schmitt, *J. Non-Cryst. Solids* 59–60 (1983) 649.

Chapter 7

**Ge-rich narrow band gap
nc-Si_xGe_{1-x} absorber layer for
tandem structure nc-Si solar cells**

7.1 Introduction

Over the last few decades, Si-based thin film solar cell technology has been largely developed towards its successful commercialization, utilizing its benefits of low material cost and flexible manufacture in large-area modules [1–4]. In order to overcome its low conversion efficiency and sensible light induced metastability limitations [5–7], a multi-junction design has been implemented with an nc-Si solar cell configuration to exploit a wider range of solar radiation [8–11]. In view of possessing a low absorption co-efficient in the infrared region, the use of nc-Si in the bottom sub-cell requires a thicker absorber layer (~1.5–2.0 μm), followed by a high production cost [12–13]. Nevertheless, an optically thick layer of the absorber material initiates significant recombination loss as the diffusion length of the carriers becomes smaller than the thickness of the absorber layer, which causes reduced carrier collection and poor built-in potential to hinder the solar cell performance [14]. Under these circumstances, nanocrystalline silicon germanium (nc-SiGe) with its increased absorption co-efficient in the infrared region appears to be an efficient material as the bottom sub-cell absorber layer of multi-junction nc-Si solar cells [15–21]. In general, Ge atoms are optimally added to the Si-rich network to produce good quality nc-Si_xGe_{1-x} alloy [22,23]. The GeH₄ feed gas has a lower dissociation energy (~164.5 kJ/mol) than that of SiH₄ (~234.5 kJ/mol) and hence, a higher decomposition rate [24]. Therefore, under appropriate conditions compatible for nc-Si growth, the introduction of a small amount of GeH₄ in the plasma results in a very high density of Ge-related radicals in the incident flux and their rapid accumulation at the film growth site [25,26]. Although the binding energies for the formation of the Si–Si, Si–Ge and Ge–Ge bonds are almost similar [27,28], the higher viscosity co-efficient and smaller diffusion length of the Ge radicals compared to those of the Si radicals lead to a higher Ge deposition rate that results in cluster formation through the arbitrary gathering of Ge–Ge bonds within the alloy film [29]. Furthermore, the dangling bonds associated with the substantial presence of Ge into the film matrix create lots of defects that usually destroy its nanocrystalline phase, leading to the amorphization of the film network [30,31]. The inclusion of an increased number of Ge atoms in the Si-rich SiGe film network extends the tunability by narrowing its optical band gap, exhibiting a better response in the infrared wavelength spectral region. However, this simultaneously deteriorates the electrical conductivity due to degradation of the film's overall crystallinity [32]. These are the main reasons why it is difficult to fabricate a high quality nc-SiGe film with balanced opto-electronic properties. Most of the reports have dealt with nc-Si_xGe_{1-x}

alloy films with low Ge contents ($x > 0.5$) with reasonable optoelectronic properties for device applications [33]. Few reports have illustrated that the use of higher hydrogen dilution facilitates the improved crystallization among the Ge atoms in the SiGe film network and strongly influences the properties of the alloy material [27,34–36]. The plasma conditions consistent for nc-Ge growth are grossly different from the conditions compatible for nc-Si growth. The inclusion of Si atoms in the film network under nc-Ge growth compatible plasma conditions may be beneficial toward preparing good quality nc-Si_xGe_{1-x} film because of the controlled dissociation of SiH₄ in the plasma. Accordingly, the controlled addition of Si in a Ge-rich plasma atmosphere may produce nc-Si_xGe_{1-x} alloy with an optimal narrow band gap and good electrical properties by virtue of its sustained crystallinity, which can be used in the bottom sub-cell of tandem structure nc-Si solar cells. The present report describes on the growth of nc-Si_xGe_{1-x} alloy films with high Ge content grown at low temperature and plasma parameters compatible for nc-Ge growth conditions and studies on their structural and optoelectronic properties.

7.2 Experimental details

A series of nc-Si_xGe_{1-x} films were grown at a low substrate temperature (T_s) of ~ 220 °C using a fixed flow of total precursor gases (GeH₄ + SiH₄) of 2 sccm with H₂ (50 sccm) as the diluent gas in a 13.56 MHz RF-PECVD (capacitively-coupled) reactor. The films were fabricated on glass, *p*-type <100> oriented c-Si wafer substrates by systematically varying the concentration fraction of SiH₄, $SC = [SiH_4]/[(GeH_4) + (SiH_4)]$ from 0 to 0.3, maintaining the gas pressure at 2 Torr and applied RF power at 100 W in the reactor. The films were also deposited on carbon coated Cu microscopic grids for transmission electron microscopy studies. The reaction chamber was retained at a base pressure of $\sim 10^{-7}$ Torr to maintain contamination-free conditions before film deposition.

The deposited thin films were investigated using X-ray diffraction studies performed on a Rich Seifert 3000P Bragg diffraction set-up with Cu-K α ($\lambda = 1.541$ Å) radiation. The Raman spectra of the films were obtained on a micro-Raman Spectrometer (Renishaw inVia) using a 514-nm wavelength Ar⁺ laser exciton source with a power density of ~ 2 mW/cm². The optical properties of the nc-Si_xGe_{1-x} samples were characterized using a double-beam UV-VIS spectrophotometer (Hitachi 330, Japan). Details of the different bonding configurations between the Si, Ge and H atoms in the samples were investigated using the Fourier transformed infrared spectra recorded on a Nicolet Magna-IR 750

spectrometer. The high-resolution microstructures of the films grown on carbon-coated Cu microscopic grids were studied using a UHR-FEG transmission electron microscope (JEOL JSM 2100) operated at 200 kV. The surface topologies of the nc-Si_xGe_{1-x} samples were analyzed using atomic force microscopy (AFM) (Veeco dI CP II). For temperature-dependent dark conductivity measurements of the samples, coplanar parallel Al electrodes were deposited on the films on glass substrates via thermal evaporation at room temperature at a base pressure of $\sim 10^{-6}$ Torr. The dark-conductivity of the thin films was evaluated from the current measured using an electrometer (Keithley 6517A) during the cooling of the sample from 170 to -30°C within a cryostat.

7.3 Results

The evolution of the crystallinity of the samples was observed using X-ray diffraction. **Fig. 7.1(a)** displays the XRD patterns of the silicon germanium (Si_xGe_{1-x}:H) thin films deposited with different concentrations of SiH₄ [$\text{SC} = \text{SiH}_4 / (\text{SiH}_4 + \text{GeH}_4)$] from 0 to 0.3. At SC = 0, the corresponding XRD spectrum exhibits three strong peaks at $2\theta = 27.3, 45.4$ and 53.75° , which correspond to the $\langle 111 \rangle, \langle 220 \rangle$ and $\langle 311 \rangle$ planes of nc-Ge,

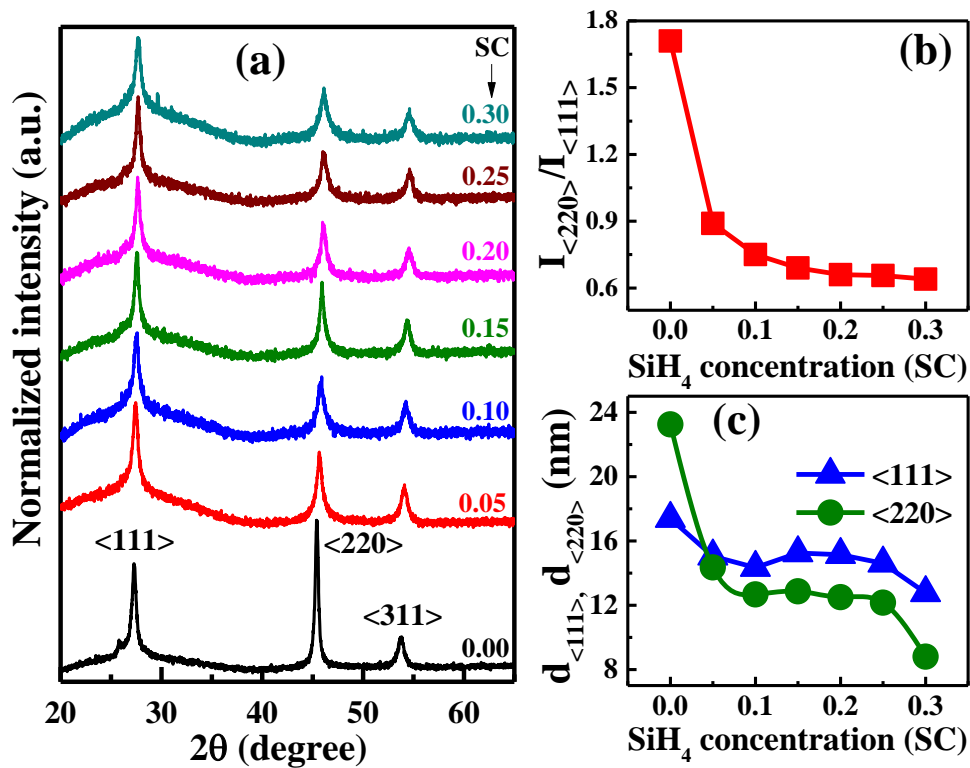


Fig. 7.1. (a) XRD patterns obtained for the samples deposited at various SiH₄ concentrations (SC). The variation in (b) $I_{\langle 220 \rangle} / I_{\langle 111 \rangle}$ and (c) grain size upon increasing the SC.

respectively. The XRD peak positions gradually shifted to higher diffraction angles at higher SiH₄ concentrations with progressively diminished intensity. A critical transformation in the network from a dominant <220> crystallographic orientation to a preferred growth alignment in the <111> direction occurred upon the introduction of SiH₄. The corresponding intensity ratios of the XRD peaks, $I_{\langle 220 \rangle} / I_{\langle 111 \rangle}$, decreased continuously upon increasing the SiH₄ concentration, as shown in **Fig. 7.1(b)**, gradually turning the network from thermodynamically preferred <220> oriented growth of the grains to the evolution of its regular <111> direction via random nucleation in the alloy system [37,38]. The average grain size of the crystallites (d) of the alloy film was calculated from the full-width-half-maximum (β) of each peak using the Debye-Scherrer relationship:

$$d = 0.9\lambda / \beta \cos\theta \quad (7.1)$$

Fig. 7.1(b) demonstrates that the average grain size for the <220> crystallites reduced sharply from 23.3 to 8.8 nm, whereas that for the <111> crystallites decreased only from 17.4 to 12.8 nm with the introduction of SiH₄ in the plasma with SC varying from 0 to 0.3. The observed XRD peak broadening was related to the crystallographic defects and alloy clustering arising due to the inclusion of Si in the Ge-rich film network.

The Raman spectra of the films prepared with increasing concentrations of SiH₄ are presented in **Fig. 7.2(a)**. The sample prepared with SC = 0 (i.e., pure Ge film) shows the characteristic nc-Ge peak with a narrow full width at half maximum (FWHM) at ~297 cm⁻¹. For SC = 0.05, a very small hump at ~462 cm⁻¹ appears in addition to two distinct peaks at ~290 cm⁻¹ and ~398 cm⁻¹, which correspond to the Si-Si, Si-Ge and Ge-Ge bonds, respectively [39,40]. A red-shift in the Ge-Ge peak occurs along with the gradual improvement in the relative intensity of both Si-Ge and Si-Si peaks with respect to the Ge-Ge peak upon increasing the SiH₄ concentration. All three peaks are gradually broadened due to the progressive inclusion of Si in the plasma. The presence of small Si-Si peaks with intense and sharper Ge-Ge peaks for all the samples signifies that the deposited nc-Si_xGe_{1-x} films are comprised mostly of the Ge-dominated network. For the films prepared with 0.05 < SC < 0.2, only a tiny Si-Si peak is observed along with a prominent Si-Ge peak. The larger area under the Si-Ge peak than that of Si-Si peak signifies that the introduction of SiH₄ in the plasma favors the formation of Si-Ge bonds over Si-Si bonds. Further increasing the SiH₄ concentration has resulted in the construction of more Si-Ge bonds in the film network. The Si-Si peak with its larger FWHM than the other two residing peaks for SC ≤ 0.25 indicates that the Si atoms are predominantly included in their

amorphous form in the Si-Si bonds. All three peaks (Ge-Ge, Si-Ge and Si-Si) are prominent in the film grown at SC = 0.3 and the intense sharp Ge-Ge peak signifies the well-developed nanocrystallinity in this alloy film. The distinguishable relative sharpness between the peaks in the Raman spectra indicates that the crystalline volume fraction of the prepared nc-SiGe film network sequentially changes from Ge-Ge to Si-Ge, followed by Si-Si bonding configurations.

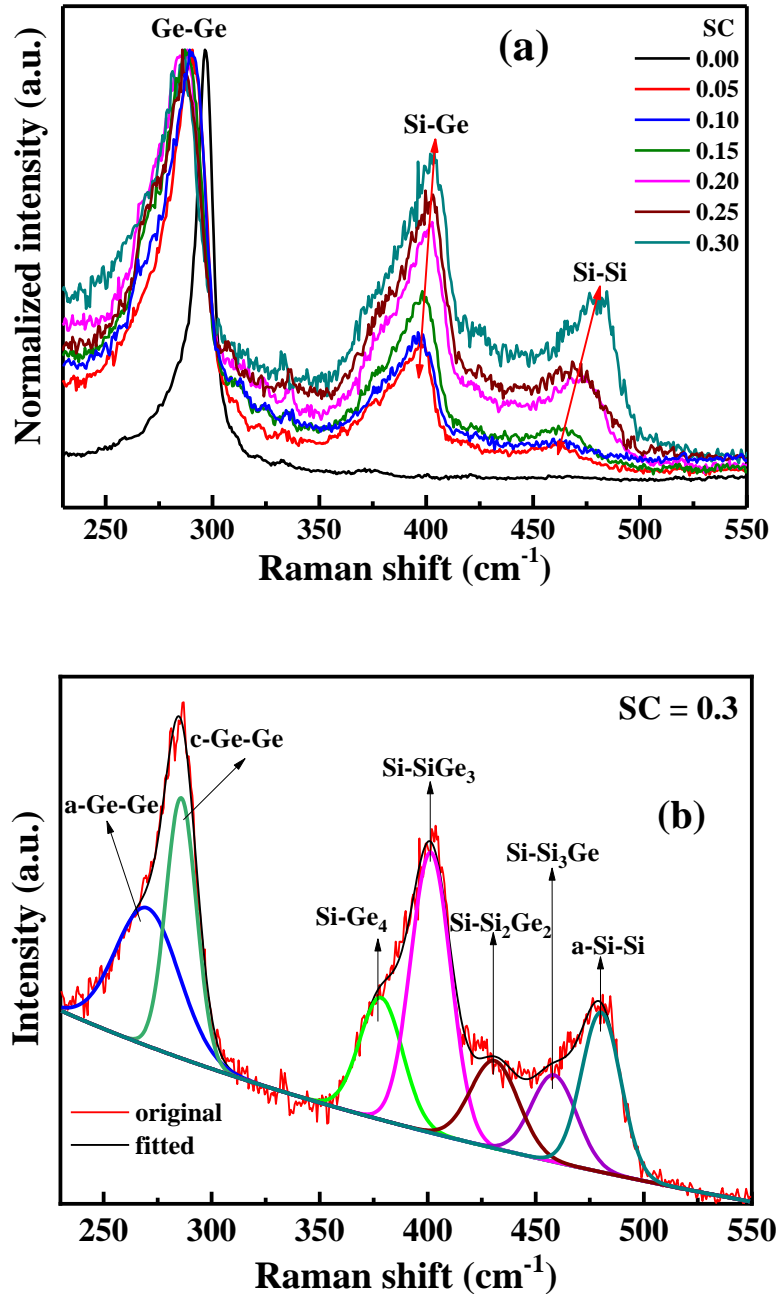


Fig. 7.2. (a) Raman spectra obtained for the samples prepared at different SiH₄ concentrations (SC = 0 to 0.3) and (b) deconvoluted Raman spectrum of the film grown with SC = 0.3.

The film prepared with the highest SiH₄ concentration (SC = 0.3) was deconvoluted into all possible satellite components and marked as their respective Ge-Ge, Si-Ge and Si-Si configurations in **Fig. 7.2(b)**. The Si-Ge band arose from the vibration of Si atoms coordinated with Ge atoms in the form of Si-Si_n-Ge_{4-n} (0 ≤ n ≤ 3). The major Si-Ge peak centered at ~398 cm⁻¹ was attributed to the Si-Si-Ge₃ bonding configurations and the Si-Ge peak center was blue-shifted along with a broader shoulder in the lower energy region [23,41]. This occurred because the probability of the Si atoms being coordinated with four Ge atoms reduced with an increase in the SiH₄ concentration in the plasma [42]. **Fig. 7.2(a)** shows that the height of the Si-Si peak increased rapidly for the film prepared with SC = 0.3. Eventually, the large blue shift in the Si-Si peak resulted in its merging with the bulk Si phonon mode at ~480 cm⁻¹ via the formation of larger Si-Si clusters.

The changes in the optical properties of the nc-Si_xGe_{1-x} films upon increasing the Si concentration were studied from the absorption co-efficient calculated from the transmittance data obtained in the UV-VIS-NIR region using the following relationship:

$$\alpha = \frac{1}{d} \ln \left(\frac{1}{T} \right) \quad (7.2)$$

where d is the thickness of the film and T is the transmittance at a particular wavelength. The typical thickness of the films was ~800–900 nm, as calculated from the optical interference fringes appearing in the lower energy region. The optical band gaps (E_g) of the nc-Si_xGe_{1-x} films were estimated using the Tauc equation [43,44]:

$$(ahv)^n = B(hv - E_g) \quad (7.3)$$

where α represents the absorption coefficient and hv is the corresponding photon energy. The magnitude of n = 2 and 2/3 correspond to the direct allowed and direct forbidden transitions and n = 1/2 and 1/3 are related to the indirect allowed and indirect forbidden transitions, respectively [45]. Considering the rational speculation of the indirect optical transition occurring in the mixed phase SiGe material containing Si/Ge-nanocrystals embedded in the amorphous matrix, the optical band gaps were obtained from the intercept of the straight portion of the (ahv)^{1/2} vs. hv plot to the energy-axis, as shown in **Fig. 7.3**. The (ahv)^{1/2} vs hv plot, in general, remains mostly linear over a reasonable span of the E-axis and the Tauc equation is typically suitable for the amorphous material. For the nc-Si/Ge alloy material containing a reasonable amount of the amorphous matrix, it is difficult to obtain an extended linear segment in the plot. Depending on the variation of the

nanocrystallinity present in the material, the slope of the $(\alpha hv)^{1/2}$ vs hv plot, known as the Tauc constant (B), usually changes in magnitude. In the present study, the data plotted in the inset of **Fig. 7.3** identifies that apart from the nc-Ge film prepared at SC = 0, the nc-SiGe films grown at SC varying from 0.05 to 0.30 demonstrate that the B value varies in the range of 495–517 eV^{-1/2} cm^{-1/2}, which rationally allows a comparison among the optical band gaps of the samples extracted from the Tauc plot.

Various approaches were adopted in the past in view of finding a unique process for making a good comparison of the optical band gaps of different samples possessing a wide range of crystallinity. The samples were compared in terms of their corresponding variations in E₀₄ and E₀₅, which correspond to the energy at which the absorption co-efficient attains a magnitude of 10⁴ and 10⁵ cm⁻¹, respectively as well as E_g(1/2) and E_g(1/3), which correspond to the energy values obtained from the Tauc plot considering n = 1/2 and 1/3 in

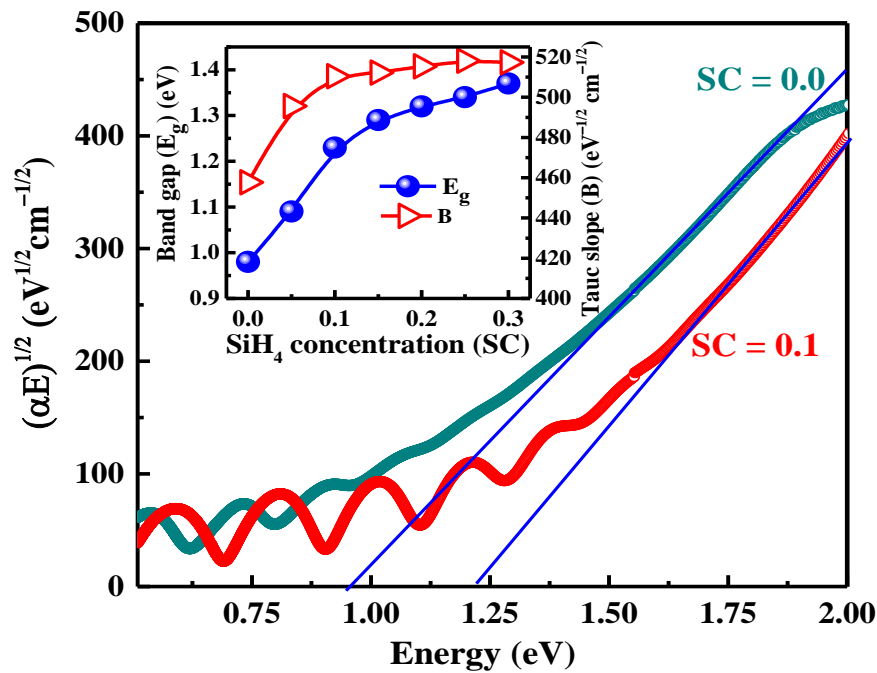


Fig. 7.3. Tauc plot [$(\alpha E)^{1/2}$ vs E] estimating the band gap for the films prepared with SC = 0 and 0.1; the inset demonstrates the changes in the optical band gap upon changing the SC.

Eqn. (7.3), respectively. Almost parallel variations in the optical band gap values had been previously reported, in which the magnitudes were found to be sensitive to the particular approach adopted [46,47]. Accordingly, each of the above techniques offers a reasonably good avenue for making a suitable comparison of the nature of the variation in the optical band gaps. In the absence of any unique process, a variety of materials with a wide range of crystallinity, including nc-Si [46,47], nc-SiO_x [48], nc-SiC_x [49] and nc-SiN_x [45], had been

reported using the $E_g(1/2)$ approach, providing optical band gap values nearly close to reality and also adequate for a realistic comparison. Subsequently, in the present case, the optical band gap of the nc-Ge film prepared at SC = 0 has been estimated to be ~0.98 eV, a sharp increase to 1.09 eV due to the primary insertion of Si atoms in the film network has been observed for the nc-Ge film prepared at SC = 0.05. The band gap gradually widens to 1.37 eV upon increasing the SC to 0.3, as shown in the inset of **Fig. 7.3**.

The Fourier transformed infrared absorption spectra were thoroughly investigated to study the chemical bonding configurations of H with Si and Ge in the nc-SiGe thin films prepared with $0 \leq SC \leq 0.3$. **Fig. 7.4(a)** shows the typical deconvoluted satellite components in the range of 500–700 cm^{-1} , illustrating the relative amount of hydrogen bonded with Si and Ge in the film network. The film prepared at SC = 0 exhibits a peak at ~565 cm^{-1} , which corresponds to the wagging mode of the Ge–H vibrations. A small concentration of SiH₄ in the plasma creates Si–H bonds in the network, which are observed as a very low intensity satellite component at ~625 cm^{-1} corresponding to the Si–H wagging mode (**Fig. 7.4(a)**, SC = 0.10). The intensity of the Si–H component increases with the further inclusion of Si atoms in the film, whereas the satellite peak intensity of the Ge–H mode also gradually increases. The bonded hydrogen content (C_H) in the films corresponds to the total amount of hydrogen bonded to Si and Ge, which was estimated using the individual integrated areas under the Si–H and Ge–H satellite peaks as follows:

$$C_H = (A_\omega/N_{Si}) \int a d\omega/\omega \times 100 \text{ at.}\% \quad (7.4)$$

where $A_\omega = 1.6 \times 10^{19} \text{ cm}^{-2}$ and $A_\omega = 1.1 \times 10^{19} \text{ cm}^{-2}$ present the wagging mode oscillator strengths for Si and Ge, respectively, and $N_{Si} = 5 \times 10^{22} \text{ cm}^{-3}$ is the atomic density of c-Si [50,51]. The C_H for the pure nc-Ge film (SC = 0) was determined to be as low as 2.6%. The variation in the magnitude of C_H of the films is presented in **Fig. 7.4(b)**, in which it increased monotonically upon increasing in the Si concentration corresponding to $0 < SC \leq 0.25$. Hydrogen atoms were preferentially attached to the Si atoms rather than the Ge atoms because the binding energy of the Si–H bond is lower than that of the Ge–H bond [36]. Interestingly, increasing the SC from 0.25 to 0.3, the total bonded hydrogen content increased sharply from ~6.23 to ~10.02 at.%. The changes in the H-content in the SiGe alloy thin films occurred due to the difference in the hydrogen solubility/diffusion in the various proportions of Ge–Ge, Si–Ge and Si–Si bonds residing in the film. This was also influenced by the increase in the overall amorphous content in the film due to the increase

in the Si content within it. The amount of hydrogen bonded in the Ge–Ge network was lower than that in the Si–Ge network and the hydrogen content in the Si–Ge network was again lower than that in the Si–Si network [22]. The rapid increase in the bonded hydrogen content can be attributed to the sharp rise in the Si–Si bond along with Si–Ge bond formation taking place in the film prepared at SC = 0.3, as shown in the Raman spectra.

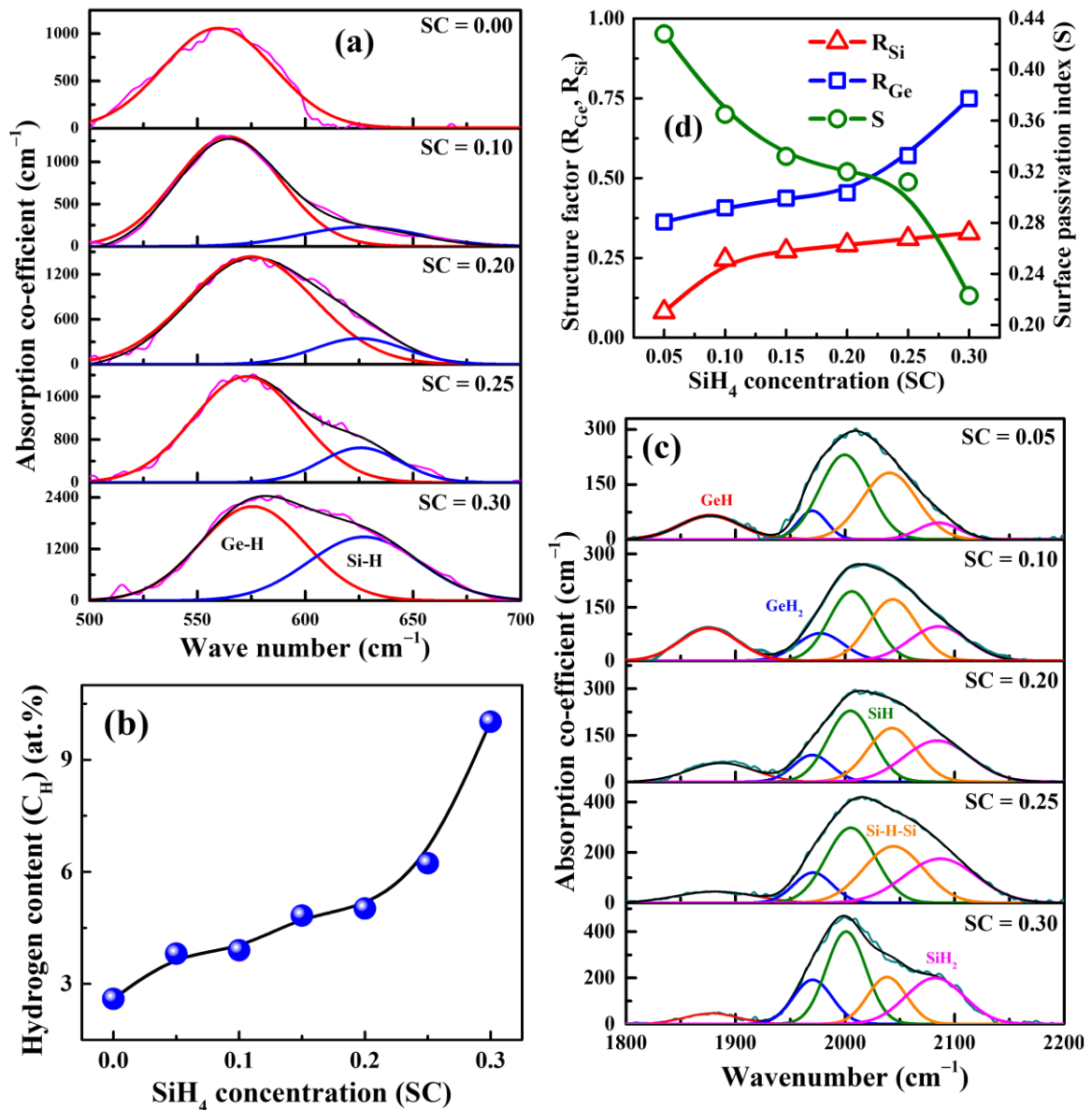


Fig. 7.4. (a) The deconvolution of the FTIR absorption co-efficient spectra in the range of 500–700 cm⁻¹, (b) changes in the hydrogen content (C_H) upon increasing the SiH₄ concentration (SC), (c) the deconvoluted FTIR absorption spectra in the range of 1800–2200 cm⁻¹, and (d) the effect of varying the SC on the structure factor (R_{Si}, R_{Ge}) and the surface passivation index (S).

The FTIR absorption spectra of the Ge and Si stretching vibrations in the wavenumber range of 1800–2200 cm⁻¹ were deconvoluted into five satellite peaks to analyze the evolution of the nanostructure of the as-prepared nc-Si_xGe_{1-x}:H network. **Fig. 7.4(c)** shows the deconvoluted absorption spectra within the wavenumber range of 1800–2200 cm⁻¹ demonstrating the well-resolved components at: (i) 1885 cm⁻¹, assigned to the monohydride stretching modes of GeH, (ii) 1970 cm⁻¹, attributed to the di-hydride stretching mode of GeH₂, (iii) 2005 cm⁻¹, associated with the monohydride stretching mode of SiH, (iv) 2040–2050 cm⁻¹, representing the Si–H–Si platelet-like configuration and (v) 2085–2090 cm⁻¹, correlated to the di-hydride SiH₂ stretching mode [25,52–54]. The microstructural changes in the SiGe alloy thin films could be estimated from the evaluation of the Ge-structure-factor and Si-structure factor, which represent the ratios of the contributions from the poly-hydride components (SiH_x and GeH_x, x ≥ 2) in the related matrix [23].

$$R_{Ge} = \frac{[GeH_2]}{[GeH] + [GeH_2]} \quad (7.5)$$

$$R_{Si} = \frac{[SiH_2]}{[SiH] + [Si-H-Si] + [SiH_2]} \quad (7.6)$$

where [GeH], [GeH₂], [SiH], [Si-H-Si] and [SiH₂] represent the area integrals of the respective absorption peaks for the stretching modes. A monotonic increase in the ratio of integrated area under the GeH₂ dihydride satellite peak to the GeH monohydride satellite peak was observed (**Fig. 7.4(c)**), which was reflected by the increasing Ge-structure factor as a function of the SiH₄ concentration (SC), as shown in **Fig. 7.4(d)**. Simultaneously, the Si-related SiH₂ dihydride vibrational peak gradually increases its contribution to the absorption co-efficient spectra upon increasing the SiH₄ concentration [10]. The higher structure factor related to Ge and Si signify the alloy network in the presence of more voids, defects and grain boundaries. The fraction of the Si–H–Si component in the Si-network is defined as the surface passivation index [55]:

$$S = \frac{[Si-H-Si]}{[SiH] + [Si-H-Si] + [SiH_2]} \quad (7.7)$$

The gradual inclusion of Si-precursors in the plasma encouraged the insertion of H in the film network (**Fig. 7.4(b)**) mostly in the form of highly defective Si-polyhydride, as reflected by the increasing Si structure-factor (R_{Si}) over the Ge structure-factor (R_{Ge}), and the Si–H–Si platelet-like configuration (S) gradually reduced upon increasing the SC (**Fig.**

7.4(d)). Furthermore, the film prepared at SC = 0.3 exhibited a sharp rise in Si-monohydride bonding in the film network (Fig. 7.4(c)) resulting in a sharp decrease in the surface passivation index (S) along with an increased magnitude of C_H, which signified the rapid decrease in the overall crystallinity by virtue of the inclusion of surplus Si in the film network grown under the nc-Ge compatible growth conditions.

Studies on the surface morphologies of the deposited films using atomic force microscopy revealed that the films prepared with different SiH₄ concentrations were comprised of clusters of different size, shape and void fraction, as shown in Fig. 7.5(a) and Fig. 7.5(b) for SC = 0 and 0.1, respectively. The notable presence of large clusters with distinguishable voids supported the significant crystallinity developed in the pure Ge film prepared at SC = 0, whereas the transformation in the surface topography for the film prepared at SC = 0.1 could be correlated to the decrease in the size of the nanocrystals, followed by the diminishing crystalline volume fraction with the cumulative incorporation of Si atoms, as shown in the XRD studies. Statistical analysis of the AFM images has revealed that the root mean square surface roughness decreased monotonically from 9.64 nm for the films prepared at SC = 0 to 5.21 nm upon increasing the SiH₄ concentration to

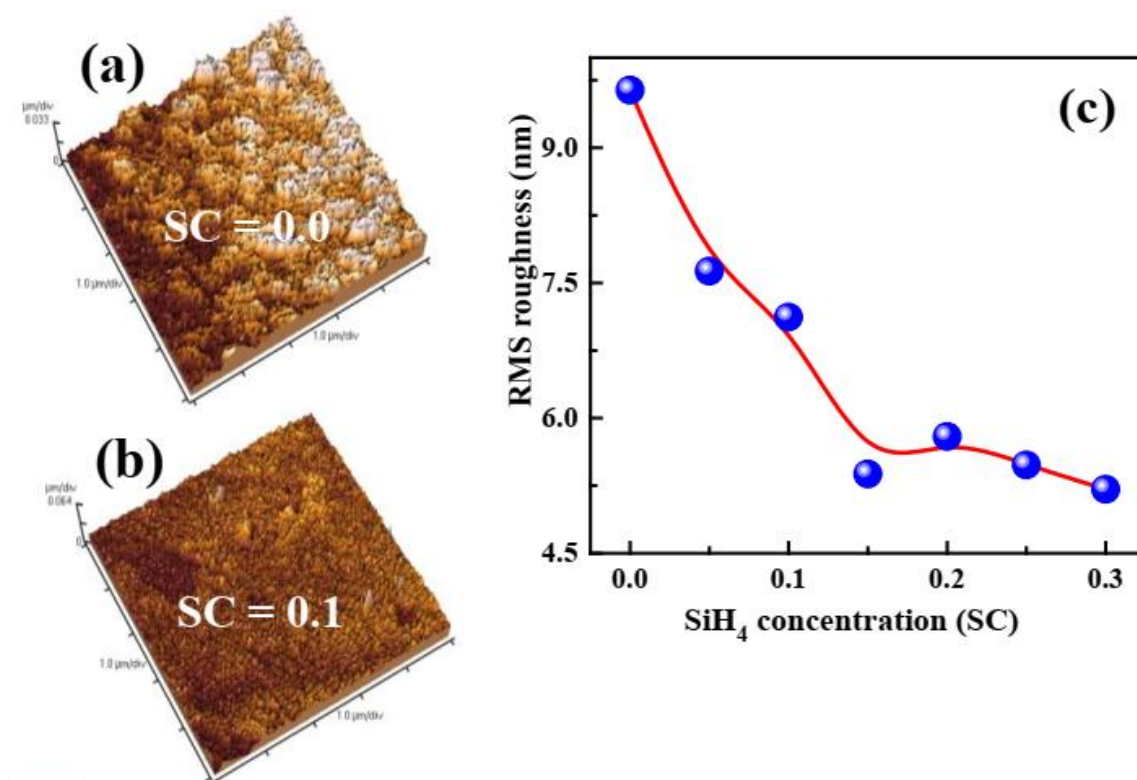


Fig. 7.5. Surface morphologies of the films prepared using two different SiH₄ concentrations: (a) SC = 0 & (b) SC = 0.1. (c) The RMS surface roughness upon increasing the SC estimated from AFM data.

0.3. The variation in the RMS roughness of the film surfaces as a function of the SiH₄ concentration is presented in Fig. 7.5(c). The enhanced inclusion of Si atoms upon increasing the SiH₄ concentration in the film matrix resulted in film surfaces with smaller clusters and consequently, reduced surface roughness.

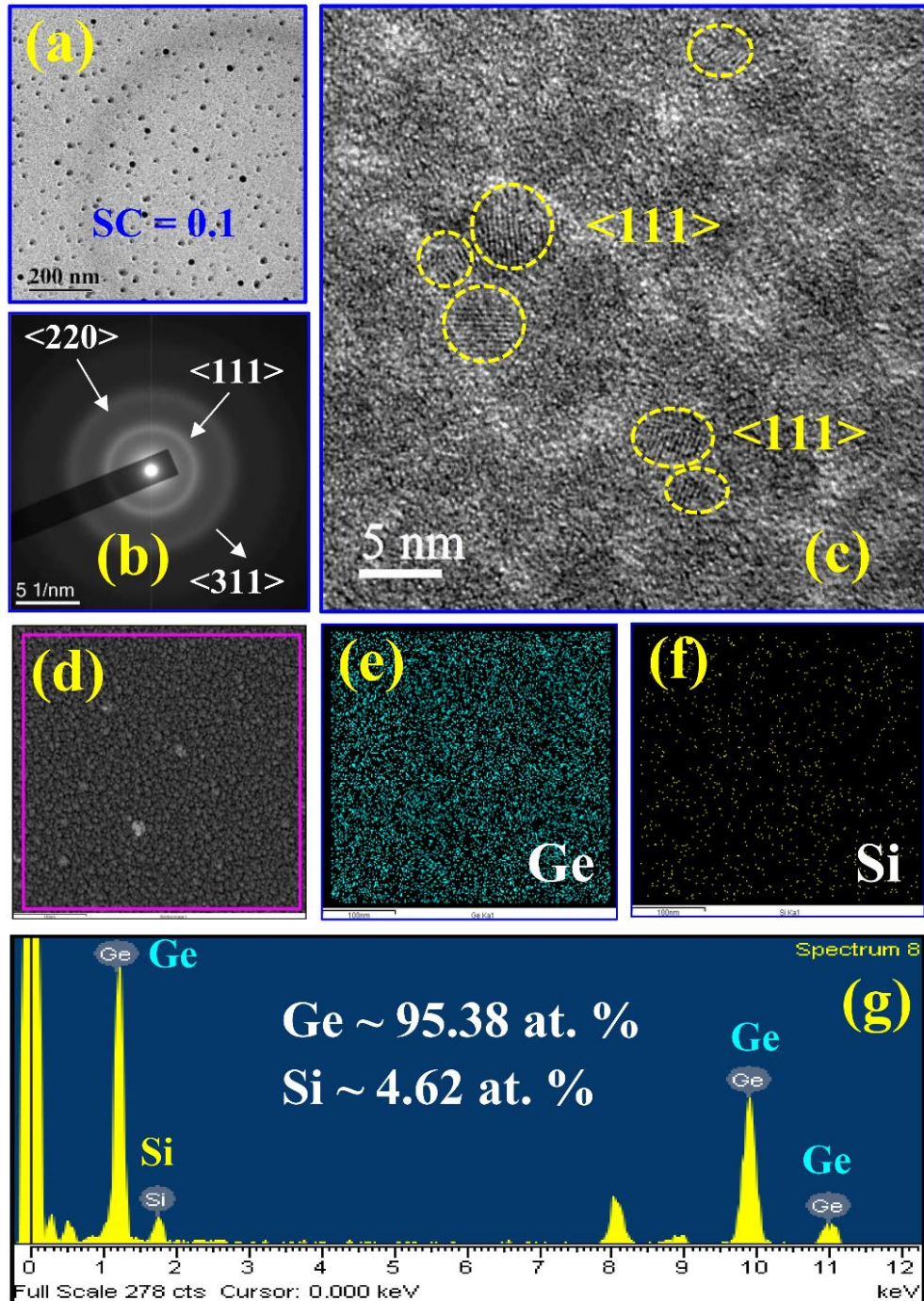


Fig. 7.6. (a) Plane-view bright field HRTEM-image of the film prepared at SC = 0.1, (b) corresponding SAED pattern, (c) magnified TEM images with distinguished planes, (d) selected area dark-field TEM images with elemental mapping of (e) Ge and (f) Si atoms in the film and (g) identification of the elemental components Ge and Si using EDAX.

Fig. 7.6(a) shows a typical plain view HR-TEM image of the nc-Si_xGe_{1-x} thin film prepared at SC = 0.1 in which the bright and dark segments depict the difference between the amorphous and crystalline regions. **Fig. 7.6(b)** shows the transmission electron diffraction (TED) pattern that identifies the bright rings corresponding to the lattice planes of <111>, <220> and <311> of c-Ge. **Fig. 7.6(c)** represents a high magnification image of the same sample prepared at SC = 0.1 in which the prominent crystal planes of the nanocrystalline grains (yellow circled) are visible. The dark-field scanning tunneling electron microscope (DF-STEM) image of the film is shown in **Fig. 7.6(d)**. The elemental composition of the dispersed spherical nanocrystals within the amorphous matrix is revealed. The mapping of the Ge and Si atoms are presented in **Fig. 7.6(e)** and **Fig. 7.6(f)**, respectively, in which the denser distribution of dark cyan spots representing the Ge-atoms in the film network and uniformly distributed less populated yellow spots corresponding to the Si-atoms identify that the sample belongs to a Ge-rich SiGe alloy material. Energy dispersive X-ray spectroscopy (EDS) of the SiGe alloy, shown in **Fig. 7.6(g)**, distinguishes the peaks corresponding to Si and Ge, which were estimated to be ~95.38 and ~4.62 at.%, respectively.

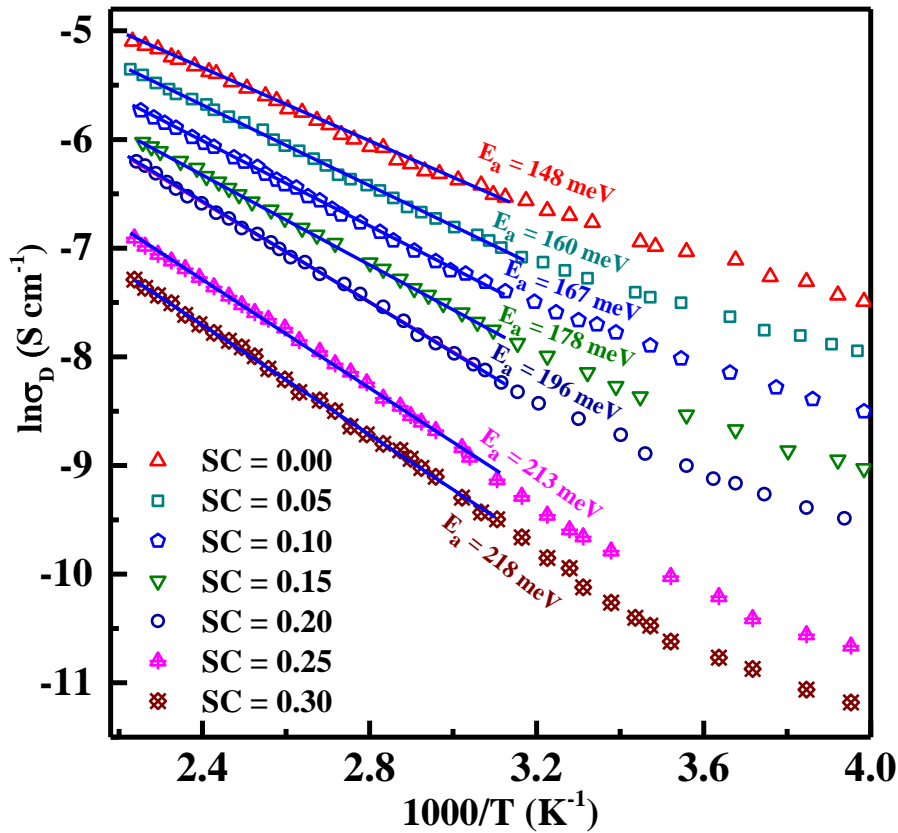


Fig. 7.7. The variation in the temperature-dependent dark conductivity of nc-Si_xGe_{1-x} films.

The electrical properties of the nc-Si_xGe_{1-x} films were examined using temperature dependent dc conductivity studies. **Fig. 7.7** shows the variation in the dark conductivities observed for the series of thin films as a function of the inverse temperature in the range 430–240 K using a logarithmic scale. The activation energies were estimated using least-square straight-line fitting of the dark conductivity data obtained at different temperatures in the range of 430–240 K in the Arrhenius plot using following equation [44,50,56]:

$$\sigma_D(T) = \sigma_0 \exp\left(\frac{-E_a}{k_B T}\right) \quad (7.8)$$

where E_a is the activation energy and σ_0 is the pre-exponential factor of the dark conductivity.

Fig. 7.8 shows the variation in the dark conductivity at room temperature and the activation energy of the films. The nc-Ge film prepared at SC = 0 exhibited a very high dark conductivity of $\sigma_D \sim 1.15 \times 10^{-3} \text{ S cm}^{-1}$ along with a low activation energy, $E_a \sim 148 \text{ meV}$. After the initial introduction of Si into the network at SC = 0.05, σ_D reduced substantially to $\sigma_D \sim 6.31 \times 10^{-4} \text{ S cm}^{-1}$, along with an increased activation energy ($E_a \sim 160 \text{ meV}$). On further increasing the SiH₄ concentration to 0.3, σ_D decreased to $\sim 5.13 \times 10^{-5} \text{ S cm}^{-1}$ along with an additional escalation in the activation energy ($E_a \sim 218 \text{ meV}$). **Fig. 7.8** shows that for SC > 0.15, the σ_D reduced relatively promptly along with a rapid increase in the

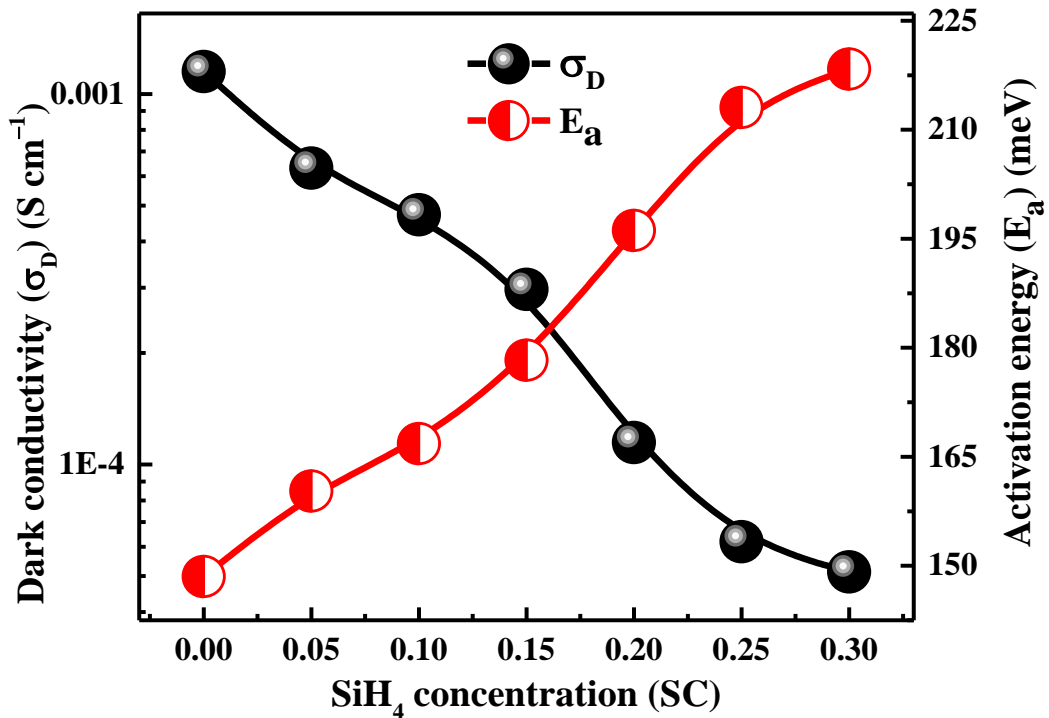


Fig. 7.8. Room-temperature dark conductivity and activation energy (E_a) of the films as a function of the SiH₄ concentration (SC).

activation energy as a consequence of the quick amorphization of the network by virtue of the abundant Si atoms incorporated into the Ge-Ge network.

7.4 Discussion

In PECVD, the composition and internal microstructure of the film depends on the individual decomposition kinetics, reactivity and stay-time of the reactant gases in the plasma under specific conditions. GeH₄ dissociates much faster than SiH₄ in the plasma because of the lower dissociation energy of GeH₄ (~164.5 kJ/mol) compared to SiH₄ (~234.5 kJ/mol) [24]. Accordingly, the optimum plasma parameters compatible for the growth of nc-Ge are grossly different from that of nc-Si growth. The growth mechanism in SiH₄/GeH₄ mixed plasma consists of radicals originating from the dissociation of the two precursor gases via individual reaction pathways [53,54,57]. Hence, to obtain a good quality nc-SiGe network, a critical balance of the plasma parameters, such as the applied electrical power, gas pressure in the plasma, growth temperature and optimum ratio of the precursor gases (SiH₄/GeH₄), is required.

In the conventional growth process, the inclusion of GeH₄ in a SiH₄-rich gas mixture under nc-Si compatible growth conditions results in the dominant consumption of the plasma excitation energy by the GeH₄ molecules and inevitably leads to a film network with random and excess Ge-Ge bonds accumulated over the Si-Ge and Si-Si bonds. The GeH₃ and GeH₂ radicals, which are heavier and stickier than SiH₃ and SiH₂, lead to Ge-dominated random growth hindering the network's nanocrystallinity and thereby, increase the carrier recombination center density [51,58].

On the contrary, in a GeH₄-rich gas mixture under nc-Ge compatible growth conditions, the probability for the decomposition of SiH₄ is smaller than that of GeH₄. Accordingly, by virtue of lower dissociation rate of SiH₄, the Si-content in the film does not abruptly increase, which becomes beneficial for maintaining adequate nanocrystallinity in the nc-SiGe network in the present work. Increasing the concentration of SiH₄ in the gas mixture increases the Si-Ge and Si-Si bonds within the Ge-Ge bond dominated film network. Because the growth parameters were maintained at nc-Ge compatible plasma conditions, the inclusion of Si into the Ge-Ge network prompts the system towards its less thermodynamically preferred state and a subsequent gradual decrease in the growth of the energetically favored <220> crystallographic orientation when compared to its <111>

counterpart. Furthermore, such deterioration in the <220> crystallographic orientation is relatively slow when compared to the state of affairs when Ge is included into the Si-Si network under nc-Si compatible plasma conditions because of the faster dissociation rate of GeH₄, as discussed above [25].

The usability of a semiconducting material in a stacked-layer photovoltaic device is primarily determined by two fundamental properties: i) The electrical conductivity and ii) optical band gap. Generally, the arbitrary incorporation of Ge in the nc-Si film network efficiently reduces its band gap, but an associated substantial decay in dark conductivity due to random alloying limits its usability. In this regard, a comparison was carried out as shown in Fig. 7.9, in terms of the dark conductivity vs. optical band gap of the different intrinsic nc-SiGe thin films produced at low temperature using PECVD, as reported in the literature. In our earlier report on nc-SiGe films prepared under nc-Si compatible growth parameters using RF-PECVD, the narrowing of the optical band gap from 1.66 to 1.50 eV was associated to an increase in the dark conductivity from $2.6 \times 10^{-5} \text{ S cm}^{-1}$ to $2.4 \times 10^{-3} \text{ S cm}^{-1}$. Further allowing by Ge, however, resulted in the amorphization of the network and the subsequent reduction in σ_D [23]. Using different Ar/H₂ dilutions, Tang *et al.* [59] prepared nc-SiGe films in which the optical band gap changed between 1.42–1.55 eV upon varying the electrical conductivity in the range of 1×10^{-3} to $5 \times 10^{-4} \text{ S cm}^{-1}$. Xui *et al.* [60] reported

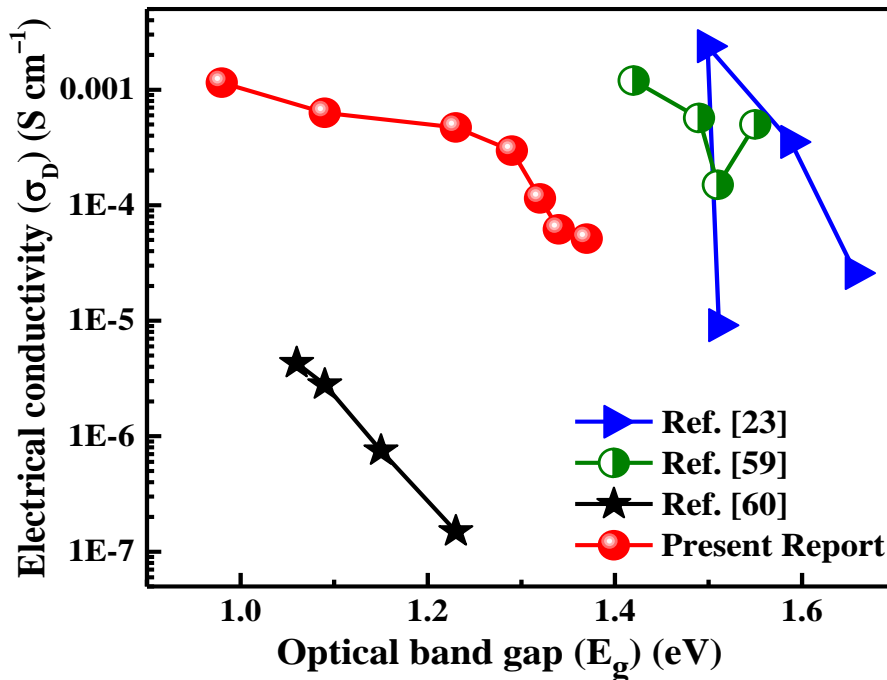


Fig. 7.9. A comparison of the room temperature dark conductivity (σ_D) vs optical band gap (E_g) data for the various nc-Si_xGe_{1-x} thin films available from past works.

the nanocrystalline SiGe alloy with varying optical band gaps within 1.06–1.23 eV that exhibited dark conductivity in the range of $4.3 \times 10^{-6} - 1.5 \times 10^{-7} \text{ S cm}^{-1}$. The present set of nc-Si_xGe_{1-x} ($x \geq 0$) films maintain very good nanocrystallinity with remarkably low optical band gap over a wide range (0.98–1.37 eV) and a combination of significant electrical conductivity in the range of $1.1 \times 10^{-3} - 5.1 \times 10^{-5} \text{ S cm}^{-1}$, in which the material deserves extensive attention for a wide range of applications in opto-electronic devices, particularly tandem structure nc-Si solar cells.

7.5 Conclusions

nc-Si_xGe_{1-x} thin films were prepared via the efficient incorporation of Si within the highly nanocrystalline Ge network and the samples were explicitly studied using structural, optical and electrical characterization methods. Si incorporation in the nc-Ge matrix shows a decrease in the crystallite grain size and the overall crystallinity of the films. The average size of the grains with <111> crystallographic orientation was found to be $17.4 > d \text{ (nm)} > 12.8$ for $0.0 \leq SC \leq 0.3$, while that for the <220> orientation reduced more prominently from 23.3 to 8.8 nm with their corresponding $I_{<220>}/I_{<111>}$ ratios reduced from 1.71 to 0.64. Upon increasing the concentration of SiH₄ in the plasma, $SC = [\text{SiH}_4]/[(\text{GeH}_4) + (\text{SiH}_4)]$, from 0 to 0.3, the band gap of the film increased from 0.98 to 1.37 eV supplemented by a decrease in the dark conductivity from 1.15×10^{-3} to $5.13 \times 10^{-5} \text{ S cm}^{-1}$. The nc-Si_xGe_{1-x} film with the optimal low band gap of $E_g \sim 1.23 \text{ eV}$ and high dark conductivity of $\sigma_D \sim 4.72 \times 10^{-4} \text{ S cm}^{-1}$, corresponding to $SC = 0.1$ appeared to be appropriate for the absorber layer at the bottom sub-cell of the nc-Si tandem structure solar cells. In the present investigation, it has been confirmed that under nc-Ge compatible growth conditions, the decomposition of SiH₄ in (GeH₄ + SiH₄) plasma occurs in a controlled manner that is beneficial for sustaining the nanocrystallinity in the binary SiGe alloy containing a Ge-dominated atomic composition that can provide the required infrared response and electrical transport for strategic applications in photovoltaics.

7.6 References

- [1] A. Shah, P. Torres, R. Tscharnner, N. Wyrsh, H. Keppner, Science 285 (1999) 692–698.
- [2] D. Das, C. Patra, Mater. Adv. 2 (2021) 2055–2067

- [3] M. Zeman, O. Isabella, S. Solntsev, K. Jager, *Sol. Energy Mater. Sol. Cells* 119 (2013) 94–111.
- [4] R. Biron, S. Hänni, M. Boccard, C. Pahud, K. Söderström, M. Duchamp, R. DuninBorkowski, G. Bugnon, L. Ding, S. Nicolay, G. Parascandolo, F. Meillaud, M. Despeisse, F.J. Haug, C. Ballif, *Sol. Energy Mater. Sol. Cells* 114 (2013) 147–155.
- [5] D. Das, P. Mondal, *Appl. Surf. Sci.* 416 (2017) 980–987.
- [6] L. Karmakar, D. Das, *Sol. Energy Mater. Sol. Cells* 206 (2020) 110278.
- [7] D. Das, L. Karmakar, *Nanoscale*, 12 (2020) 15371.
- [8] J. Yang, A. Banerjee, S. Guha, *Sol. Energy Mater. Sol. Cells* 78 (2003) 597–612.
- [9] B. Yan, G. Yue, X. Xu, J. Yang, S. Guha, *Phys. Status Solidi*, 207 (2010) 671.
- [10] S. Guha, J. Yang, B. Yan, *Sol. Energy Mater. Sol. Cells* 119 (2013) 1–11.
- [11] X. Deng, X. Cao, Y. Ishikawa, W. Du, X. Yang, C. Das, A. Vijn, *IEEE 4th World Conf. on Photovoltaic Energy Conversion*, 2006.
- [12] A. Chowdhury, S. Mukhopadhyay, S. Ray, *Thin Solid Films* 516 (2008) 6858–6862.
- [13] A.V. Shah, J. Meier, E. Vallat-Sauvain, N. Wyrsh, U. Kroll, C. Droz, U. Graf, *Sol. Energy Mater. Sol. Cells* 78 (2003) 469–491.
- [14] S. Pizzini, *Advanced silicon materials for photovoltaic applications*, Wiley, (2012).
- [15] G. Ganguly, T. Ikeda, T. Nishimiya, K. Saitoh, M. Kondo, A. Matsuda, *Appl. Phys. Lett.* 69 (1996) 4224.
- [16] J. Ni, Q. Liu, J. Zhang, J. Ma, H. Wang, X.D. Zhang, Y. Zhao, *Sol. Energy Mater. Sol. Cell.* 126 (2014) 6–10.
- [17] T. Matsui, H. Jia, M. Kondo, *Prog. Photovolt. Res. Appl.* 18 (2010) 48–53.
- [18] L. Zhang, J. Zhang, X. Zhang, Y. Cao, Y. Zhao, *Thin Solid Films* 520 (2012) 5940–5945.
- [19] Y. Cao, J. Zhang, C. Li, T. Li, Z. Huang, J. Ni, Z. Hu, X. Geng, Y. Zhao, *Sol. Energy Mater. Sol. Cells* 114 (2013) 161–164.
- [20] T. Matsui, C.W. Chang, T. Takada, M. Isomura, H. Fujiwara, M. Kondo, *Sol. Energy Mater. Sol. Cells* 93 (2009) 1100–1102.
- [21] T. Matsui, M. Kondo, K. Ogata, T. Ozawa, M. Isomura, *Appl. Phys. Lett.* 89 (2006) 142115.

- [22] Y. Cao, Y. Liu, J. Zhou, Y. Wang, J. Ni, J. Zhang, *Sol. Energy Mater. Sol. Cells* 151 (2016) 1–6.
- [23] A. Dey, D. Das, *J. Alloys Comp.* 806 (2019) 1529–1535.
- [24] D. Polino, A. Barbato, C. Cavallotti, *Phys. Chem. Chem. Phys.* 12 (2010) 10622–10632.
- [25] D. Das, A. Dey, *Physica E: Low-dimensional Systems and Nanostructures* 111 (2019) 20–28.
- [26] T. Li, J. Zhang, Y. Ma, Y. Yu, Y. Zhao, *Mod. Phys. Lett. B* 31 (2017) 1740010.
- [27] S. Kim, C. Park, J.C. Lee, J.S. Cho, Y. Kim, *Curr. Appl. Phys.* 13 (2013) 457–460.
- [28] S. Arvind, *Thin-film silicon solar cells*, EPFL Press, Boca Raton, (2010) pp. 79.
- [29] M. Stutzmann, R.A. Street, C.C. Tsai, J.B. Boyce, S.E. Ready, *J. Appl. Phys.* 66 (1989) 569–592.
- [30] C.W. Chang, T. Matsui, M. Kondo, *J. Non-Cryst. Solids* 354 (2008) 2365–2368.
- [31] M. Krause, H. Stiebig, R. Carius, U. Zastrow, H. Bay, H. Wagner, *J. Non-Cryst. Solids* 158 (2002) 299–302.
- [32] J.K. Rath, F.D. Tichelaar, R.E.I. Schropp, *Sol. Energy Mater. Sol. Cells* 74 (2002) 553–560.
- [33] A. Kosarev, A. Torres, Y. Hernandez, R. Ambrosio, C. Zuniga, T.E. Felter, R. Asomoza, Y. Kudriavtsev, R. Silva-Gonzalez, E. Gomez-Barojas, A. Ilinski, A.S. Abramov, *J. Mater. Res* 21 (2006) 88.
- [34] M.I. Alonso, K. Winer, *Phys. Rev. B* 39 (1989) 10056.
- [35] Y. Huang, H. Hsu, S. Liang, C. Hsu, C. Tsai, *Int. J. Photoenergy* 2014 (2014) 579176.
- [36] T.W. Li, Y.Q. Xu, S.Y. Wang, Y.W. Yu, Y. Ma, W.Y. Niu, *IOP Conf. Series: Mater. Sci. Eng.* 761 (2020) 012005.
- [37] D. Kar, D. Das, *J. Mater. Chem. A* 1 (2013) 14744.
- [38] A. Banerjee, D. Das, *Appl. Surf. Sci.* 330 (2015) 134–141.
- [39] M.A. Renucci, J.B. Renucci, M. Cardona, “Light Scattering in Solids”, ed. M.A. Balkanski (Flammarion, Paris, 1971), pp. 326–329.
- [40] M. Isomura, K. Nakahata, M. Shima, S. Taira, K. Wakisaka, M. Tanaka, S. Kiyama, *Sol. Energy Mater. Sol. Cells* 74 (2002) 519–524.

- [41] T. Tah, C.K. Singh, S. Amirthapandian, K.K. Madapu, A. Sagdeo, S. Ilango, T. Mathews, S. Dash, *Mater. Sci. Semicond. Process.* 80 (2018) 31–37.
- [42] S.F. Ren, W. Cheng, P.Y. Yu, *Phys. Rev. B* 69 (2004) 235327.
- [43] C.J. Fang, K.J. Gruntz, L. Ley, M. Cardona, F.J. Demond, G. Muller, S. Kalbitzer, *J. Non-Cryst. Solids* 35-36 (1980) 255–260.
- [44] K.D. Mackenzie, J.R. Eggert, D.J. Leopold, Y.M. Li, S. Lin, W. Paul, *Phys. Rev. B* 31 (1985) 2198.
- [45] B. Sain, D. Das, *Sci. Adv. Mater.* 5 (2013) 188–198.
- [46] D. Das, *Jpn. J. Appl. Phys.* 33 (1994) L 571–574.
- [47] D. Raha, D. Das, *J. Phys. D Appl. Phys.* 41 (2008) 085303.
- [48] A. Samanta, D. Das, *J. Electrochem. Soc.* 158 (2011) H1138–H1144.
- [49] D. Kar, D. Das, *J. Appl. Phys.* 120 (2016) 025102.
- [50] C. Patra, D. Das, *J. Appl. Phys.* 126 (2019) 155305.
- [51] S. Hazra, A.R Middy, S. Ray, *J. Phys. D: Appl. Phys.* 29 (1996) 1666–1674.
- [52] D. Das, P. Mondal, *Appl. Surf. Sci.* 423 (2017) 1161–1168.
- [53] D. Das, M Jana, *Sol. Energy Mater. Sol. Cells* 81 (2004) 169–181.
- [54] F. J. Kampas, *Semicon. Semimet. A* 21 (1984) 153–177.
- [55] S. Samanta, D. Das, *J. Phys. Chem. Solids* 105 (2017) 90–98.
- [56] D. Das, B. Sain, *J. Appl. Phys.* 114 (2013) 073708.
- [57] J. R. Doyle, D.A. Doughty, A. Gallagher, *J. Appl. Phys.* 71 (1992) 4727.
- [58] D. Das, S.C. De, S. Ray, A.K. Batabyal, A.K. Barua, *J. Non-Cryst. Solids* 114 (1989) 552–554.
- [59] Z. Tang, W. Wang, D. Wang, D. Liu, Q. Liu, D. He, *J. Alloys Comp.* 504 (2010) 403–406.
- [60] R. Xu, W. Li, J. He, Y. Sun, Y.D. Jiang, *J. Non-Cryst. Solids* 365 (2013) 37–41.



Chapter 8

**Low temperature synthesis of
nc-SiGe:H thin films
prepared in sputtering technique
for nc-Si tandem solar cell**

8.1 Introduction

In the last few decades, careful attention has been paid to the upgradation of nc-Si thin-film technologies in view of their commercialization through increasing their efficiency and reducing production costs [1–3]. The nc-Si thin film solar cell lacks efficiency compared to crystalline silicon solar cells [4]. Accordingly, tandem-structure design has been implemented in photovoltaic technology to use the broader part of the sunlight [5,6]. It demands a narrow-band gap material to absorb the infrared wavelength of the sunlight in the bottom cell of the multi-junction nc-Si thin film solar cell. Primarily, nc-Si with a moderately low band gap was used here, but it lacks a good absorption coefficient in the infrared wavelength. Therefore, it contradicts the low-cost manufacturing strategy as it requires an increased layer thickness for efficient absorption of sunlight. Later, amorphous silicon-germanium thin film appeared as alternative material with improved light absorption properties, specifically in the infrared wavelength region. In recent years, nanocrystalline silicon-germanium (nc-SiGe) thin film has attracted attention as the bottom sub-cell material. It has good infrared absorption capabilities and reduced light-induced degradation properties compared to a-SiGe [7–9]. The nc-SiGe film is conventionally prepared by the plasma-enhanced chemical vapour deposition method, in which harmful toxic gases like GeH_4 and SiH_4 are used as source gases [18–20]. These toxic gases have a negative environmental impact, whereas the sputtering technique is an alternate and environment-friendly method to prepare SiGe thin films. In the conventional method, two separate Si and Ge sputtering targets are used to grow the SiGe thin film. In this process, the nanocrystallization in the SiGe thin films occurs via solid-phase crystallization (SPC) that demands a high thermal budget as the Ge and Si both possess considerably high melting points of 937 °C and 1414 °C, respectively [21,22]. It follows higher production costs and limits its usefulness in stacked-layer device applications and use of low-cost substrates with lower melting points. Therefore, in most studies on SiGe alloy thin films deposited in the sputtering process available in the literature, post-deposition high-temperature annealing or laser-induced annealing is used to develop nanocrystallinity in the films [23–27]. In that consideration, the strategic use of an nc-Si wafer partially covering a Ge target is attempted to grow nc-SiGe alloy thin film. It can be beneficial for the crystallization of the alloy network as Si moieties can be included in the film matrix in the form of Si-nanocrystallites from the nc-Si wafer in nc-Ge growth compatible conditions. It imposes

a less persistent hindrance in attaining nanocrystallinity in the alloy film network. Many dangling bond related defects and structural disorders originate in the growth of binary alloy SiGe film in the sputtering by Ar gas, which sets back the nanocrystallization process across the material. Using H₂ gas with Ar reduces the defect density and disorders in the film matrix through hydrogen passivation and improves the crystallization [23]. Accordingly, the present investigation deals with the low-temperature synthesis (~250 °C) of nc-SiGe by using a combined nc-Si wafer and Ge target in (Ar+H₂) plasma. The microstructural and optoelectronic properties of the prepared nc-SiGe thin films have been studied in detail.

8.2 Experimental details

A 13.56 MHz RF-magnetron sputtering system is used to deposit intrinsic silicon germanium (SiGe) films on Corning®Eagle 2000™ glass substrates at a temperature of ~250 °C. The deposition system consists of a circular planar sputter source (KJ Lesker, USA) with a diameter of 76 mm with Cu backing plate (Vin Karola, USA). The effective erosion area of the target was roughly a circular band having an outer radius and an inner radius of 25 mm and 15 mm, respectively. Four Si strips (lightly doped *n*-type, of the shape of a quarter circle with a radius of approximately 30 cm) are used to partially cover the Ge sputtering target (purity 99.999%). The surface area opening on the Ge target with the Si strips (Ψ) was varied to change the composition of the deposited SiGe films. The ejection of Ge atoms is considered to be proportional to the exposed area (in %) of the Ge target to the plasma through the gap between the Si strips. The c-Si strips used as the target have been cleaned with conventional RCA cleaning followed by etching with 5% HF for 30 s and then dried with N₂ gas to ensure the elimination of surface oxide before being mounted in the deposition chamber. The chamber pressure is kept at 50 mTorr during the deposition, using 1 sccm of Ar as the sputtering gas and 10 sccm of H₂ as the diluent gas. The base vacuum of the sputtering chamber is kept at ~10⁻⁶ Torr before the deposition, using a diffusion pump backed by a rotary pump. The substrate holder, placed at a distance of 6 cm from the sputtering target, is rotated at 10 rev/min to have a uniform deposition of the films. A K-type thermocouple is associated with the substrate holder (in non-rotating mode) to get the exact temperature of the substrate. The temperature is controlled and monitored using an automated temperature controller. A quartz crystal monitor (Sycon Thickness Monitor, Model STM-100/MF) is placed in the vicinity of the growth site to monitor the film thickness of 250 nm. The thickness of the films is further

cross-verified using a Dektak stylus 6M profilometer, within a deviation limit of 2%. The X-ray diffraction studies of the films have been done using a Seifert 3000P Bragg diffraction set-up, applying Cu-K α X-ray ($\lambda = 1.5418 \text{ \AA}$) radiation. High-resolution transmission micrographs of the films grown on carbon-coated Cu micro-grids have been obtained in FEG-HRTEM (JEOL 2100 TEM/STEM transmission electron microscope) driving at 200 kV. Furthermore, the energy dispersive X-ray data recorded in the HRTEM studies is used to estimate the elemental composition of the films.

8.3 Results and discussion

The X-ray diffraction pattern presented in **Fig. 8.1** illustrates a continuous change in the structural morphology of the prepared SiGe films with the increase in the surface area opening (Ψ) of the intrinsic Ge target. The XRD peaks corresponding to $\langle 111 \rangle$, $\langle 220 \rangle$ and $\langle 311 \rangle$ planes of crystalline Si at $2\theta \sim 27.15^\circ$, 45.2° and 53.6° were detected for the pure Si sample where the $\langle 111 \rangle$ lattice plane results from the random nucleation and $\langle 220 \rangle$ plane arises from the thermodynamically favoured growth [28]. The

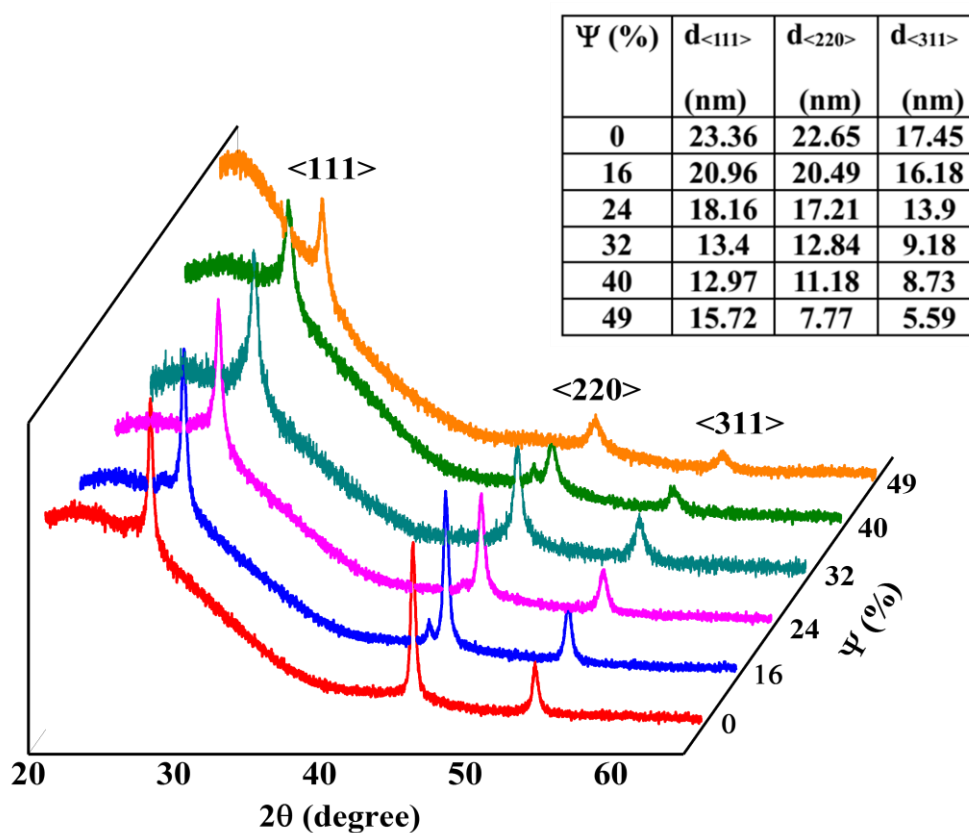


Fig 8.1. XRD diffraction spectra of the SiGe films grown at different Ψ , with average grain size given in the table in the inset.

intensities of all the peaks gradually decreased along with an increase in their full-width half maximum (FWHM) with an increase in the Ge incorporation in the film. The average size of the nanocrystals (d) was estimated according to Scherrer's formula [29]:

$$d = \frac{0.9 \lambda}{\beta \cos \theta} \quad (8.1)$$

where λ is the wavelength of X-ray, and β is the FWHM of the corresponding XRD peaks. The variation of the grain size with the increase in the Ψ , is presented in the inset of Fig. 8.1. The average size of the $\langle 111 \rangle$ crystallographic oriented nanocrystallites was reduced monotonically from 23.36 nm to 12.97 nm and the size of the grains with $\langle 220 \rangle$ orientation was reduced from 22.65 nm to 7.77 nm. In addition, a systematic shift of the peak positions to the lower diffraction angle is observed due to the inclusion of more Ge atoms in the film matrix and associated change in the lattice parameter. The proportional strength of the intensity of the $\langle 220 \rangle$ peaks with the intensity of the $\langle 111 \rangle$ peaks was decreased with an increase in the relative strength of the Ge in the composition of the film.

Fig. 8.2 displays the Raman spectra for the SiGe films prepared at different compositions by the sputtering method, where a single sharp peak was observed with its centre at $\sim 514 \text{ cm}^{-1}$ for the nc-Si sample. Ge-Ge and Si-Ge bonding vibrations arise in the Raman spectra with the introduction of an exposed area of the Ge target. Further

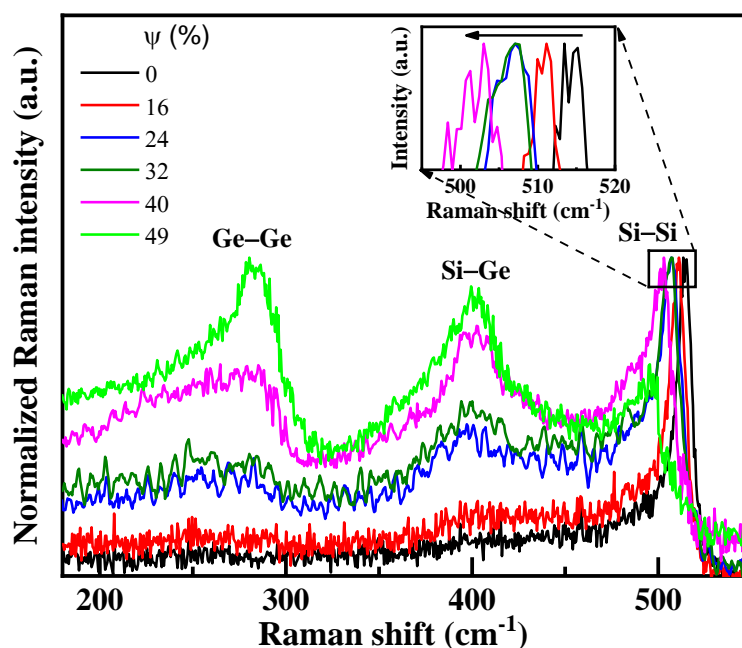


Fig 8.2. Raman spectra of the SiGe films grown at different area opening of Ge target covered by Si wafer strips and the shift of the Si-Si peak shown in the inset.

increase in the exposed area of the Ge target resulted in strengthening the relative intensity of the Ge–Ge and the Si–Ge peak regarding the intensity of the Si–Si peak. Three characteristic Raman peaks were detected for the sample prepared with Ge as $\Psi \geq 24\%$: Ge–Ge peak at about 285 cm^{-1} , Si–Ge peak centred at 400 cm^{-1} and the Si–Si peak at 503 cm^{-1} [9]. The gradual blue shift in the Si–Si peak (as illustrated in the inset of **Fig. 8.2**) with the strain induced within the network due to the tensile stress because of the lattice mismatch due to larger size of the Ge atoms than that of the Si atoms and proportional to the amount of Ge atoms incorporated in the network. The full width half maximum (FWHM) of the Ge–Ge peak is quite large for the films with minimal Ge content.

The Raman spectra for the films prepared with surface area opening of Ge target, $\Psi = 24\%$ and $\Psi = 40\%$ were deconvoluted in all possible satellite components corresponding to the different bonding configurations of (Si,Ge)–(Si,Ge) with their amorphous and crystalline counterparts, as shown in **Fig. 8.3**. The Si–Ge band is composed of different satellite components arising from the vibrations of Si and Ge atoms bonded with different configurations in the form of Si–Si_nGe_{4-n} [30]. It is noted

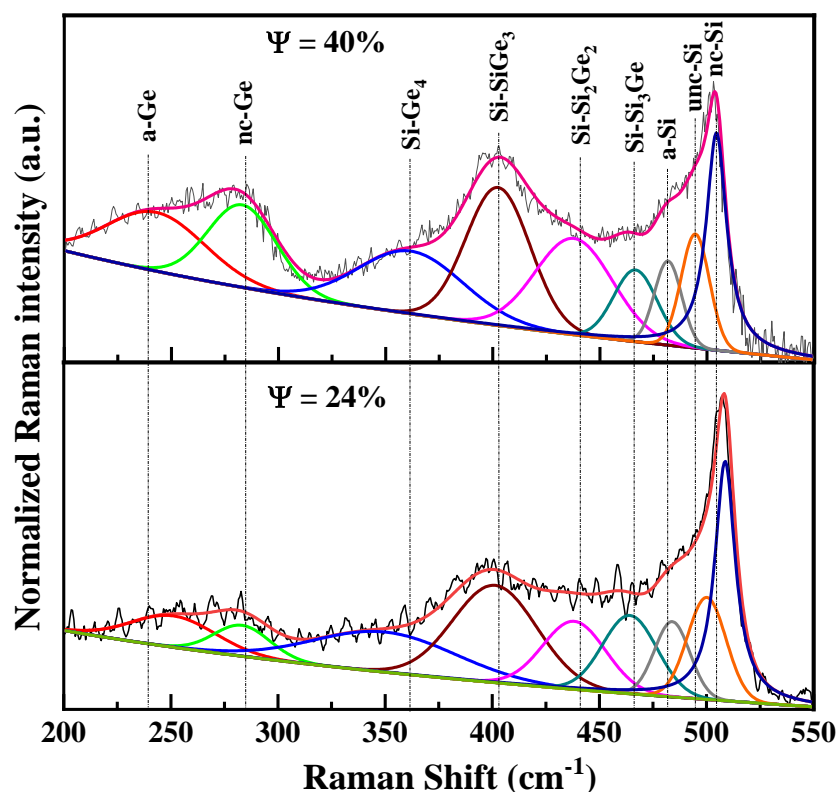


Fig 8.3. Deconvoluted Raman spectra obtained for the SiGe films prepared with (a) $\Psi = 40\%$, (b) $\Psi = 24\%$.

that the Ge–Ge peak became more asymmetric as the surface area of the Ge target increased due to the strengthening of the nanocrystalline counterpart of the Ge–Ge peak compared to its amorphous network. The intensity of the Si–Si peak decreased significantly along with strong Ge–Ge peak with its governing crystalline counterpart (at $\sim 285\text{ cm}^{-1}$) for the film prepared with surface area opening of the Ge target ($\Psi = 49\%$), indicating a gross reduction in the Si content within the film resulting in the growth of Ge-dominated nanocrystalline silicon-germanium network. So, the hetero-structured nc-SiGe binary alloy is transformed to a Ge-dominated network from a Si-rich network, with the increase in the Ψ . The sharp increase in the relative intensity of the Ge-Ge peak along with reduced peak width indicated the crystallization in the Ge-Ge network.

The deviations in the optical properties of the nc-SiGe thin films with the variation in the composition were studied by UV-Vis spectroscopy. The absorption coefficient (α) of the films were estimated from the transmission spectra using the following relation:

$$\alpha = \frac{1}{d} \ln \left(\frac{1}{T} \right) \quad (8.2)$$

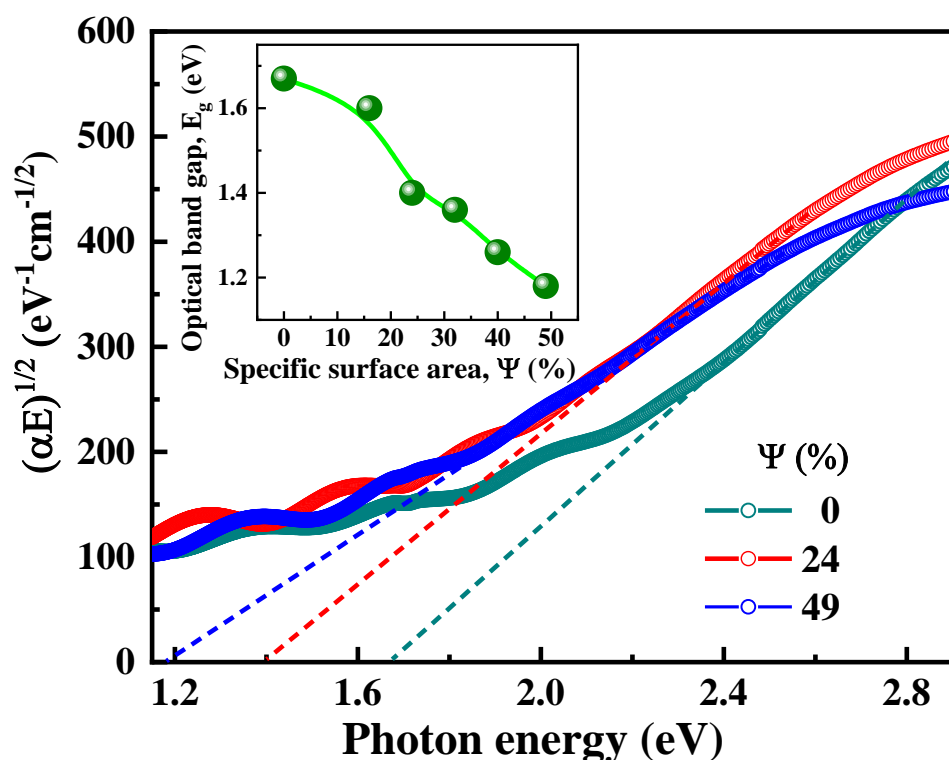


Fig. 8.4. Variation in the Tauc's plot with the change in the Ge content via an increase in the specific surface area of Ge target (Ψ) and the corresponding modification in the band gap is presented in the inset.

where the film's transmittance is T at a particular wavelength and d is the thickness of the film. Being an indirect band gap material, the optical band gap of the nc-SiGe thin films have been assessed using the conventional approach for estimating the band gap of other nc-Si alloy thin films [31,32], following the Tauc's relation ($\sqrt{\alpha hv}$ vs. hv) [33],

$$(\alpha hv)^{1/2} = B(hv - E_g) \quad (8.3)$$

where α is the absorption coefficient and B stands for Tauc's constant. The Tauc's plots are represented in **Fig. 8.4**. The optical band gap gradually reduced from 1.67 eV to 1.18 eV with increasing the Ge target's surface area opening (Ψ) from 0 to 49%, as revealed in the inset of **Fig. 8.4**.

The chemical bonding arrangements of H with Si and Ge in the nc-SiGe thin films produced with different Ψ , were thoroughly explored using the Fourier transformed infrared absorption spectra. **Fig. 8.5(a)** represents the deconvoluted spectra in the wavenumber region 500–700 cm^{-1} for the SiGe films. The film deposited at $\Psi = 0\%$, i.e., for the nc-Si film, exhibited a Gaussian component corresponding to the Si–H wagging mode centred at $\sim 620 \text{ cm}^{-1}$. The absorption spectra for the films prepared with $\Psi \geq 16\%$ detected another satellite component centred at $\sim 570 \text{ cm}^{-1}$ corresponding to the Ge–H vibrations. The integrated areas under the Ge–H peak were increased with an associated decrease in the integrated areas under the Si–H, increasing the Ge specific surface area in the target. The total hydrogen content (C_H) of the films is the sum of the hydrogen bonded with Ge and Si as estimated using the integrated areas of the individual satellite peaks corresponding to the wagging modes of Ge–H and Si–H, following the equation [34]:

$$C_H = (A_\omega / N_{Si}) \int \alpha d\omega / \omega \times 100 \text{ at. \%} \quad (8.4)$$

where the oscillator strengths corresponding to the wagging modes of Si and Ge are presented by $A_\omega = 1.6 \times 10^{19} \text{ cm}^{-2}$ and $A_\omega = 1.1 \times 10^{19} \text{ cm}^{-2}$, respectively, and $N_{Si} = 5 \times 10^{22} \text{ cm}^{-3}$ is the atomic density of crystalline silicon [35,36]. The magnitude of C_H is found as 8.34% for the nc-Si film prepared at $\Psi = 0\%$. **Fig. 8.5(b)** shows the variation in the total bonded hydrogen content (C_H) in the films, in which it decreases from 8.34% to 3.3% with increase in Ge content in the film. One of the main reasons behind the variation in the hydrogen content in the SiGe films is difference in hydrogen solubility/diffusion in the Si–Si, Si–Ge and Ge–Ge bonds which varies essentially with the different

composition of the microstructure of the films [9]. This uneven distribution of hydrogen in different kinds of the network is regulated by the fact that the binding energy of Si–H

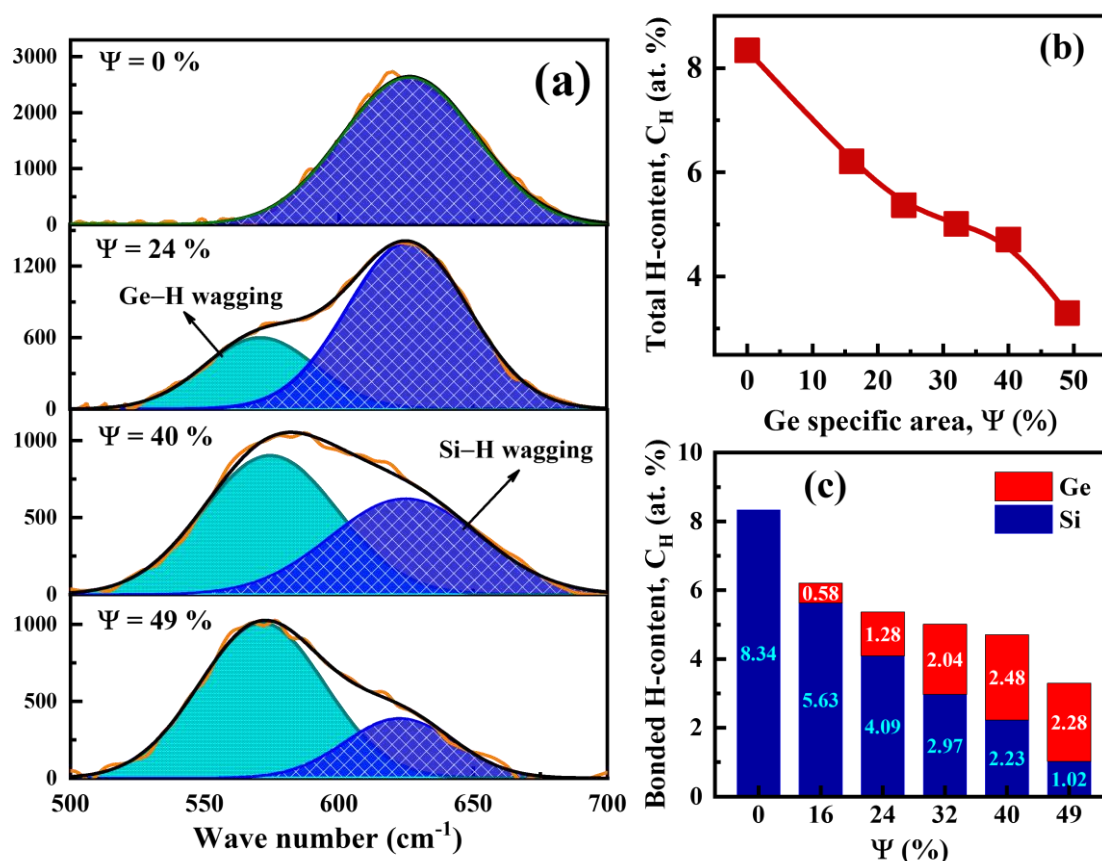


Fig. 8.5. (a) Deconvoluted FTIR spectra in the range 500–700 cm⁻¹. (b) Variation of the total bonded hydrogen content in the film matrix with Ψ . (c) Bar diagram showing the individual contribution of hydrogen bonded with the Ge and Si in the C_H.

is smaller than that of Ge–H, which fundamentally enhances the probability of attachment of hydrogen with Si than Ge [37]. In addition, the crystalline volume fraction in the different networks in the heterostructure of binary alloy strongly affects the bonded hydrogen content. **Fig. 8.5(c)** shows the relative change in the quantity of hydrogen bonded with Ge and Si in the film network. In the bar diagram, it was observed that the hydrogen-bonded with Si monotonically reduced with Ψ , whereas, the hydrogen bonded with the Ge was increased to 2.48 at. % at $0 \leq \Psi \leq 40\%$, after which it was diminished to 2.28% on further elevation in Ψ . This is due to the elevated increase in the proportion of the Ge–Ge and Si–Ge bonds over the Si–Si bonds, and the C_H was further declined due to the less solubility of the bonded hydrogen in the nanocrystalline Ge–Ge matrix, as observed with the rise in the relative intensity of the crystalline Ge–Ge peak in the Raman spectra.

The FTIR spectra in the wavenumber span of 1800–2200 cm^{-1} for the SiGe films were deconvoluted into five Gaussian components to analyse the stretching mode vibrational behaviour of the Ge and Si in the film matrix. The deconvoluted spectra, as

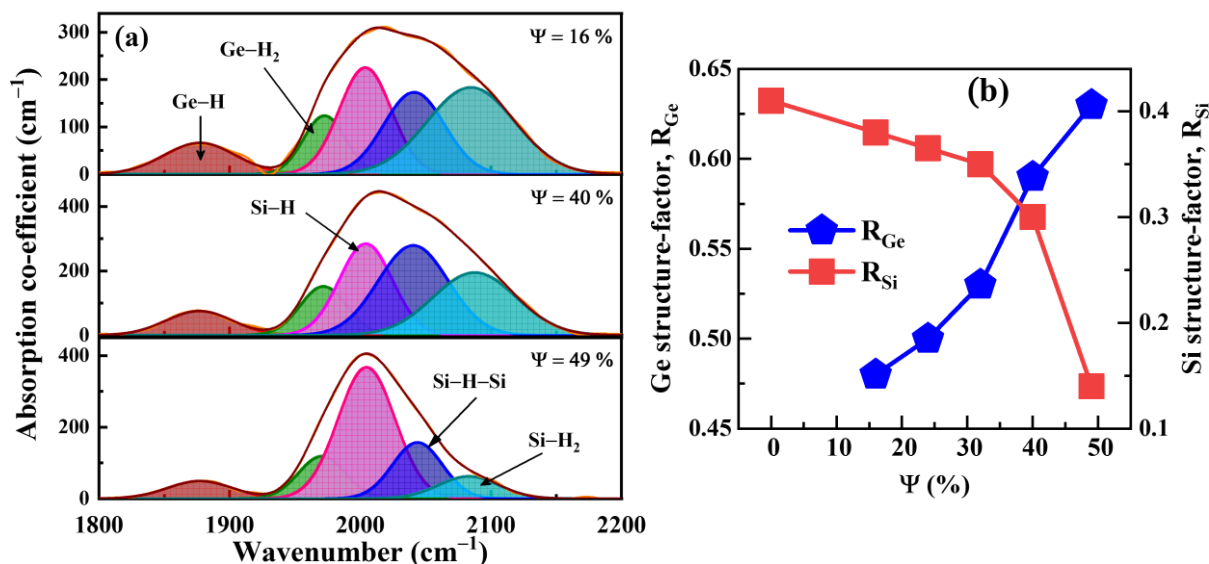


Fig. 8.6. (a) Deconvoluted FTIR spectra in the range 1800–2200 cm^{-1} .
(b) Variation of the Ge structure-factor (R_{Ge}) and Si structure-factor (R_{Si}) with Ψ .

presented in **Fig. 8.6(a)**, identifies the following peaks centred at (1) ~1880–1885 cm^{-1} , (2) ~1970 cm^{-1} , (3) ~2005–2010 cm^{-1} , (4) ~2040–2045 cm^{-1} and (5) ~2085 cm^{-1} signifying the Ge–H monohydride stretching mode, Ge–H₂ di-hydride stretching mode, Si–H mono-hydride stretching mode, Si–H–Si platelet-like-configuration and the Si–H₂ di-hydride stretching mode respectively [34,38]. The Ge-structure factor (R_{Ge}) and Si-structure factor (R_{Si}), that describe the relative contributions of the corresponding poly-hydride components (GeH_x and SiH_x , $x \geq 2$) in their individual network's stretching mode, are used to quantify the overall microstructural changes in SiGe alloy thin films [34].

$$R_{\text{Ge}} = \frac{[\text{GeH}_2]}{[\text{GeH}] + [\text{GeH}_2]} \quad (8.5)$$

$$R_{\text{Si}} = \frac{[\text{SiH}_2]}{[\text{SiH}] + [\text{Si-H-Si}] + [\text{SiH}_2]} \quad (8.6)$$

The integrated area of the corresponding satellite components constituting the stretching modes is represented by $[\text{GeH}]$, $[\text{GeH}_2]$, etc. In **Fig. 8.6(b)**, the variation of R_{Ge} and R_{Si} with Ψ is represented. R_{Ge} has monotonically enhanced from 0.48 to 0.53 with variation in Ψ from 16% to 32%, as the integrated area under the Ge–H₂ satellite components rises with respect to the integrated area of the Ge–H monohydride peak. Further increase in

the Ψ to 49% resulted in a sharper rise in the R_{Ge} to 0.63. However, the Si-structure factor slowly reduced in the range $0\% \leq \Psi \leq 32\%$, whereas, further increase in Ψ resulted in sharp decline in R_{Si} . The contribution of the SiH_2 dihydride vibrational peak gradually weakened upon increasing the Ψ .

High-resolution transmission electron microscopy of the SiGe films has been carried out to have a deeper insight into the film's microstructure. In **Fig. 8.7(a)**, the dark patches with sharp boundaries in the plane view HRTEM (high-resolution transmission electron micrograph) image of the sample prepared with $\Psi = 24\%$ demonstrates that the nanocrystallites are randomly dispersed in the amorphous matrix and the corresponding selected area diffraction pattern (SAED) indicated sharp and bright rings are corresponding to $\langle 111 \rangle$, $\langle 220 \rangle$ and $\langle 311 \rangle$ lattice planes of c-Si, shown in the inset of **Fig. 8.7(a)**. The higher magnified TEM images in **Fig. 8.7(b)**, the nanocrystals with $\langle 111 \rangle$ lattice planes are visible, whereas the reduced FFT images in **Fig. 8.7(b-i)** shows the presence of $\langle 111 \rangle$ and $\langle 220 \rangle$ planes in the TEM micrograph. The energy-dispersive

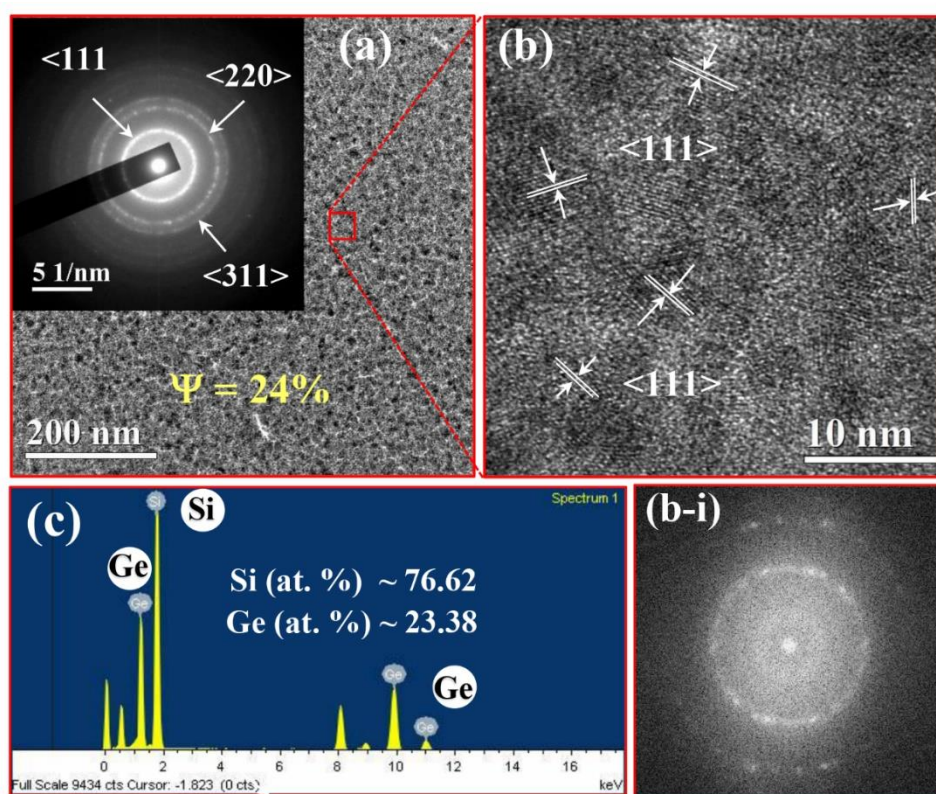


Fig. 8.7. (a) Plane-view HRTEM image of the sample prepared with $\Psi = 24\%$, with the corresponding diffraction pattern presented in the inset. (b) Magnified TEM micrograph with prominent crystallographic planes with FFT image presented in (b-i). (c) EDX spectra recognizing the elements, with mentioning the elemental atomic percentage of Si and Ge.

X-ray spectroscopy (EDS) studies of the SiGe alloy, presented in **Fig. 8.7(c)**, distinguishes the particular peaks associated with the Ge and Si, from which the atomic percentage of these two elements were estimated to be $\sim 23.38\%$ and $\sim 76.62\%$, respectively.

Changes in the surface morphology of the nc-SiGe films, with the variation in Ge content through changing the Ψ , is speculated in the $5\ \mu\text{m} \times 5\ \mu\text{m}$ three-dimensional AFM (atomic force microscope) images as depicted in **Fig. 8.8(a) – (d)**, in which the

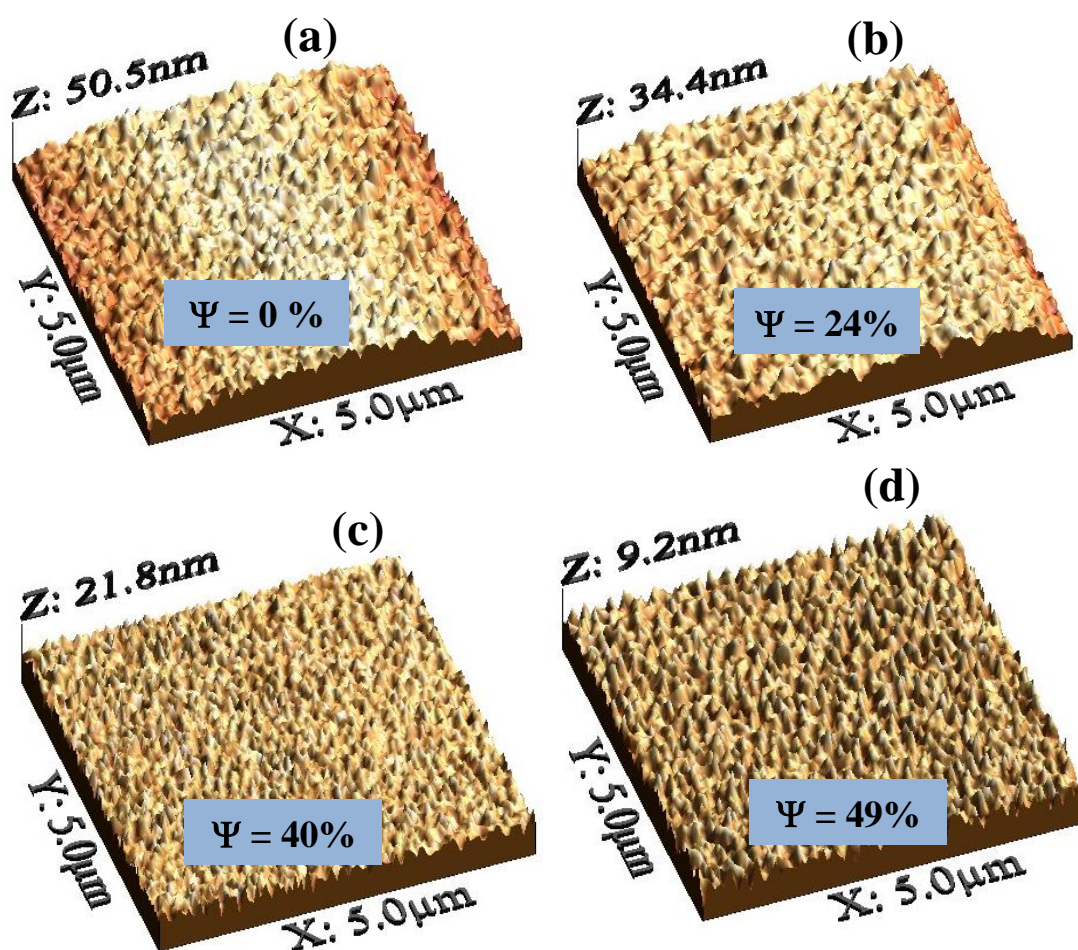


Fig. 8.8. Typical $5\ \mu\text{m} \times 5\ \mu\text{m}$ three-dimensional AFM images of nc-SiGe films prepared with (a) $\Psi = 0\%$, (b) $\Psi = 24\%$, (c) $\Psi = 40\%$ and (d) $\Psi = 49\%$.

variation of clusters and crystallites of different shape and size is observed. In the AFM images presented in **Fig. 8.8(a)** and **Fig. 8.8(b)**, large clusters and recognized voids have been observed, which is corroborated through the good crystallinity in the film matrix. However, at a higher Ge incorporation in the film matrix transformed the surface morphology with smaller clusters (in **Fig. 8.8(c)** and **Fig. 8.8(d)**) with increase in Ψ could

be attributed to the decrease in the grain size and the crystallinity, as evidenced in the XRD studies. **Fig. 8.9** shows the variation of root-mean-square (RMS) roughness estimated from the AFM measurements. The change in the microstructure of the films firmly controls the morphology and the roughness [39]. The RMS roughness decreases monotonically with the increase in the Ψ , from 7.62 nm corresponding to the sample prepared with $\Psi= 0\%$ to 1.01 nm corresponding to the sample $\Psi= 40\%$. The fall in the surface roughness signifies the decrease in the crystallization with an increase in Ge content in the film. Interestingly, further, increase Ψ to 49% resulted in a slight rise in the RMS roughness. This might be due to the improvement in the crystallization developed in the Ge-Ge network for the film prepared at $\Psi= 49\%$, as depicted in the Raman data.

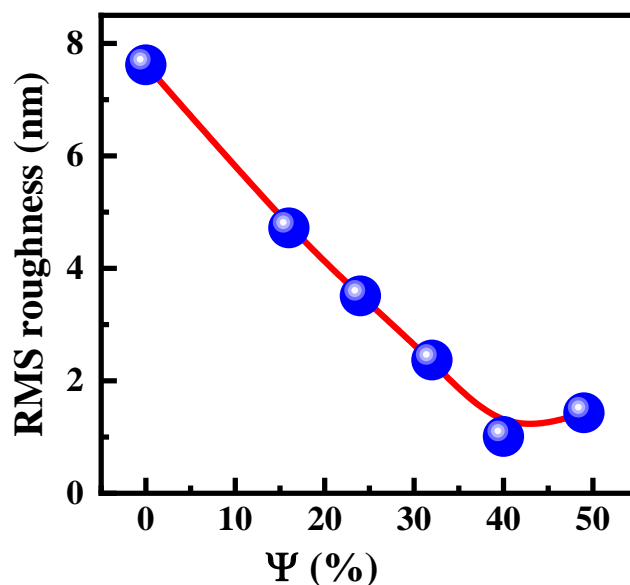


Fig. 8.9. Variation of the RMS roughness of the nc-SiGe films with change in Ψ .

The electrical transport properties of the nanocrystalline silicon germanium films were investigated through temperature-dependent dark conductivities. The change in the dark conductivity and the activation energy are presented in **Fig. 8.10**. The nc-Si film prepared at $\Psi = 0\%$ exhibited dark conductivity $\sigma_D \sim 3.17 \times 10^{-3} \text{ S cm}^{-1}$ with a corresponding activation energy $\sim 0.37 \text{ eV}$. The dark conductivity has substantially reduced to $\sigma_D \sim 1.12 \times 10^{-3} \text{ S cm}^{-1}$ for the nc-SiGe film ($\Psi = 16\%$) with the initial inclusion of Ge in the film matrix, and the ΔE has increased to 0.4 eV . With further increase in the Ψ to 49%, σ_D has decreased to $\sim 7.61 \times 10^{-5} \text{ S cm}^{-1}$ with an escalated activation energy of $\sim 0.57 \text{ eV}$.

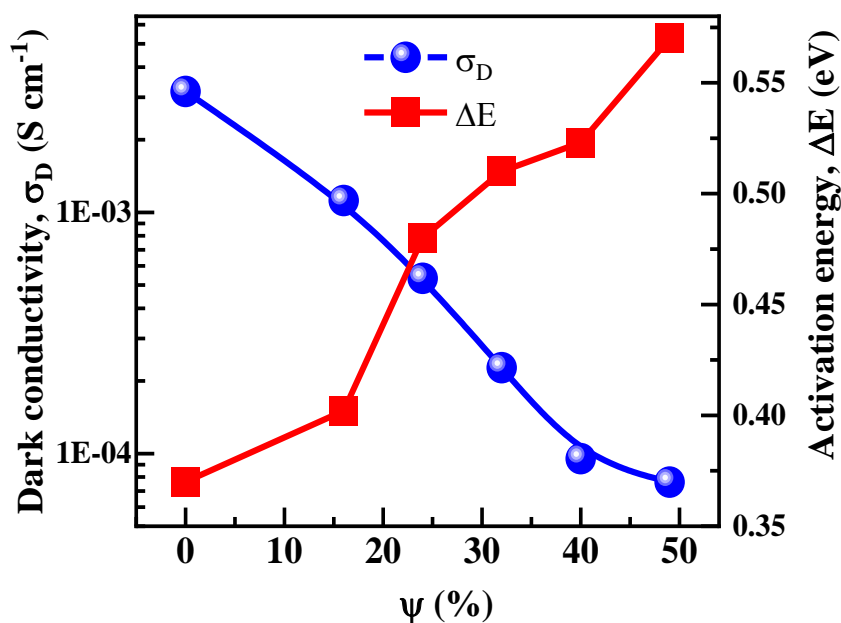


Fig. 8.10. Variation of the dark conductivity and activation energy of the nc-SiGe films with change in Ψ .

The effect of the increase in Ψ demonstrated a significant contribution in narrowing the optical band gap of the alloy thin films through increasing the Ge incorporation in the Si-rich nc-SiGe alloy; however, use of Ψ as 49% resulted in the growth of Ge-dominated nc-SiGe thin film. In the present study, although the band gap of the SiGe material is strongly determined on the basis of Si/Ge composition of the films, it is strongly influenced by the residing crystallinity in the heterogeneous binary material and the bonded hydrogen within the matrix. The monotonic decrease in the optical band gap here is the function of an increase in the Ge content and the reducing bonded hydrogen content in the film matrix. Under the present growth conditions, the increase in the Ge content in the film leads to an increase in the poly-hydrogenation in the Ge-Ge matrix, as reflected in the sharp rise in the Ge-structure factor, R_{Ge} , whereas R_{Si} has reduced, with an increase in the surface area opening of the Ge target.

Nakamura *et al.* [22] reported the reduction in crystallization temperature from 600°C to 400°C with introducing hydrogen into the sputtering gases, with associated dark conductivity varying in between $2.1 \times 10^{-6}\ S\ cm^{-1}$ to $1.2 \times 10^{-2}\ S\ cm^{-1}$, where they did not report the corresponding change in the optical band gap. Tsao *et al.* [21] reported the growth of Ge-rich nc-SiGe films with an accompanying optical band gap in between 1.07 eV and 0.78 eV with corresponding dark conductivity varying as $3 \times 10^{-2}\ S\ cm^{-1}$ – $20\ S\ cm^{-1}$; however, this nanocrystalline growth has taken place at a higher temperature

of $\sim 500^\circ\text{C}$ in the sputtering process using Ar/H₂ mixture. Shahahmadi *et al.* [40] studied the synthesis of Ge-rich SiGe thin films by RF magnetron sputtering for photovoltaic applications. The nanocrystallization in the films was obtained via annealing at different temperatures 450°C – 550°C for 5 h and having a band gap of 1.2–1.26 eV. In this present investigation, nc-SiGe thin films has been grown in single-step process at low temperature of 250°C , that have optical band gap in between 1.68 eV–1.18 eV with corresponding dark conductivity varying from $3.17 \times 10^{-3} \text{ S cm}^{-1}$ to $7.61 \times 10^{-5} \text{ S cm}^{-1}$ (as presented in Fig. 8.11).

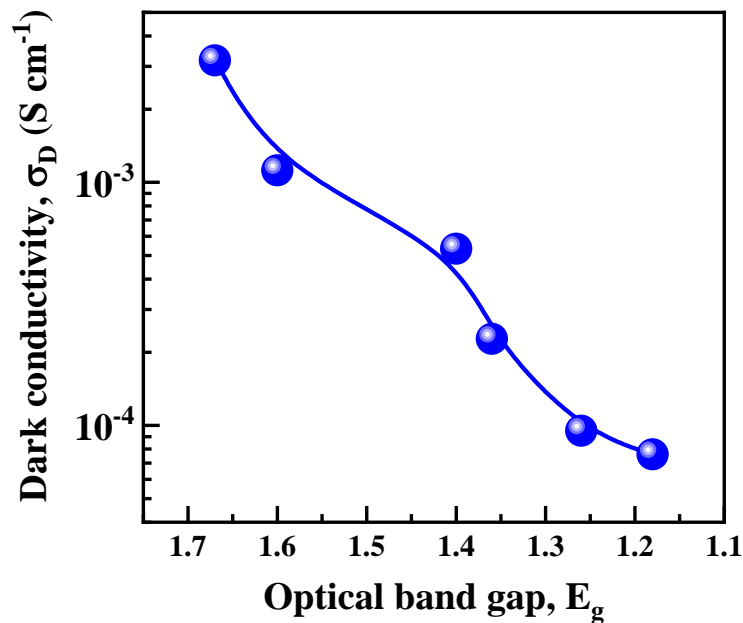


Fig. 8.11. Changes in the dark conductivity as a function of the changing optical band gap of the nc-SiGe network.

8.4 Conclusion

Optoelectronic, structural and morphological properties of the nc-SiGe films sputtered on glass substrates at a low substrate temperature of 250°C have been investigated. The nc-SiGe films have been deposited by changing the area opening ($\Psi\%$) of the Ge target's erosion area using a crystalline Si wafer in the RF magnetron sputtering process. The nanostructural evolutions of the deposited SiGe films as characterized by Raman and XRD measurements, are in good agreement. The increased inclusion of Ge atoms in the film matrix leads to reduced bonded hydrogen content in the film matrix and decreases the optical band gap. The average grain size for $\langle 111 \rangle$ crystallographic orientation has decreased from 23.36 nm to 12.97 nm, increasing $\Psi \leq 40\%$. However, at

more elevated $\Psi = 49\%$, the average grain size of the SiGe film has increased marginally, which indicates the increased incorporation of Ge atoms in the matrix at a certain level resulted in mostly Ge-dominated SiGe film matrix, in which the crystallization has taken place rather in the Ge–Ge network, with amorphous Si–Si network present there. The RMS roughness of the sputtered alloy films was found to be an inherent function of the crystallinity present in the film matrix. The nc-SiGe films prepared at $24\% \leq \Psi \leq 32\%$, with an optimal narrow optical band gap of $\sim 1.36 - 1.41$ eV along with good electrical properties ($\sigma_D \sim 5.33 \times 10^{-4} - 2.77 \times 10^{-4} \text{ Scm}^{-1}$), seems remarkable as it has been prepared in single-step processing at a low temperature of $\sim 250^\circ\text{C}$, which appeared to be good absorber layer at the bottom sub-cell of the nc-Si multi-junction solar cell.

8.5 References

- [1] S. Guha, J. Yang, B. Yan, *Sol. Energy Mater. Sol. Cells* 119 (2013) 1–11.
- [2] A. Shah, P. Torres, R. Tscharnner, N. Wyrsh, H. Keppner, *Science* 285 (1999) 692–698.
- [3] J. Yang, A. Banerjee, S. Guha, *Sol. Energy Mater. Sol. Cells* 78 (2003) 597–612.
- [4] R.B. Bergmann, *Appl. Phys. A* 69 (1999) 187–194.
- [5] F. Schindler, A. Fell, R. Müller, J. Benick, A. Richter, F. Feldmann, P. Krenckel, S. Riepe, M.C. Schubert, S.W. Glunz, *Sol. Energy Mater. Sol. Cells* 185 (2018) 198–204.
- [6] Q. Ren, S. Li, S. Zhu, H. Ren, X. Yao, C. Wei, B. Yan, Y. Zhao, X. Zhang, *Sol. Energy Mater. Sol. Cells* 185 (2018) 124–129.
- [7] G. Ganguly, T. Ikeda, T. Nishimiya, K. Saitoh, M. Kondo, A. Matsuda, *Appl. Phys. Lett.* 69 (1996) 4224–4226.
- [8] A. Dey, D. Das, *J. Phys. Chem. Solids* 154 (2021) 110055.
- [9] Y. Cao, Y. Liu, J. Zhou, Y. Wang, J. Ni, J. Zhang, *Sol. Energy Mater. Sol. Cells* 151 (2016) 1–6.
- [10] R. Jiménez, M. Moreno, A. Torres P. Rosales, M.T. Sanz, R. Ambrosio, *Phys. Status Solidi* 215 (2018) 1700736.
- [11] Q. Wang, H. Vogt, *J. Electron. Mater.* 48 (2019) 7360–7365.
- [12] F.L. Huerta, R.M.W. García, L.G. González, A.L.H. May, W.C. Arriaga, R. Vega, E. Soto, *IOP Conf. Ser. Mater. Sci. Eng.* 628 (2019) 012003.

- [13] L. Tsybeskov, D. J. Lockwood, Proc. IEEE 97 (2009) 1284.
- [14] Z. Yu, X. Zhang, H. Zhang, Y. Huang, Y. Li, X. Zhang, Z. Gan, J. Alloys Compd. 803 (2019) 260–264.
- [15] X. Ji, H.Y. Cheng, A.J. Grede, A. Molina, D. Talreja, S.E. Mohny, N.C. Giebink, J.V. Badding, V. Gopalan, APL Mater. 6 (2018) 046105.
- [16] M. Shima, A. Terakawa, M. Isomura, H. Haku, M. Tanaka, K. Wakisaka, S. Kiyama, S. Tsuda, J. Non-Cryst. Solids 442 (1998) 227–230.
- [17] D. J. Paul, Semicond. Sci. Technol. 19 (2004) R75.
- [18] A. Dey, D. Das, J. Alloys Compd. 806 (2019) 1529–1535.
- [19] M. Stutzmann, R.A. Street, C.C. Tsai, J.B. Boyce, S.E. Ready, J. Appl. Phys. 66 (1989) 569.
- [20] M. Krause, H. Stiebig, R. Carius, U. Zastrow, H. Bay, H. Wagner, J. Non-Cryst. Solids 299–302 (2002) 158–162.
- [21] C.Y. Tsao, Z. Liu, X. Hao, M.A. Green, Appl. Surf. Sci. 257 (2011) 4354–4359.
- [22] I. Nakamura, T. Ajiki, H. Abe, D. Hoshi, M. Isomura, Vacuum 80 (2006) 712–715.
- [23] F. Qiu, W. Shin, M. Matsumiya, N. Izu, N. Murayama, Jpn. J. Appl. Phys. 2 (42) (2003) 1563–1567.
- [24] K. Tajima, F. Qiu, W. Shin, N. Sawaguchi, N. Izu, I. Matsubara, N. Murayama, Jpn. J. Appl. Phys. 43 (2004) 5978–5983.
- [25] W.K. Choi, L.K. Teh, L.K. Bera, W.K. Chim, A.T.S Wee, Y.X. Jie, J. Appl. Phys. 91 (2002) 444–450.
- [26] E.V. Jelenkovic, K.Y. Tong, Z. Sun, C.L. Mak, W.Y. Cheung, J. Vac. Sci. Technol. A 15 (1997) 2836–2841.
- [27] D.D. Cannon, J. Liu, D.T. Danielson, S. Jongthammanurak, U.U. Enuha, K. Wada, J. Michel, L.C. Kimerling, Appl. Phys. Lett. 91 (2007) 252111–252113.
- [28] D. Raha, D. Das, J. Phys. D: Appl. Phys. 41 (2008) 085303.
- [29] U. Holzwarth, N. Gibson, Nature Nanotech 6 (2011) 534.
- [30] T. Tah, C.K. Singh, S. Amirthapandian, K.K. Madapu, A. Sagdeo, S. Ilango, T. Mathews, S. Dash, Mater. Sci. Semicond. Process. 80 (2018) 31–37.
- [31] K. Bhattacharya, D. Das, J. Phys. D Appl. Phys. 41 (2008) 155420.
- [32] D. Wang, Z. Yang, F. Li, D. He, Appl. Surf. Sci. 257 (2011) 8350–8354.

- [33] J. Tauc, R. Grigorovici, A. Vancu, *Phys. Status Solidi (b)* 15 (1966) 627–637.
- [34] D. Das, A. Dey, *Phys. E: Low-dimens. Syst. and Nanostruct.* 111 (2019) 20–28.
- [35] S. Hazra, A.R. Middy, S. Ray, *J. Phys. D: Appl. Phys.* 29 (1996) 1666–1674.
- [36] C. Patra, D. Das, *J. Appl. Phys.* 126 (2019) 155305.
- [37] T.W. Li, Y.Q. Xu, S.Y. Wang, Y.W. Yu, Y. Ma, W.Y. Niu, *IOP Conf. Series: Mater. Sci. Eng.* 761 (2020) 012005.
- [38] P. Mondal, D. Das, *RSC Adv.* 5 (2015) 54011.
- [39] D. Das, B. Sain, *J. Appl. Phys.* 114 (2013) 073708.
- [40] S.A. Shahahmadi, A. Aizan, B. Bais, M. Akhtaruzzaman, A.R.M. Alamoud, N. Amin, *Mater. Sci. Semicond. Process.* 56 (2016) 160–165.



Chapter 9

**Summary, conclusion
& future outlook**

9.1 Summary

The prime objective of the present work is the development of intrinsic nanocrystalline silicon germanium thin films from the single-step spontaneous plasma processing at low temperature in a capacitively coupled plasma CVD for its efficient applications in multi-junction tandem-structure nanocrystalline silicon solar cells. In a parallel approach, nanocrystalline silicon-germanium thin films are prepared by the physical vapour deposition technique at a low temperature in the 13.56 MHz magnetron sputtering method.

The work begins with developing the nc-SiGe thin films by substantially incorporating Ge atoms into the matrix using an optimum RF power in the hydrogen diluted ($\text{SiH}_4 + \text{GeH}_4$) plasma in a capacitively coupled PECVD. At a lower RF power, the faster dissociation of GeH_4 over SiH_4 leads to a Si-deficient Ge-populated amorphous SiGe film network with a low band gap and poor dark conductivity. At the increased RF power, the relative population of the Si moieties with the Ge moieties gradually increases along with gradual crystallization in the Si-Si network. The nc-SiGe thin film with superior crystallinity and a substantial amount of Ge moieties in the film matrix has been obtained. The structure factor related to Si and Ge networks increases continuously with elevating RF power. At higher RF power, the severe increase in the Ge-structure factor relative to the Si-structure factor indicates the overpopulation of the Ge-polyhydrides in the film matrix, leading to a sharp deterioration of the electrical properties of the film. Additionally, the bonded-H content of the network sharply decreases with the initial nanocrystallization of the film network with the increase in RF power. Later, it has been increased marginally with a further increase in the RF power. The substantial presence of the Ge atoms in the nc-Si network contributes to the lowering of the band gap, whereas the improved crystallinity at an optimum (minimum) RF power resulted in high electrical conductivity ($\sigma_D \sim 2.38 \times 10^{-3} \text{ S cm}^{-1}$) along with narrow band gap ($\sim 1.50 \text{ eV}$). Another significance and novelty in this work is that the nanocrystallization in both the Si-Si and Ge-Ge network in the SiGe alloy plays a significant role in narrowing the optical band gap.

The main constraint lies in its rapid decline of optoelectronic properties at enhanced Ge-inclusion, through the two-phase hetero-structure contributes two transport paths, overpopulation of dangling bonds and non-uniform distribution of hydrogen bonding within its two competent counterparts, towards complete amorphization of the

film network. In the next part, nanocrystalline silicon germanium thin films have been prepared using different hydrogen dilutions. A Ge-dominated low band gap amorphous silicon germanium network with subsequent low dark conductivity is obtained. At an increased H₂-dilution, highly nanocrystalline SiGe-network with a significant nc-Ge component is produced; however, a reduced Ge-content with its H-bonding in mostly poly-hydride configuration opposes bandgap narrowing. An intense flux of impacting atomic-H enhances the surface mobility of the arriving radicals at the growth sites and plays an important role in further reinforcing the nanocrystallinity in the alloy network through the preferential etching of the weak Ge–Ge bonds in the film. The inclusion of Ge atoms in its crystalline network is beneficial for sustaining the nanocrystallinity in the alloy network and keeping the residence of Ge moieties within it.

It is found that the preparation of nc-SiGe thin film in the nc-Si growth compatible plasma conditions in PECVD happens at the restricted presence of Ge atoms that follows less adequate execution of band gap narrowing. The conventional approach of gradual addition of GeH₄ in the nc-Si growth-consistent plasma condition grossly changes the dissociation kinematics of the (SiH₄ + GeH₄), extends the tunability by narrowing its optical band gap but hinders in sustaining delicate electrical properties by eventually destroying the nanocrystallinity in the SiGe network. Keeping that in consideration, in the next part of the thesis work, an nc-SiGe thin film has been prepared in the capacitively coupled RF-PECVD through the efficient incorporation of the Si atoms in the nanocrystalline Ge network via increasing the SiH₄ gas flow ratio in the (SiH₄ + GeH₄) plasma; as the growth conditions consistent for nc-Ge growth are completely different from the deposition conditions compatible for nc-Si growth. The Si incorporation in the nc-Ge matrix shows a decrease in the films' grain size and overall crystallinity. The optical band gap of the film increases, accompanied by a decrease in the dark conductivity and an increase in the SiH₄ concentration. The nc-Si_xGe_{1-x} film with the optimal low band gap of 1.23 eV and a high dark conductivity $\sim 4.72 \times 10^{-4} \text{ S cm}^{-1}$ appeared appropriate for the absorber layer at the bottom sub-cell of the nc-Si tandem structure solar cells. In this investigation, it has been confirmed that the decomposition of SiH₄ under nc-Ge compatible growth conditions occurs in a controlled manner that is beneficial for sustaining the nanocrystallinity in the binary SiGe alloy containing a Ge-dominated atomic composition that can provide the required infrared response and electrical transport for strategic applications in photovoltaics.

And at the end of the thesis, nanocrystalline silicon germanium thin films have been achieved at a low temperature of 250 °C, from a one-step process by co-sputtering of Ge target (99.999% purity) and nc-Si wafers, using (Ar + H₂) plasma in the RF magnetron sputtering deposition system. Changes in the structural morphology and optical band gap due to the change in composition are studied.

9.2 Conclusion

In the present thesis work, nanocrystalline silicon germanium thin films, have been prepared at a low substrate temperature in a capacitively coupled PECVD system (13.56 MHz), narrowing the optical band gap efficiently sustaining the electrical properties, compatible for the application in nanocrystalline silicon tandem-structure solar cells. Restricted presence of Ge in the SiGe film grown under nc-Si growth compatible conditions only allow growth of nc-SiGe in PECVD. It has been confirmed that the decomposition of SiH₄ in (GeH₄ + SiH₄) plasma occurs in a controlled manner under nc-Ge compatible growth conditions that is beneficial for sustaining the nanocrystallinity in the binary SiGe alloy containing a Ge-dominated atomic composition that can provide the required infrared response and electrical transport for strategic applications in photovoltaics. Comprehensive investigations of these nc-SiGe thin films on their structural, optical and electrical properties have been studied in view of their optimization and application in devices.

Further, nanocrystalline SiGe thin films have been developed in an RF magnetron sputtering system in a single-step process, via tactically co-sputtering of nc-Si wafer and Ge target in (Ar+H₂) plasma under nc-Ge growth compatible plasma conditions, with embedding nc-Si and nc-Ge grains embedding the binary alloy matrix with significant nanocrystallinity, low band gap and electrical properties. In the preparation of SiGe alloy, involving sputtered nc-Si grains from the nc-Si wafer becomes beneficial for its low-temperature single-step growth. As no harmful gases such as SiH₄ and GeH₄ are involved, this is a more environment-friendly technique for nc-SiGe thin film growth than PECVD. We hope that the present work, which has explored a new process of producing of nanocrystalline silicon germanium thin films in the sputtering deposition technique, could open up a convenient avenue for the fabricating devices with nc-SiGe thin films. This technique also looks suitable for the growth of the nc-SiGe absorber layer for tandem-structured nc-Si solar cells, as this synthesis occurred at a low temperature of

250 °C. However, slower deposition rate of the nc-SiGe thin films in this sputtering technique compared to that in PECVD growth is a major disadvantage in it.

9.3 Future outlook

From the extensive literature survey and the propelled inquiry about nanocrystalline silicon germanium thin films, it is well established that they are a significant material for photovoltaic as well as electronic, optoelectronic device applications.

One of the important avenues in achieving high-efficiency solar cells at low production cost (i.e. third-generation solar cells) is the multi-junction solar cell, which can progressively boost efficiency by utilizing the extended solar spectrum. In multi-junction solar cells, different absorber materials can be used in stacked-layer configurations. Each layer's optical and electrical properties, whether doped or intrinsic, should be tuned so that light can be efficiently absorbed in each absorber layer. During this project, such tuning of the properties has been successfully achieved, which can be utilized in the practical application of photovoltaic devices. Using the CVD process, the next study will surely be involved in the critical utilization of nc-SiGe thin films in the bottom cell of multi-junction solar cells. The accomplishment of the all silicon multi-junction solar cells also requires the development of other chosen intrinsic and doped materials for the top and middle cells by proper plasma processing.

In view of its application in device fabrications, the single-step processing of nc-SiGe thin film in the sputtering deposition technique, we will continue the further optimization of the plasma parameters for tailoring its optoelectrical properties by virtue of changing the composition ratio, accommodating higher density nanocrystallites in the film matrix and attempt its device applications.